Low-Complexity Adaptive Digital Equalizers for Electronic Dispersion Compensation in Optical Fiber Links

Vorgelegt von

Daniel Efinger

aus Aixheim

Contents

Acronyms and Abbreviations

ADC	analog-to-digital converter
ASE	amplified spontaneous emission
AWGN	additive white Gaussian noise
b2b	back-to-back
BER	bit error ratio
BPF	band-pass filter
CD	chromatic dispersion
CDF	cumulative distribution function
CDR	clock and data recovery
CM	constant modulus
CMOS	complementary metal-oxide semiconductor
CSI	channel state information
CSRZ	carrier suppressed return-to-zero
CW	continuous wave
DBBS	DeBruijn binary sequence
DCF	dispersion-compensating fiber
DD	direct detection
DFE	decision feedback equalizer
DFT	discrete Fourier transform
DGD	differential group delay
DSF	disperison-shifted fiber
EDC	electronic dispersion compensation
EDFA	Erbium-doped fiber amplifier
EP	electronic predistortion
ES-LMS	error-sign LMS
FEC	forward error correction
FFE	feed-forward equalizer
FFT	fast Fourier transform
FIR	finite impulse response
FSFFE	fractionally spaced feed-forward equalizer
FWM	four-wave mixing
GF	Galois field
GVD	group velocity dispersion

HD	high-definition
i.i.d.	independent and identically distributed
IFFT	inverse fast Fourier transform
ISI	intersymbol interference
ITU	International Telecommunication Union
KF	Kalman filter
LAN	local area network
LD	laser diode
LFSR	linear feedback shift register
LMN	least mean $2n$-th order
LMS	least mean square
LPF	low-pass filter
LLS	linear least squares
LUT	look-up table
MAN	metropolitan area network
MAP	maximum a posteriori
MAV	moving average
MGF	moment-generating function
MIN-BER	minimal bit error ratio
ML	maximum likelihood
MLSE	maximum likelihood sequence estimation
MLSE-VE	maximum likelihood sequence estimation based Viterbi equalizer
MMSE	minimum mean squared error
MMN	minimum mean $2n$-th order
MSB	most significant bit
MSE	mean squared error
MZM	Mach-Zehnder modulator
NLMS	normalized least mean square
NRZ	non-return-to-zero
OA-IM/DD	optically amplified intensity modulation with direct detection
OEO	optical-electrical conversion and optical-electrical reconversion
OSNR	optical signal-to-noise ratio
PBS	polarization beam splitter
PD	photodiode
PDF	probability density function
PDL	polarization dependent loss
PLC	planar lightwave circuit
PMD	polarization mode dispersion
PnP	Plug'n Play
PRBS	pseudo-random binary sequence
PSP	principal states of polarization

QI-LMS	quantized input LMS
RLS	recursive least squares
RMS	root-mean-square
RX	receiver
sbs	symbol-by-symbol
SBS	stimulated Brillouin scattering
SiGe	Silicon-Germanium
SLD	square law detection
SNR	signal-to-noise ratio
SPM	self-phase modulation
SSMF	standard single mode fiber
TEM	transverse electromagnetic
TES-LMS	thresholded error-sign LMS
TX	transmitter
VA	Viterbi algorithm
VLSI	very-large-scale integration
WAN	wide area network
WDM	wavelength division multiplex
XPM	cross-phase modulation
ZF	zero-forcing

Notation and Symbols

Notation

$\cdot^{\mathrm{T}}$	transposition
$*$	convolution operator
$\binom{n}{i}$	binomial coefficient
$\cdot_x$	subscript for x-polarization
$\cdot_y$	subscript for y-polarization
$\cdot^*$	conjugate complex
$\cdot_{th}$	subscript for (decision) thresholds
$\circ\!\!-\!\!\bullet, \bullet\!\!-\!\!\circ$	Fourier and inverse Fourier transform correspondence
$\cdot^{\mathrm{H}}$	Hermitian transposition
$\lceil \cdot \rceil$	smallest integer equal or larger than the argument
$\lfloor \cdot \rfloor$	largest integer equal or smaller than the argument
$\nabla\cdot$	nabla operator
$\tilde{\cdot}$	tilde for the equivalent baseband representation of a variable
$0x9$	hexadecimal number (example)
1001_2	binary number (example)
$\arg\max\limits_{x} f(x)$	maximization of $f(x)$ with respect to x and returning x
$\arg\min\limits_{x} f(x)$	minimization of $f(x)$ with respect to x and returning x
$C(\cdot \mid \cdot)$	conditional cumulative distribution function (CDF)
$\cdot \mathrm{div} \cdot$	integer division
$\mathsf{E}[\cdot]$	expectation value of a random variable
$\mathscr{F}\{\cdot\}, \mathscr{F}^{-1}\{\cdot\}$	Fourier and inverse Fourier transform operator
$\mathrm{FFT}^{-1}\{\cdot\}$	inverse fast Fourier transform (IFFT) operator
$\mathrm{GF}(2^n)$	Galois field with characteristic prime number p and exponent n
$h_p(\cdot \mid \cdot)$	conditional histogram as a measurement for a conditional probability density function (PDF)
j	imaginary unit
$\mathrm{ld}(\cdot)$	logarithm to the base 2
$\mathrm{lg}(\cdot)$	logarithm to the base 10
$\mathrm{ln}(\cdot)$	logarithm to the base 2
$\lim\cdot$	limit of an expression
$\max\cdot$	maximization of an expression

min $\cdot$	minimization of an expression
$\cdot$ mod $\cdot$	modulo operation (remainder after integer division)
$\mathbb{N}$	set of natural numbers
$\mathbb{N}_n$	subset of the natural numbers starting with the element n
$p\left(\cdot\,\vert\,\cdot\right)$	conditional probability density function (PDF)
$p\left(\cdot\right)$	probability density function (PDF)
$P[\cdot]$	probability of discrete random variables
$\mathbb{Q}$	set of rational numbers
$\mathbb{R}$	set of real numbers
$\mathbb{R}_+$	set of positive real numbers including zero
$\mathrm{Re}\{\cdot\}$	real part
$\mathrm{sgn}(\cdot)$	signum function
$\mathrm{sinc}(\cdot)$	$\sin\left(\cdot\,/\,\cdot\right)$ (sinus cardinalis)
$\mathbb{Z}$	set of integer numbers
$q(\cdot)$	lower case letters for time domain signals and impulse responses
$Q(\cdot)$	upper case letters for frequency spectra, transfer functions and constants in time and frequency domain
$\mathbf{q}(\cdot), \mathbf{Q}(\cdot)$	bold face letters for multidimensional signals and frequency spectra
Symbols	
α	attenuation constant in Np/m
α_{dB}	attenuation constant in dB/km
$\alpha_x\left(f\right), \alpha_y\left(f\right)$	attenuation constants in Np/m
$\tilde{\mathbf{a}}_e(t) \circ\!\!-\!\!\bullet \tilde{\mathbf{A}}_e\left(f\right)$	complex-valued envelope of the optical TX signal vector
$\tilde{\mathbf{a}}_{\mathrm{RX}}(t) \circ\!\!-\!\!\bullet \tilde{\mathbf{A}}_{\mathrm{RX}}\left(f\right)$	equivalent baseband description of the optical RX signal vector
$\tilde{\mathbf{a}}(z,t) \circ\!\!-\!\!\bullet \tilde{\mathbf{A}}\left(z,f\right)$	equivalent baseband description of the optical signal at location z
$\tilde{a}_x(z,t), \tilde{a}_{\mathrm{TX},y}(z)t$	equivalent baseband description of the x- and y-polarization modes at location z
$\tilde{\mathbf{a}}_{\mathrm{AF}}(t)$	equivalent baseband description of the reamplified and filtered optical RX signal vector
$\tilde{\mathbf{a}}_{\mathrm{TX}}(t) \circ\!\!-\!\!\bullet \tilde{\mathbf{A}}_{\mathrm{TX}}\left(f\right)$	equivalent baseband description of the optical TX signal vector
$\tilde{a}_{\mathrm{TX},x}(t) \circ\!\!-\!\!\bullet \tilde{A}_{\mathrm{TX},x}\left(f\right)$	equivalent baseband description of the TX x-polarization mode
$\tilde{a}_{\mathrm{TX},y}(t) \circ\!\!-\!\!\bullet \tilde{A}_{\mathrm{TX},y}\left(f\right)$	equivalent baseband description of the TX y-polarization mode
$a_{\mathrm{RX}}(t) \circ\!\!-\!\!\bullet A_{\mathrm{RX}}\left(f\right)$	optical RX signal
$a(z,t) \circ\!\!-\!\!\bullet A\left(z,f\right)$	optical signal at location z
$a_e(t) \circ\!\!-\!\!\bullet A_e\left(f\right)$	real-valued envelope of the optical TX signal
$a_{\mathrm{AF}}(t) \circ\!\!-\!\!\bullet A_{\mathrm{AF}}\left(f\right)$	reamplified and filtered optical RX signal
$a_{\mathrm{TX}}(t) \circ\!\!-\!\!\bullet A_{\mathrm{TX}}\left(f\right)$	optical TX signal
b_{k_i}	upsampled bit at discrete-time instant k_i used for linear least squares (LLS) finite impulse response (FIR) channel approximation of the optically amplified intensity modulation with direct detection (OA-IM/DD) link

b_k	bit at discrete-time instant k
$\hat{b}_k$	bit estimate
B_x	number of bits for the digital representation of the variable x
$\mathbf{b}_K$	bit sequence of length K
$\mathbf{b}_{k_i}$	upsampled bit sequence
$\mathbf{b}_{k_i}$	upsampled input bit vector for the linear least squares (LLS) finite impulse response (FIR) channel approximation of the optically amplified intensity modulation with direct detection (OA-IM/DD) link
$\mathbf{b}_{LFSR,K'}$	linear feedback shift register (LFSR) output sequence of length K'
$\hat{\mathbf{b}}_{k-1}$	decision feedback equalizer (DFE) input bit vector
$\hat{\mathbf{b}}_{L_{tb}}$	bit sequence estimate of length L_{tb}
$B_{3\,\mathrm{dB,opt}}$	3 dB bandwidth of the optical band-pass filter (BPF)
$\beta\left(f\right)$	polarization independent wave number
β_i	Taylor series expansion coefficient for the polarization independent wave number
$\beta_x\left(f\right),\beta_y\left(f\right)$	wave numbers
$B_{k_1,(\ldots)}$	state transition probability at time instant k (dedicated as branch metric for the Viterbi algorithm (VA))
$B_{\mathrm{lg},k_1,(\ldots)}$	logarithmized state transition probability at time instant k (dedicated as branch metric for the Viterbi algorithm (VA))
B_{opt}	useful component of the optical signal bandwidth
BER	bit error ratio
$\mathbf{c}_k$	time-dependent feed-forward equalizer (FFE) coefficient vector
$\mathbf{c}$	time-independent feed-forward equalizer (FFE) coefficient vector
$c_{m,k}$	time-dependent feed-forward equalizer (FFE) coefficient
c_m	time-independent feed-forward equalizer (FFE) coefficient
$\check{\mathbf{c}}_k$	time-dependent feed-forward and decision feedback equalizer (FFE-DFE) coefficient vector
$\check{\mathbf{c}}_{BER}$	minimum bit error ratio (MIN-BER) feed-forward and decision feedback equalizer (FFE-DFE) coefficient vector
$\check{\mathbf{c}}_{MMN}$	optimum minimum mean $2n$-order (MMN) feed-forward and decision feedback equalizer (FFE-DFE) coefficient vector
$\check{\mathbf{c}}_{MMSE}$	optimum minimum mean squared error (MMSE) feed-forward and decision feedback equalizer (FFE-DFE) coefficient vector
$\check{\mathbf{c}}_{ZF}$	optimum zero-forcing (ZF) feed-forward and decision feedback equalizer (FFE-DFE) coefficient vector
$\check{\mathbf{c}}$	time-independent feed-forward and decision feedback equalizer (FFE-DFE) coefficient vector
c_0	speed of light in vacuum
$\Delta_{rel,\cdot}$	mean steady state coefficient offset of the considered adaptation algorithm

$\delta(t)$	Dirac delta function
δ_k	discrete-time unit impulse
$\mathbf{d}_k$	time-dependent decision feedback equalizer (DFE) coefficient vector
$\mathbf{d}$	time-independent decision feedback equalizer (DFE) coefficient vector
$d_{n,k}$	time-dependent decision feedback equalizer (DFE) coefficient
d_n	time-independent DFE coefficient
D_λ	chromatic dispersion coefficient
$\tilde{\mathbf{D}}(z,f)$	dispersion matrix at location z
$\tilde{\mathbf{e}}(t) \circ\!\!-\!\!\bullet \tilde{\mathbf{E}}(f)$	equivalent baseband description of the optical continuous wave (CW) signal vector
$\tilde{e}_x(t), \tilde{e}_y(t)$	equivalent baseband description of the x- and y-polarization of the optical continuous wave (CW) signal
$\tilde{e}(t)$	equivalent baseband description of the scalar optical continuous wave (CW) signal
e_{k_i}	error of the linear least squares (LLS) finite impulse response (FIR) channel approximation of the optically amplified intensity modulation with direct detection (OA-IM/DD) link
e_k	discrete-time error signal
E_0	amplitude of the electrical continuous wave (CW) output field of the laser diode (LD)
$e(t)$	scalar electrical continuous wave (CW) output field of the LD
ε	power extinction ratio of the Mach-Zehnder modulator (MZM)
$f_{3\,\mathrm{dB,el}}$	3 dB cutoff frequency of the electrical low-pass filter (LPF)
ΔF_s	frequency domain sample interval
f	frequency
f_N	Nyquist frequency with respect to the Nyquist intersymbol interference (ISI) criterion
f_0	frequency of the optical continuous wave (CW) signal
f_s	sampling frequency
G_0	amplitude of the non-return-to-zero (NRZ) driver impulse
$g(t)$	non-return-to-zero (NRZ) driver impulse
G	constant gain factor of the Erbium-doped fiber amplifier (EDFA)
γ_{SNR}	signal-to-noise ratio (SNR) in dB
γ_{OSNR}	optical signal-to-noise ratio (OSNR) in dB
γ	power split ratio between x- and y-polarization
$\mathbf{h}$	channel coefficient vector for the linear least squares (LLS) approximation of the optically amplified intensity modulation with direct detection (OA-IM/DD) link
$\mathbf{h}'(\mathbf{c})$	coefficient vector resulting from the convolution of the linear least

	squares (LLS) approximation filter for the optically amplified intensity modulation with direct detection (OA-IM/DD) link and the feed-forward equalizer (FFE) coefficients
$\mathbf{h}'_{ZF,FFE}$	zero-forcing (ZF) condition vector reduced to the lines defined by $\mathbb{I}_{FFE}$
$\mathbf{h}'_{ZF}$	zero-forcing (ZF) condition vector
h_j	channel coefficient for the linear least squares (LLS) approximation filter of the optically amplified intensity modulation with direct detection (OA-IM/DD) link
$h'_{ZF,i}$	single coefficient if the zero-forcing (ZF) condition vector
$H_{\mathrm{el}}(f) \bullet\!\!-\!\!\circ h_{\mathrm{el}}(t)$	electrical low-pass filter (LPF) transfer function
$\tilde{h}_{\mathrm{f}}(t) \circ\!\!-\!\!\bullet \tilde{H}_{\mathrm{f}}(f)$	equivalent baseband description of the standard single mode fiber (SSMF) impulse response
$\tilde{\mathbf{H}}_{\mathrm{f}}(f)$	equivalent baseband description of the standard single mode (SSMF) transfer matrix
$\tilde{\mathbf{H}}_{\mathrm{f}}(z,f)$	equivalent baseband description of the standard single mode fiber (SSMF) transfer matrix up to location z
$\tilde{H}_{\mathrm{opt}}(f) \bullet\!\!-\!\!\circ \tilde{h}_{\mathrm{opt}}(t)$	equivalent baseband description of the scalar optical band-pass filter (BPF) transfer function
$H_{\mathrm{f}}(f) \bullet\!\!-\!\!\circ h_{\mathrm{f}}(t)$	scalar standard single mode fiber (SSMF) transfer function
$H_{\mathrm{f}}(z,f) \bullet\!\!-\!\!\circ h_{\mathrm{f}}(z,f)$	scalar standard single mode fiber (SSMF) transfer function up to location z
$h_p(\cdot)$	histogram as a measurement for a probability density function (PDF)
$\mathbf{H}$	convolution matrix for the linear least squares (LLS) channel approximation filter of the optically amplified intensity modulation with direct detection (OA-IM/DD) link
$\mathbf{H}_{FFE}$	convolution matrix for the linear least squares (LLS) finite impulse response (FIR) channel approximation of the optically amplified intensity modulation with direct detection (OA-IM/DD) system reduced the lines defined by $\mathbb{I}_{FFE}$
$H_{\mathrm{opt}}(f) \bullet\!\!-\!\!\circ h_{\mathrm{opt}}(t)$	scalar optical band-pass filter (BPF) transfer function
I_{E0}	field responsivity of the photo diode
$\mathbb{I}_{DFE}$	set of equations in the zero-forcing (ZF) solution eliminated by the decision feedback equalizer (DFE)
$\mathbb{I}_{FFE}$	set of equations used to determine the zero-forcing (ZF) solution for the feed-forward equalizer (FFE)
$\mathbb{I}_{ISI}$	set of equations contributing to intersymbol interference (ISI) in the zero-forcing (ZF) solution
$\mathbb{I}_{ISI}$	set of equations which is neglected in the zero-forcing (ZF) solution and produces the residual intersymbol interference (ISI)
$\mathbf{I}$	identity matrix

$i(t) \circ\!\!-\!\!\bullet I(f)$	photo current
I_{P0}	power responsivity of the photodiode
K	length of the bit sequence
K'	length of the linear feedback shift register (LFSR) output sequence
K_{LS}	number of evaluated bits to determine the linear least squares (LLS) finite impulse response (FIR) channel approximation of the optically amplified intensity modulation with direct detection (OA-IM/DD) link
K_{MMSE}	number of evaluated bits to determine the minimum mean squared error (MMSE) feed-forward and decision feedback equalizer (FFE-DFE) coefficients
k_i	electronic dispersion compensation (EDC) input sample index
k	discrete time index with respect to one bit interval
λ_{LMS}	discrete-time adaptation rate of the LMS algorithm
λ'_{LMS}	continuous-time adaptation rate of the least mean square (LMS) algorithm
L_f	length of the standard single mode fiber (SSMF)
L	oversampling factor
l	oversampling index within one bit interval
L_{tb}	trace back length of the Viterbi algorithm (VA)
λ_0	wavelength of the optical continuous wave (CW) signal in vacuum
M_c	memory of a finite impulse response (FIR) channel filter
$\tilde{m}_{\mathrm{MZM}}\{\cdot\}$	equivalent baseband description of the Mach-Zehnder modulator (MZM) characteristic with electrical drive signal as argument
$\tilde{m}^2_{\mathrm{MZM}}\{\cdot\}$	equivalent baseband description of the Mach-Zehnder modulator (MZM) power transfer characteristic with electrical drive signal as argument
μ_s	mean length of a single waveplate in the coarse step standard single mode fiber (SSMF) model
$m_{\mathrm{MZM}}\{\cdot\}$	Mach-Zehnder modulator (MZM) transfer characteristic with electrical drive signal as argument
$\varepsilon_{\mathrm{dB}}$	power extinction ratio of the Mach-Zehnder modulator (MZM) in dB
$\tilde{m}^2_{max}$	maximal excitation of the Mach-Zehnder modulator (MZM) power transfer characteristic
$\tilde{m}^2_{min}$	minimal excitation of the Mach-Zehnder modulator (MZM) power transfer characteristic
M	number of feed-forward equalizer (FFE) coefficients
μ	adaptation step size
$\tilde{\mathbf{n}}(t)$	equivalent baseband description of the amplified spontaneous emission (ASE) noise process

N_0	spectral power density of the amplified spontaneous emission (ASE) noise process per vector dimension
N_B	order of the Bessel polynomials
N_G	order of the Gaussian transfer function of the optical band-pass filter (BPF)
N	number of decision feedback equalizer (DFE) coefficients
ω	angular frequency
ω_0	angular frequency of the optical continuous wave (CW) signal
$\mathbf{p}_{b\check{x}}$	cross-correlation vector between the TX bits and the electronic dispersion compensation (EDC) input sample vector
$\mathbf{p}_{x\mathbf{b}}$	cross-correlation vector between the electrical RX signal samples and the upsampled input bit vector for the linear least squares (LLS) finite impulse response (FIR) channel approximation of the optically amplified intensity modulation with direct detection (OA-IM/DD) link
P_{LD}	mean optical laser power
P_{opt}	mean optical signal power
$p_{\mathrm{AF}}(t)$	instantaneous power of the reamplified and filtered optical RX signal
P	degree of a primitive polynomial
$P_{\mathrm{lg},k,(...)}$	logarithmized path probability of the Viterbi algorithm (VA) at time instant k
$P_{k,(...)}$	path probability of the Viterbi algorithm (VA) at time instant k
P_e	probability of bit errors
$\varphi_d(t)$	phase difference between the upper and lower branch of the Mach-Zehnder modulator (MZM)
$\varphi_{lb}(t)$	induced phase change in the lower branch of the Mach-Zehnder modulator (MZM)
$\varphi_{ub}(t)$	induced phase change in the upper branch of the Mach-Zehnder modulator (MZM)
φ_s	phase angle of the principle states of polarization (PSP) of a single waveplates in the coarse step standard single mode fiber (SSMF) model
φ_0	zero phase angle of the optical continuous wave (CW) signal
$Q_{Q_x}(x_{k_1})$	quantization function used for the quantized input least mean square (QI-LMS) algorithm
Q_x	number of quantization steps for the quantized representation of the signal x
R_b	bit rate
$R_{b,\mathrm{Hz}}$	numerical value of the bit rate in Hz
$\mathbf{R_{bb}}$	autocorrelation matrix of the upsampled input bit vector for the lin-

	ear least squares (LLS) finite impulse response (FIR) channel approximation of the optically amplified intensity modulation with direct detection (OA-IM/DD) link
$\mathbf{R}_{\breve{\mathbf{x}}\breve{\mathbf{x}}}$	autocorrelation matrix of the electronic dispersion compensation (EDC) input sample vector
$R_{\text{fsim}}(f) \bullet\!\!-\!\!\circ r_{\text{fsim}}(t)$	rectangular frequency domain baseband simulation window
$r_{\text{tsim}}(t) \circ\!\!-\!\!\bullet R_{\text{tsim}}(f)$	rectangular time domain simulation window
r_D	(residual) chromatic dispersion (CD) value
ρ	roll-off factor of the non-return-to-zero (NRZ) impulse
$\rho_e(\mathbf{c})$	peak eye distortion
$\sigma_{\tilde{n}}^2$	variance of the amplified spontaneous emission (ASE) noise process
S_λ	chromatic dispersion slope
σ_s	standard deviation of the waveplate length in the coarse step standard single mode fiber (SSMF) model
$\tilde{\mathbf{S}}(z,f)$	unitary polarization scattering matrix of the standard single mode fiber (SSMF) up to location z
$\tilde{s}_1(z,f),\, \tilde{s}_2(z,f)$	basic elements of the unitary polarization scattering matrix
T_b	bit interval
τ_d	decision delay of the feed-forward and decision feedback equalizer (FFE-DFE)
$\Delta\tau_g$	differential group delay (DGD)
ΔT_i	electronic dispersion compensation (EDC) input sample interval
τ_i	electronic dispersion compensation (EDC) input sampling phase
T_g	effective width of the non-return-to-zero (NRZ) impulse
$\tau_g(z,f)$	frequency and location dependent group delay
$\Delta\tau_{g,max}$	worst-case differential group delay (DGD) limit to be handled by electronic dispersion compensation (EDC)
$\theta(t)$	relative phase factor of the upper and lower branch of the Mach-Zehnder modulator (MZM)
τ_{PMD}	polarization mode dispersion (PMD) coefficient
ϑ_s	rotation angle of the principle states of polarization (PSP) of a single waveplates in the coarse step standard single mode fiber (SSMF) model
$\Delta\tau_{RMS}$	root-mean-square (RMS) value of the differential group delay (DGD)
$\tau_{g,x}(z),\, \tau_{g,y}(z)$	group delay of the x- and y-polarization modes
ΔT_s	time domain sample interval
t	continuous time
U_{bias}	bias voltage of the Mach-Zehnder modulator (MZM)
$u(t)$	non-return-to-zero (NRZ) drive signal
U_π	π voltage of the Mach-Zehnder modulator (MZM)

u_ε	scaling factor which incorporates the finite extinction ratio of the Mach-Zehnder modulator (MZM)
v	sample index for frequency domain sampling
x_{k_i}	general electronic dispersion compensation (EDC) input sample
x'_{k_i}	general output of the linear least squares (LLS) finite impulse response (FIR) channel approximation of the optically amplified intensity modulation with direct detection (OA-IM/DD) link
$\mathbf{x}_{k_i}$	general fractionally spaced feed-forward equalizer (FSFFE) input sample vector
$x(t) \circ\!\!\!-\!\!\bullet X(f)$	electrical RX signal
$\check{\mathbf{x}}_{k_i}$	general fractionally spaced feed-forwad and decision feedback equalizer (FSFFE-DFE) input sample vector
y'_k	decision feedback equalizer (DFE) output signal
y_k	feed-forward equalizer (FFE) output signal
$\tilde{y}_{k_i}$	general fractionally spaced feed-forward equalizer (FSFFE) output signal
z_k	feed-forward and decision feedback equalizer (FFE-DFE) output signal
z	location variable of the standard single mode fiber (SSMF)

Abstract

This thesis addresses electronic equalization of intersymbol interference caused by chromatic and polarization mode dispersion in intensity-modulated optical communication links with direct detection. The simple and cost-efficient system setup is, even at high bit rates of 40 Gbit/s and beyond, of interest for short-haul optical links in metropolitan, aggregation or local area networks. Therefore, this thesis investigates preferably simple and low-complexity equalizer structures, which are able to compensate well for the nonlinear characteristics and influences of the intensity-modulated optical communication link with direct detection. Starting with system modeling and the introduction to different equalization methods, we identify low-complexity feed-forward and decision-feedback equalizers in the first part of this thesis. We further put their chromatic and polarization mode dispersion compensation performance to the broader context by comparison to maximum likelihood sequence estimation. Finally, we come to the investigation of adaptation algorithms for equalizer coefficient adjustment, which accounts for the time-variant nature of polarization mode dispersion, while still targeting preferably simple and efficient realization.

Kurzfassung

Die vorliegende Arbeit befasst sich mit der elektronischen Entzerrung von Intersymbolinterferenzen, wie sie in einfachen intensitätsmodulierten optischen Übertragungssystemen mit direkter Detektion durch chromatische oder Polarisationsmodendispersion hervorgerufen werden. Aufgrund des einfachen und kostengünstigen Aufbaus sind solche Systeme auch bei hohen Bitraten von 40 Gbit/s und darüber hinaus vor allem für optische Kurzstreckenverbindungen in Metro-, Zugangs- oder lokalen Netzen von Interesse. Deshalb werden in dieser Arbeit möglichst einfache und aufwandsreduzierte Entzerrerstrukturen untersucht, die die nichtlinearen Eigenschaften und Einflüsse des intensitätsmodulierten optischen Übertragungskanals mit direkter Detektion trotzdem möglichst gut kompensieren. Ausgehend von der Modellbildung und Vorstellung verschiedener Entzerrungsverfahren wird in einem ersten Teil deshalb die aufwandsreduzierte Auslegung von vorwärts- und entscheidungsrückgekoppelten Entzerrerstrukturen bestimmt. Ihre Leistungsfähigkeit bzgl. der Kompensation von chromatischer und Polarisationsmodendispersion wird in einem weiteren Schritt durch Vergleich mit der Maximum-Likelihood Sequenzschätzung in einen größeren Kontext gesetzt. Abschließend widmet sich diese Arbeit der Untersuchung von Adaptionsalgorithmen, um dem zeitvarianten Verhalten der Polarisationsmodendispersion durch Nachführen der Entzerrerkoeffizienten begegnen zu können. Hierbei liegt ebenfalls ein wichtiger Aspekt auf der möglichst einfachen und aufwandsreduzierten Realisierung.

Abstract

Chapter 1

Introduction

Since the first Nobel Prize winning feasibility announcement of low-loss optical waveguiding with dielectric media by Kao and Hockham in 1966 [1], optical data transmission has evolved to become the backbone technology of modern telecommunication networks. In the early days, researchers had mainly to cope with the reduction of signal attenuation by improving materials and manufacturing processes. Another important issue was the development of preferably cheap transmitter (TX) and receiver (RX) device technologies. Since the data rates were quite low for pure voice traffic at that time, bandwidth seemed to be no limiting factor. The advent of wavelength division multiplex (WDM) systems in the 1990s has even emphasized the statement that optical fiber communications would offer almost unlimited capacity. However, the multimedia-based Internet of today with the recent roll-out of triple play and enhanced multimedia services over fixed and mobile networks has revealed that the transmission capacity and transmission techniques of present optical networks will no longer satisfy future requirements. This has put some pressure on equipment manufacturers and researchers all over the world to push optical transmission technology to its limits. For example, the already deployed fiber infrastructure could offer more potential if dynamic optical routing and switching were applied. This is one possible approach by which network operators seek to increase their network efficiency. Hence, Ethernet technologies, which are well established for dynamic bandwidth allocation and medium sharing in wireline communication systems [2], are adopted to the optical domain by so-called Carrier-Grade Ethernet. This comes along with increasing data rates and higher spectral efficiency [3, 4, 5, 6] to satisfy the bandwidth demand by end users, e. g. for applications like high-definition (HD) video streaming over the Internet. This will make optical networks also penetrate into the aggregation network domain where cheap installation cost and economy of scale are major drivers. All those impacts will challenge the underlying optical and electrical transmission technologies.

In optically amplified intensity modulation with direct detection (OA-IM/DD) links using standard single mode fibers (SSMFs) (possibly enhanced by optical chromatic dispersion (CD) compensation using fixed length dispersion-compensating fibers (DCFs)), polarization dependent impairments could be neglected for bit rates up to 10 Gbit/s. However, despite

the nomenclature *single mode*, two degenerate orthogonal polarization modes may propagate along a SSMF. Minimal manufacturing deviations from the circular fiber geometry and external mechanical stress [7] may change the effective refractive index profile along the fiber cross section and, consequently, result in different group velocities. Mechanical stress may arise from temperature changes, fiber bending and accidental shock impacts from the environment, which makes the resulting polarization mode dispersion (PMD) a random time-variant phenomenon. Consequently, the optical channel impairments of CD and time-variant PMD together with prospective optical routing and switching lead us to consider an optical end-to-end connection as a dynamic system now. Therefore, system design requires to take this dynamic behavior into account, and the transmission equipment must be able to follow the changes of the optical link characteristics and to compensate for the resulting impairments of signal quality.

There has already been spent some effort in investigating appropriate and adaptive TX and RX PMD mitigation techniques. While optoelectronic devices offer good compensation performance because they can act directly on the electromagnetic field [8, 9, 10, 11, 12], they are bulky, require high mechanical precision and are difficult to adapt to changing link conditions. This leads to high manufacturing, installation and operational costs. These are the reasons why investigation of electronic dispersion compensation (EDC) has gained interest although it is a suboptimal solution in OA-IM/DD links because it can only act on the electrical RX signal, i. e. not directly in the optical domain from where the main signal impairments originate. Furthermore, direct detection removes all phase information when the optical signal is converted to an electrical one. Nevertheless, EDC devices are promising Plug'n Play (PnP) alternatives which might also be used to enhance fixed optical compensation techniques. The main advantage of EDC arises from the possibility to make use of mature complementary metal-oxide semiconductor (CMOS) very-large-scale integration (VLSI) fabrication technologies. This offers some cost, space and scale advantages compared to optical technologies and allows to integrate the compensation device and its adaptation unit digitally on the same die. This simplifies network installation and operations to great extents.

The proposed EDC methods range from electronic predistortion (EP) [13] at the TX side to linear feed-forward equalizers (FFEs) with decision feedback equalizers (DFEs) [14] and maximum likelihood sequence estimation (MLSE) devices [15, 16, 17, 18] at the RX side. Since EP requires an additional feedback channel for channel state information (CSI), FFE-DFE and MLSE are the most promising approaches for dynamic EDC with no additional overhead. Among these two, MLSE offers better compensation potential at the expense of high computational complexity, which scales exponentially with channel memory. Purely digital EDC solutions are rare in OA-IM/DD systems [19, 20, 21] because data rates of $40 - 100$ Gbit/s require almost clock rates in the same region if serial data stream processing is intended. Therefore, analog tapped delay lines in Silicon-Germanium (SiGe) technology have been the technology of choice for first FFE-DFE realizations [22, 23, 24, 25, 26]. However, this approach makes joint integration with the adaptation unit difficult and inherently

suffers from inaccurate adaptation [27]. Pioneering work on digital realization of MLSE has already been reported for a data rate of 43 Gbit/s [28], too. While its higher computational complexity and operational cost in terms of power dissipation are well justified for long-haul optical links, this thesis investigates FFE-DFEs as a comparably low-complexity and low-cost alternative for the short-haul range. It tries to bridge the gap towards higher data rates by introducing algorithmic simplifications for the adaptation unit. As a more general prospect, digital design in CMOS technology could further allow to integrate more functionality like forward error correction (FEC) decoding [29] on the same die.

This thesis is organized as follows. Ch. 2 gives a general overview on the components of a OA-IM/DD link and points out the main device and signal characteristics of this transmission format. Ch. 3 deals with the detailed modeling of the considered optical fiber link using commonly known description and simulation techniques. Special emphasis is placed on induced SSMF impairments like CD, PMD and self-phase modulation (SPM) and their impacts on the electrical RX signal, which is further processed by the EDC unit. Then, Ch. 4 first reviews major methods for EDC ranging from MLSE to less computationally complex FFE-DFEs with different coefficient adjustment criteria like minimal bit error ratio (MIN-BER), zero-forcing (ZF) and minimum mean squared error (MMSE). A first goal of the presented simulation results is to identify the most suitable number of coefficients of the FFE-DFEs based on the MMSE criterion. A further subsection deals with the suitability of the MMSE criterion in noise-limited OA-IM/DD fiber links. The potential of fractionally spaced sample processing for all considered EDC methods is discussed in another subsection. Ch. 4 concludes with a comprehensive performance analysis comparing all considered EDC methods.

Ch. 5 introduces adaptive FFE-DFE equalization using the least mean square (LMS) algorithm as an iterative solution to the MMSE criterion. Having implementation in mind, it also investigates the impact of algorithmic simplifications on the adaptation performance and presents a dedicated solution.

As a general notation formalism,

- lower case letters are used for time domain signals and impulse responses, e. g. $q(t)$,

- upper case letters are used for frequency spectra, transfer functions and constants in time and frequency domain, e. g. $Q(f)$ or Q_0,

and

- multidimensional signals and frequency spectra as well as vectors and matrices are highlighted by bold face letters, e. g. $\mathbf{q}(t)$, $\mathbf{Q}(f)$, $\mathbf{v}$ or $\mathbf{M}$,

if not stated otherwise. All signal variables in equations are considered to be normalized with respect to their physical unit.

Chapter 2

Intensity-Modulated Optical Links with Direct Detection

This chapter gives an overview on OA-IM/DD fiber transmission with respect to its analog real-world physical signals. Having system modeling in Ch. 3 in mind, the description requires at some stages a switch from time to frequency domain and vice versa. That is why in some schematics and block diagrams the labeling of various entities may alternate between impulse responses and transfer functions in order to emphasize the corresponding modeling approach. However, consistency is always guaranteed owing to the linearity of the Fourier transform.

A typical link setup, as depicted in Fig. 2.1, consists of three major building blocks:

- An optical TX, which modulates the optical continuous wave (CW) signal with the information signal to be transmitted,

- an optical fiber, along which the optical signal propagates,

- and the optical RX front end, which performs the conversion from the optical back to the electrical domain.

The binary information $b_k \in \{0, 1\}$ at the TX side, which might originate from any multimedia or data source, is fed into the optical fiber link at a rate of $R_b \sim 1/T_b \in \mathbb{R}_+$. The discrete-time index $k = 0, \ldots, K - 1$ in b_k aligns with the time interval kT_b. The parameter $K \in \mathbb{N}_1$ specifies the length of the bit sequence. Since all modern digital communication systems are equipped by some FEC capabilities to combat noise distortions [30, 31, 32, 33, 34, 35], we assume that the bits b_k in Fig. 2.1 have already been preprocessed by applying an appropriate channel code. The actual value of R_b is not a net but a gross value therefore.

The following non-return-to-zero (NRZ) impulse shaper transforms the binary information into an electrical signal with the impulse $g(t) \in \mathbb{R}$ in Fig. 2.1. The considered values of
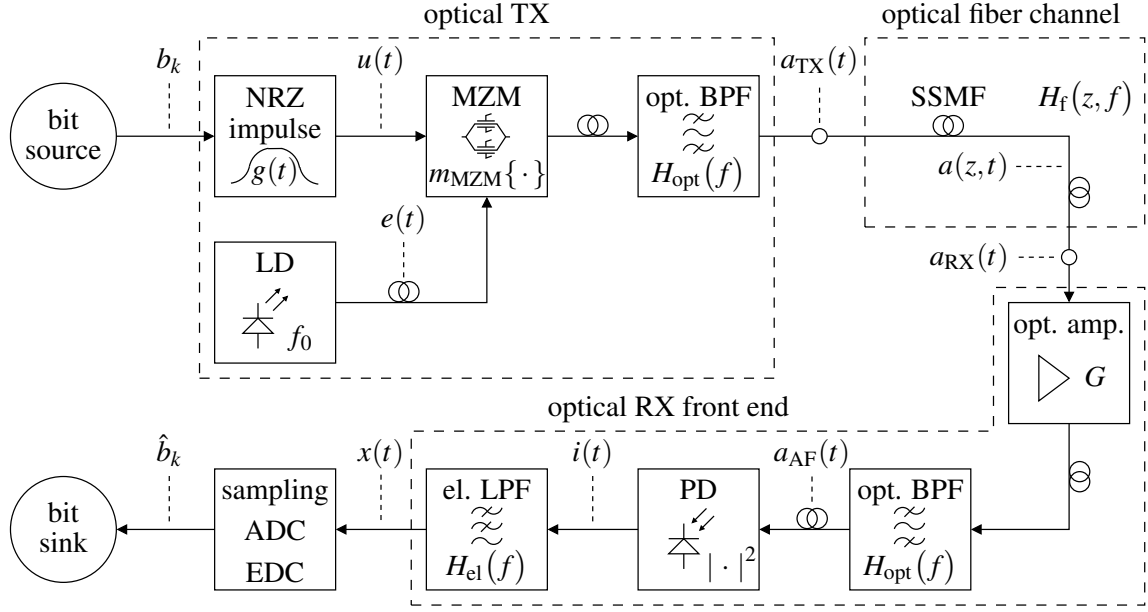
Figure 2.1: Principal structure of an OA-IM/DD fiber link

$R_b > 10\,\text{Gbit/s}$ favors external modulation of the optical CW signal by a Mach-Zehnder modulator (MZM). The modulating electrical signal $u(t) \in \mathbb{R}$ driving the MZM is

$$u(t) = \sum_{k=0}^{K-1} b_k\, g(t - kT_b) \in \mathbb{R}. \tag{2.1}$$

The second input to the MZM is the unmodulated optical CW signal, which originates from a semiconductor laser diode (LD). For now let us consider the LD output signal to be a linearly polarized transverse electromagnetic (TEM) wave, which results from the solution of Maxwell's Equations for a homogeneously cylindrical and dielectric transmission medium as an idealized model of an optical fiber. The electric and magnetic field components of the optical CW signal are orthogonal, and their numerical values interdepend linearly by the characteristic wave impedance. Therefore, either the scalar electric or magnetic field component determines solely the optical CW signal with respect to the plane of polarization. During our initial considerations, we describe the optical CW signal, which leaves the LD, by

$$e(t) = E_0 \cos\left(2\pi f_0 t + \varphi_0\right), \quad E_0, f_0 \in \mathbb{R},\ \varphi_0 \in [0, 2\pi), \tag{2.2}$$

with the scalar amplitude E_0. The angular frequency is $\omega_0 = 2\pi f_0$. The frequency f_0 is connected to the optical wavelength in vacuum by $\lambda_0 = c_0/f_0$, and the zero phase angle φ_0 represents an arbitrary but fixed phase offset. The impact of frequency chirp is neglected. Further, the propagation along the short pigtail connection from the LD to the MZM does not affect the shape of the optical CW signal. This justifies that we take $e(t)$ of Eq. (2.2) directly as input to the MZM and neglect the exact description as a TEM wave with location dependency along the direction of propagation. Note that we must extend the simple scalar

notation of Eq. (2.2) for the electrical field component to include PMD effects later on (cf. Ch. 3).

The MZM exploits the electro-optic Pockels effect of e. g. Lithium niobate ($LiNbO_3$) [36] to modulate the optical CW signal $e(t)$ with the electrical drive signal $u(t)$. Since the MZM transfer characteristic, which is denoted by $m_{MZM}\{\cdot\}$, is of nonlinear shape, intermodulation products with spectral broadening occur in the optical output spectrum of the MZM. If the SSMF of Fig. 2.1 was part of a WDM system, direct feed of the SSMF by the MZM output signal would interfere and disturb neighboring wavelength channels. For this reason, an optical band-pass filter (BPF) is placed between the MZM and the SSMF in order to reduce this intermodulation interference. WDM channel spacing grids for 10 Gbit/s metropolitan area networks are commonly either 100 GHz or 50 GHz according to several International Telecommunication Union (ITU) Recommendations [37, 38, 39, 40, 41]. Assuming that the useful component of the optical TX frequency spectrum, generally denoted by B_{opt}, is determined by the Nyquist frequency f_N [42] of the electrical impulse $g(t)$, i.e.

$$B_{opt} \approx 2f_N \approx 2 \cdot 5\,\text{GHz} = 10\,\text{GHz}$$

for $R_b = 10\,\text{Gbit/s}$, we have almost a factor of five between utilized bandwidth for a channel spacing grid of 50 GHz. Throughout this thesis, we assume the same relation for $R_b = 40\,\text{Gbit/s}$ with

$$B_{opt} \approx 2f_N \approx 2 \cdot 20\,\text{GHz} = 40\,\text{GHz}$$

and a channel spacing grid of 200 GHz. This can be viewed as using either the even or odd channels suggested by the 100 GHz ITU channel spacing grid. As a consequence of this assumption, the 3 dB bandwidth of the optical BPF is set to $B_{3\,\text{dB,opt}} \approx 200\,\text{GHz}$, i.e. that frequencies marking the 3 dB bandwidths of adjacent WDM channels coincide. The quite large gap with $B_{3\,\text{dB,opt}} \approx 5\,B_{opt}$ owes to the fact that steep frequency slopes are hard to realize for optical BPFs. Consequently, the useful component of the optical TX frequency spectrum is hardly touched by the optical BPF transfer function $H_{opt}(f)$ (cf. Ch. 3.2), and we can fairly approximate the signal entering the SSMF with

$$
\begin{aligned}
a_{TX}(t) &= \Big(e(t)\, m_{MZM}\{u(t)\}\Big) * \underbrace{\mathscr{F}^{-1}\Big\{H_{opt}(f)\Big\}}_{=h_{opt}(t)\in\mathbb{R}}, \quad m_{MZM}\{u(t)\} \in \mathbb{R}, \qquad (2.3)\\
&= \Big(\underbrace{E_0\, m_{MZM}\{u(t)\}}_{=a_e(t)} \cos\big(2\pi f_0 t + \varphi_0\big)\Big) * h_{opt}(t)\\
&= \Big(a_e(t)\cos\big(2\pi f_0 t + \varphi_0\big)\Big) * h_{opt}(t)\\
&\overset{B_{3\,\text{dB,opt}}\uparrow}{\approx} a_e(t)\cos\big(2\pi f_0 t + \varphi_0\big). \qquad (2.4)
\end{aligned}
$$

The approximation made in Eq. (2.4) will also simplify notation during the following derivations. The braces of $m_{MZM}\{\cdot\}$ in Eq. (2.3) indicate that the argument is a time function, and

$\mathscr{F}^{-1}\{\cdot\}$ denotes the inverse Fourier transform operator. The term $a_e(t)$ in Eq. (2.4) serves as a shorthand notation for the real-valued envelope of $a_{\mathrm{TX}}(t)$.

When propagating along the SSMF of length L_f, the optical TX signal is exposed to several degrading effects. These are attenuation, CD or PMD as linear ones, or SPM and stimulated Brillouin scattering (SBS) as nonlinear ones. WDM systems are further affected by nonlinearities like cross-phase modulation (XPM) and four-wave mixing (FWM). Since we restrict ourselves to the linear transmission regime so far and due to the more convenient description of dispersion effects in frequency domain, the optical TX signal at location $z \in [0, L_f]$ of the SSMF is given by

$$a(z,t) \circ\!\!-\!\!\bullet A(z,f) = A_{\mathrm{TX}}(f)\, H_{\mathrm{f}}(z,f), \quad H_{\mathrm{f}}(z,f) \bullet\!\!-\!\!\circ h_{\mathrm{f}}(z,t) \in \mathbb{R}, \qquad (2.5)$$

with the Fourier correspondence $a_{\mathrm{TX}}(t) \circ\!\!-\!\!\bullet A_{\mathrm{TX}}(f)$ and the location dependent SSMF transfer function $H_{\mathrm{f}}(z,f)$, which represents the above mentioned linear impairments.

The input to the optical receiver front end results from Eq. (2.5) evaluated at $z = L_f$, i.e.

$$a_{\mathrm{RX}}(t) \circ\!\!-\!\!\bullet A_{\mathrm{RX}}(f) := A(L_f, f) = A_{\mathrm{TX}}(f) \underbrace{H_{\mathrm{f}}(L_f, f)}_{:= H_{\mathrm{f}}(f)} \qquad (2.6)$$

$$= A_{\mathrm{TX}}(f)\, H_{\mathrm{f}}(f). \qquad (2.7)$$

We omit the location variable z in $H_{\mathrm{f}}(z,f)$ and use the shorthand notation $H_{\mathrm{f}}(f)$ if we want to address the SSMF transfer function from transmitter to receiver in the following. It depends on the dominating effect whether the optical fiber link is called either dispersion- or noise-limited. Dispersion-limited links are mainly degraded by CD and PMD where noise-limited links suffer more from attenuation and the noise generated by the amplifier device required to restore appropriate signal levels.

The advent of purely optical Erbium-doped fiber amplifiers (EDFAs) has made optical-electrical conversion and optical-electrical reconversion (OEO) obsolete for signal reamplification. An EDFA uses a pump LD to excite the electrons of the doped ions into higher energy states. The incoming optical signal itself triggers those electrons to fall back into lower energy states while emitting the energy difference as coherent radiation. This results in coherent light amplification. Unfavorably, a so-called amplified spontaneous emission (ASE) process leads to optical noise generation in the doped fiber segment of the EDFA. Nevertheless, installation and operation of EDFAs has become much more comfortable because of their optical transparency supporting joint reamplification of several wavelength channels. If the optical fiber link covers a range of several hundreds or thousands of kilometers, a couple of EDFAs must be distributed along this distance as is done e. g. in long-haul undersea networks. However, the considered system in this thesis comprises only one amplifier right at the end of the optical fiber link (cf. Ch. 3.2.3).

The optical BPF at the receiver front end is placed for channel demultiplexing in WDM systems and for suppression of out of band noise from the EDFA to improve the signal-to-noise ratio (SNR) at the RX. Its transfer function has the same shape and 3 dB bandwidth $B_{3\,\mathrm{dB,opt}}$ as the one at the TX. Neglecting noise at the moment and assuming that the fiber attenuation has been completely compensated by the EDFA, we may write for the reamplified and filtered optical RX signal

$$
\begin{aligned}
a_{\mathrm{AF}}(t) \quad &= \quad G\,a_{\mathrm{RX}}(t) * h_{\mathrm{opt}}(t) \\
&\overset{B_{3\,\mathrm{dB,opt}}\uparrow}{\approx} \quad G\,a_{\mathrm{RX}}(t), \quad G \in \mathbb{R}_+ .
\end{aligned}
\tag{2.8}
$$

The factor G is the constant gain of the EDFA. Once again, the impact of optical RX filtering on the useful component of the optical RX signal is negligible in Eq. (2.8) for the same reasons as already explained at the TX side.

OA-IM/DD systems belong to the class of envelope detectors compared to the coherent homo- or heterodyne principles in other wireline or wireless systems [42]. In the past, the reason for the absence of homo- or heterodyne receivers in optical communication systems was that it has been very difficult to control coherence of the local LD at the receiver due to frequency chirp and time-varying PMD. However, recent advances in high-speed signal processing capabilities allow to mitigate the frequency deviations by chirp at the expense of higher processing overhead [43]. We keep to the well developed and simple to realize direct detection technique in this thesis. The photodiode (PD) acts as a compact envelope detector with a square law detection (SLD) operation on the optical RX signal and inherent low-pass filtering. These joint properties of the PD are distributed among two different entities in the schematic of Fig. 2.1. This detached description is closer to our modeling approach, in which the electrical low-pass filter (LPF) $H_{\mathrm{el}}(f)$ may also include the frequency spectrum shaping and amplification of a transimpedance amplifier placed right after the PD. Since we assume that the noise from optical amplifiers dominates, additional electronic noise sources in the transimpedance amplifier stage will not be considered in this thesis.

The physics of a PD shows a dependence of the photo current $i(t)$ being proportional to the optical power $p_{\mathrm{AF}}(t)$. This optical power itself depends linearly on the square of the incident electrical field $a_{\mathrm{AF}}(t)$. We can write

$$
i(t) \quad = \quad I_{P0}\,p_{\mathrm{AF}}(t), \quad I_{P0} \in \mathbb{R}_+ ,
\tag{2.9}
$$

$$
\overset{p_{\mathrm{AF}}(t)\sim a_{\mathrm{AF}}(t)^2}{=} \quad I_{E0}\,a_{\mathrm{AF}}(t)^2, \quad I_{E0} \in \mathbb{R}_+ .
\tag{2.10}
$$

The power responsivity of the photodiode is denoted by I_{P0}. The linear relation $p_{\mathrm{AF}}(t) \sim a_{\mathrm{AF}}(t)^2$ represents the already mentioned SLD rule of the the photo current $i(t)$ and the received electrical field $a_{\mathrm{AF}}(t)$. The factor I_{E0} can be viewed as the field responsivity. Note that, besides the modulator transfer characteristic $m_{\mathrm{MZM}}\{\cdot\}$, it is mainly the SLD operation of the PD, which makes an OA-IM/DD system a nonlinear one. The phase information of

the optical signal gets lost, and, when we introduce noise from the EDFA in Ch. 3.2.3, its statistical properties change by direct detection.

The demodulation in direct detection is completed by final low-pass filtering with $h_{\mathrm{el}}(t) \circ\!\!-\!\!\bullet$ $H_{\mathrm{el}}(f)$. We can write for the result of this operation

$$x(t) = i(t) * h_{\mathrm{el}}(t), \quad h_{\mathrm{el}}(t) \in \mathbb{R}, \tag{2.11}$$

$$= I_{E0}\, a_{\mathrm{AF}}(t)^2 * h_{\mathrm{el}}(t). \tag{2.12}$$

At this point, a transform of Eq. (2.12) to frequency domain is advisable. The squaring is consequently replaced by a frequency domain convolution and results in

$$X(f) = I(f)\, H_{\mathrm{el}}(f) \tag{2.13}$$

$$= I_{E0}\, \Big(A_{\mathrm{AF}}(f) * A_{\mathrm{AF}}(f) \Big)\, H_{\mathrm{el}}(f). \tag{2.14}$$

App. A illustrates the inherent steps involved in Eq. (2.14). It gives further insight how $I(f)$ is generated by self-mixing $a_{\mathrm{AF}}(t)\, a_{\mathrm{AF}}(t) \bullet\!\!-\!\!\circ A_{\mathrm{AF}}(f) * A_{\mathrm{AF}}(f)$ as a result of direct detection. The resulting frequency spectrum $I(f)$ contains spectral components at $f = 0\,\mathrm{Hz}$ and at $f = \pm 2 f_0$. The (naturally imposed) cutoff frequency $f_{3\,\mathrm{dB,el}}$ of the electrical LPF is appropriate to retain the baseband component $X(f)$ of $I(f)$ and to suppress the components near $\pm 2 f_0$.

Finally, the electrical RX signal is sampled and processed by the EDC unit to determine the estimate $\hat{b}_k$ on the TX bit b_k.

Chapter 3

Physical Layer Simulation Model

After having reviewed the major building blocks of an OA-IM/DD link in Ch. 2, this chapter features the basic concepts of physical modeling for simulation. We generally derive an appropriate signal representation for computer simulations and discuss the impacts of the most important parameters on simulation accuracy. This is followed by a detailed look at the preferably simple physical models of the system entities. In addition, inclusion of PMD effects requires to extend the scalar optical signal description of Ch. 2 to a two-dimensional one.

3.1   General Approach

3.1.1   Discrete-Time Signal Representation

Considering most linear wireline or wireless digital communication systems, a single-tap equivalent time domain description is adequate to bundle up all signal properties sufficiently in the final discrete-time symbol-spaced output of the model [42]. Symbol-spaced in the context of this thesis means a sampling frequency of $f_s = 1/T_b$, i.e. one discrete-time sample per bit interval. Direct application of this quite efficient approach to OA-IM/DD systems would implicate difficulties in capturing intermodulation effects and the nonlinearity of direct detection accurately [44] (cf. App. A). Some exist [18, 35, 45], but they require much preparatory work or rely on less restrictive assumptions. Therefore, we have to take the continuous-time signal description of Ch. 2 and transfer it into the corresponding discrete-time floating-point representation for the purpose of accurate computer simulations. Systems theory demands compliance with the sampling theorem for this transformation, and the sampling frequency $f_s \in \mathbb{R}_+$ must fulfill $f_s \geq 2f_{max}$ to avoid frequency aliasing with $f_{max} < \infty$ being the highest nonzero frequency component in the frequency spectrum of the continuous-time signal. However, real-world physical signals are time-limited and consequently feature a nonzero infinite frequency range. Nevertheless, the shape of real-world physical signals is smooth in time domain. Often, the frequency components carrying most of the signal power are

concentrated within a distinct frequency range and decay towards zero for $|f| \to \infty$. These properties resolve the conflicting requirement between the sampling theorem and the natural impact of time limitation effectively. By choosing the sampling frequency f_s sufficiently high, just a small amount of frequency aliasing occurs, which affects accuracy to minor extent.

Let $q(t)$ be such a time-limited signal with

$$q(t) = \begin{cases} \neq 0 & : \quad t \in [0 \, \text{s}, KT_b] \\ 0 & : \quad \textit{elsewhere} \end{cases} \tag{3.1}$$

as a placeholder for any of the physical signals of the OA-IM/DD link in Fig. 2.1 of Ch. 2, i.e.

$$q(t) \in \left\{ u(t), e(t), a_{\text{TX}}(t), a(z,t), a_{\text{RX}}(t), a_{\text{AF}}(t), i(t), x(t) \right\}. \tag{3.2}$$

Causality of $q(t)$ is just for convenience and to emphasize the modeling of real-world physical signals here, but it is not a necessary requirement for computer simulations. Since $q(t)$ is time-limited, the frequency spectrum $Q(f) \bullet\!\!-\!\!\circ q(t)$ is of infinite frequency as a property of the Fourier transform.

If we define a time domain sample interval ΔT_s through the number of samples $L \in \mathbb{N}_1$ within the bit interval T_b by

$$\Delta T_s = \frac{1}{f_s} := \frac{T_b}{L} \iff L = \frac{T_b}{\Delta T_s}, \tag{3.3}$$

the ideally sampled version of $q(t)$ with special segmentation according to the bit interval T_b is given by

$$q_{\Delta T_s}(t) = \underbrace{q(t)}_{=0 \, \forall k \neq 0, \dots, K-1} \sum_{k=-\infty}^{\infty} \sum_{l=0}^{L-1} \delta\left(t - (kL+l)\Delta T_s\right) \tag{3.4}$$

$$= \sum_{k=0}^{K-1} \sum_{l=0}^{L-1} \underbrace{q\left((kL+l)\Delta T_s\right)}_{=:q_{kL+l}} \delta\left(t - (kL+l)\Delta T_s\right). \tag{3.5}$$

The parameter L is also known as oversampling factor. Setting $l = 0, \dots, L-1$ as the oversampling index within one bit interval, we introduce the time series representation

$$\mathbf{q}_{KL} := \left(q_{kL+l}\right)_{k=0,\dots,K-1; \, l=0,\dots,L-1} \tag{3.6}$$

for the samples of $q(t)$. This series representation serves as the time domain input into the computer simulation model used in this thesis.

Since $q(t) \circ\!\!-\!\!\bullet Q(f)$ is not band-limited as per our definition above, the corresponding peri-

odic spectrum[1]

$$Q_{\Delta T_s}(f) = \frac{1}{\Delta T_s} \sum_{\mu=-\infty}^{\infty} Q(f - \mu f_s), \quad \mu \in \mathbb{Z}, \tag{3.7}$$

$$= \sum_{k=0}^{K-1} \sum_{l=0}^{L-1} q_{kL+l} \, e^{-j2\pi f(kL+l)\Delta T_s}. \tag{3.8}$$

contains frequency aliasing. However, we can reduce the effect of aliasing by shifting the partial spectra $Q(f - \mu f_s)$ further apart and reduce the overlapping areas by increasing the sampling frequency f_s. This is done according to Eq. (3.3) by increasing the oversampling factor L.

In order to use the primitive period of $Q_{\Delta T_s}(f)$ within the range $f \in [-f_s/2, f_s/2]$ in Eq. (3.7) as an approximation to $Q(f)$, we introduce a rectangular frequency domain simulation window of the form

$$R_{\text{fsim}}(f) := \begin{cases} \frac{1}{f_s} : |f| \leq f_s/2 \\ 0 : |f| > f_s/2 \end{cases} \quad \bullet\!\!-\!\!\circ \; r_{\text{fsim}}(t) = \text{sinc}(\pi f_s t). \tag{3.9}$$

Frequency domain windowing leads to the signal

$$q'(t) = q_{\Delta T_s}(t) * r_{\text{fsim}}(t) \circ\!\!-\!\!\bullet \; Q'(f) = Q_{\Delta T_s}(f) R_{\text{fsim}}(f) \tag{3.10}$$

which represents the actual continuous-time signal modeled by discrete-time simulations in this thesis, i.e.

$$q'(t) \approx q(t) \quad \text{and} \quad Q'(f) \approx Q(f). \tag{3.11}$$

The accuracy of this approximation can be adjusted through the choice of an appropriately large oversampling factor L.

Figs. 3.1(a) and 3.1(b) illustrate the impact of the oversampling factor on simulation accuracy for a single bit sequence, i.e. $K = 1$. Both show the same time-limited signal $q(t)$ in the range $t \in [0\,\text{s}, T_b]$, the sampled versions $q_{\Delta T_s}(t)$ and the approximations $q'(t)$ for $L = 4$ and $L = 32$, respectively. Compared to $q(t)$, the approximations $q'(t)$ are of infinite duration since the impulse response $r_{\text{fsim}}(t)$ of the rectangular simulation window is a sinc-function with zeros at $t = m\Delta T_s$, $m \in \mathbb{Z} \setminus \{0\}$. The locations of the zeros of $r_{\text{fsim}}(t)$ imply that

$$q(m\Delta T_s) \equiv q_{\Delta T_s}(t) \equiv q'(m\Delta T_s), \quad m\Delta T_s \in [0\,\text{s}, KT_b]. \tag{3.12}$$

This means that despite the differences in continuous-time shape between the sampling instants, $q(t)$ and $q'(t)$ have their time series representation $\mathbf{q}_{KL}$ in common.

---

[1] $\delta(t - (kL+l)\Delta T_s) \circ\!\!-\!\!\bullet \; e^{-j2\pi f(kL+l)\Delta T_s}$ has been applied to get Eq. (3.8).

(a) Modeling accuracy with $L = 4$
(for $K = 1$): $\Delta T_s = T_b/4 \rightarrow f_s = 4/T_b$

(b) Modeling accuracy with $L = 32$
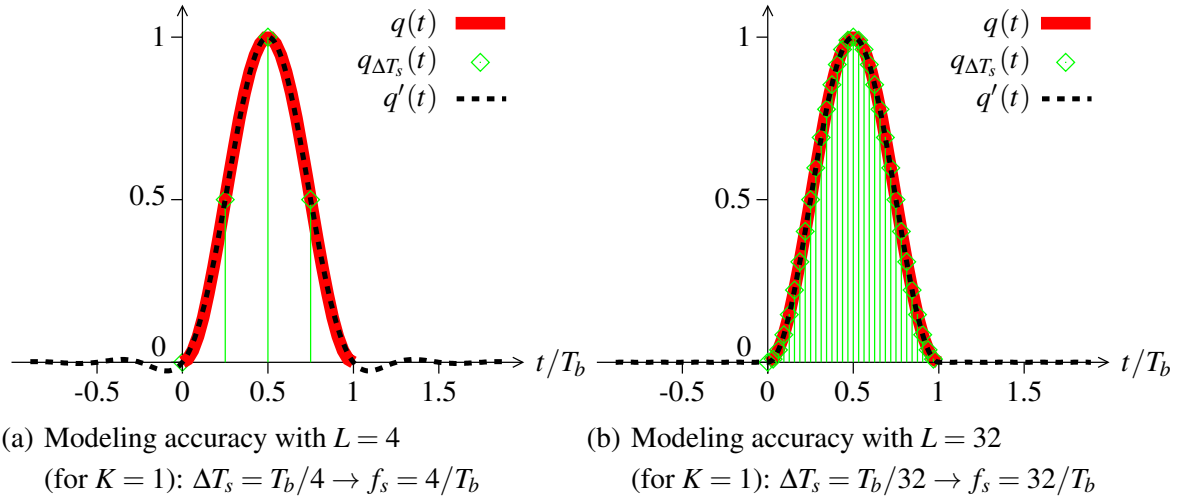(for $K = 1$): $\Delta T_s = T_b/32 \rightarrow f_s = 32/T_b$

Figure 3.1: Influence of the oversampling factor L on simulation accuracy

3.1.2 Discrete-Frequency Signal Representation

At the very beginning of Ch. 2, there has already been mentioned that some entities of the OA-IM/DD link are rather modeled in frequency than in time domain. If we use the time domain description of the previous subsection as our basis, the time domain input signal to a frequency domain model of an entity has to be transformed before, and the resulting frequency spectrum has to be retransformed after being processed.

The frequency range of the approximation $q'(t) \circ\!\!-\!\!\bullet Q'(f)$ is limited by the rectangular frequency domain simulation window, i.e. the applicable frequencies for simulation modeling are given by $f \in [-f_s/2, f_s/2]$. However, $Q'(f)$ itself is still continuous-frequency although we can only process discrete-frequency spectra within our computer model. Therefore, it is necessary to transform the continuous-frequency spectrum $Q'(f)$ into an appropriate discrete-frequency one. In analogy to the time domain, this can be considered as a frequency domain sampling process, which has principally to conform to the sampling theorem.

If we define a frequency domain sample interval $\Delta F_s \in \mathbb{R}_+$, the ideally sampled frequency spectrum of $Q'(f)$ is then given by

$$Q'_{\Delta F_s}(f) = Q'(f) \sum_{v=-\infty}^{\infty} \delta\left(f - v\Delta F_s\right) \tag{3.13}$$

$$= \sum_{v=-\infty}^{\infty} Q'(v\Delta F_s)\, \delta\left(f - v\Delta F_s\right) \tag{3.14}$$

$$= \sum_{v=-\infty}^{\infty} Q_{\Delta T_s}(v\Delta F_s) \underbrace{R_{\text{fsim}}(v\Delta F_s)}_{=0\,:\,|v|>\lfloor\frac{f_s}{2\Delta F_s}\rfloor}\, \delta\left(f - v\Delta F_s\right)$$

$$= \sum_{v=\lceil -\frac{f_s}{2\Delta F_s} \rceil}^{\lfloor \frac{f_s}{2\Delta F_s} \rfloor} \underbrace{Q_{\Delta T_s}(v\Delta F_s)}_{=:Q_v} \delta\left(f - v\Delta F_s\right) \tag{3.15}$$

with the definition of the discrete-frequency series

$$\mathbf{Q}_V := (Q_v)_{v=\lceil -\frac{f_s}{2\Delta F_s} \rceil,\dots,\lfloor \frac{f_s}{2\Delta F_s} \rfloor} \tag{3.16}$$

representing the discrete-frequency version of $Q'(f)$. This is the general form, frequency spectra and transfer functions are represented in our computer simulation model.

We know from time domain sampling that the spectra of sampled signals are periodic. The same analogy holds for sampled frequency spectra if transformed back to time domain with

$$q'_{\Delta F_s}(t) = \frac{1}{\Delta F_s} \sum_{\mu=-\infty}^{\infty} q'\left(t - \mu\frac{1}{\Delta F_s}\right), \quad \mu \in \mathbb{Z}. \tag{3.17}$$

If the time domain signal is not time-limited like the approximation $q'(t)$, time-domain aliasing occurs. The aliasing can be adjusted by setting ΔF_s appropriately. The qualitative impressions of Figs. 3.1(a) and 3.1(b) for time domain sampling may also serve as an indication for the accuracy of frequency domain sampling if we associate the time domain with their corresponding frequency domain counterparts. Especially, we can state that time domain aliasing effects may be reduced reasonably by decreasing the frequency domain sample interval ΔF_s.

We can repeat the procedure of the previous section and define a time-domain simulation window of the form

$$r_{\text{tsim}}(t) := \begin{cases} \Delta F_s : |t| \leq 2/\Delta F_s \\ 0 : |t| > 2/\Delta F_s \end{cases} \circ\!\!-\!\!\bullet R_{\text{tsim}}(f) = \text{sinc}\left(\pi\frac{f}{\Delta F_s}\right). \tag{3.18}$$

Application of this window to $q'_{\Delta F_s}(t)$ leads to

$$q''(t) = q'_{\Delta T_s}(t)\, r_{\text{tsim}}(t) \circ\!\!-\!\!\bullet Q''(f) = Q'_{\Delta T_s}(f) * R_{\text{tsim}}(f), \tag{3.19}$$

which represents the actual continuous-time signal after being processed in frequency domain modeled by discrete-frequency simulations in this thesis, i.e.

$$q''(t) \approx q'(t) \approx q(t) \quad \text{and} \quad Q''(f) \approx Q'(f) \approx q(f). \tag{3.20}$$

Again, the choice of an appropriately small frequency domain sample interval ΔF_s guarantees accuracy to the approximations made here.

3.1.3 Efficient Transformation between Discrete-Time and Discrete-Frequency Signal Representation

If we consider the definition of the frequency series $\mathbf{Q}_V$ in Eq. (3.14) and use Eqs. (3.8) and (3.10) to express its elements by the time series representation $\mathbf{q}_{KL}$, we arrive at

$$
\begin{aligned}
Q_v &= Q'(v\Delta F_s) = Q_{\Delta T_s}(v\Delta F_s)\,R_{\text{fsim}}(v\Delta F_s) \\
&= \sum_{k=0}^{K-1}\sum_{l=0}^{L-1} q_{kL+l}\,\mathrm{e}^{-\mathrm{j}2\pi v\Delta F_s(kL+l)\Delta T_s}\, \underbrace{R_{\text{fsim}}(v\Delta F_s)}_{=1\,:\,|v|\leq\lfloor\frac{f_s}{2\Delta F_s}\rfloor} \\
&= \sum_{k=0}^{K-1}\sum_{l=0}^{L-1} q_{kL+l}\,\mathrm{e}^{-\mathrm{j}2\pi v\Delta F_s(kL+l)\Delta T_s}.
\end{aligned}
\tag{3.21}
$$

Now, if we set

$$
\Delta F_s := \frac{1}{KT_b} = \frac{1}{KL\Delta T_s} = \frac{f_s}{KL},
\tag{3.22}
$$

we arrive at

$$
Q_v = \sum_{k=0}^{K-1}\sum_{l=0}^{L-1} q_{kL+l}\,\mathrm{e}^{-\mathrm{j}\frac{2\pi}{KL}v(kL+l)}, \quad v = \left(-\frac{KL}{2},\ldots,\frac{KL}{2}-1\right).
\tag{3.23}
$$

The range of the frequency domain sample index is $v = -KL/2,\ldots,KL/2-1$ if the total number of series elements KL is even. This is always the case in the simulation models in this thesis. Otherwise, it would be $v = -KL \text{ div } 2,\ldots,KL \text{ div } 2$[2]. Through the special setup of ΔF_s in Eq. (3.22), the frequency series, whose notation turns into $\mathbf{Q}_{KL}$ according to Eq. (3.16), has the same number of elements as the time series $\mathbf{q}_{KL}$ now. Substitution and elimination of the double sum with $l' := kL+l$ in Eq. (3.23) makes this obvious and leads to

$$
Q_v = \sum_{l'=0}^{KL-1} q_{l'}\,\mathrm{e}^{-\mathrm{j}\frac{2\pi}{KL}vl'}, \quad v = -\frac{KL}{2},\ldots,\frac{KL}{2}-1.
\tag{3.24}
$$

This equation resembles much the definition of the discrete Fourier transform (DFT) which can be efficiently computed by the fast Fourier transform (FFT) algorithm. Assuming the number of series elements KL to be even, the time domain series $\mathbf{q}_{KL}$ can be recomputed by applying the inverse fast Fourier transform (IFFT) algorithm to get

$$
q_{kL+l} = \frac{1}{KL}\sum_{v=-\frac{KL}{2}}^{\frac{KL}{2}-1} Q_v\,\mathrm{e}^{\mathrm{j}\frac{2\pi}{KL}v(kL+l)}
$$

---

[2] div is integer division.

$$= \frac{1}{KL} \sum_{v=-\frac{KL}{2}}^{-1} Q_v \, \mathrm{e}^{\mathrm{j}\frac{2\pi}{KL}v(kL+l)} + \sum_{v=0}^{\frac{KL}{2}-1} Q_v \, \mathrm{e}^{\mathrm{j}\frac{2\pi}{KL}v(kL+l)}$$

$$\overset{v':=v+KL}{=} \frac{1}{KL} \sum_{v'=\frac{KL}{2}}^{KL-1} \underbrace{Q_{v'-KL}}_{=\,Q_{v'}} \, \mathrm{e}^{\mathrm{j}\frac{2\pi}{KL}v'(kL+l)} \, \underbrace{\mathrm{e}^{-\mathrm{j}\frac{2\pi}{KL}KL(kL+l)}}_{=1} + \sum_{v=0}^{\frac{KL}{2}-1} Q_v \, \mathrm{e}^{\mathrm{j}\frac{2\pi}{KL}v(kL+l)}$$

(periodic extension of $\mathbf{Q}_{KL}$)

$$\overset{v':=v}{=} \frac{1}{KL} \sum_{v=0}^{KL-1} Q_v \, \mathrm{e}^{\mathrm{j}\frac{2\pi}{KL}v(kL+l)}, \quad k = 0, \dots, K-1; l = 0, \dots, L-1. \tag{3.25}$$

The final step to arrive at this result makes use of a periodic extension of the frequency series $\mathbf{Q}_{KL}$ by setting

$$Q_{v'} := Q_{v'-KL}, \quad v' = KL/2, \dots, KL-1, \tag{3.26}$$

and the circular symmetry of the complex exponential function to get the conventional IFFT indexing scheme with $v = 0, \dots, KL-1$.

In conclusion, we have summarized the general modeling approach in Fig. 3.2. It shows the interaction of input and output signals among the entities of Fig. 2.1 on page 6 when simulating the behavior of the OA-IM/DD link, whether in time or frequency domain. The depicted entity with its impulse response $h(t)$ and transfer function $H(f)$ and their discrete-time counterparts h_{kL+l} and H_v may be viewed as
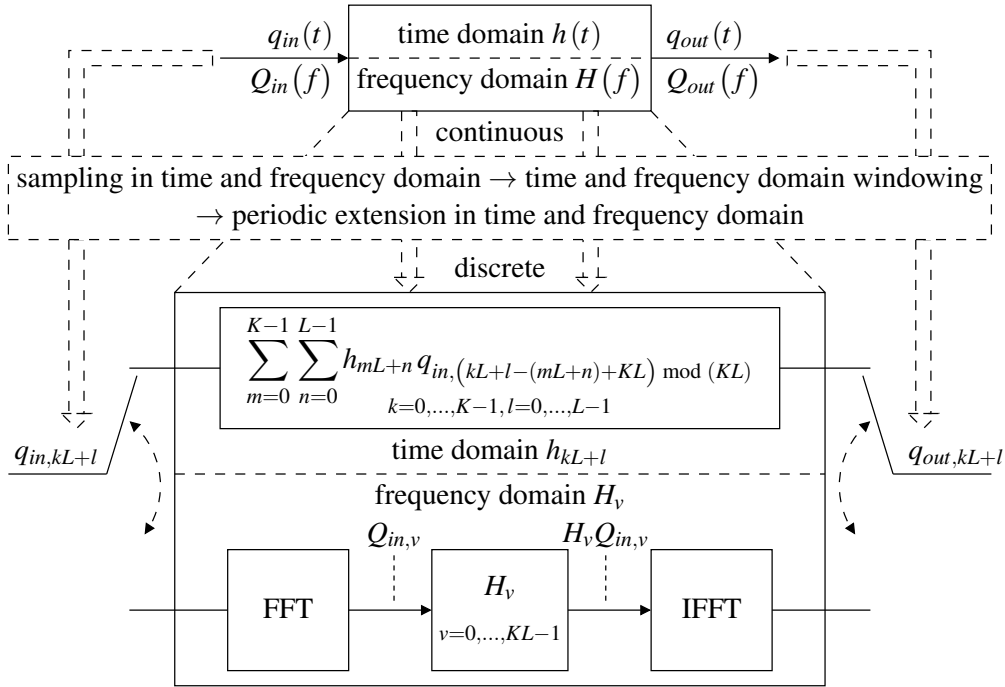

Figure 3.2: General modeling approach from continuous to discrete and periodic time and frequency domain representation

a placeholder for any entity in Fig. 2.1, which models a physical operation on its labeled input to calculate the corresponding output signal, i.e.

$$H(f) \in \left\{ \mathscr{F}\{g(t)\}, H_{\text{opt}}(f), H_{\text{f}}(z,f), H_{\text{el}}(f) \right\}. \tag{3.27}$$

Fig. 3.2 adds the labels "in" and "out" to $q(t)$ for distinction. Eqs. (3.4) − (3.25) are the guidelines to generate the time and frequency domain series elements, $q_{in,kL+l}$ and h_{kL+l} as well as $Q_{in,v}$ and H_v, from their continuous time or frequency descriptions. While frequency domain simulation relies mainly on Eqs. (3.24) and (3.25) with

- FFT execution on the input time series elements $q_{in,kL+l}$,

- sample by sample multiplication of $Q_{in,v}$ with H_v,

- and final IFFT execution on the resulting frequency series elements $H_v Q_{in,v}$ to get $q_{out,kL+l}$,

the corresponding time domain operation is a special kind of convolution which is known as *circular convolution* [46] and calculated by

$$
\begin{aligned}
q_{out,kL+l} &= \text{FFT}^{-1}\left\{ H_v Q_{in,v} \right\} \\
&= \sum_{m=0}^{K-1} \sum_{n=0}^{L-1} h_{mL+n}\, q_{in,\left(kL+l-(mL+n)+KL\right) \bmod (KL)} \\
& \quad k = 0, \dots, K-1; l = 0, \dots, L-1.
\end{aligned}
\tag{3.28}
$$

The index term $(kL + l - (mL + n) + KL) \bmod (KL)^3$ cares for the correct series elements of $q_{in,kL+l}$ within the convolution sum of Eq. (3.28). It becomes obvious from Eq. (3.28) that circular convolution of the input series $\mathbf{q}_{in,KL}$ with any impulse response series $\mathbf{h}_{KL}$ with memory (i.e $h_{kL+l} \neq 0$ for $kL + l > 0$) has the consequence that the tail signal components of the input series $\mathbf{q}_{in,KL}$ with $kL + l = \dots, KL - 2, KL - 1$ contribute to the first ones of the output sequence $\mathbf{q}_{out,KL}$ with $kL + l = 0, 1, \dots$.

Although we will not explicitly refer to the discrete nature of simulation signals and the existence of the rectangular simulation windows in time and frequency domain anymore, the procedures and operations illustrated in Fig. 3.2 have always to be kept in mind when we focus more on the physical description of the various entities in Ch. 3.2.

---

[3] mod is the modulo operation (remainder after integer division).

3.1.4 Equivalent Baseband Description

The approach of the *equivalent baseband channel* is often used to simplify things for the analysis and simulation of bandpass digital communication systems [42, 47]. Especially, when it comes to represent continuous-time signals by their discrete-time versions, the equivalent baseband model is favorable. It is obvious that direct simulation of a bandpass system with carrier frequency f_0 and signal bandwidth B_{opt} would have to cover the frequency range $f \in [0, f_0 + B_{opt}/2]$. In contrast, the equivalent baseband system with a cutoff frequency at $f_c = B_{opt}/2$ only requires to consider the range $f \in [0, B_{opt}/2]$. The difference becomes more severe if $f_0 \gg B_{opt}$. This is especially true for optical communication systems, in which the frequency of the optical CW signal is in the THz-range, and the signal bandwidth B_{opt} is in the GHz-range. Less restrictive requirements on the choice of the sampling frequency f_s lead directly to a smaller oversampling factor L, which is necessary to keep the influence of aliasing reasonably low as shown before (cf. Eq. (3.3)). The number of series elements KL for signal representation decreases the same way, and the data memory as well as the processing time of computer simulations is reduced. Clear notations and equations are additional advantages of the equivalent baseband description.

As the name equivalent baseband model implies, we have to replace parts of the transmission system carrying real-valued bandpass signals by their complex equivalent baseband description. Recalling the findings of Ch. 2 with Eqs. (2.12) – (2.14) and inserting Eqs. (2.4), (2.7) and (2.8), the analog input to the EDC unit can be rewritten in time domain by[4]

$$x(t) = \frac{I_{E0}G^2}{2} \left(\left(a_e(t) \cos\left(2\pi f_0 t + \varphi_0\right) \right) * h_{\mathrm{f}}(t) \right)^2 * h_{\mathrm{el}}(t)$$

$$= \frac{I_{E0}G^2}{2} \left| a_e(t) * \left(h_{\mathrm{f}}(t) \, \mathrm{e}^{-\mathrm{j}2\pi f_0 t} \right) \right|^2 * h_{\mathrm{el}}(t). \tag{3.29}$$

A closer view on the squared magnitude expression in Eq. (3.29) reveals that it consists of the envelope of the optical TX signal $a_e(t)$ convolved with $h_{\mathrm{f}}(t) \, \mathrm{e}^{-\mathrm{j}2\pi f_0 t} \circ\!\!-\!\!\bullet H_{\mathrm{f}}(f + f_0)$. While $a_e(t)$ is a baseband signal by nature, the complex exponential term $\mathrm{e}^{-\mathrm{j}2\pi f_0 t}$ in time domain causes a shift by $-f_0$ in frequency domain. Consequently, the upper spectral component of the original SSMF bandpass channel $h_{\mathrm{f}}(t) \circ\!\!-\!\!\bullet H_{\mathrm{f}}(f)$ is shifted in the baseband region, while the lower is relocated at $-2f_0$. This shift is illustrated in Fig. 3.3, in which the SSMF transfer functions $H_{\mathrm{f}}(\cdot)$ shall only represent CD for the moment. Since the SSMF is then an all-pass filter with nonlinear phase (cf. Ch. 3.2.2), we only present the corresponding phase plot. The asymmetry of $H_{\mathrm{f}}(f + f_0)$ in frequency domain also justifies why $h_{\mathrm{f}}(t) \, \mathrm{e}^{-\mathrm{j}2\pi f_0 t}$ is a complex-valued time domain signal. Since the frequency components at $-2f_0$ are filtered out by the electrical LPF $h_{\mathrm{el}}(t)$ with $f_{3\,\mathrm{dB,el}} \approx B_{opt}/2 \ll f_0$ (indicated as dashed inner rectangular window in Fig. 3.3), they do not have to be simulated at all. Thus, we can narrow

---

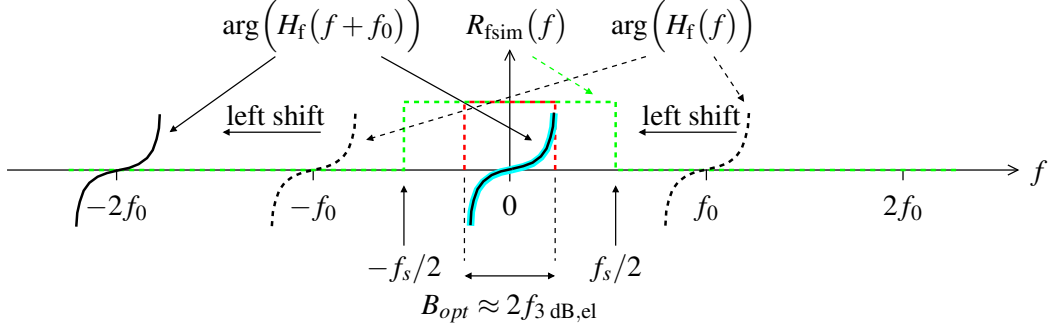[4]The detailed derivation of the resulting expression in Eq. (3.29) is given in App. B.

Figure 3.3: Equivalent baseband description of the SSMF for the example of CD: $H_\mathrm{f}(f)$ is represented by its phase

down the rectangular frequency domain simulation window $R_\mathrm{fsim}(f)$ defined in Ch. 3.1.1 by decreasing f_s to the baseband region. Now, the appropriate choice of the sampling frequency $f_s = L/T_b$ not only serves to set the simulation accuracy, but it is also used to suppress the spectral components of the shifted optical bandpass channel near $-2f_0$ and to preserve sufficient space for the equivalent baseband spectrum with expected spectral broadening after direct detection. The preferable relations among the frequency parameters are

$$f_{3\,\mathrm{dB,el}} \ll \frac{f_s}{2} = \frac{L}{2T_b} \lll 2f_0 - \frac{B_{opt}}{2} \approx 2f_0 - \frac{1}{2T_b} \tag{3.30}$$

assuming that the useful component of the optical TX spectrum is almost the reciprocal of the bit interval, i.e. $B_{opt} \approx 1/T_b$. Fig. 3.3 indicates these conditions qualitatively. Eq. (3.30) reveals that the oversampling factor L is our main control parameter for the discrete signal representation and the equivalent baseband model in computer simulations. After having set the oversampling factor L to fulfill Eq. (3.30), we may include the rectangular frequency domain simulation window into the consideration of the optical fiber link in Eq. (3.29) without changing the EDC input signal notably and get

$$x(t) \approx \frac{I_{E0}G^2}{2} \left| a_e(t) * \underbrace{\left(h_\mathrm{f}(t)\,\mathrm{e}^{-\mathrm{j}2\pi f_0 t}\right) * r_\mathrm{fsim}(t)}_{=:\tilde{h}_\mathrm{f}(t)} \right|^2 * h_\mathrm{el}(t)$$

$$= \frac{I_{E0}G^2}{2} \left| a_e(t) * \tilde{h}_\mathrm{f}(t) \right|^2 * h_\mathrm{el}(t). \tag{3.31}$$

The stand-alone equivalent baseband description of the optical fiber channel is given by

$$\tilde{h}_\mathrm{f}(t) := \left(h_\mathrm{f}(t)\,\mathrm{e}^{-\mathrm{j}2\pi f_0 t}\right) * r_\mathrm{fsim}(t) \circ\!\!-\!\!\bullet\ \tilde{H}_\mathrm{f}(f) = H_\mathrm{f}(f + f_0)\,R_\mathrm{fsim}(f). \tag{3.32}$$

Application of the equivalent baseband model for simulating the optical fiber channel implies that all associated signals and entities which are related to or act on the optical signal have to be transformed into their equivalent baseband description. The transformation rule of Eq. (3.32) has to be applied to any impulse responses, spectra or transfer functions repre-

senting an optical signal or entity in Fig. 2.1 on page 6. The tilde, as for $\tilde{h}_{\mathrm{f}}(t) \circ\!\!\!-\!\!\bullet \tilde{H}_{\mathrm{f}}(f)$, is used as a mark to make the distinction to the real-world bandpass signals in the following.

3.2 Device Modeling

We introduce the physical models of the entities depicted in Fig. 2.1 on page 6. We just present the mathematical formula while discretization of signals and implementation of the corresponding simulation algorithms have to be worked out according to the the previous section and instructions given in literature [47]. The depicted waveforms are mostly generated by linear interpolation of the output from the implemented simulator tool box. Note that the notation of signals, impulse responses and transfer functions in the optical domain differ to those of Fig. 2.1 by its vector or matrix character to account for PMD effects. This two-dimensional description is commonly referred to as *Jones calculus* [36], which describes two orthogonal polarization modes propagating along the fiber. Any state of linear polarization can be directly described by a linear combination of both. If we further allow a phase shift between the two states, circular or, more general, elliptical polarization can be described, too. Nevertheless, the previous derivations with scalar treatment of the whole system still hold and may easily be transferred to the two-dimensional case as will be shown.

3.2.1 Optical Transmitter

Fig. 3.4 summarizes the components of the optical intensity modulation TX with enhanced two-dimensional labeling to account for PMD effects in equivalent baseband notation.
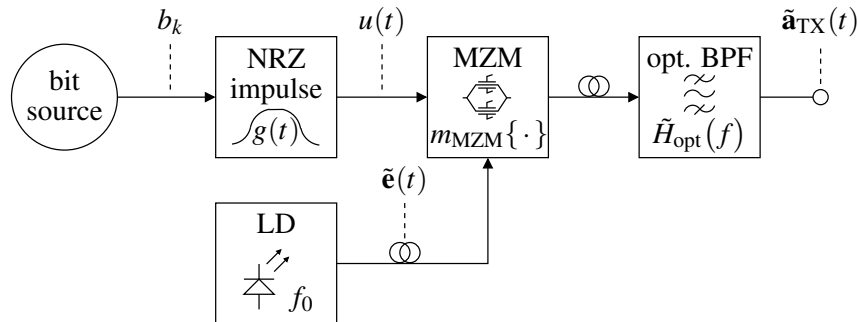

Figure 3.4: Optical transmitter

3.2.1.1 Bit Source

The bit source is modeled as a pseudo-random binary sequence (PRBS)

$$\mathbf{b}_K = (b_k)_{k=0,\ldots,K-1}, \quad K \in \mathbb{N}_1, \tag{3.33}$$

whose bits $b_k \in \{0, 1\}$ are basically taken from the output of a linear feedback shift register (LFSR) [42]. In general, a polynomial description in the finite Galois field (GF) $\text{GF}(2^1)$ with mod 2-arithmetic is used to indicate the tap positions of this LFSR. A nonzero initial state of the LFSR generates an output sequence

$$\mathbf{b}_{LFSR,K'} := \left(b_{LFSR,k'} \right)_{k'=0,\ldots,2^P-1} \tag{3.34}$$

which repeats itself after a period of $2^P - 1$ if the employed polynomial with degree P is primitive. The output sequence $\mathbf{b}_{LFSR,K'}$ is then a maximal length sequence and contains all different bit patterns of length P except the one with P zeros [42]. Since the response of nonlinear systems is not independent of the specific input signal, covering all possible bit patterns is favorable to investigate the intersymbol interference (ISI) effects of neighboring symbols in OA-IM/DD links. It guarantees that all possible signal transitions within the temporal spread of ISI are excited and ensures statistical confidence of simulation results. An appropriate PRBS consequently features a polynomial degree P which takes all expected ISI of preceding and trailing symbols into account. We include the missing all-zero pattern of length P in such a PRBS by inserting an additional zero to the longest run of zeros in the output sequence $\mathbf{b}_{LFSR,K'}$ of the LFSR. PRBSs with these characteristics are called DeBruijn binary sequence (DBBS) and have

$$K = 2^P \tag{3.35}$$

elements with equal occurrence of zeros and ones with

$$P[b_k = 0] = P[b_k = 1] = 0.5. \tag{3.36}$$

Fig. 3.5 and Table 3.1 give an example on the generation of such a PRBS for the primitive polynomial $0x9 = 1001_2$ in hexadecimal and the corresponding binary notation. It has a degree of $P = 4$.
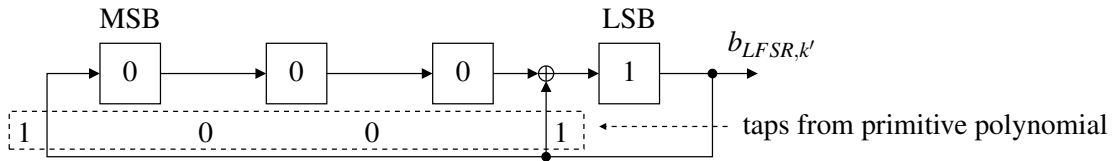

Figure 3.5: LFSR example in Galois structure for the primitive polynomial $0x9 = 1001_2$ with degree $P = 4$

$\mathbf{b}_{LFSR,15}$	$(1,1,1,1,0,1,0,1,1,0,0,1,0,0,0)$
$\mathbf{b}_{16}$	$(1,1,1,1,0,1,0,1,1,0,0,1,0,0,0,0)$

Table 3.1: PRBS example as output of an LFSR for a primitive polynomial of degree $P = 4$ and length $K = 16$

The net bit rate of the investigated optical fiber links is 40 Gbit/s with additional FEC over-

head of almost 6.8 % [48]. Thus, the effective bit rate is set to $R_b = 42.7$ Gbit/s for the computer simulations. We have employed a PRBS with polynomial degree $P = 11$ and length $K = 2048$, which is far enough for the impairing ISI characteristics of the considered SSMF lengths at 42.7 Gbit/s.

3.2.1.2 NRZ Impulse Shaping

The impulse shaping device for the generation of the NRZ drive signal of the MZM is modeled as a time domain raised cosine impulse of the form

$$
g(t) = \begin{cases}
G_0 & : \ t \in \left(\frac{T_b}{2} - \frac{T_g}{2} \left(1 - \rho \right), \frac{T_b}{2} + \frac{T_g}{2} \left(1 - \rho \right) \right) \\[2ex]
G_0 \cos^2 \left(\frac{\pi}{4} \frac{\left| t - \frac{T_b}{2} \right| - \frac{T_g}{2} (1-\rho)}{\rho \frac{T_g}{2}} \right) & : \ t \in \left(\frac{T_b}{2} - \frac{T_g}{2} \left(1 + \rho \right), \frac{T_b}{2} - \frac{T_g}{2} \left(1 - \rho \right) \right] \vee \\[2ex]
& \qquad t \in \left[\frac{T_b}{2} + \frac{T_g}{2} \left(1 - \rho \right), \frac{T_b}{2} + \frac{T_g}{2} \left(1 + \rho \right) \right) \\[2ex]
0 & : \ elsewhere.
\end{cases}
\tag{3.37}
$$

We set the amplitude $G_0 = 1$ for convenience, and a realistic impulse shape is given for a roll-off factor of $\rho = 0.35$. The parameter T_g is the effective impulse width defined by the relation

$$
\int_{-\infty}^{\infty} g(t) \, dt = \int_{-\infty}^{\infty} r_{T_g} dt
\tag{3.38}
$$

with

$$
r_{T_g} := \begin{cases} 1 & : \ t \in \left[-\frac{T_g}{2}, \frac{T_g}{2} \right] \\ 0 & : \ elsewhere \end{cases}.
\tag{3.39}
$$

Figs. 3.6(a) and 3.6(b) illustrate the properties of $g(t)$. The eye diagram of the electrical drive signal $u(t)$ of the MZM (cf. Eq. (2.1)) has been recorded with an oversampling factor of $L = 32$. It is drawn using different colors for the signal transitions with respect to the bits $b_k = 0$ and $b_k = 1$ in Fig. 3.6(b). The time origin coincides with the center point of the eye, which is maximally open in horizontal and vertical direction. Thus, the electrical part of the TX supports ISI-free signaling.

3.2.1.3 CW Laser

At first, the optical CW signal is modeled as a linearly polarized electrical field. In the plane of polarization, the exact equivalent baseband description, which is derived from Eq. (2.2) on page 6, is

$$
\tilde{e}(t) = \frac{E_0}{2} \, e^{j \varphi_0}.
\tag{3.40}
$$

(a) Time domain raised cosine impulse with $\rho = 0.35$ and $T_g = T_b$

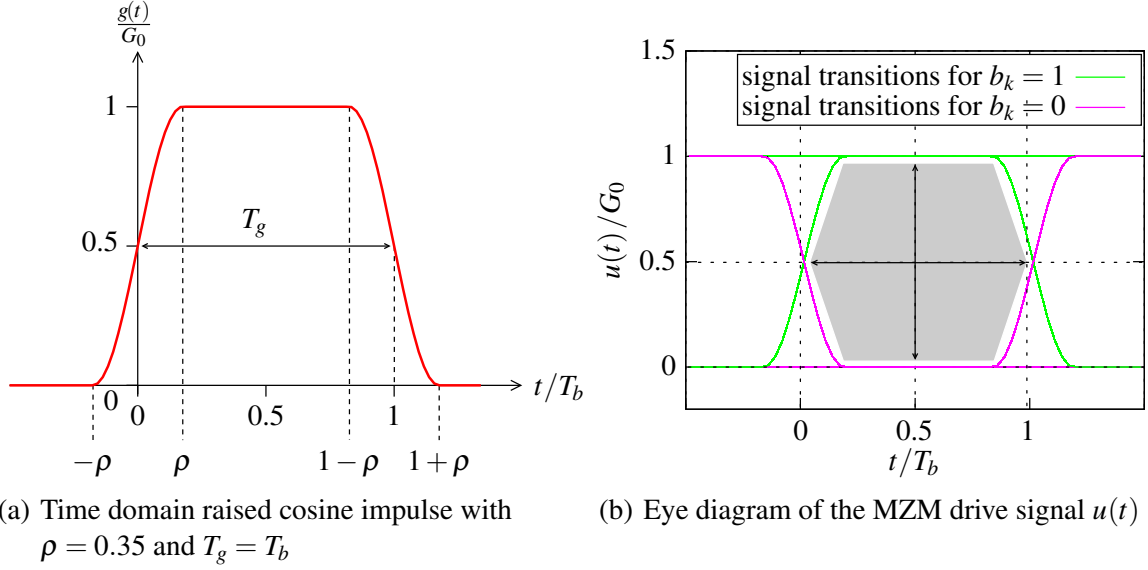(b) Eye diagram of the MZM drive signal $u(t)$

Figure 3.6: Electrical impulse shaping

Since we neglect nonlinear optical impairments like SPM and SBS and define the optical signal-to-noise ratio (OSNR) at the EDFA (cf. Ch. 3.2.3.1), the relative system performance in terms of bit error ratio (BER) vs. OSNR is not affected if we omit the factor of $1/2$ in Eq. (3.40). Therefore, we set per definition

$$\tilde{e}(t) := E_0 = \sqrt{P_{LD}} \tag{3.41}$$

using the mean optical LD power of the equivalent baseband system as an adjustable parameter in the simulation environment. The arbitrary but fixed zero phase angle φ_0 has also been omitted since direct detection (DD) removes all phase information of the optical signal (cf. Eq. (3.29)). A reasonable value for the mean optical LD power is 1 mW for LDs used in optical communication systems.

In order to include polarization dependent behavior, we further assume the propagation of a TEM wave in the optical domain of the OA-IM/DD system. This description makes use of a three-dimensional Cartesian coordinate system, whose xy-plane is orthogonal to the direction of propagation z. Thus, x- and y-polarization modes are indicated by the subscripts x and y. The mean optical LD power $P_{LD} = E_0^2$ is distributed among these two polarization modes by the power split ratio $\gamma \in [0,1)$. The two-dimensional equivalent baseband description of the optical CW signal is therefore

$$\tilde{\mathbf{e}}(t) = \begin{pmatrix} \tilde{e}_x(t) \\ \tilde{e}_y(t) \end{pmatrix} = \begin{pmatrix} \sqrt{\gamma} \\ \sqrt{1-\gamma} \end{pmatrix} E_0, \tag{3.42}$$

which describes a linearly polarized electrical field since the two field components $\tilde{e}_x(t)$ and

$\tilde{e}_y(t)$ are in phase. We fix $\gamma = 0.5$ in this thesis, i.e.

$$\tilde{e}_x(t) = \tilde{e}_y(t) = \frac{E_0}{\sqrt{2}}, \tag{3.43}$$

because this causes the worst case scenario for PMD induced distortions.

3.2.1.4 MZ Modulator

A MZM is a planar lightwave circuit (PLC) featuring a cascade of a 3 dB power splitter, two modulator branches and a power combiner with respect to the optical CW signal. The material of the waveguide structure is $LiNbO_3$, whose refractive index can be adjusted by applying an electrical field. This property can be used to induce a phase difference between the split optical CW signals propagating along the two modulator branches. The induced phase difference leads to constructive or destructive interference when the two signals are combined again. Neglecting the common propagation delay term from the input to the output port, the general MZM characteristic in equivalent baseband notation is

$$\tilde{m}_{\mathrm{MZM}}\{\varphi_{ub}(t), \varphi_{lb}(t)\} = \frac{\mathrm{e}^{-\mathrm{j}\varphi_{ub}(t)} + \mathrm{e}^{-\mathrm{j}\varphi_{lb}(t)}}{2}$$
$$= \mathrm{e}^{-\mathrm{j}\frac{\varphi_d(t)}{2}\theta(t)} \cos\left(\frac{\varphi_d(t)}{2}\right) \tag{3.44}$$

with

$$\varphi_d(t) = \varphi_{ub}(t) - \varphi_{lb}(t) \quad \text{and} \quad \theta(t) = \frac{\varphi_{ub}(t) + \varphi_{lb}(t)}{\varphi_{ub}(t) - \varphi_{lb}(t)}. \tag{3.45}$$

The variable $\varphi_d(t)$ represents the phase difference between the phase change $\varphi_{ub}(t)$ of the upper and $\varphi_{lb}(t)$ of the lower modulator branch, and $\theta(t)$ represents a relative phase factor. Eq. (3.44) reveals that the first exponential term causes pure phase modulation while the second one stands for pure intensity modulation. Since we only investigate systems with the latter modulation format, we have to ensure that the phase modulation term disappears. The push-pull operation mode with $\varphi_{lb}(t) = -\varphi_{ub}(t)$, which results in $\theta(t) = 0$, is appropriate for this purpose. Its effective characteristic is

$$\tilde{m}_{\mathrm{MZM}}\{\varphi_d(t)\} = \cos\left(\frac{\varphi_d(t)}{2}\right). \tag{3.46}$$

Using a MZM with balanced single drive electrode configuration as in Fig. 3.7(a), push-pull operation can easily be realized. A single drive voltage connected to the inner electrodes generates electrical fields of opposite directions in the two modulator branches. Thus, the

phase difference $\varphi_d(t)$ is given by

$$\varphi_d(t) = \pi\frac{U_{bias}}{U_\pi} - \pi\frac{u_\varepsilon\left(u(t) - \frac{G_0}{2}\right)}{G_0 U_\pi}, \quad U_{bias}, U_\pi \in \mathbb{R}, u_\varepsilon \in [0,1), \tag{3.47}$$

with separate feed of the bias U_{bias} and the MZM drive signal $u(t)$. The normalization voltage U_π is a characteristic parameter, which causes a phase change of π in one modulator branch. The MZM drive signal $u(t)$ is not directly connected to the electrodes, but first transformed from a unipolar to a bipolar signal by subtracting $G_0/2$ and then multiplied with the scaling factor u_ε/G_0 to account for the finite extinction ratio and an appropriate excitation range of the resulting signal. The numerator of this scaling factor is related to the absolute numerical value of the power extinction ratio ε, whose definition will be explained during the discussion of Fig. 3.7(b), by

$$u_\varepsilon = 1 - \frac{4}{\pi}\arctan\frac{1}{\sqrt{\varepsilon}}. \tag{3.48}$$

Insertion of Eq. (3.47) in (3.46) results in

$$\tilde{m}_{\text{MZM}}\{u(t)\} = \cos\left(\frac{\pi}{2}\frac{U_{bias}}{U_\pi} - \frac{\pi}{2}\frac{u_\varepsilon\left(u(t) - \frac{G_0}{2}\right)}{G_0 U_\pi}\right). \tag{3.49}$$

The power transfer characteristic, which is of major interest for OA-IM/DD links, is

$$\tilde{m}_{\text{MZM}}^2\{u(t)\} = \cos^2\left(\frac{\pi}{2}\frac{U_{bias}}{U_\pi} - \frac{\pi}{2}\frac{u_\varepsilon\left(u(t) - \frac{G_0}{2}\right)}{G_0 U_\pi}\right)$$

$$= \frac{1}{2}\left(1 + \cos\left(\pi\frac{U_{bias}}{U_\pi} - \pi\frac{u_\varepsilon\left(u(t) - \frac{G_0}{2}\right)}{G_0 U_\pi}\right)\right). \tag{3.50}$$

We have depicted the power transfer characteristic in Fig. 3.7(b) together with a single impulse corresponding to the occurring temporal change of the phase difference $\varphi_d(t)$ according to Eq. (3.47) with the NRZ impulse shape of Eq. (3.37). Apparently, the mean optical power at the output of the MZM is just half of the mean optical power at the input if we set $U_{bias} = U_\pi/2$ and if the bit sequence $\mathbf{b}_K$ contains an equal number of zeros and ones. Unavoidable fabrication deficiencies and the limited bandwidth of the electrode electronics in real devices leads to a finite power extinction ratio, which prevents the power transfer characteristic from full excitation. Consequently, the mean optical power level for $\varphi_d(t) = 0$ does not fall below $\tilde{m}_{min}^2 P_{LD}$ for a logical zero, and the mean optical power level for $\varphi_d(t) = 1$ does not exceed $\tilde{m}_{max}^2 P_{LD}$ for a logical one. The power extinction ratio of the MZM is defined
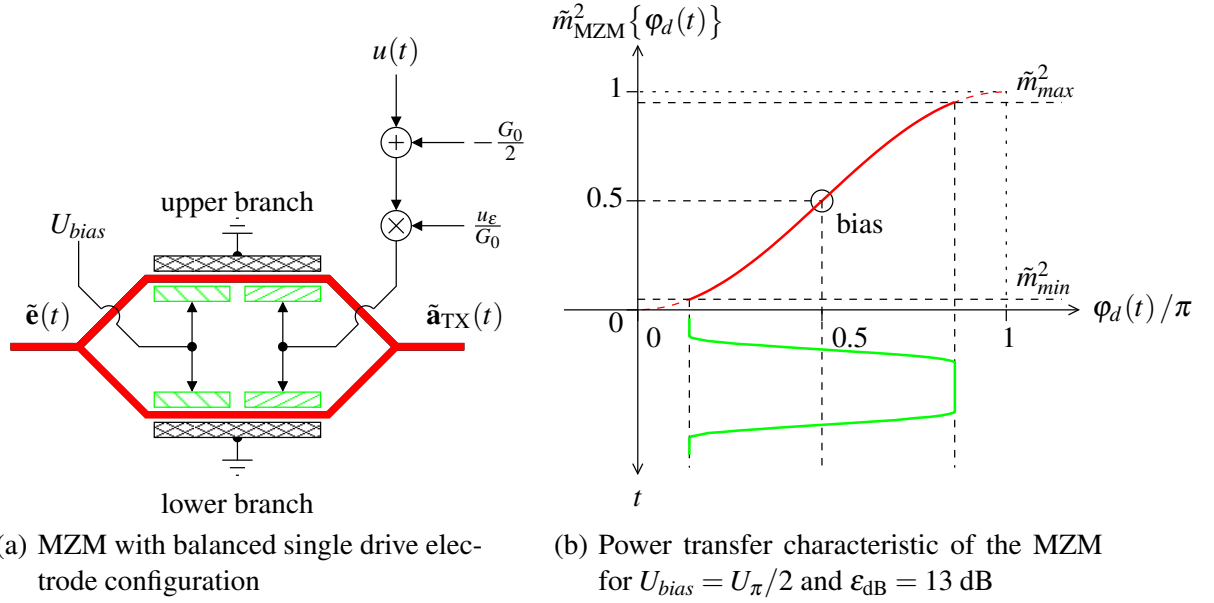
(a) MZM with balanced single drive electrode configuration

(b) Power transfer characteristic of the MZM for $U_{bias} = U_\pi/2$ and $\varepsilon_{dB} = 13$ dB

Figure 3.7: External optical modulation by a MZM

as the relation of the maximal and minimal optical power level with

$$\varepsilon = \frac{\tilde{m}_{max}^2}{\tilde{m}_{min}^2} \tag{3.51}$$

and is often given in dB with

$$\varepsilon_{dB} = 10 \lg \varepsilon. \tag{3.52}$$

The content of Fig. 3.7(b) features $\varepsilon_{dB} = 13$ dB, which is mentioned in several data sheets of available MZM devices.

3.2.1.5 Optical Band-Pass Filter

The equivalent baseband description of the optical TX signal according to Fig. 3.4 is

$$\tilde{\mathbf{a}}_{TX}(t) = \underbrace{\left(\tilde{\mathbf{e}}(t)\, \tilde{m}_{MZM}\{u(t)\} \right)}_{=\tilde{\mathbf{a}}_e(t)} * \tilde{h}_{opt}(t), \tag{3.53}$$

in which we have assumed polarization transparency of the MZM and the optical BPF. The complex envelope is given by the term in parentheses, and we use Eq. (3.42) and the MZM characteristic of Eq. (3.49) to express it with

$$\tilde{\mathbf{a}}_e(t) = \left(\frac{\sqrt{\gamma}}{\sqrt{1-\gamma}} \right) \sqrt{P_{LD}}\; \tilde{m}_{MZM}\{u(t)\} \tag{3.54}$$

$$= \begin{pmatrix} \sqrt{\gamma} \\ \sqrt{1-\gamma} \end{pmatrix} \sqrt{P_{LD}} \, \cos \left(\frac{\pi}{2} \frac{U_{bias}}{U_{\pi}} - \frac{\pi}{2} \frac{u_{\varepsilon} \left(u(t) - \frac{G_0}{2} \right)}{G_0 U_{\pi}} \right). \tag{3.55}$$

We model the shape of the optical BPF transfer function as a Gaussian filter, whose main parameters are the optical bandwidth $B_{3\,\mathrm{dB,opt}}$ and the Gaussian order N_G. The transfer function in equivalent baseband notation is

$$\tilde{h}_{\mathrm{opt}}(t) \circ\!\!-\!\!\bullet \tilde{H}_{\mathrm{opt}}(f) = \exp \left(-\ln\left(\sqrt{2}\right) \cdot \left(\frac{f}{\frac{B_{3\,\mathrm{dB,opt}}}{2}} \right)^{2N_G} \right), \quad N_G \in \mathbb{N}_1. \tag{3.56}$$

We generally set $B_{3\,\mathrm{dB,opt}} = 5\,R_{b,\mathrm{Hz}}$ with $R_{b,\mathrm{Hz}}$ being the numerical value of the bit rate in the frequency unit Hz. The factor of five provides an optical bandwidth of $B_{3\,\mathrm{dB,opt}} = 213.5$ GHz for $R_b = 42.7$ Gbit/s which almost conforms to the 100 GHz ITU channel spacing grid by omitting either even or odd channel numbers to arrive at a 200 GHz grid. The relative setting of bandwidth parameters to the bit rate allows for easier comparison and scaling of simulation results. The exponential order is $N_G = 2$. The resulting shape is depicted in Fig. 3.8(a) together with the rectangular baseband simulation window for an oversampling factor of $L = 32$ (dashed line) to illustrate the bandwidth proportions. Figs. 3.8(b) – 3.8(d) verify that the parameter choice for optical TX filtering with respect to a 200 GHz channel spacing grid hardly affects the useful component of the optical TX frequency spectrum indicated by B_{opt}. The power spectra of Fig. 3.8(b) reveal a typical characteristic of OA-IM/DD systems showing that the optical CW signal is transmitted alongside the information bearing signal. The nonlinear MZM characteristic causes intermodulation, which becomes visible in the periodic repetition of frequency spikes from the optical CW signal at multiples of $R_{b,\mathrm{Hz}}$. The transmission of the optical CW signal does not provide any information content from an information theoretic point of view and is principally a waste of TX power. Therefore, the use of carrier suppressed return-to-zero (CSRZ) transmission is an alternative solution at the cost of higher TX complexity [49]. Figs. 3.8(c) and 3.8(d) oppose the eye diagrams of the optical TX signal $\tilde{\mathbf{a}}_{\mathrm{TX}}(t)$ and the corresponding complex envelope $\tilde{\mathbf{a}}_e(t)$ after direct detection as if an ideal photodiode was connected to the optical BPF and the MZM, respectively. The vertical relative eye opening has already decreased at the output of the optical TX compared to the MZM drive signal $u(t)$ in the electrical domain (cf. Fig. 3.6(b)). The finite extinction ratio is responsible for this effect and reduces the noise and ISI tolerance of the system a priori. Fig. 3.8(c) and 3.8(d) show that the relative eye openings are almost equal with and without optical TX filtering. Nevertheless, the signal in Fig. 3.8(c) shows slight overshoot and a displacement of the position of the maximal horizontal eye opening. The small deviations justify the approximation made in Eq. (2.4) on page 7 where we have omitted the optical TX filter for ease of notation in the initial system description.
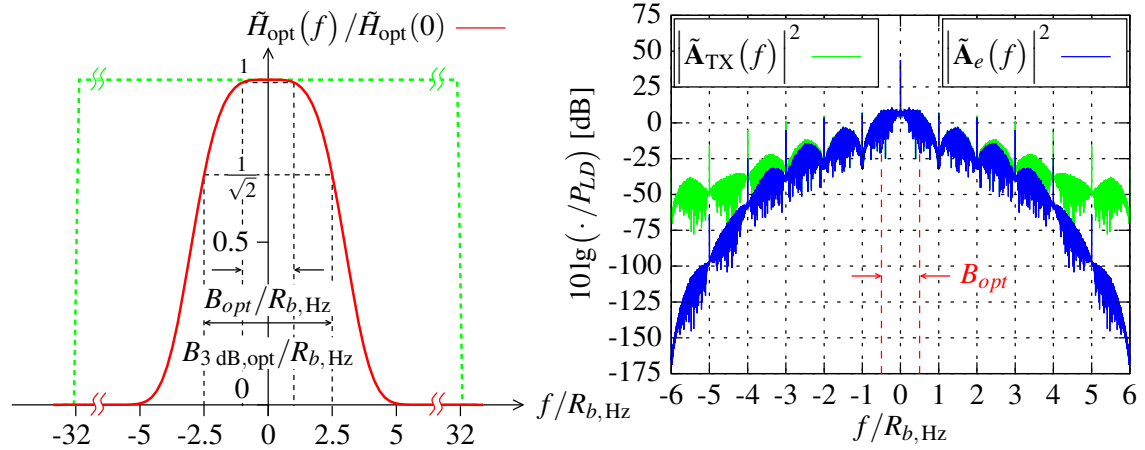
(a) Gaussian transfer function of the optical BPF ($B_{3\,\mathrm{dB,opt}} = 5R_{b,\mathrm{Hz}}$, $N_G = 2$, $R_{\mathrm{fsim}}(f)$ with $L = 32$ (dashed))

(b) Power frequency spectra of the optical TX signal and the complex envelope
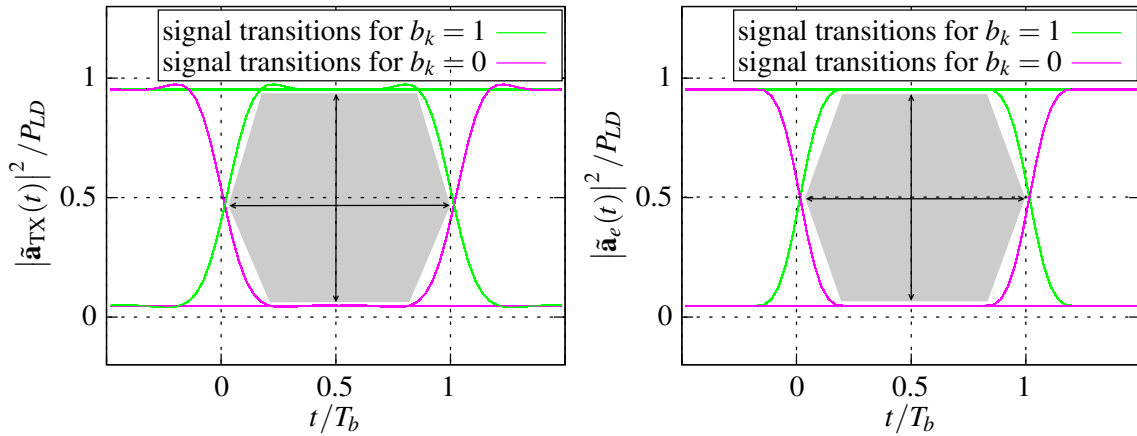
(c) Eye diagram of the squared magnitude of the optical TX signal

(d) Eye diagram of the squared magnitude of the complex envelope

Figure 3.8: Optical TX filtering

3.2.2 Optical Fiber Channel

The optical fiber channel is determined by the characteristics of the SSMF. The main impacts on the propagating optical signal are CD and PMD in the linear and SPM and SBS in the nonlinear transmission regime for a single wavelength channel. WDM systems are moreover affected by XPM between adjacent wavelength channels. These nonlinear effects scale with optical power and transmission distance and therefore play a minor role for short-haul OA-IM/DD links. That is why we consider direct detection to be the dominating source of nonlinearity in the end-to-end consideration of an OA-IM/DD link, and the influence of the optical fiber channel for CD and PMD with possible polarization scattering can be described

linearly by a transfer matrix in frequency domain with the general approach

$$\tilde{\mathbf{H}}_{\mathrm{f}}(z,f) = \underbrace{\begin{bmatrix} \mathrm{e}^{-\left(\alpha_x(f)+\mathrm{j}\beta_x(f)\right)z} & 0 \\ 0 & \mathrm{e}^{-\left(\alpha_y(f)+\mathrm{j}\beta_y(f)\right)z} \end{bmatrix}}_{=:\tilde{\mathbf{D}}(z,f)} \underbrace{\begin{bmatrix} \tilde{s}_1(z,f) & \tilde{s}_2(z,f) \\ -\tilde{s}_2^*(z,f) & \tilde{s}_1^*(z,f) \end{bmatrix}}_{=:\tilde{\mathbf{S}}(z,f)}. \qquad (3.57)$$

If we intend to address the SSMF as a whole, we have to evaluate this transfer matrix at $z = L_f$ and use the notation

$$\tilde{\mathbf{H}}_{\mathrm{f}}(f) := \tilde{\mathbf{H}}_{\mathrm{f}}\left(L_f, f\right). \qquad (3.58)$$

The dispersion matrix $\tilde{\mathbf{D}}(z,f)$ models CD and attenuation. Since we assume that the attenuation constants are almost independent of frequency within the utilized optical signal spectrum and neglect polarization dependent loss (PDL), we set

$$\alpha_x(f) = \alpha_y(f) =: \alpha, \qquad (3.59)$$

and SSMFs typically show $\alpha_{\mathrm{dB}} = 0.2 \, \mathrm{dB/km}$ with

$$\alpha_{dB} = 20\lg(\mathrm{e}) \cdot \alpha \approx 8.686\,\alpha. \qquad (3.60)$$

Using this simplified assumptions, the dispersion matrix is

$$\tilde{\mathbf{D}}(z,f) = \mathrm{e}^{-\alpha z} \begin{bmatrix} \mathrm{e}^{-\mathrm{j}\beta_x(f)z} & 0 \\ 0 & \mathrm{e}^{-\mathrm{j}\beta_y(f)z} \end{bmatrix}. \qquad (3.61)$$

The polarization scattering matrix $\tilde{\mathbf{S}}(z,f)$ with basic elements $\tilde{s}_1(z,f)$ and $\tilde{s}_2(z,f)$ models the mutual exchange of signal energy between the two polarization modes. $\tilde{\mathbf{S}}(z,f)$ is unitary obeying

$$\tilde{\mathbf{S}}(z,f)\,\tilde{\mathbf{S}}(z,f)^{\mathrm{H}} = \mathbf{I} \qquad (3.62)$$

and

$$\left|\tilde{s}_1(z,f)\right|^2 + \left|\tilde{s}_2(z,f)\right|^2 = 1. \qquad (3.63)$$

The unitary of $\tilde{\mathbf{S}}(z,f)$ accounts for the passive characteristic of polarization scattering, i.e. the polarization modes may exchange energy, but no energy is dissipated or generated.

Since this thesis investigates EDC concepts with respect to different impairments, several

models have been developed which focus on the specific simulation task based on

$$
\tilde{\mathbf{H}}_{\mathrm{f}}(z,f) \overset{(3.61)}{=} \mathrm{e}^{-\alpha z} \underbrace{\begin{bmatrix} \mathrm{e}^{-\mathrm{j}\beta_x(f)z} & 0 \\ 0 & \mathrm{e}^{-\mathrm{j}\beta_y(f)z} \end{bmatrix}}_{=\tilde{\mathbf{D}}(z,f)} \underbrace{\begin{bmatrix} \tilde{s}_1(z,f) & \tilde{s}_2(z,f) \\ -\tilde{s}_2^*(z,f) & \tilde{s}_1^*(z,f) \end{bmatrix}}_{=\tilde{\mathbf{S}}(z,f)} .
\tag{3.64}
$$

A separate section for each of those models presents their physical description in the following.

3.2.2.1 CD Model

In this simulation model, which only considers CD, we may skip the polarization dependence by setting

$$
\beta(f) := \beta_x(f) = \beta_y(f) \quad \text{and} \quad \tilde{\mathbf{S}}(z,f) = \mathbf{I}.
\tag{3.65}
$$

The transfer matrix approach of the Eq. (3.64) simplifies to

$$
\tilde{\mathbf{H}}_{\mathrm{f}}(z,f) = \mathrm{e}^{-\alpha z}\,\mathrm{e}^{-\mathrm{j}\beta(f)z} \begin{bmatrix} 1 & 0 \\ 0 & 1 \end{bmatrix}.
\tag{3.66}
$$

The main constituent of SSMF is silica (SiO_2), whose refractive index is wavelength, or equivalently, frequency dependent. CD, which is also referred to as group velocity dispersion (GVD), is a material dispersion therefore. The corresponding wave number $\beta(f)$ is a nonlinear function in frequency often approximated by its third order Taylor series expansion. It is given in equivalent baseband domain by[5]

$$
\beta(f) \approx \beta_0 + \frac{\beta_1}{1!}f + \frac{\beta_2}{2!}f^2 + \frac{\beta_3}{3!}f^3
\tag{3.67}
$$

with expansion coefficients

$$
\beta_i = \frac{\partial^i \beta(f_0)}{\partial f^i}, \quad i = 0,\ldots,3,
\tag{3.68}
$$

evaluated at the center frequency of the utilized optical spectrum. This is the LD frequency f_0 here. It is obvious that the group delay of a TEM wave, given by

$$
\tau_g(z,f) = \frac{1}{2\pi}\frac{\partial \beta(f)}{\partial f} z
\tag{3.69}
$$

$$
\overset{(3.67)}{=} \frac{1}{2\pi}\left(\beta_1 + \beta_2 f + \frac{\beta_3}{2}f^2\right) z
\tag{3.70}
$$

---

[5]In bandpass domain, f has to be replaced by $(f - f_0)$.

becomes also frequency dependent for $\beta_2 \neq 0$ and $\beta_3 \neq 0$. While the constant term β_0, representing the absolute phase difference between the optical TX signal and the signal at location z, vanishes after differentiation, the linear term with β_1 in Eq. (3.67) leads to a common delay for all frequency components and does not alter the signal shape therefore. Hence, we can restrict the Taylor series expansion to

$$\beta(f) := \frac{\beta_2}{2!}f^2 + \frac{\beta_3}{3!}f^3 \tag{3.71}$$

to simulate the effect of CD.

This definition for $\beta(f)$ is used in place of the more general $\beta(f)$ in Eq. (3.67) for the simulation model

$$\tilde{\mathbf{H}}_{\mathrm{f}}(f) = \mathrm{e}^{-\alpha L_f}\, \mathrm{e}^{-\mathrm{j}\left(\frac{\beta_2}{2!}f^2 + \frac{\beta_3}{3!}f^3\right)L_f} \begin{bmatrix} 1 & 0 \\ 0 & 1 \end{bmatrix}. \tag{3.72}$$

The remaining higher order terms related to β_2 and β_3 make the frequency components contained in the optical TX frequency spectrum travel at different speeds along the fiber. A single transmitted impulse appears broader in time at the RX. In the case of consecutive impulses, this broadening causes an overlap with the neighboring ones leading to ISI [36].

Commercially available fibers are characterized by the dispersion coefficient D_λ and dispersion slope S_λ. They are connected to the expansion coefficients β_2 and β_3 by[6]

$$D_\lambda = -\frac{2\pi c_0}{\lambda_0^2}\frac{\beta_2}{(2\pi)^2} \quad \text{and} \quad S_\lambda = \frac{4\pi c_0}{\lambda_0^4}\left(\lambda_0\frac{\beta_2}{(2\pi)^2} + \pi c_0\frac{\beta_3}{(2\pi)^3}\right). \tag{3.73}$$

Common values for SSMFs are $D_\lambda = 17\,\mathrm{ps}/(\mathrm{nm\cdot km})$ and $S_\lambda = 0.08\,\mathrm{ps}/(\mathrm{nm^2 \cdot km})$. Fig. 3.3 on page 20 already contains the qualitative phase characteristic arising from these values.

According to Eq. (3.69), the amount of CD induced ISI mainly depends on the group delay profile, which is characterized by D_λ and S_λ, and the distance z to the TX. In order to make the exposure of OA-IM/DD to CD comparable for different fiber types (e.g. SSMFs, disperison-shifted fibers (DSFs) or DCFs [36]) and also for concatenations among them with possibly differing section lengths, textbooks and publications often refer to the (residual)[7] CD value

$$r_D := D_\lambda L_f. \tag{3.74}$$

---

[6]Note that, in textbooks using angular frequency notation, the denominators $(2\pi)^2$ and $(2\pi)^3$ in Eq. (3.73) are missing since the expansion coefficients are related by (cf. Eq. (3.68)):

$$\frac{\partial^i \beta(\omega)}{\partial \omega^i} = \frac{\partial^i \beta(f)}{\partial f^i}\underbrace{\frac{\partial^i f}{\partial \omega^i}}_{=\frac{1}{(2\pi)^i}} = \frac{1}{(2\pi)^i}\frac{\partial^i \beta(f)}{\partial f^i}, \quad i = (0,\ldots,3).$$

[7]The attribute *residual* in the context of CD originates from the usage of DCFs because not all CD is actually compensated. Since we do not distinguish between partially compensated and uncompensated OA-IM/DD links, we only refer to the term CD *value* for r_D.

It has the unit ps/nm. If we concatenate two (different types of) fibers, the total CD value will be the sum of the individual CD values of each section. Using r_D to characterize CD has the advantage of abstracting from the actual OA-IM/DD link parameters to any others with possibly different fiber sections yet with the same CD characteristic.

There exists another interesting relation for r_D if we approximate the impact of CD by its second-order Taylor series expansion coefficient β_2 only. We assume two OA-IM/DD links with different bit rates $R_{b,1} \neq R_{b,2}$ and fiber lengths $L_{f,1} \neq L_{f,2}$, and that the optical signal bandwidths are approximately given by $B_{opt,1} \approx R_{b,Hz,1}$ and $B_{opt,2} \approx R_{b,Hz,2}$. If we evaluate the second order phase terms in Eq. (3.72) at $f = R_{b,Hz,1}$ and $f = R_{b,Hz,1}$, respectively, we see that they are related to

$$\sim \beta_2 R_{b,Hz,1}^2 L_{f,1} \quad \text{and} \quad \sim \beta_2 R_{b,Hz,2}^2 L_{f,2}. \tag{3.75}$$

Since $D_\lambda \sim \beta_2$, it follows that $r_D \sim \beta_2 L_f$, and we realize that the phase terms are also related to

$$\sim r_{D,1} R_{b,Hz,1}^2 \quad \text{and} \quad \sim r_{D,2} R_{b,Hz,2}^2. \tag{3.76}$$

Obviously, two OA-IM/DD links observe the same amount of CD-related second-order phase distortion within B_{opt} if the phase terms are equal. Thus, if we want to transfer the link behavior with respect to CD from one to the other, we may set

$$r_{D,1} R_{b,Hz,1}^2 = r_{D,2} R_{b,Hz,2}^2 \quad \Longleftrightarrow \quad \frac{r_{D,1}}{r_{D,2}} = \left(\frac{R_{b,Hz,2}}{R_{b,Hz,1}} \right)^2. \tag{3.77}$$

Thus, the simulation results presented in this thesis and recorded for $R_b = 42.7$ Gbit/s at different fiber lengths might be transferred to any other OA-IM/DD link configuration featuring other bit rates and/or fiber lengths.

3.2.2.2 PMD Models

So far, we have assumed the SSMF to be a homogeneously cylindrical structure, for which the wave number $\beta(f)$ is equal for both polarization modes, and for which no polarization scattering occurs. However, manufacturing processes cannot yield a perfect cylindrical symmetry, and installation of fibers around edges may cause material stress and torsion which may also vary over time and temperature. These inhomogeneities lead to birefringence, i.e. $\beta_x(f) \neq \beta_y(f)$, and the two polarization modes propagate at different speeds along the SSMF, which is referred to as PMD.

In general, PMD is a statistical process depending on time, frequency and location [50]. This favors to consider this phenomenon as a statistical ensemble and to describe the statistical nature of PMD as a concatenation of small fiber segments with constant but altering birefringence. Fig. 3.9 shows this modeling approach with parameters describing the birefringence

of the segments. For numerical simulations, these parameters are changed randomly. Polarization scattering at the intersection of two fiber segments accounts for polarization mode coupling. This is indicated by the change of the coordinate system, and polarization scattering as a whole can be considered as a kind of scrambling.
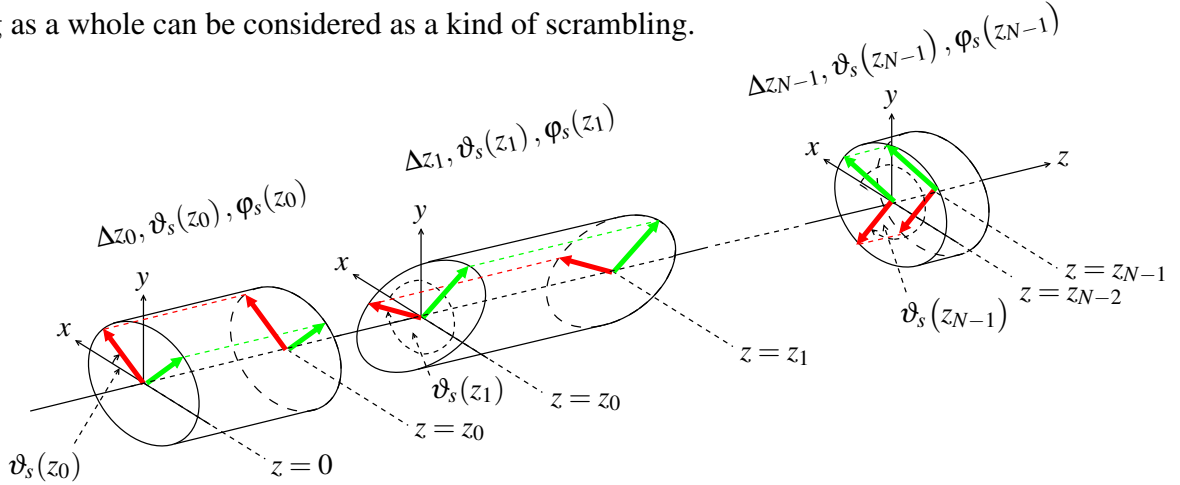
Figure 3.9: Statistical PMD modeling

Based on this, different approaches for modeling of PMD exist:

- In the first-order PMD model, two preeminent modes of polarization describe the birefringence of the optical fiber in a mean temporal and frequency independent sense.

- The combined CD and first-order PMD model simply adds the effect of CD to the first-order PMD model.

- The higher order PMD model introduces time dependent randomness which takes the measured statistical nature of birefringence in optical fibers into account.

3.2.2.2.1 First-Order PMD Model

This simple model has its foundation on the concept of the principal states of polarization (PSP), whose definition is: the PSP represent those two orthogonal polarization states at the input of the fiber for which the corresponding output polarization states do not depend on frequency to the first-order [51, 52]. This implies that optical signals, whose states of polarization coincide with the PSP, keep their polarization at the output to the first-order in frequency. In other words, they do not couple linearly in f into each other[8]. Furthermore, the behavior of the SSMF with respect to the PSP can be described by two independent signal paths, which observe a mutual delay since birefringence causes $\beta_x(f) \neq \beta_y(f)$. The SSMF model for PMD reduces to a single, long waveplate as depicted in Fig. 3.10. It illustrates the PSP defining a Cartesian system with axes x and y. Given this definition of PSP and its implications, the simple first-order model discussed here assumes that the optical TX signal is launched into the fiber with respect to the PSP as indicated by the subscript labels $\cdot_x$ and $\cdot_y$ for the signal description.

---

[8]Note that the concept of PSP does not say anything about higher order dependence on frequency.
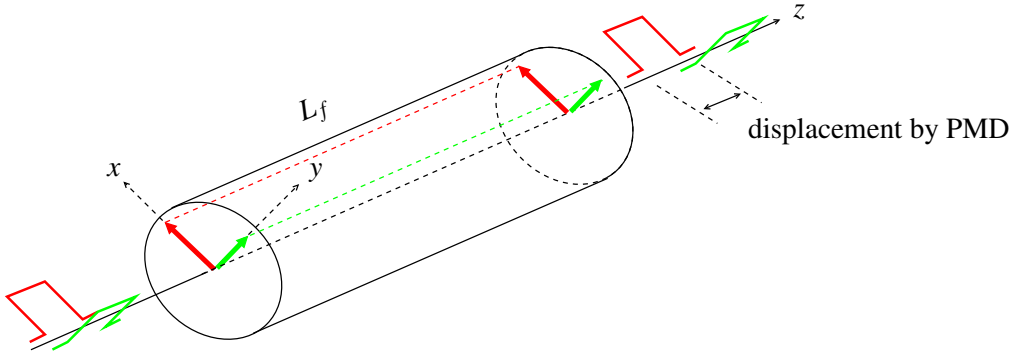
Figure 3.10: Illustration of the waveplate model

Concerning the mathematical model for first-order PMD, we may neglect polarization scattering as implied by the concept of PSP and the launch of the optical TX signal along the PSP, i.e. we set $\tilde{\mathbf{S}}(z, f) = \mathbf{I}$. In addition, the first-order PMD model shall allow for an isolated considerations of principal PMD impairments. Therefore, we use the same Taylor series expansion approach as in Eq. (3.67) for $\beta_x(f)$ and $\beta_y(f)$ but with polarization specific expansion coefficients and truncation after the first-order terms. This implies

$$\beta_x(f) := \beta_{x,1} f \quad \text{and} \quad \beta_y(f) := \beta_{y,1} f. \tag{3.78}$$

Again, we have neglected the constant phase terms of $\beta_{x,0}$ and $\beta_{y,0}$, since they do not affect direct detection in OA-IM/DD systems. The effective transfer matrix with respect to the coordinate system of the PSP is then

$$\tilde{\mathbf{H}}_{\mathrm{f}}(z, f) = \mathrm{e}^{-\alpha z} \begin{bmatrix} \mathrm{e}^{-\mathrm{j}\beta_{x,1} f z} & 0 \\ 0 & \mathrm{e}^{-\mathrm{j}\beta_{y,1} f z} \end{bmatrix}. \tag{3.79}$$

The elements $\mathrm{e}^{-\mathrm{j}\beta_{x,1} f z}$ can be considered as one-tap linear-phase filter, and the corresponding group delays according to Eq. (3.69) depend only on the location with

$$\tau_{g,x}(z) = \frac{1}{2\pi}\beta_{x,1} z \quad \text{and} \quad \tau_{g,y}(z) = \frac{1}{2\pi}\beta_{y,1} z. \tag{3.80}$$

This means the two optical signals carried by the two polarization modes do preserve shape, but they observe mutual delay at the RX, which causes ISI due to direct detection. Their difference after the optical TX signal has propagated along the SSMF is

$$\Delta\tau_g := \left| \tau_{g,x}(L_f) - \tau_{g,y}(L_f) \right|$$

$$= \frac{1}{2\pi}\left| \beta_{x,1} - \beta_{y,1} \right| L_f \tag{3.81}$$

and is known as differential group delay (DGD). This value, in analogy to r_D for CD, shall serve as our main parameter to characterize the first-order PMD behavior in the sense as

mean value for the statistical phenomenon of PMD.

If we apply the DGD definition to Eq. (3.79), we may express the first-order PMD transfer matrix by

$$
\begin{aligned}
\tilde{\mathbf{H}}_{\mathrm{f}}(f) &= \mathrm{e}^{-\alpha L_f}\,\mathrm{e}^{-\mathrm{j}\frac{\beta_{x,1}+\beta_{y,1}}{2}fL_f}
\begin{bmatrix}
\mathrm{e}^{-\mathrm{j}\frac{\beta_{x,1}-\beta_{y,1}}{2}fL_f} & 0 \\
0 & \mathrm{e}^{\mathrm{j}\frac{\beta_{x,1}-\beta_{y,1}}{2}fL_f}
\end{bmatrix} \\
&= \mathrm{e}^{-\alpha L_f}\,\mathrm{e}^{-\mathrm{j}\frac{\beta_{x,1}+\beta_{y,1}}{2}fL_f}
\begin{bmatrix}
\mathrm{e}^{-\mathrm{j}2\pi\frac{\Delta\tau_g}{2}f} & 0 \\
0 & \mathrm{e}^{\mathrm{j}2\pi\frac{\Delta\tau_g}{2}f}
\end{bmatrix}.
\end{aligned}
\tag{3.82}
$$

Since we do not require causality in a computer simulation, we can omit the common phase term and finally set

$$
\tilde{\mathbf{H}}_{\mathrm{f}}(f) := \mathrm{e}^{-\alpha L_f}
\begin{bmatrix}
\mathrm{e}^{-\mathrm{j}2\pi\frac{\Delta\tau_g}{2}f} & 0 \\
0 & \mathrm{e}^{\mathrm{j}2\pi\frac{\Delta\tau_g}{2}f}
\end{bmatrix}
\tag{3.83}
$$

for the first-order PMD transfer matrix of the SSMF.

Interpretation and Implications on EDC

Fig. 3.11 shows an equivalent, signal processing related block diagram for the first-order PMD model according to Eq. (3.83) in time domain. It shows a polarization beam split-
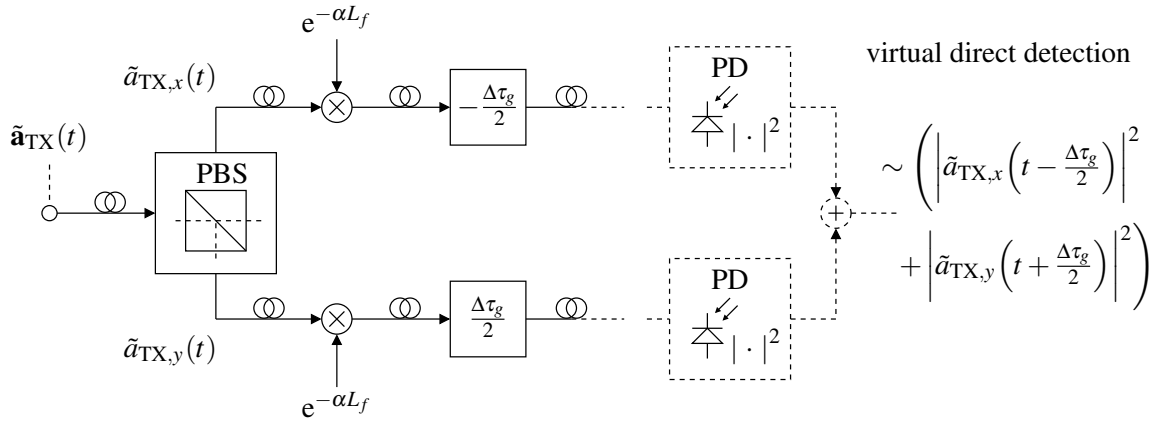

Figure 3.11: Equivalent block diagram for the first-order PMD model

ter (PBS), which is directly oriented towards the two PSP. Attenuation and optical delay elements follow in each signal path. The interconnecting fiber segments are assumed to be ideal. Virtual application of photodetection at location L_f by summing the power of the

orthogonal polarization modes shows

$$
\begin{aligned}
\left| \tilde{\mathbf{a}}\left(L_f, t \right) \right|^2 &= \left| \tilde{a}_x \left(L_f, t \right) \right|^2 + \left| \tilde{a}_y \left(L_f, t \right) \right|^2 \\
&= \left| \mathscr{F}^{-1} \left\{ \tilde{\mathbf{H}}_{\mathrm{f}}(f)\, \tilde{\mathbf{A}}_{\mathrm{TX}}(f) \right\} \right|^2 \\
&= \left| \mathscr{F}^{-1} \left\{ \mathrm{e}^{-\alpha L_f} \begin{bmatrix} \mathrm{e}^{-\mathrm{j}2\pi \frac{\Delta \tau_g}{2} f} & 0 \\ 0 & \mathrm{e}^{\mathrm{j}2\pi \frac{\Delta \tau_g}{2} f} \end{bmatrix} \begin{pmatrix} \tilde{A}_{\mathrm{TX},x}(f) \\ \tilde{A}_{\mathrm{TX},y}(f) \end{pmatrix} \right\} \right|^2 \\
&= \left| \mathscr{F}^{-1} \left\{ \mathrm{e}^{-\alpha L_f} \begin{pmatrix} \tilde{A}_{\mathrm{TX},x}(f)\, \mathrm{e}^{-\mathrm{j}2\pi \frac{\Delta \tau_g}{2} f} \\ \tilde{A}_{\mathrm{TX},y}(f)\, \mathrm{e}^{\mathrm{j}2\pi \frac{\Delta \tau_g}{2} f} \end{pmatrix} \right\} \right|^2 \\
&= \mathrm{e}^{-2\alpha L_f} \left(\left| \tilde{a}_{\mathrm{TX},x}\left(t - \frac{\Delta \tau_g}{2} \right) \right|^2 + \left| \tilde{a}_{\mathrm{TX},y}\left(t + \frac{\Delta \tau_g}{2} \right) \right|^2 \right).
\end{aligned}
\tag{3.84}
$$

The result reveals that we can treat both signal paths independently by two separate PDs, and that fist-order PMD remains a linear ISI with respect to the squared magnitude of the polarization modes after direct detection [35], i.e. the time shifts by $\mp \Delta \tau_g / 2$ and direct detection are interchangeable.

Since we have assumed equal power splitting between the two PSP in Eq. (3.43)

$$
\tilde{a}_{\mathrm{TX},x}(t) = \tilde{a}_{\mathrm{TX},y}(t)
$$

and Eq. (3.84) becomes

$$
\left| \tilde{\mathbf{a}}\left(L_f, t \right) \right|^2 = \mathrm{e}^{-2\alpha L_f} \left(\left| \tilde{a}_{\mathrm{TX},x}\left(t - \frac{\Delta \tau_g}{2} \right) \right|^2 + \left| \tilde{a}_{\mathrm{TX},x}\left(t + \frac{\Delta \tau_g}{2} \right) \right|^2 \right).
\tag{3.85}
$$

If we interchange time shift and direct detection, Eq. (3.85) becomes

$$
\left| \tilde{\mathbf{a}}\left(L_f, t \right) \right|^2 = \mathrm{e}^{-2\alpha L_f} \left(\delta\left(t - \frac{\Delta \tau_g}{2} \right) + \delta\left(t + \frac{\Delta \tau_g}{2} \right) \right) * \left| \tilde{a}_{\mathrm{TX},x}(t) \right|^2.
\tag{3.86}
$$

Partially transforming this expression in frequency domain gives us further insight with

$$
\left| \tilde{\mathbf{a}}\left(L_f, t \right) \right|^2 = \mathscr{F}^{-1} \left\{ \mathrm{e}^{-2\alpha L_f} \underbrace{\left(\mathrm{e}^{-\mathrm{j}2\pi \frac{\Delta \tau_g}{2} f} + \mathrm{e}^{\mathrm{j}2\pi \frac{\Delta \tau_g}{2} f} \right)}_{= 2\cos\left(2\pi \frac{\Delta \tau_g}{2} f \right)} \right\} * \left| \tilde{a}_{\mathrm{TX},x}(t) \right|^2
$$

$$= \mathscr{F}^{-1} \left\{ \underbrace{2\,\mathrm{e}^{-2\alpha L_f} \cos\left(2\pi \frac{\Delta \tau_g}{2} f\right)}_{=:\tilde{H}_{\mathrm{f,eff.}}(f)} \right\} * \left| \tilde{a}_{\mathrm{TX},x}(t) \right|^2 \tag{3.87}$$

and with $\tilde{H}_{\mathrm{f,eff.}}(f)$ being the effective first-order PMD transfer matrix after direct detection at the RX.

Obviously, $\tilde{H}_{\mathrm{f,eff.}}(f)$ has zeros at

$$\cos\left(2\pi \frac{\Delta \tau_g}{2} f\right) = 0 \quad \Longleftrightarrow \quad f = (2n+1)\frac{1}{2\Delta \tau_g}, \; n \in \mathbb{N}. \tag{3.88}$$

Compared to the power spectrum of the optical TX signal depicted in Fig. 3.8(b) on page 29 with bandwidth $B_{opt} \approx 1/T_b$, the zeros of $\tilde{H}_{\mathrm{f,eff.}}(f)$ take effect if

$$\frac{1}{2\Delta \tau_g} \leq \frac{1}{2T_b} \quad \Longleftrightarrow \quad \Delta \tau_g \geq T_b. \tag{3.89}$$

Since a zero in the channel transfer function may impact the performance of a linear filter based EDC method, we will come back to the implications of Eq. (3.89) later. For a detailed derivation and illustration of $\tilde{H}_{\mathrm{f,eff.}}(f)$, we refer to [53][9].

3.2.2.2.2 Combined CD and First-Order PMD Model

This model is just but a concatenation of the CD and first-order PMD model. It refers to the CD Taylor series expansion for $\beta(f)$ according to Eq. (3.71) and extends this to two dimensions for the first-order term. The first order terms are set according to Eq. (3.78). With the notation of differential group delay, the transfer matrix is given by

$$\tilde{\mathbf{H}}_{\mathrm{f}}(f) := \mathrm{e}^{-\alpha L_f}\, \mathrm{e}^{-\mathrm{j}\left(\frac{\beta_2}{2!}f^2 + \frac{\beta_3}{3!}f^3\right)L_f} \begin{bmatrix} \mathrm{e}^{-\mathrm{j}2\pi\frac{\Delta\tau_g}{2}f} & 0 \\ 0 & \mathrm{e}^{\mathrm{j}2\pi\frac{\Delta\tau_g}{2}f} \end{bmatrix}. \tag{3.90}$$

3.2.2.2.3 Time-Variant Higher Order PMD Model

The derivations in the preceding sections have already set the foundations for the time-variant PMD simulation model with higher order effects, which features a mix of the CD and the first-order PMD model with additional polarization scattering.

Concerning the statistics of DGD variations over time and frequency, it is known from measurements [51, 52, 50, 56, 57] that it follows a Maxwell-Boltzmann probability density func-

---

[9]This characteristic of first-order PMD induced ISI resembles a multipath propagation and fading scenario known from mobile communications [54, 55].

tion (PDF) with

$$p\left(\Delta\tau_g\right) = \begin{cases} 0 & : \quad \Delta\tau_g < 0 \\ \sqrt{\dfrac{6}{\pi}}\,\dfrac{3\Delta\tau_g^2}{\Delta\tau_{RMS}^3}\,\mathrm{e}^{-\frac{3\Delta\tau_g^2}{2\Delta\tau_{RMS}^2}} & : \quad \Delta\tau_g \geq 0 \end{cases}. \tag{3.91}$$

Its statistical mean $\mathsf{E}\left[\Delta\tau_g\right]$ is known by the term *PMD value of the fiber* [36], and its root-mean-square (RMS) value is defined by

$$\Delta\tau_{RMS} = \sqrt{\mathsf{E}\left[\Delta\tau_g^2\right]}. \tag{3.92}$$

Both are interrelated by the approximation

$$\mathsf{E}\left[\Delta\tau_g\right] \approx 0.921 \cdot \Delta\tau_{RMS} \tag{3.93}$$

as a general property of the Maxwell-Boltzmann PDF.

Commercially available fibers usually contain a PMD coefficient in their data sheet. This relates the PMD behavior to length with

$$\tau_{PMD} = \sqrt{\frac{\Delta\tau_{RMS}^2}{\mathrm{km}}}. \tag{3.94}$$

Typical values range from $2\,\mathrm{ps}/\sqrt{\mathrm{km}}$ for elderly to $0.1\,\mathrm{ps}/\sqrt{\mathrm{km}}$ for modern fibers. Comparably to the second- and third-order Taylor series expansion coefficients β_2 and β_3 being related to the dispersion coefficient D_λ and the dispersion slope S_λ, the first-order expansion coefficients and the PMD coefficient have their relation with

$$\left|\beta_{x,1} - \beta_{y,1}\right| = 2\pi\frac{\tau_{PMD}}{\sqrt{z}}. \tag{3.95}$$

Eq. (3.95) actually states that the difference of the first-order expansion coefficients depends on the location z now.

Joining the previous Taylor series expansions for the wave numbers of Eq. (3.71) for CD and Eq. (3.78) for first-order PMD together, we get

$$\beta_x\left(f\right) := \frac{\beta_{x,1}}{1!}f + \frac{\beta_2}{2!}f^2 + \frac{\beta_3}{3!}f^3 \tag{3.96}$$

$$\text{and} \quad \beta_y\left(z,f\right) := \frac{\beta_{x,1} - 2\pi\frac{\tau_{PMD}}{\sqrt{z}}}{1!}f + \frac{\beta_2}{2!}f^2 + \frac{\beta_3}{3!}f^3. \tag{3.97}$$

In Eq.(3.97) $\beta_{y,1}$ has been expressed by $\beta_{x,1}$ and τ_{PMD} using Eq. (3.95) while assuming $\beta_{x,1} \geq \beta_{y,1}$ without loss of generality. The first-order terms of Eqs. (3.96) and (3.97) account for PMD and the equal second- and third-order ones for CD distortion, which are common to both.

Despite of introducing the statistical parameter τ_{PMD} into our model, Maxwell-Boltzmann statistics of $\Delta\tau_g$ is not present until we generate different fiber realizations with random segmentation of the SSMF into $N \in \mathbb{N}_2$ waveplates as in Fig. 3.12. The concatenation of several waveplates with randomly chosen parameters is referred to as *coarse step model* [58, 59].
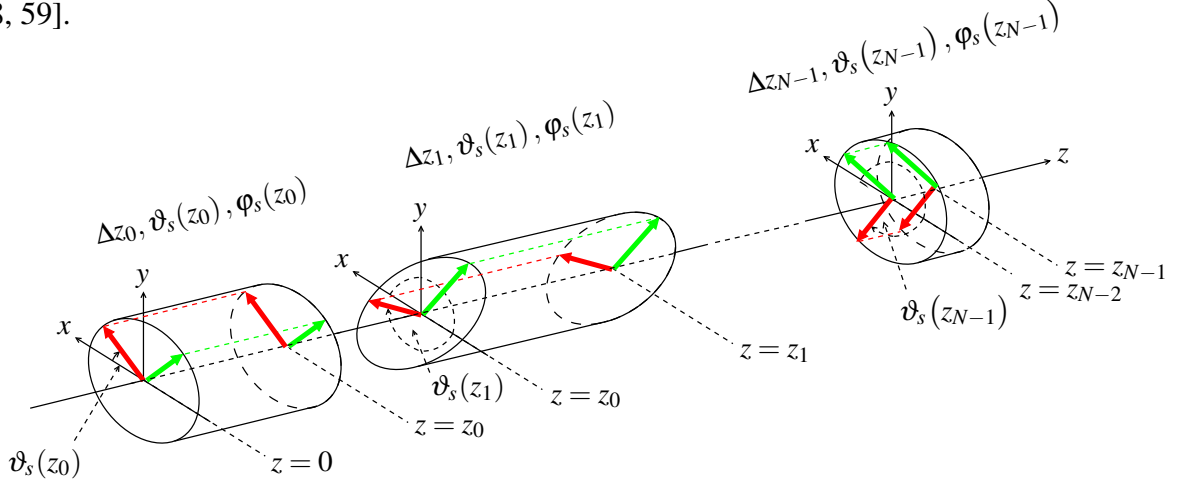

Figure 3.12: Illustration of the coarse step model

Each fiber section in the coarse step model is characterized by its length $\Delta z_n = z_n - z_{n-1}$, the rotation angle $\vartheta_s(z_n)$ and the phase angle $\varphi_s(z_n)$. Both angles determine the PSP of a single waveplate section. The phase angle $\varphi_s(z_n)$ is responsible for the temporal phase difference between the *x*- and *y*-polarization states and illustrated by the different polarization ellipsis in Fig. 3.12. The rotation angle $\vartheta_s(z_n)$ determines the rotation of the PSP within the *xy*-plane.

The section lengths $\Delta z_n = z_n - z_{n-1}$, the rotation and phase angles, $\vartheta_s(z_n)$ and $\varphi_s(z_n)$, which determine the PSP of a single waveplate, are generated randomly with the underlying PDFs

$$p(\Delta z_n) = \frac{1}{\sqrt{2\pi}\sigma_s} e^{-\frac{(\Delta z_n - \mu_s)^2}{2\sigma_s^2}}, \quad \sigma_s \leq \frac{\mu_s}{2}, \tag{3.98}$$

$$p(\vartheta_s(z_n)) = \begin{cases} \frac{1}{2\pi} & : \quad \vartheta_s(z_n) \in [0, 2\pi) \\ 0 & : \quad elsewhere \end{cases}, \tag{3.99}$$

$$\text{and} \quad p(\varphi_s(z_n)) = \begin{cases} \frac{1}{\pi} & : \quad \varphi_s(z_n) \in [0, \pi) \\ 0 & : \quad elsewhere \end{cases}, \quad n = (0, \ldots, N-1). \tag{3.100}$$

Empirical investigations have shown that the Maxwell-Boltzmann distribution of Eq. (3.91) is well approximated using about $N = 12$ waveplates [60]. The mean value μ_s and standard deviation σ_s of the Gaussian random number generator for generating the random sectioning have to be adjusted appropriately. Negative values for Δz_n are discarded during the sectioning process. The PSP of adjacent waveplates can be biased by introducing correlation between the angles $\vartheta_s(z_n)$ and $\vartheta_s(z_{n-1})$ as well as $\varphi_s(z_n)$ and $\varphi_s(z_{n-1})$ [61]. Full correlation leads to a single waveplate with no change of PSP as for the first-order PMD model.

The transfer matrix of one waveplate element is given by

$$
\begin{aligned}
\tilde{\mathbf{H}}_{f,n}\left(\Delta z_n, f, z_n\right) &= \mathbf{D}_n\left(\Delta z_n, f\right) \tilde{\mathbf{S}}_n(z_n) \\
&= e^{-\alpha \Delta z_n}\, e^{-j\left(\frac{\beta_2}{2!}f^2 + \frac{\beta_3}{3!}f^3\right)\Delta z_n}
\begin{bmatrix}
e^{-j\beta_{x,1}f\Delta z_n} & 0 \\
0 & e^{-j\left(\beta_{x,1}-2\pi\frac{\tau_{PMD}}{\sqrt{\Delta z_n}}\right)f\Delta z_n}
\end{bmatrix}
\tilde{\mathbf{S}}_n(z_n) \\
&= e^{-\alpha \Delta z_n}\, e^{-j\left(\frac{\beta_2}{2!}f^2 + \frac{\beta_3}{3!}f^3\right)\Delta z_n} \\
&\quad e^{-j\left(\beta_{x,1}-2\pi\frac{\tau_{PMD}}{2\sqrt{\Delta z_n}}\right)f\Delta z_n}
\begin{bmatrix}
e^{-j2\pi\frac{\tau_{PMD}}{2}f\sqrt{\Delta z_n}} & 0 \\
0 & e^{j2\pi\frac{\tau_{PMD}}{2}f\sqrt{\Delta z_n}}
\end{bmatrix}
\tilde{\mathbf{S}}_n(z_n),
\end{aligned}
\tag{3.101}
$$

and the explicit non-causal form for simulation, which neglects the common first-order phase term of Eq. (3.101), is

$$
\begin{aligned}
\tilde{\mathbf{H}}_{f,n}\left(\Delta z_n, f, z_n\right) &= e^{-\alpha \Delta z_n}\, e^{-j\left(\frac{\beta_2}{2!}f^2 + \frac{\beta_3}{3!}\right)f^3\Delta z_n}
\begin{bmatrix}
e^{-j2\pi\frac{\tau_{PMD}}{2}f\sqrt{\Delta z_n}} & 0 \\
0 & e^{j2\pi\frac{\tau_{PMD}}{2}f\sqrt{\Delta z_n}}
\end{bmatrix} \\
&\quad
\begin{bmatrix}
\cos\left(\vartheta_s(z_n)\right) & \sin\left(\vartheta_s(z_n)\right) e^{-j\varphi_s(z_n)} \\
-\sin\left(\vartheta_s(z_n)\right) e^{j\varphi_s(z_n)} & \cos\left(\vartheta_s(z_n)\right)
\end{bmatrix}.
\end{aligned}
\tag{3.102}
$$

Since $L_f = \sum_{n=0}^{N-1} \Delta z_n$, the corresponding transfer matrix for one fiber realization is calculated by

$$
\tilde{\mathbf{H}}_f(f) = \prod_{n=0}^{N-1} \tilde{\mathbf{H}}_{f,n}\left(\Delta z_n, f, z_n\right) = \prod_{n=0}^{N-1} \mathbf{D}_n\left(\Delta z_n, f\right) \tilde{\mathbf{S}}_n(z_n),
\tag{3.103}
$$

in which the polarization scattering matrices $\tilde{\mathbf{S}}_n(z_n)$ is responsible for polarization mode coupling at location z_{n-1}.

Analyzing the effective PSP of the coarse step model as highlighted in [51] allows to calculate $\Delta\tau_g$ for each fiber realization. An example resulting from this procedure for 100000 fiber realizations is depicted in Fig. 3.13 for $\tau_{PMD} = 2 \text{ ps}/\sqrt{\text{km}}$ and for $L_f = 5 \text{ km}$. The histogram $h_p\left(\Delta\tau_g\right)$, where all $\Delta\tau_g$ for different fiber realizations have been collected, coincides well with the corresponding theoretical Maxwell-Boltzmann PDF of Eq. (3.91). It is worth to note that a DGD of about 10 % of the bit interval already requires doubled optical input power to keep the same BER level [36] although the interval $0 \leq \Delta\tau_g \leq 0.1 T_b$ contains only a small portion of the cumulative distribution function. This fact reveals the necessity and possible benefits of PMD compensation, which is normally laid out for $\Delta\tau_g(z) \leq 3\mathsf{E}\left[\Delta\tau_g\right]$ of the specific link [53] since $p(\Delta\tau_g) > 0$ still holds for $\Delta\tau_g \to \infty$.

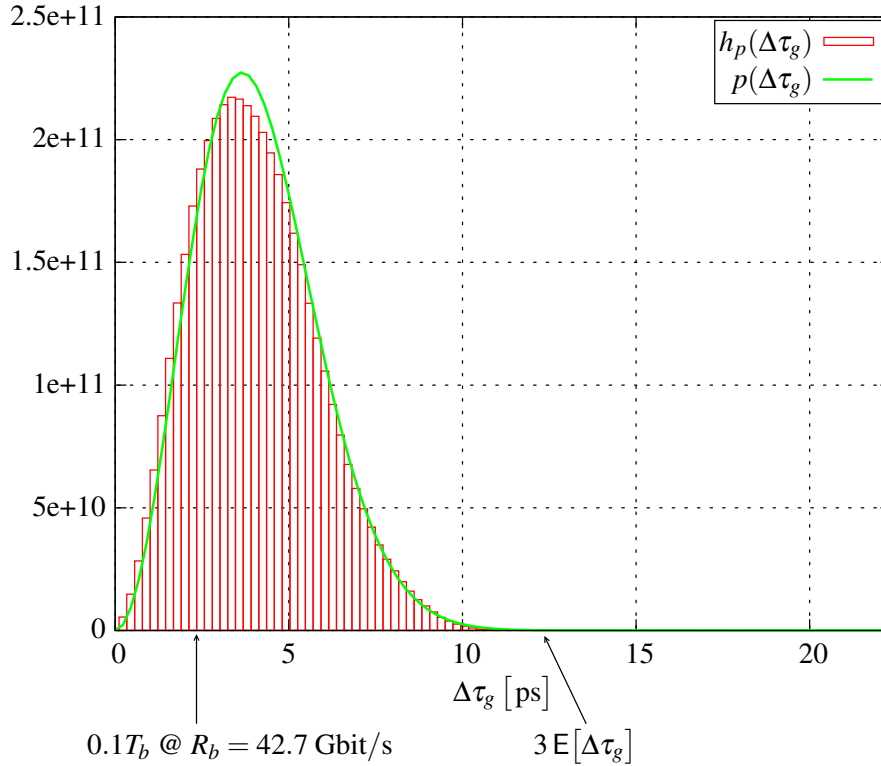**Figure 3.13:** Normalized DGD histogram of the time-variant higher order PMD model
($\tau_{PMD} = 2$ ps/$\sqrt{\text{km}}$ at $z = 5$ km, $\Delta\tau_g$ collected for 100000 fiber realizations)

3.2.3 Optical RX Front End

Fig. 3.14 shows the optical RX front end with appropriate labeling in equivalent baseband notation. Since we employ the same optical BPF as for the optical TX, we do not repeat its characteristics and refer to Ch. 3.2.1.5.
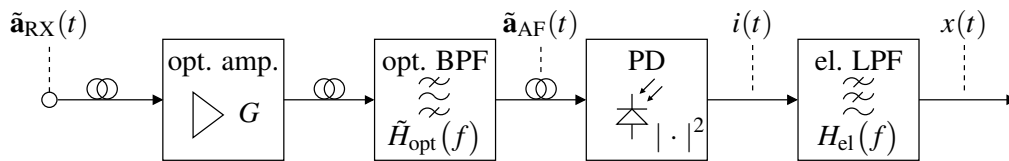

Figure 3.14: Optical receiver front end

3.2.3.1 EDFA and OSNR Definition

Fig. 3.15(a) shows the simple model of the EDFA. First, we reamplify the optical RX signal $\tilde{\mathbf{a}}_{RX}(t)$, and then, we add an ASE noise process $\tilde{\mathbf{n}}(t)$.

(a) ASE noise addition   (b) OSNR definition
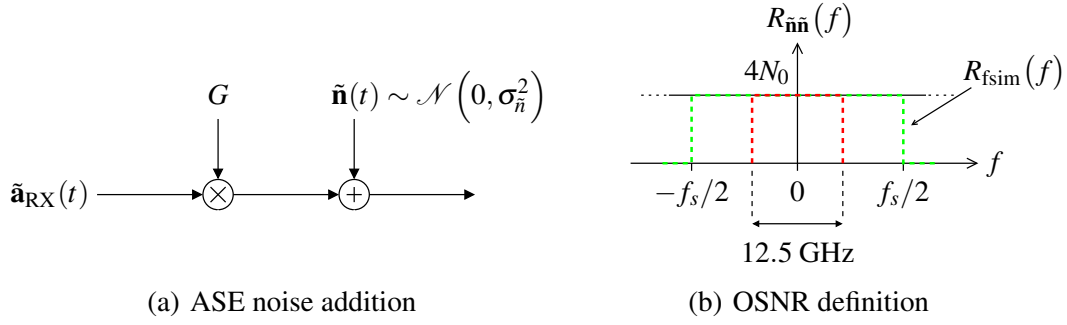
Figure 3.15: Optical amplifier with ASE noise

The equivalent baseband output of the SSMF is given by

$$\tilde{\mathbf{a}}_{\mathrm{RX}}(t) \circ\!\!-\!\!\bullet\, \tilde{\mathbf{A}}_{\mathrm{RX}}(f) = \tilde{\mathbf{A}}\left(L_f, f\right) = \tilde{\mathbf{H}}_{\mathrm{f}}\left(L_f, f\right) \tilde{\mathbf{A}}_{\mathrm{TX}}(f) = \tilde{\mathbf{H}}_{\mathrm{f}}(f)\, \tilde{\mathbf{A}}_{\mathrm{TX}}(f). \qquad (3.104)$$

The transfer matrix $\tilde{\mathbf{H}}_{\mathrm{f}}(f)$ from TX to RX shall represent those introduced in the last section and model various dispersion effects. Amplification by the factor G shall equalize the attenuation related to $\mathrm{e}^{-\alpha L_f}$. This is common to all SSMF models introduced in Ch. 3.2.2.

Recalling Eq. (3.31), which has derived the equivalent baseband description in general, we use it now to normalize the output of our simulation model after direct detection with

$$G\mathrm{e}^{-\alpha L_f} := 1 \quad \Longleftrightarrow \quad G = \mathrm{e}^{\alpha L_f}. \qquad (3.105)$$

The factor $1/2$, which would actually occur here on the very left side as direct input from Eq. (3.31), misses since it has already been eliminated through the special choice for the mean optical LD power in Eq. (3.41). Thus, the mean optical power at the point of noise addition is

$$
\begin{aligned}
P_{opt} &= \mathsf{E}\left[\left|G\tilde{\mathbf{a}}_{\mathrm{RX}}(t)\right|^2\right] \\
&= G^2\, \mathsf{E}\left[\left|\tilde{\mathbf{a}}_{\mathrm{RX}}(t)\right|^2\right] \\
&= \mathrm{e}^{2\alpha L_f}\, \mathsf{E}\left[\left|\tilde{\mathbf{a}}_{\mathrm{RX}}(t)\right|^2\right].
\end{aligned}
\qquad (3.106)
$$

Since $\tilde{\mathbf{a}}_{\mathrm{RX}}(t)$ is a two-dimensional signal with complex components in equivalent baseband description, we model the ASE noise source as four-dimensional real-valued additive white Gaussian noise (AWGN) process, whose components are mutually independent and identically distributed (i.i.d.) with spectral power density N_0 per dimension. As derived in Ch. 3.1, the signal bandwidth of our simulation model is restricted to the rectangular frequency domain baseband simulation window $R_{\mathrm{fsim}}(f)$. Thus, the effective contributing noise power is

$$P_{\mathbf{\tilde{n}}} = 4N_0 f_s = 4\sigma_{\tilde{n}}^2 \tag{3.107}$$

with variance $\sigma_{\tilde{n}}^2$ for all four dimensions. Fig. 3.15(b) depicts the noise power density, however with the total noise power being mapped to a single, equivalent one-dimensinal noise source. The equivalence is given since the contributing noise sources are i.i.d..

Disregarding the actual signal bandwidth, the definition of OSNR distinguishes itself to convenient SNR definitions[10] by just using the portion of the noise power within the reference bandwidth 12.5 GHz as indicated in Fig. 3.15(b). Using Eq. (3.107) and Eq. (3.3) (cf. page 12), we can express the OSNR in decibel with

$$\gamma_{OSNR} = 10 \lg \left(\frac{P_{opt}}{4N_0 \cdot 12.5 \text{ GHz}} \right) = 10 \lg \left(\frac{P_{opt}}{4\sigma_{\tilde{n}}^2 \frac{12.5 \text{ GHz}}{f_s}} \right)$$

$$= 10 \lg \left(\frac{P_{opt}}{4\sigma_{\tilde{n}}^2 \frac{12.5 \text{ GHz} \cdot T_b}{L}} \right). \tag{3.108}$$

After having set the numeric value for γ_{OSNR}, this formula is solved for $\sigma_{\tilde{n}}^2$ to set up the Gaussian random number generators to model a $\mathcal{N}(0, \sigma_{\tilde{n}}^2)$-distributed signal.

Given two different bit rates $R_{b,1} = 1/T_{b,1}$ and $R_{b,2} = 1/T_{b,2}$ and the same oversampling factor L used for simulation, the relation

$$\Delta\gamma_{OSNR} = \gamma_{OSNR,2} - \gamma_{OSNR,1} = 10 \lg \left(\frac{T_{b,1}}{T_{b,2}} \right) = 10 \lg \left(\frac{R_{b,2}}{R_{b,1}} \right) \tag{3.109}$$

allows to map the BER vs. OSNR results of one to the other by the OSNR offset $\Delta\gamma_{OSNR}$.

Using Eqs. (3.53) and (3.104), we can finally summarize the reamplified and filtered optical RX signal together with ASE noise in equivalent baseband notation by

---

[10] The OSNR is related to the convenient SNR definition, in which signal and noise bandwidths are equal, by

$$\gamma_{SNR} = 10 \lg \left(\frac{P_{opt}}{P_{\mathbf{\tilde{n}}}} \right) = 10 \lg \left(\frac{P_{opt}}{4N_0 f_s} \right) = 10 \lg \left(\frac{P_{opt}}{4N_0 \cdot 12.5 \text{ GHz}} \cdot \frac{12.5 \text{ GHz}}{f_s} \right)$$

$$= \underbrace{10 \lg \left(\frac{P_{opt}}{4N_0 \cdot 12.5 \text{ GHz}} \right)}_{\gamma_{OSNR}} + 10 \lg \left(\frac{12.5 \text{ GHz}}{f_s} \right)$$

$$= \gamma_{OSNR} + 10 \lg \left(\frac{12.5 \text{ GHz}}{f_s} \right).$$

$$\tilde{\mathbf{a}}_{\mathrm{AF}}(t) = \left(G\,\tilde{\mathbf{a}}_{\mathrm{RX}}(t) + \tilde{\mathbf{n}}(t)\right) * \tilde{h}_{\mathrm{opt}}(t) \tag{3.110}$$

$$= \left(\mathscr{F}^{-1}\left\{G\tilde{\mathbf{H}}_{\mathrm{f}}(f)\,\tilde{\mathbf{A}}_{\mathrm{TX}}(f)\right\} + \tilde{\mathbf{n}}(t)\right) * \tilde{h}_{\mathrm{opt}}(t) \tag{3.111}$$

$$= \left(\mathscr{F}^{-1}\left\{G\tilde{\mathbf{H}}_{\mathrm{f}}(f)\,\tilde{\mathbf{A}}_{e}(f)\,H_{\mathrm{opt}}(f)\right\} + \tilde{\mathbf{n}}(t)\right) * \tilde{h}_{\mathrm{opt}}(t) \tag{3.112}$$

3.2.3.2 Photodetection and Electrical Low-Pass Filter

The PD converts the reamplified and filtered optical RX signal into the photocurrent by simple SLD with

$$i(t) = I_{E0}\left|\tilde{\mathbf{a}}_{\mathrm{AF}}(t)\right|^{2} = I_{E0}\left|\left(G\,\tilde{\mathbf{a}}_{\mathrm{RX}}(t) + \tilde{\mathbf{n}}(t)\right) * \tilde{h}_{\mathrm{opt}}(t)\right|^{2}. \tag{3.113}$$

Direct detection is completed by final lowpass filtering with the electrical Bessel LPF

$$H_{\mathrm{el}}(f) = \frac{B_{N_B}(0)}{B_{N_B}\left(\frac{\mathrm{j}\kappa f}{f_{3\,\mathrm{dB,el}}}\right)}. \tag{3.114}$$

The Bessel polynomials $B_{N_B}(p)$ with argument $p = \mathrm{j}\kappa f / f_{3\,\mathrm{dB,el}}$ are recursively defined by

$$B_{N_B}(p) = (2n-1)\,B_{N_B-1}(p) + p^2 B_{N_B-2}(p),$$
$$B_1(p) = 1 + p \quad \text{and} \quad B_0(p) = 1. \tag{3.115}$$

We use a filter order of $N_B = 3$ and a 3 dB cutoff frequency of $f_{3\,\mathrm{dB,el}} = 0.5 R_{b,\mathrm{Hz}}$. The argument scaling factor $\kappa \in \mathbb{R}$ is necessary to adjust the transfer function at $f_{3\,\mathrm{dB,el}}$ to $|\mathrm{H}_{\mathrm{el}}(f_{3\,\mathrm{dB,el}})| = 1/\sqrt{2}$ as depicted in Fig. 3.16(a). The constant group delay within the passband range is a special feature of a Bessel LPF as indicated by the almost linear phase for $|f| \le f_{3\,\mathrm{dB,el}}$ in Fig. 3.16(b). Thus, no additional phase dispersion is introduced into the signal.
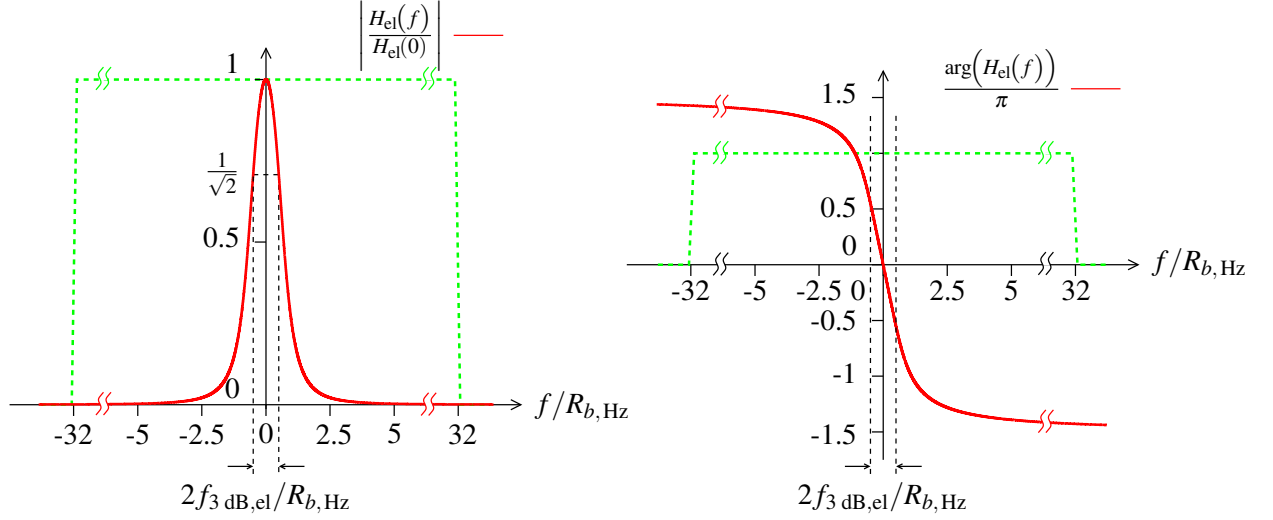
After electrical filtering the electrical RX signal of the OA-IM/DD link is given by

$$x(t) = i(t) * h_{\mathrm{el}}(t), \tag{3.116}$$

which can be explicitly expressed with Eqs. (3.110) – (3.113) by

$$x(t) = I_{E0}\left|\left(G\,\tilde{\mathbf{a}}_{\mathrm{RX}}(t) + \tilde{\mathbf{n}}(t)\right) * \tilde{h}_{\mathrm{opt}}(t)\right|^{2} * h_{\mathrm{el}}(t) \tag{3.117}$$

$$= I_{E0}\left|\left(\mathscr{F}^{-1}\left\{G\tilde{\mathbf{H}}_{\mathrm{f}}(f)\,\tilde{\mathbf{A}}_{\mathrm{TX}}(f)\right\} + \tilde{\mathbf{n}}(t)\right) * \tilde{h}_{\mathrm{opt}}(t)\right|^{2} * h_{\mathrm{el}}(t) \tag{3.118}$$

(a) Magnitude of the electrical Bessel LPF ($f_{3\,\mathrm{dB,el}} = 0.5R_{b,\mathrm{Hz}}$, $N_B = 3$ with $L = 32$ (dashed))

(b) Phase of the electrical Bessel LPF ($f_{3\,\mathrm{dB,el}} = 0.5R_{b,\mathrm{Hz}}$, $N_B = 3$ with $L = 32$ (dashed))

Figure 3.16: Electrical RX filtering

$$= I_{E0} \left| \left(\mathscr{F}^{-1}\left\{ G\,\tilde{\mathbf{H}}_{\mathrm{f}}(f)\,\tilde{\mathbf{A}}_e(f)\,\tilde{H}_{\mathrm{opt}}(f) \right\} + \tilde{\mathbf{n}}(t) \right) * \tilde{h}_{\mathrm{opt}}(t) \right|^2 * h_{\mathrm{el}}(t). \qquad (3.119)$$

3.2.4 Sampling

Sampling of the electrical RX signal in order to feed the discrete-time operated EDC unit in the conventional T_b-spaced sample interval with $\Delta T_1 = T_b$ is straightforward with

$$x_{\Delta T_1}(t) = \sum_{k_1=0}^{K-1} x(t)\,\delta(t - k_1\Delta T_1 - \tau_1)$$

$$= \sum_{k_1=0}^{K-1} \underbrace{x(k_1\Delta T_1 + \tau_1)}_{=:x_{k_1}}\,\delta(t - k_1\Delta T_1 - \tau_1), \quad \tau_1 \in [0, \Delta T_1), \qquad (3.120)$$

and the samples constitute the discrete-time series

$$\mathbf{x}_K = \left(x_{k_1} \right)_{k_1=(0,\ldots,K-1)}. \qquad (3.121)$$

The additional parameter τ_1 in Eq. (3.120) denotes the temporal sampling phase within the sample interval ΔT_1 and can be used to adjust the optimal sampling instant. While real-world signals are tied to causality in physically implemented systems, computer simulations allow for removal of the accumulated group delay along the signal processing chain. Therefore, we directly refer the sample index k_1 to the time slot $t \in [kT_b, (k+1)T_b)$ and relate it to the

corresponding bit b_k at the TX, i.e.

$$k_1 \equiv k. \tag{3.122}$$

We will see in Ch. 4 that all EDC methods can improve their compensation performance by so-called fractionally spaced processing. Fractionally spaced processing comprises sampling and internal processing at a higher rate than the symbol or bit rate while the decision to get the estimate $\hat{b}_k$ at the output of the EDC unit samples down to bit rate speed. The sampling device depicted in Fig. 3.17 is modeled with the adjustable parameters of fractionally spaced sample interval ΔT_i and fractionally spaced sampling phase τ_i with subscript $\cdot_i$, whose meaning for fractionally spaced sample processing will become clear in the following.
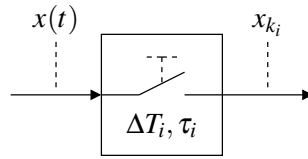
Figure 3.17: Adjustable sampling device

If we use these parameters to describe fractionally spaced sampling of the electrical RX signal, we end up with

$$\begin{aligned}
x_{\Delta T_i}(t) &= \sum_{k_i=0}^{iK-1} x(t) \, \delta\left(t - k_i \Delta T_i - \tau_i\right) \\
&= \sum_{k_i=0}^{iK-1} \underbrace{x(k_i \Delta T_i + \tau_i)}_{=:x_{k_i}} \, \delta\left(t - k_i \Delta T_i - \tau_i\right),
\end{aligned}$$

$$i \in \mathbb{N}_1, \, k_i = (0,\dots,iK-1), \, \Delta T_i = \frac{T_b}{i}, \, \tau_i \in [0, \Delta T_i). \tag{3.123}$$

The corresponding fractionally spaced discrete-time series is

$$\mathbf{x}_{iK} = \left(x_{k_i}\right)_{k_i=(0,\dots,iK-1)}. \tag{3.124}$$

As can be seen from the mathematical description in Eq. (3.123), the small subscript $\cdot_i$ accounts for the number of samples taken within the bit interval T_b, i.e. the fractionally spaced sample interval is $\Delta T_i = T_b/i$, $i \in \mathbb{N}_1$ [11]. With the mathematical formulation of Eq. (3.123), convenient T_b-spaced sampling turns out to be a special case of fractionally spaced sampling for $i = 1$.

---

[11]In theory or if the electrical RX signal should be processed by analog tapped delay line filters, we could also allow $i \in \mathbb{Q}$, $i \geq 1$, e.g. $i = 4/3$. However, this would be somehow difficult to realize in clocked discrete-time signal processing hardware as it requires further interpolation and clock domain crossing steps.

Similar to the approach of removing accumulated group delay within the simulation environment for convenient T_b-spaced sampling in Eq. (3.122), we assign the fractional sample index k_i to the corresponding TX bit b_k in the time slot $t \in \left[kT_b, (k+1) T_b \right)$ by

$$k = k_i \text{ div } i. \tag{3.125}$$

Concerning the fractionally spaced sampling phase ΔT_i, its adjustable granularity is restricted for simulations since the originally analog signals are already approximated by their discrete-time series with an oversampling factor of L. Hence, the possible numeric values for the fractionally spaced sample interval ΔT_i must align with the discrete-time signal resolution with

$$i \overset{(3.123)}{=} \frac{T_b}{\Delta T_i} = \frac{L \Delta T_s}{\Delta T_i} \overset{!}{\in} \mathbb{N}_1 \quad \Longleftrightarrow \quad \frac{L}{i} = \frac{\Delta T_i}{\Delta T_s} \overset{!}{\in} \mathbb{N}_1 \quad \Longleftrightarrow \quad L \bmod i = 0, \tag{3.126}$$

and, within one fractionally spaced sample interval, the sampling phase may take on the values

$$\tau_i \overset{(3.123)}{\in} [0, \Delta T_i) \quad \Longleftrightarrow \quad \tau_i = \left(0, \ldots, (i-1) \Delta T_i \right). \tag{3.127}$$

Fig. 3.18 shows exemplarily two different sample intervals with T_b-spaced (ΔT_1-spaced) and ΔT_2-fractionally spaced sample intervals and $L = 32$, that have been generated by the simulation toolbox. Each has a sampling phase located in the middle of the corresponding sample interval with

$$\tau_i = \frac{\Delta T_i}{2} = \frac{T_b}{2i} = \frac{L}{2i} \Delta T_s. \tag{3.128}$$

This shall be the usual adjustment in this thesis if not stated otherwise.

3.3 Signal Impairments in OA-IM/DD Links

3.3.1 Linear and Nonlinear ISI

Eyes diagrams are useful to study the deterministic ISI caused by a dispersive communication channel. If we neglect random noise, we can clearly identify the effect of the optical fiber channel on the electrical RX signal as illustrated by Figs. 3.19(b) – 3.19(d) for various types of impairments. Compared to the eye openings of the TX signal of Fig. 3.19(a), we observe a degradation for CD at $L_f = 5$ km and first-order PMD with $\Delta \tau_g = 12.5$ ps in Figs. 3.19(b) and 3.19(c), respectively. This means that the susceptibility for noise and sampling phase adjustment has pretty much increased. Furthermore, both eyes tend to become asymmetric with respect to the time origin due to optical and electrical RX filtering, and sampling phase optimization becomes necessary to identify the point of the maximal vertical eye opening.

CD causes nonlinear ISI if we consider an OA-IM/DD link end to end, i.e. from electrical TX to electrical RX signal. This end-to-end nonlinearity is caused by direct detection and
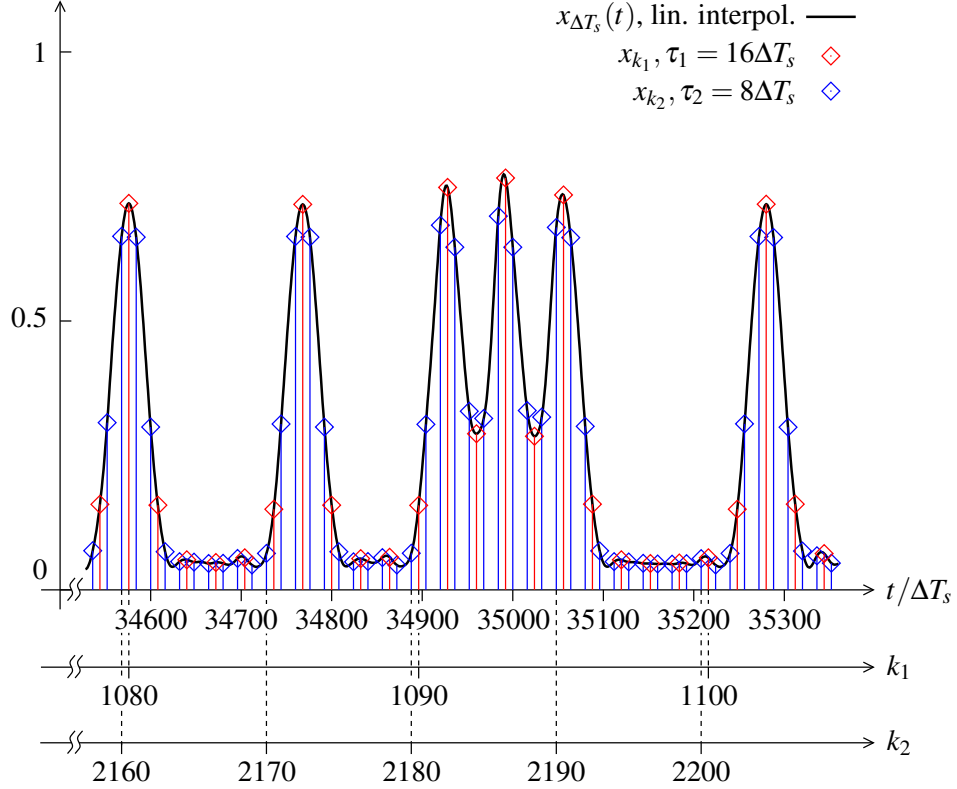
Figure 3.18: Illustration of two possible sample intervals with ΔT_1- and ΔT_2-spaced sample interval based on a bit sequence length of $K = 2048$ and oversampling by $L = 32$

is intrinsic to OA-IM/DD links therefore. Further simulations of the modeled OA-IM/DD link at $R_b = 42.7$ Gbit/s have proven that overshoot and jitter in the eye crossings steadily increase up to $L_f \approx 7 - 8$ km. At this point, the eye becomes completely closed.

First-order PMD does not show any overshoot or jitter effects in the eye crossings. The reason is that first-order PMD remains a linear distortion with respect to direct detection as already addressed in Ch. 3.2.2.2.1 where we have introduced the first-order PMD model. If we transfer the findings of Eqs. (3.84) to electrical RX signal of Eq. (3.118), we can write

$$
\begin{aligned}
x(t) &= I_{E0} \left| \left(\mathscr{F}^{-1} \left\{ \begin{bmatrix} e^{-j2\pi \frac{\Delta \tau_g}{2} f} & 0 \\ 0 & e^{j2\pi \frac{\Delta \tau_g}{2} f} \end{bmatrix} \tilde{\mathbf{A}}_{\text{TX}}(f) \right\} \right) * \tilde{h}_{\text{opt}}(t) \right|^2 * h_{\text{el}}(t) \\
&\overset{B_{3\,\text{dB,opt}}\uparrow}{\approx} I_{E0} \left| \mathscr{F}^{-1} \left\{ \begin{pmatrix} \tilde{A}_{\text{TX},x}(f)\, e^{-j2\pi \frac{\Delta \tau_g}{2} f} \\ \tilde{A}_{\text{TX},y}(f)\, e^{j2\pi \frac{\Delta \tau_g}{2} f} \end{pmatrix} \right\} \right|^2 * h_{\text{el}}(t) \\
&= I_{E0} \left(\left| \tilde{a}_{\text{TX},x}\left(t - \frac{\Delta \tau_g}{2}\right) \right|^2 + \left| \tilde{a}_{\text{TX},y}\left(t + \frac{\Delta \tau_g}{2}\right) \right|^2 \right) * h_{\text{el}}(t).
\end{aligned} \tag{3.129}
$$

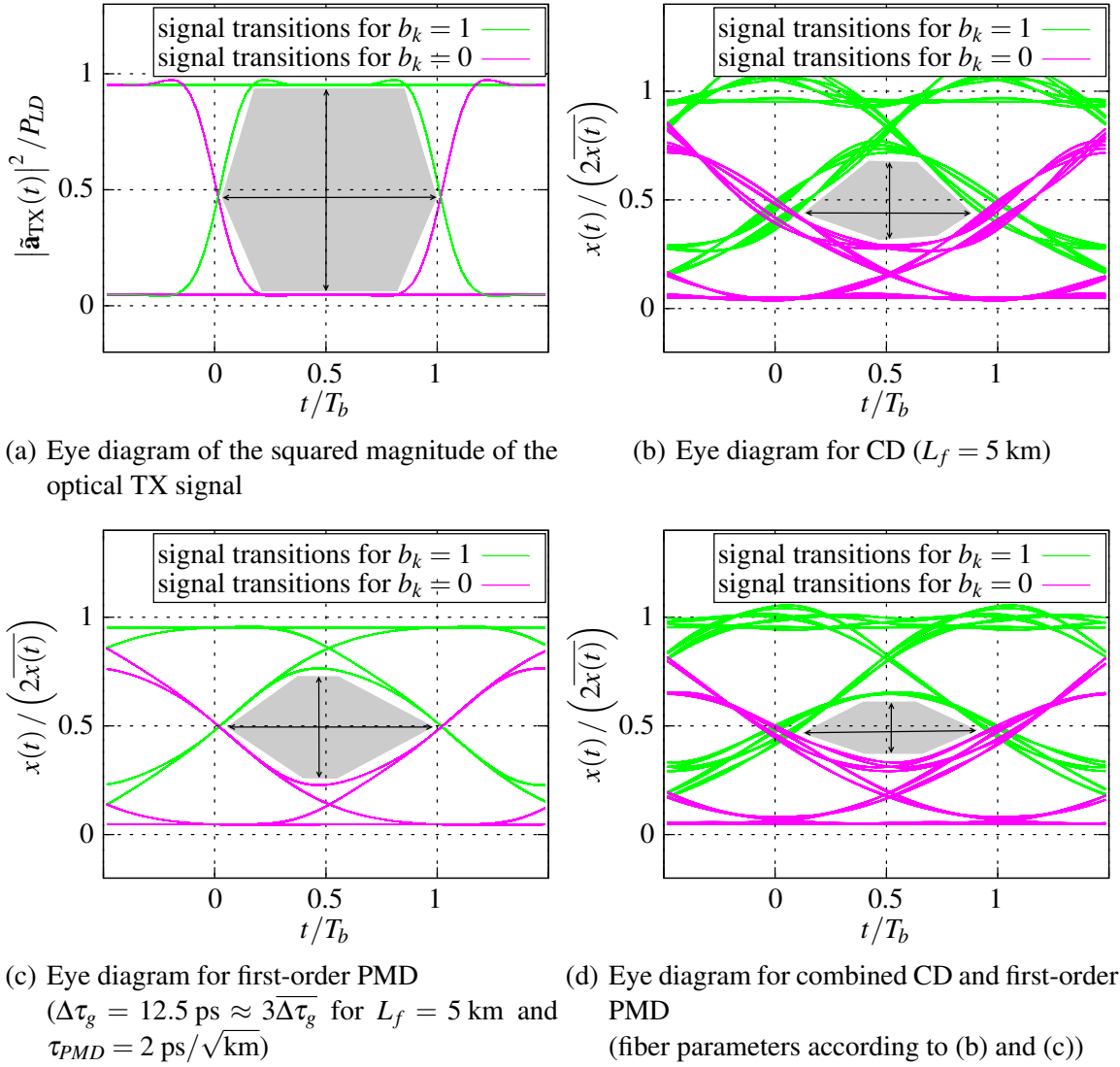(a) Eye diagram of the squared magnitude of the optical TX signal

(b) Eye diagram for CD ($L_f = 5$ km)

(c) Eye diagram for first-order PMD
($\Delta \tau_g = 12.5$ ps $\approx 3 \overline{\Delta \tau_g}$ for $L_f = 5$ km and $\tau_{PMD} = 2$ ps/$\sqrt{\text{km}}$)

(d) Eye diagram for combined CD and first-order PMD
(fiber parameters according to (b) and (c))

Figure 3.19: Eye diagrams for various impairments at $R_b = 42.7$ Gbit/s

Eq. (3.129) states that the general reason for PMD induced ISI is that increasing $\Delta \tau_g$ shifts the two signal components along the two PSP more and more apart. If $\Delta \tau_g = T_b$, the leading optical signal part carrying the information for bit b_k exactly overlaps with the trailing part of the previously transmitted bit b_{k-1}. The same holds in the other direction for the trailing optical signal part carrying the information for bit b_k and the leading part of the next bit b_{k+1}, and so forth. Hence, we observe an electrical RX signal which is composed by addition of two different signal parts originating from different bits at the TX. It is obvious that the uncertainty about the actually transmitted bit becomes maximal in this case. For example, if we assume that the current bit is $b_k = 1$ and the following one is $b_{k+1} = 0$, then the sample value for b_{k+1} within the time interval $[(k+1)T_b, (k+2)T_b)$ is approximately the mean signal value of both, which is often nearby the optimal decision threshold. Although $b_{k+1} = 0$ was transmitted, a small additive noise distortion might toggle the slicer to indicate $b_{k+1} = 1$. In other words, the corresponding eye diagram is closed if $\Delta \tau_g = T_b$, which is

mathematically justified by Eq. (3.89), which indicates a zero in the effective first-order PMD transfer function at $f = 1/(2T_b)$.

In a real optical fiber link, we have to consider the effect of CD and first-order PMD together because they occur simultaneously. The combined distortions lead to the eye of Fig. 3.19(d), which shows that vertical and horizontal eye openings have further decreased.

3.3.2 Signal-Dependent Noise

Optimal symbol-by-symbol (sbs) maximum likelihood (ML) detection [42] requires to evaluate the sampled electrical RX signal x_{k_0} at the output of our simulation model with respect to the decision threshold X_{th} by the rule

$$\hat{b}_k = \begin{cases} 1 & : & x_{k_1} \geq X_{th} \\ 0 & : & x_{k_1} < X_{th} \end{cases}. \tag{3.130}$$

In theory, we have to determine the optimal decision threshold minimizing the probability of bit errors by extreme value analysis of

$$
\begin{aligned}
P_e &= P\left[x_{k_1} \geq X_{th} \wedge b_k = 0\right] + P\left[x_{k_1} < X_{th} \wedge b_k = 1\right] \\
&= P[b_k = 0] \underbrace{\int_{X_{th}}^{\infty} p\left(x_{k_1} \mid b_k = 0\right)}_{1 - C\left(X_{th} \mid b_k = 0\right)} + P[b_k = 0] \underbrace{\int_{-\infty}^{X_{th}} p\left(x_{k_1} \mid b_k = 1\right)}_{C\left(X_{th} \mid b_k = 1\right) - 0} \\
&= P[b_k = 0] \left(1 - C\left(X_{th} \mid b_k = 0\right)\right) + P[b_k = 1] C\left(X_{th} \mid b_k = 1\right).
\end{aligned} \tag{3.131}
$$

$C\left(x_{k_1} \mid b_k = 0\right)$ and $C\left(x_{k_1} \mid b_k = 1\right)$ denote the conditional cumulative distribution functions (CDFs) corresponding to the PDFs $p\left(x_{k_1} \mid b_k = 0\right)$ and $p\left(x_{k_1} \mid b_k = 1\right)$. Performing this extreme value analysis with respect to X_{th} and using the fundamental theorem of calculus yields

$$
\begin{aligned}
\frac{\partial P_e}{\partial X_{th}} &= -P[b_k = 0] p\left(X_{th} \mid b_k = 0\right) + P[b_k = 1] p\left(X_{th} \mid b_k = 1\right) \overset{!}{=} 0 \\
&\Longleftrightarrow \quad P[b_k = 0] p\left(X_{th} \mid b_k = 0\right) = P[b_k = 1] p\left(X_{th} \mid b_k = 1\right) \\
&\overset{P[b_k = 0] = P[b_k = 1]}{\Longleftrightarrow} \quad p\left(X_{th} \mid b_k = 0\right) = p\left(X_{th} \mid b_k = 1\right).
\end{aligned} \tag{3.132}
$$

Consequently, the optimal decision threshold is given by the intersection point of the two conditional PDFs assuming equal a priori probabilities as already claimed in Eq. (3.36) with $P[b_k = 0] = P[b_k = 1] = 0.5$. Presuming an ideal transmission channel with symmetric additive noise statistics, as for example in a simple AWGN channel, we may easily set the decision threshold for binary modulation to the mean value of the two electrical RX signal

levels corresponding to $b_k = 0$ and $b_k = 1$, respectively. Unfortunately, the optical channel impairments of CD and PMD together with direct detection and the optical and electrical RX filters do not allow such a simple setup. If we reformulate Eq. (3.117)

$$
\begin{aligned}
x(t) &= I_{E0} \left| \left(G\tilde{\mathbf{a}}_{\mathrm{RX}}(t) + \tilde{\mathbf{n}}(t) \right) * \tilde{h}_{\mathrm{opt}}(t) \right|^2 * h_{\mathrm{el}}(t) \\
&= I_{E0} \left| G\tilde{\mathbf{a}}_{\mathrm{RX}}(t) * \tilde{h}_{\mathrm{opt}}(t) \right|^2 * h_{\mathrm{el}}(t) \\
&\quad + 2 I_{E0} \operatorname{Re}\left\{ \left(G\tilde{\mathbf{a}}_{\mathrm{RX}}(t) * \tilde{h}_{\mathrm{opt}}(t) \right) \left(\tilde{\mathbf{n}}(t) * \tilde{h}_{\mathrm{opt}}(t) \right)^* \right\} * h_{\mathrm{el}}(t) \\
&\quad + I_{E0} \left| \tilde{\mathbf{n}}(t) * \tilde{h}_{\mathrm{opt}}(t) \right|^2 * h_{\mathrm{el}}(t),
\end{aligned}
\tag{3.133}
$$

we can identify three parts:

- The first term contains the optical RX signal affected by CD and PMD.

- The second is a beat term, which mixes signal and noise. It represents a signal-dependent, additive Gaussian noise process.

- The third is a pure noise term with almost χ^2-characteristic [42].

Since signal and noise pass the optical filter before and the electrical filter after direct detection, the resulting noise process becomes colored to some extent. This makes theoretical analysis complicated or even impossible. Some Gaussian [62, 63, 64, 65, 66] and non-central χ^2-approximations [34] have been reported, and some semi-analytical calculations using moment-generating functions (MGFs) [5, 18, 67, 35] exist, too. However, the approximations made are either based on quite simplified assumptions, or they do not provide significant savings in simulation time. If we also apply further signal processing to the sampled electrical RX signal for EDC, noise characteristics might change with each of those steps. Therefore, we rely on histogram recording as an ergodic estimation of PDFs in this thesis.

The conditional histograms $h_p\left(x_{k_1} | b_k = 0\right)$ and $h_p\left(x_{k_1} | b_k = 1\right)$ in Fig. 3.20 result from simulation with the same parameter set as those of Fig. 3.19(d) on page 50. The ASE noise level has been set to $\gamma_{OSNR} = 21$ dB. The histograms serve as a measured estimate for the conditional PDFs $p\left(x_{k_1} | b_k = 0\right)$ and $p\left(x_{k_1} | b_k = 1\right)$. For orientation, the corresponding electrical RX signal levels for the back-to-back (b2b) case with $L_f = 0$ km have been drawn, i.e. the TX is directly connected to the RX, and no distortion by CD and PMD is present. The mean value of these two signal levels is also included as a reference line to indicate the optimal decision threshold for AWGN. However, signal-dependent noise becomes evident in the difference of shape of the two conditional histograms showing that the variance of $h_p\left(x_{k_1} | b_k = 1\right)$ is larger than the variance of $h_p\left(x_{k_1} | b_k = 0\right)$. The point of intersection deviates from the mean of the two TX signal levels therefore. Since we target a BER of 1e-03 before FEC [48], optimization of the decision threshold X_{th} with respect to CD, PMD and OSNR can improve

the link margin of OA-IM/DD systems to a non-negligible amount [68, 69, 70]. So if not stated otherwise, any result presented in this thesis implicitly includes the optimization of the decision threshold. We perform this optimization on the basis of Eq. (3.132) by conditional histogram evaluation using the rule

$$X_{th} = \arg \min_{X_{th}} BER(X_{th})$$

$$= \arg \min_{X_{th}} \left(\sum_{n=\lceil \frac{X_{th}}{\Delta x} \rceil}^{N_h-1} h_p\big(n\Delta x | b_k = 0\big) + \sum_{n=0}^{\lfloor \frac{X_{th}}{\Delta x} \rfloor} h_p\big(n\Delta x | b_k = 1\big) \right) \quad (3.134)$$

with Δx denoting the width of one histogram bin and N_h being the number of histogram bins. Of course, the accuracy of X_{th} with this approach depends on the adjustment of Δx and N_h with respect to the range of values of the samples x_{k_1}, which has been determined empirically for each OA-IM/DD link parameter set.
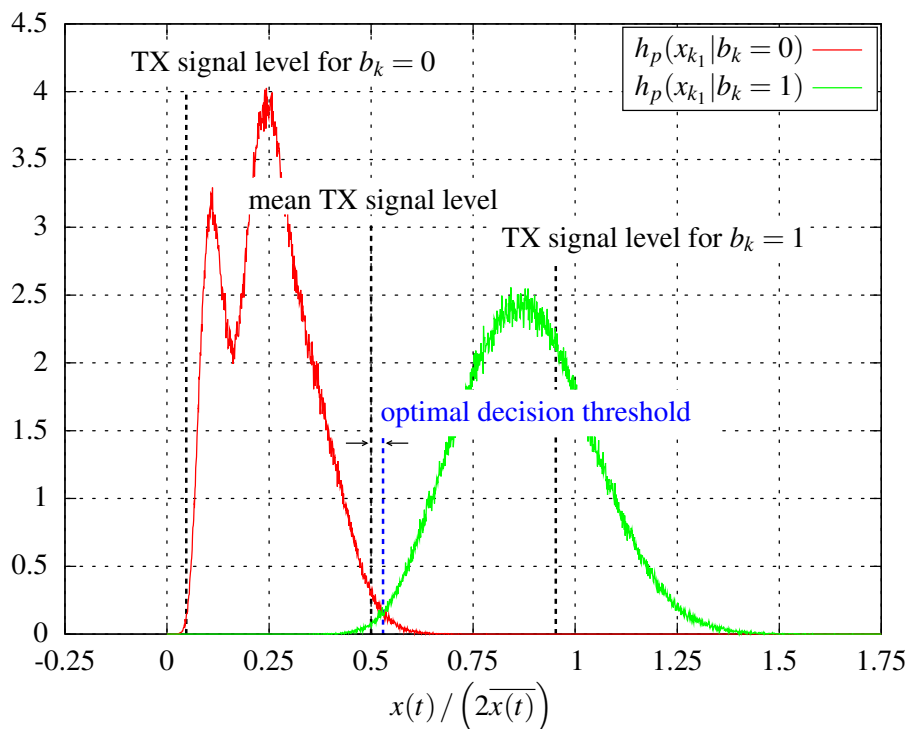
Figure 3.20: Conditional histograms of x_{k_1} (combined CD ($L_f = 5$ km) and first-order PMD ($\Delta\tau_g = 12.36$ ps), $\gamma_{OSNR} = 21$ dB)

Figs. 3.21(a) and 3.21(b) give reasons for decision threshold optimization. We have plotted the BER vs. OSNR with and without decision threshold optimization for a given OA-IM/DD link parameter set. The constant decision threshold corresponds to the middle of the noiseless eye. This would be the optimal decision threshold setup for a system with AWGN. The BER curves with and without optimization coincide with each other in the region where the fixed

decision threshold almost equals the optimal ones. Obviously, this happens for a system with simple threshold RX in the high OSNR region and for a system with EDC by a linear FFE, which is an anticipation of Ch. 4, in the low OSNR region. We also observe an opposing trend for the curves of optimal decision thresholds plotted aside. The different behavior can be explained by the reshaping of the conditional histograms due to the processing of the electrical RX signal samples x_{k_1} by the linear FFE. Fig. 3.21(b) further reveals that decision threshold optimization for a system with EDC by a FFE yields an OSNR gain of almost 1 dB in the interesting BER region from 1e-03 to 1e-04.
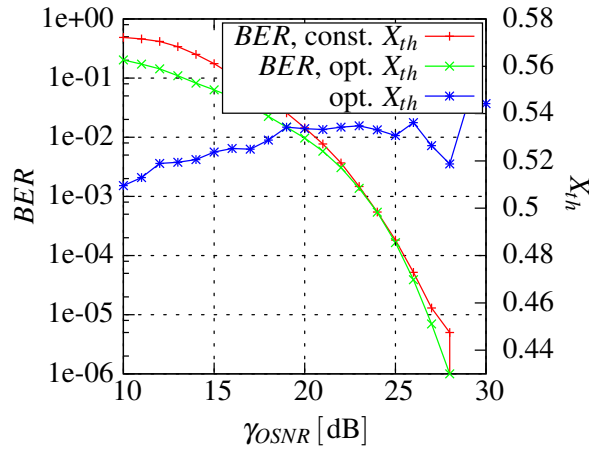
(a) Threshold RX
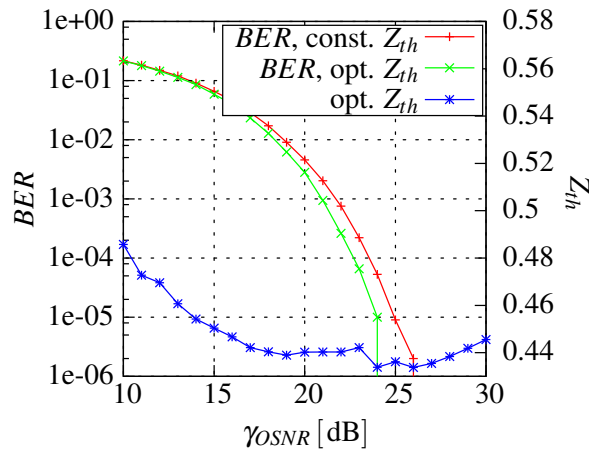
(b) FFE ($M = 5$, cf. Ch. 4)

Figure 3.21: Comparison of BERs with and without decision threshold optimization and optimal thresholds aside (combined CD ($L_f = 5$ km) and first-order PMD ($\Delta\tau_g = 12.36$ ps), $\gamma_{OSNR} = 21$ dB)

Chapter 4

Electronic Dispersion Compensation - Methods and Performance in OA-IM/DD Links

After having described the impacts of CD, PMD, ASE noise and filtering on the final electrical RX signal of OA-IM/DD links, we turn to the discussion of EDC methods and evaluate their dispersion compensation performance if the link characteristics are known in advance. Although the optimal method for EDC would be maximum a posteriori (MAP) equalization featuring concatenated coding and iterative turbo decoding [71, 72, 34, 35], we consider MLSE as the more practical benchmarking technique as already indicated in the introductory chapter. Both, turbo equalization and MLSE, are superior to FFE-DFE methods, but their computational complexity scales exponentially with channel memory. Coping with the very high bit rates of optical fiber communication links by digital signal processing techniques is more or less complicated due to the required processing speeds. This favors simple FFE-DFE having lower implementation cost and power consumption. However, at least for the short-haul range, FFE-DFE has to bear up competition with the more advanced methods to justify its implementation.

4.1   Maximum Likelihood Sequence Estimation

4.1.1   MLSE Viterbi Equalizer

In contrast to sbs ML detection, which reduces to simple threshold comparison as indicated in Ch. 3.3.2, MLSE bases its decision on a sequence of electrical RX signal samples. That is why it is optimal in the sense that it minimizes the occurrence of sequence errors. Sequence error minimization is almost accompanied by a lower BER because MLSE outweighs uncertain or even wrong single bit decisions.

If we denote the joint sequence estimation length by L_{tb} and summarize the electrical RX signal samples in the sequence

$$\mathbf{x}_{L_{tb}} = \left(x_{k_1}\right)_{k_1=0,\ldots,L_{tb}-1},\tag{4.1}$$

we can express the general MLSE decision rule for T_b-spaced sampling by

$$\hat{\mathbf{b}}_{L_{tb}} = \arg\max_{\mathbf{b}_{L_{tb}}} p\left(\mathbf{x}_{L_{tb}}\big|\mathbf{b}_{L_{tb}}\right),$$

$$L_{tb} \in \mathbb{N}_1, \mathbf{b}_{L_{tb}} = \left(b_k \in \{0,1\}\right)_{k=0,\ldots,L_{tb}-1},\tag{4.2}$$

in which the maximization takes all $2^{L_{tb}}$ possible TX sequences $\mathbf{b}_{L_{tb}}$ of length L_{tb} into account. For convenience, we set $L_{tb} = K$, which is the bit sequence length already defined in Eq. (3.35) on page 22. With $L_{tb} = 1$, sbs ML turns out to be the trivial case of MLSE. Since we have to evaluate Eq. (4.2) $2^{L_{tb}}$ times for each binary composition of the TX bit sequence $\mathbf{b}_{L_{tb}}$, the number of required operations scales exponentially with L_{tb}. Fortunately, working on optimal decoding for convolutional codes over noisy digital communication links at the end of the 1960s [73], Viterbi recognized the similarity to the traveling salesman problem, for which efficient solutions already existed. The Viterbi algorithm (VA) [74, 75] reduces the computational complexity of Eq. (4.2) with every processed sample x_{k_1} by consecutive exclusion of those sequences which are less likely. Since any communication channel with memory can be interpreted as an encoding device, the VA has been tailored for equalization purposes later on [74], and this requires to approximate Eq. (4.2) with the following decomposition

$$\hat{\mathbf{b}}_{L_{tb}} = \arg\max_{\mathbf{b}_{L_{tb}}} p\left(\mathbf{x}_{L_{tb}}\big|\mathbf{b}_{L_{tb}}\right)$$

$$\approx \arg\max_{\mathbf{b}_{L_{tb}}} \prod_{k_1=0}^{L_{tb}-1} p\left(x_{k_1}\big|b_0,\ldots,b_{L_{tb}-1}\right)\tag{4.3}$$

$$= \arg\max_{\mathbf{b}_{L_{tb}}} \prod_{k_1=0}^{L_{tb}-1} p\left(x_{k_1}\big|b_{L_{tb}-1},\ldots,b_0\right)$$

$$\approx \arg\max_{\mathbf{b}_{L_{tb}}} \prod_{k\equiv k_1=0}^{L_{tb}-1} p\left(x_{k_1}\bigg|b_{k+\frac{M_c}{2}},\ldots,b_{k-\frac{M_c}{2}}\right), \quad M_c = 2n, n \in \mathbb{N}.\tag{4.4}$$

The change of the order in the bit sequence $\mathbf{b}_{L_{tb}}$ in the intermediate step from Eq. (4.3) to Eq. (4.4) has been done for convenience. The channel memory M_c describes the finite number of influencing TX bits on a single electrical RX signal sample x_{k_1}. We assume that the electrical RX sample x_{k_1} is independent of the TX bits outside the time window $k = -M_c/2,\ldots,M_c/2$. The assumptions leading to Eq. (4.3) and finally to Eq. (4.4) are exactly fulfilled if the signal statistics of the electrical RX signal samples is that of an i.i.d. random variable. This is given for the output of an AWGN channel with $M_c = 0$ as in [73]. But if

$M_c > 0$, i.e. the channel is dispersive and introduces ISI, the electrical RX signal samples are not statistically independent anymore because consecutive samples jointly depend on the same TX bits. Even in the theoretical case of a memory-less channel affected by colored noise, the decomposition of the multivariate PDF in Eq. (4.2) into a product of single ones in Eq. (4.3) is not justified anymore. That is why channel equalization using the VA is a suboptimal MLSE implementation. Note that for $M_c > 0$, the evaluation of the conditional PDF of the first and last few samples, $x_0, \ldots, x_{M_c/2-1}$ and $x_{L_{tb}-M_c/2}, \ldots, x_{L_{tb}-1}$, depends on the TX bits $b_{-M_c/2}, \ldots, b_{-1}$ and $b_{L_{tb}}, \ldots, b_{L_{tb}+M_c/2-1}$ of the previous and following sequence. This might seem somehow inconsistent to the initial MLSE decision rule of Eq. (4.2) but becomes immediately clear if we have a state based view on the system. The overlap with adjacent TX bit sequences can be interpreted as a sliding window approach.

If we look at Eq. (4.4) from a system perspective, a single electrical RX signal sample x_{k_1} is conditioned or, in other words, originates from the independent signal waveforms which have been excited by the TX bits $b_{k+M_c/2}, \ldots, b_{k-M_c/2}$. Those signal waveforms have been dispersed by CD, PMD and by optical as well as electrical filtering when propagating along the fiber. The following electrical RX signal sample x_{k_1+1} depends on the TX bit pattern $b_{k+M_c/2+1}, \ldots, b_{k-M_c/2+1}$, in which $b_{k-M_c/2}$ from the previous pattern has been dropped and $b_{k+M_c/2+1}$ appears as a new input. We can describe this scenario by a delay chain with M_c memory elements. This interpretation leads to the state based system view depicted in Fig. 4.1. It can be considered as a black box, which represents an equivalent system model of the OA-IM/DD link and which directly maps the binary input into the electrical RX signal samples according to the characteristics of the optical fiber link. In general

$$x_{k_1} = f\left(b_{k+M_c/2}, \ldots, b_{k-M_c/2}\right) \tag{4.5}$$

can represent any arbitrary mapping and must not necessarily conform to an analytical mathematical expression, e.g. it might also consist of a look-up table (LUT).
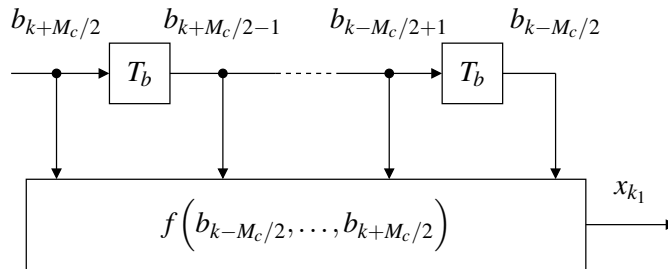

Figure 4.1: State based system model

It is obvious that, depending on the value for $b_{k+M_c/2} \in \{0, 1\}$, the channel state at time instant k may end up in two possible following states at time instant $k+1$. If we exercise this for each binary composition of the state pattern $(b_{k+M_c/2-1}, \ldots, b_{k-M_c/2})$, we can draw a state transition diagram as depicted in Fig. 4.2(a) for $M_c = 2$. From the point of view of the TX, the state transitions occur equally probable since we assume equal a priori probabilities.

However, at the RX side, we can only observe the electrical RX signal samples x_{k_1} and must evaluate them with respect to their likelihood to extract the most probable TX sequence. The conditional PDFs $p(x_{k_1}|b_{k+M_c/2}, \ldots, b_{k-M_c/2})$ are these measures to estimate the state transitions at the RX. They are highlighted for $M_c = 2$ in Fig. 4.2(a).

If we add a temporal dimension to the state transition diagram of Fig. 4.2(a), we end up in the so-called trellis diagram of Fig. 4.2(b). Relating Eq. (4.4) to the trellis description is the key step towards the VA, which is an iterative algorithm acting on the trellis structure.

Given an arbitrary but fixed state $(b_{k+M_c/2}, \ldots, b_{k-M_c/2+1})$ at time instant $k+1$, the most likely path to it through the trellis starting at $k = 0$ in state $(b_{M_c/2-1}, \ldots, b_{-M_c/2})$ is recursively calculated by

$$
\underbrace{p\left(x_{k_1}, \ldots, x_0 \,\middle|\, b_{k+M_c/2}, \ldots, b_{k-M_c/2+1}, \ldots, b_0\right)}_{=:P_{k+1,\left(b_{k+M_c/2}, \ldots, b_{k-M_c/2+1}\right)}} =
$$

$$
\max \left\{ \underbrace{p\left(x_{k_1-1}, \ldots, x_0 \,\middle|\, b_{k+M_c/2-1}, \ldots, b_{k-M_c/2}=0, \ldots, b_0\right)}_{=:P_{k,\left(b_{k+M_c/2-1}, \ldots, b_{k-M_c/2}=0\right)}} \right.
$$

$$
\cdot \underbrace{p\left(x_{k_1} \,\middle|\, b_{k+M_c/2}, \ldots, b_{k-M_c/2}=0\right)}_{=:B_{k_1,\left(b_{k+M_c/2}, \ldots, b_{k-M_c/2}=0\right)}},
$$

$$
\underbrace{p\left(x_{k_1-1}, \ldots, x_0 \,\middle|\, b_{k+M_c/2-1}, \ldots, b_{k-M_c/2}=1, \ldots, b_0\right)}_{=:P_{k,\left(b_{k+M_c/2-1}, \ldots, b_{k-M_c/2}=1\right)}}
$$

$$
\left. \cdot \underbrace{p\left(x_{k_1} \,\middle|\, b_{k+M_c/2}, \ldots, b_{k-M_c/2}=1\right)}_{=:B_{k_1,\left(b_{k+M_c/2}, \ldots, b_{k-M_c/2}=1\right)}} \right\}. \tag{4.6}
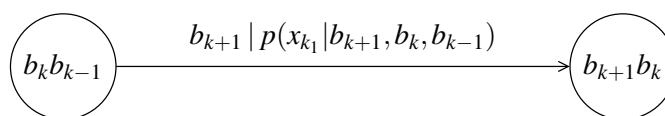$$

from the two preceding states given by the M_c-tuples $(b_{k+M_c/2-1}, \ldots, b_{k-1}, \ldots, b_{k-M_c/2}=0)$ and $(b_{k+M_c/2-1}, \ldots, b_{k-1}, \ldots, b_{k-M_c/2}=1)$, which differ only in the last bit $b_{k-M_c/2}$.

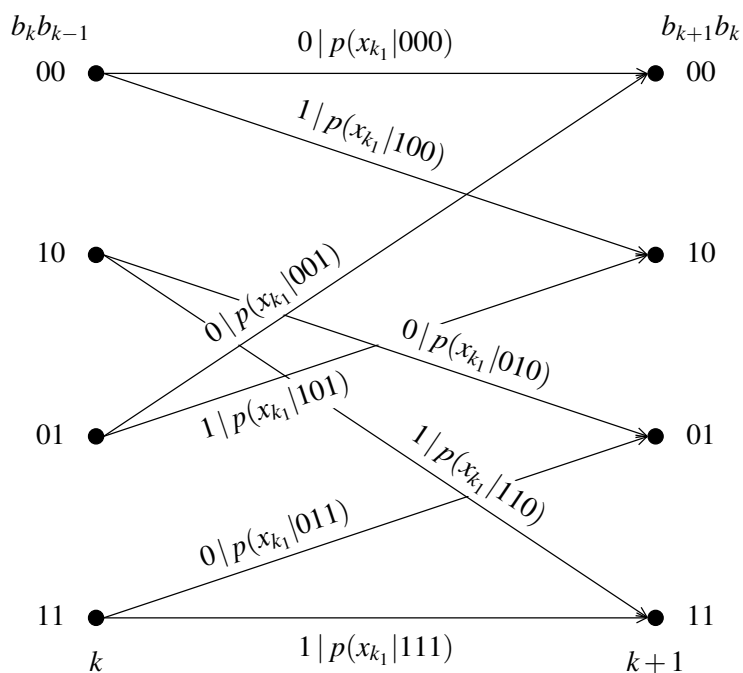Using a shorthand notation for the involved terms in Eq. (4.6), we end up with

$$
P_{k+1,\left(b_{k+M_c/2}, \ldots, b_{k-M_c/2+1}\right)} = \max \left\{ P_{k,\left(b_{k+M_c/2-1}, \ldots, b_{k-M_c/2}=0\right)} \cdot B_{k_1,\left(b_{k+M_c/2}, \ldots, b_{k-M_c/2}=0\right)}, \right.
$$

$$
\left. P_{k,\left(b_{k+M_c/2-1}, \ldots, b_{k-M_c/2}=1\right)} \cdot B_{k_1,\left(b_{k+M_c/2}, \ldots, b_{k-M_c/2}=1\right)} \right\}. \tag{4.7}
$$

(a) State transition diagram
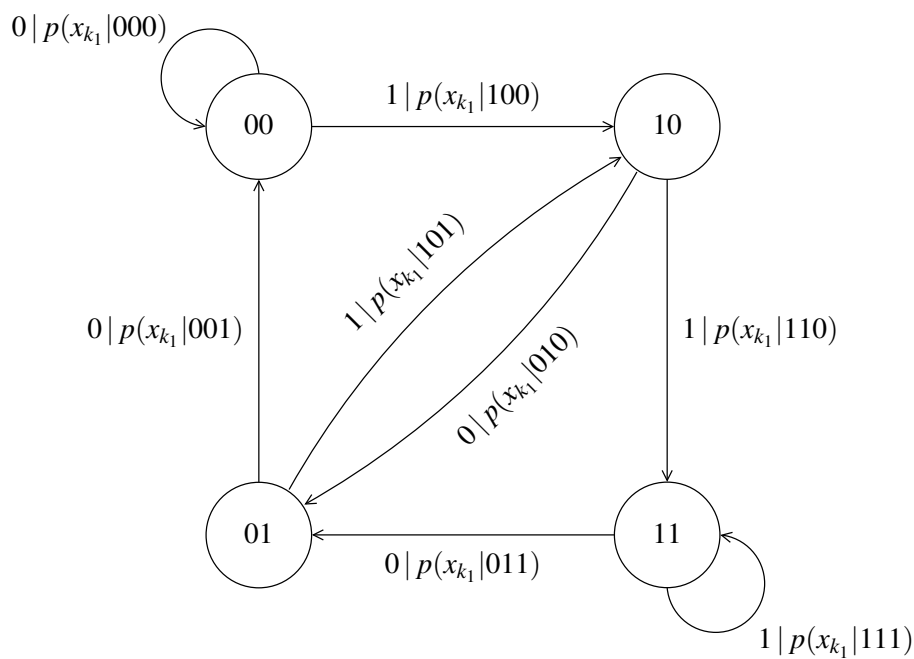
(b) Trellis diagram for one transition

Figure 4.2: State transition and trellis diagram for $M_c = 2$

Having the trellis representation in mind, the terms $P_{k,(\ldots)}$ are generally referred to as path metric and the terms $B_{k_1,(\ldots)}$ as branch metrics. Performing the iterative step of Eq. (4.7) for all 2^{M_c} possible states at each time instant $k = 0, \ldots, L_{tb} - 1$ and finally selecting the most probable state and its path through the trellis at $k = L_{tb}$ is equivalent to the maximization over all possible TX bit sequences $\mathbf{b}_{L_{tb}}$ in the initial MLSE decision rule of Eq. (4.2). Furthermore, from Eq. (4.7) it turns out that any time a single step maximization operation is executed, one transition in the trellis, i.e. one possible TX sequence $\mathbf{b}_{L_{tb}}$, is discarded. The computational complexity of the VA scales with $2^{M_c+1}L_{tb}$, which leads to considerable savings of computational operations if $\mathrm{ld}(L_{tb}) < L_{tb} - M_c - 1$. Finally, a so-called trace back operation is required, in which each trace back step adds one bit estimate $\hat{b}_k$ to the sequence $\hat{\mathbf{b}}_{L_{tb}}$ in reverse direction, i.e. it starts with $\hat{b}_{L_{tb}-1}$ and ends up with $\hat{b}_0$. The joint estimation length L_{tb} is often called trace back length in this context, which explains the chosen subscript for this parameter.

Note that concerning implementation, we may transform Eq.(4.7) into logarithmic domain because the multiplications turn into additions. The logarithmic path metrics are given by

$$
P_{\mathrm{lg},k+1,\left(b_{k+M_c/2},\ldots,b_{k-M_c/2+1}\right)} =
$$

$$
\max \left\{ P_{\mathrm{lg},k,\left(b_{k+M_c/2-1},\ldots,b_{k-M_c/2}=0\right)} + B_{\mathrm{lg},k_1,\left(b_{k+M_c/2},\ldots,b_{k-M_c/2}=0\right)}, \right.
$$

$$
\left. P_{\mathrm{lg},k,\left(b_{k+M_c/2-1},\ldots,b_{k-M_c/2}=1\right)} + B_{\mathrm{lg},k_1,\left(b_{k+M_c/2},\ldots,b_{k-M_c/2}=1\right)} \right\},
$$

$$
(4.8)
$$

and the additional subscript $\cdot_{\mathrm{lg}}$ implicitly indicates to use the logarithm base 10 for the corresponding terms in Eq. (4.7).

In summary, the VA consists of a path metric update unit according to Eq. (4.8), a branch metric and a trace back unit. Since we use VA based MLSE for EDC as a referencing benchmark only in this thesis, the work of [28, 76, 77, 78, 79] is given as a reference for a profound discussion about efficient implementation.

4.1.2 Branch Metric Acquisition

The branch metrics $B_{\mathrm{lg},k_1,(b_{k+M_c/2},\ldots,b_{k-M_c/2}=1)}$ to execute the VA are given by conditional PDFs, which represent the underlying characteristic of the communication channel. For the same reasons as already stated for the optimization of decision thresholds in Ch. 3.3.2, we approximate the branch metrics for the considered OA-IM/DD link by conditional histogram measurements obtained from simulations. Thus, conditional histograms replace the

conditional PDFs in Eq. (4.8) with

$$
\begin{aligned}
P_{\mathrm{lg},k+1,\left(b_{k+M_c/2},\ldots,b_{k-M_c/2+1}\right)} = \\
\max \Bigg\{ & P_{\mathrm{lg},k,\left(b_{k+M_c/2-1},\ldots,b_{k-M_c/2}=0\right)} + \lg\left(h\left(x_{k_1}\Big|b_{k+M_c/2},\ldots,b_k,\ldots,b_{k-M_c/2}=0\right)\right), \\
& P_{\mathrm{lg},k,\left(b_{k+M_c/2-1},\ldots,b_{k-M_c/2}=1\right)} + \lg\left(h\left(x_{k_1}\Big|b_{k+M_c/2},\ldots,b_k,\ldots,b_{k-M_c/2}=1\right)\right) \Bigg\},
\end{aligned}
$$

$$(4.9)$$

which forms the basis of the implemented VA used in this thesis.

Using the state based system model of Fig. 4.1, it is straightforward in a computer simulation environment to collect the electrical RX signal samples x_{k_1} and fill histograms with respect to the TX bit pattern $b_{k+M_c/2},\ldots,b_{k-M_c/2}$ as illustrated by Fig. 4.3. VA implementations either have to be supplied by the branch metrics in advance, or they make use of a so-called *decision-directed mode*, in which the samples x_{k_1} are stored until an estimate for the bit sequence $\hat{\mathbf{b}}_{L_{tb}}$ is available. As soon as this happens, the corresponding branch metrics are updated assuming no bit errors.
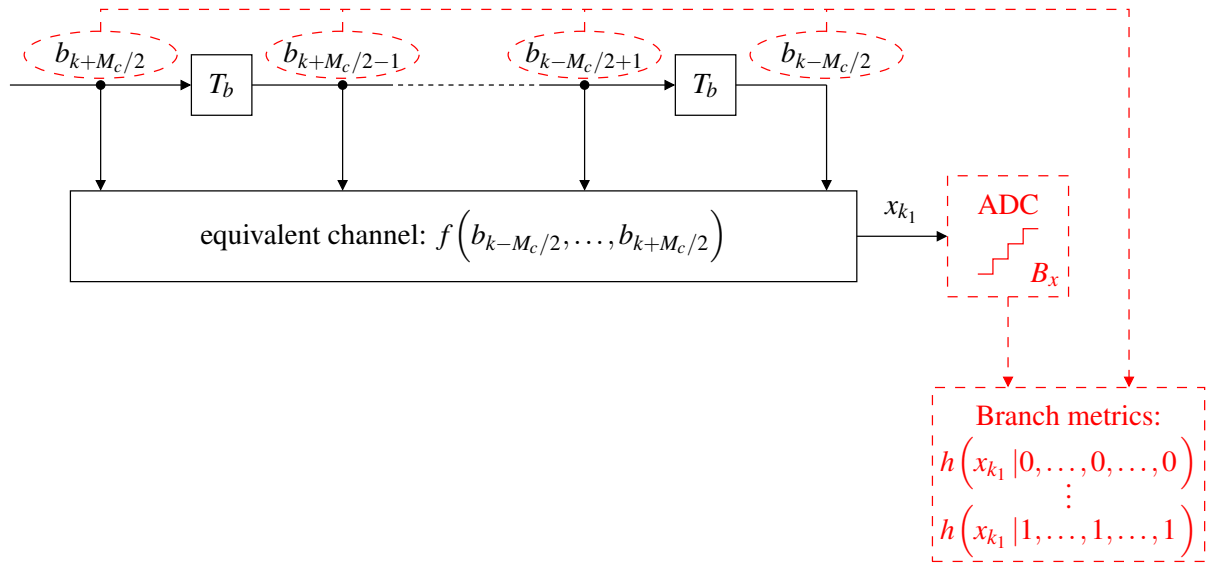

Figure 4.3: Conditional histogram measurement

The non-infinitesimal width of the histogram bins implicitly quantizes the electrical RX signal samples, i.e. this VA implementation is digital per se. The resolution and dynamic range of the analog-to-digital converter (ADC) determines the accuracy of the conditional histograms. Although maximum likelihood sequence estimation based Viterbi equalizers (MLSE-VEs) are already able to improve the link margin for an ADC resolution of $B_x = 3$ bits [20, 80, 28], we do not want to waste its full potential and set $B_x = 5$ bits, which

corresponds to $2^5 = 32$ quantization levels.

The result of a branch metric measurement for $B_x = 5$ bit is depicted in Fig. 4.4 for $M_c = 2$ and CD as well as first-order PMD. While the integral over the full range of a PDF evaluates to 1, the histograms of Fig. 4.4 do not show this normalization. Instead, we have just logarithmized their absolute count. However, this is intended since normalization has no effect on the performance of the VA because the relative differences in the path metrics remain, i.e. their are just scaled. The main disadvantage of branch metric measurement is the absence of histogram values in the tail regions. This is difficult to overcome because simulation events are rare here. If necessary, some extrapolation techniques can be useful.
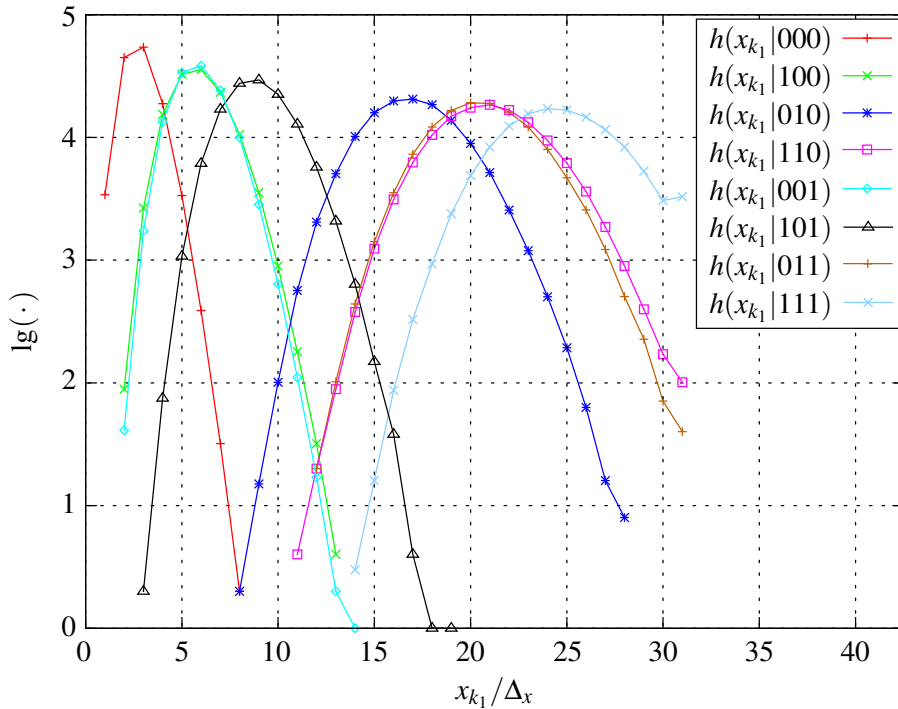

Figure 4.4: Branch metrics for $M_c = 2$ with $B_x = 5$ bit (combined CD ($L_f = 5$ km) and first-order PMD ($\Delta\tau_{g,max} = 12.36$ ps), $\gamma_{OSNR} = 21$ dB)

4.1.3 Fractionally Spaced MLSE Viterbi Equalizer

As already indicated in Ch. 3.2.4, sampling with a narrower than T_b-spaced sample interval can be beneficial for EDC performance. Besides the obviously higher internal processing speed, the VA and its computations have to be changed slightly. We just highlight the basic ideas and summarize the final equations here because they are in principle a straightforward extension of the T_b-spaced case discussed previously.

The state based system view must be extended to deliver $i\Delta T_i$-spaced samples x_{k_i} per bit interval, of which each is dependent on the input bit $b_{k+M_c/2}$ and the current channel state

$(b_{k+M_c/2-1}, \ldots, b_{k-M_c/2})$. We account for this by including upsampling of the input to the equivalent discrete-time system model as illustrated in Fig. 4.5 for $\Delta T_2 = T_b/2$.
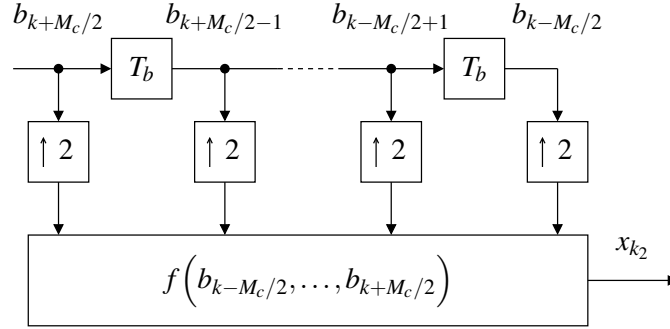

Figure 4.5: State based system model for a sample interval of $\Delta T_2 = T_b/2$

The advantage of fractionally spaced processing within the VA arises from the fact that we are able to reproduce and distinguish the state transitions much better out of the observation of multiple electrical RX signal samples. The assumptions made for the VA in Eq. (4.6) apply also for fractionally spaced processing with

$$
\begin{aligned}
\hat{\mathbf{b}}_{L_{tb}} &= \arg\max_{\mathbf{b}_{L_{tb}}} p\left(\mathbf{x}_{iL_{tb}} \middle| \mathbf{b}_{L_{tb}}\right) \\
&\approx \arg\max_{\mathbf{b}_{L_{tb}}} \prod_{\substack{k=0,\\k_i=ik}}^{L_{tb}-1} p\left(x_{k_i}, \ldots, x_{k_i+i-1} \middle| b_{L_{tb}-1}, \ldots, b_0\right) \\
&\approx \arg\max_{\mathbf{b}_{L_{tb}}} \prod_{\substack{k=0,\\k_i=ik}}^{L_{tb}-1} p\left(x_{k_i}, \ldots, x_{k_i+i-1} \middle| b_{k+M_c/2}, \ldots, b_{k-M_c/2}\right), \\
\mathbf{x}_{iL_{tb}} &= \left(x_{k_i}\right)_{k_i=0,\ldots,iL_{tb}-1}.
\end{aligned}
\tag{4.10}
$$

The sequence $\mathbf{x}_{iL_{tb}}$ contains the electrical RX signal samples which are related to the bit sequence $\mathbf{b}_{L_{tb}}$. Concerning the state transition and trellis diagram, we have to alter the state transition probabilities to multivariate conditional PDFs, which include all electrical RX signal samples for one transition from time instant k to $k+1$. This is shown again for $\Delta T_2 = T_b/2$ and $M_c = 2$ in Figs. 4.6(a) and 4.6(b).

If we think about implementation, the number of multivariate conditional PDFs for branch metric calculation scales exponential in the number of samples taken per bit interval. If we followed the approximation of conditional PDFs by histograms, we would have to record them with respect to multidimensional bins. A simplification to circumvent this complexity
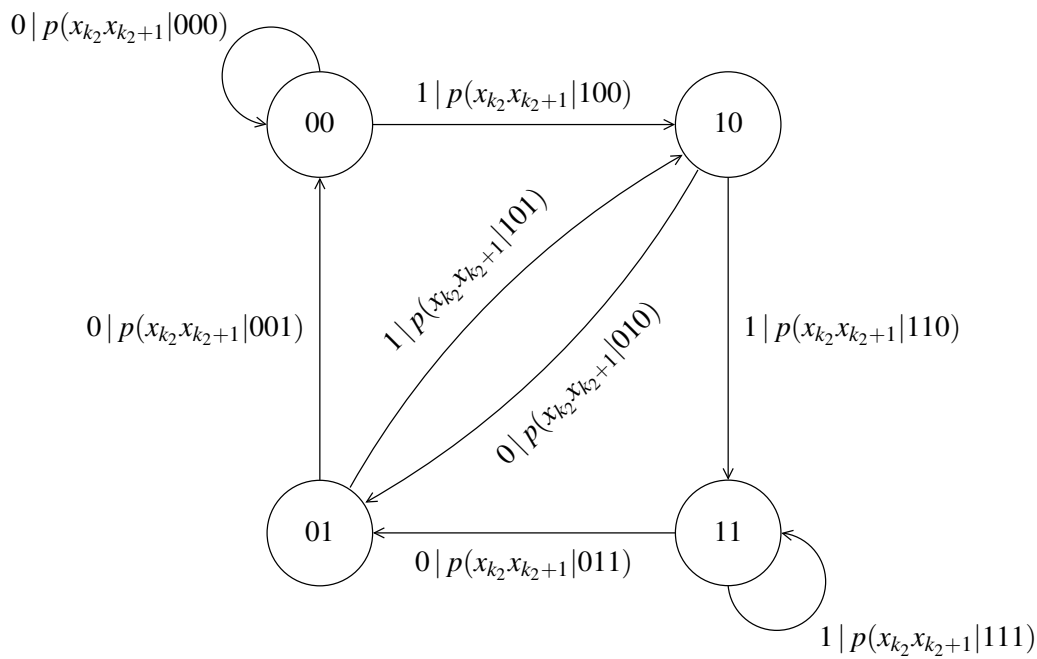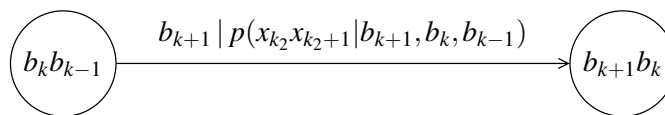
(a) State transition diagram
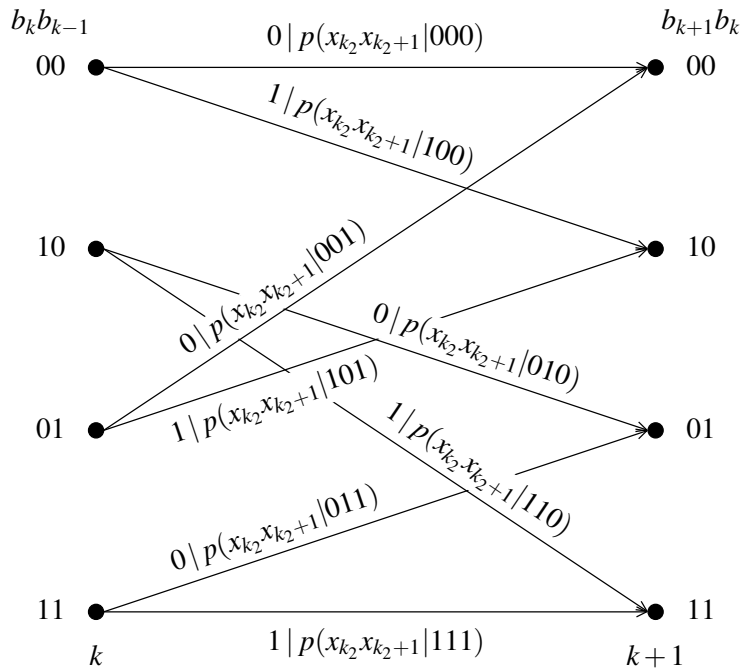
(b) Trellis diagram for one transition

Figure 4.6: State transition and trellis diagram for $\Delta T_2 = T_b/2$ and $M_c = 2$

is therefore

$$\hat{\mathbf{b}}_{L_{tb}} \approx \arg \max_{\mathbf{b}_{L_{tb}} \in B_{L_{tb}}} \prod_{\substack{k=0, \\ k_i=ik}}^{L_{tb}-1} \prod_{j=0}^{i-1} p\left(x_{k_i+j} \,\middle|\, b_{k+M_c/2}, \ldots, b_{k-M_c/2}\right), \qquad (4.11)$$

which relies on univariate PDFs. However, equality of Eq. (4.11) to Eq. (4.10) is only given if the electrical RX signal samples $x_{k_i}, \ldots, x_{k_i+i-1}$ within one bit interval are statistically independent. Thus, we intentionally reduce mathematical accuracy in favor of implementation. The deviation of the rule in Eq. (4.11) compared to plain MLSE increases as the electrical RX signal samples get more and more correlated. This obviously happens if we reduce the temporal sample spacing.

The final iterative and trellis based equation with histogram based path metrics updates for fractionally spaced sample processing is then given by

$$P_{\mathrm{lg},k+1,\left(b_{k+M_c/2},\ldots,b_k,\ldots,b_{k-M_c/2+1}\right)} =$$

$$\max \left(\begin{array}{l} P_{\mathrm{lg},k,\left(b_{k+M_c/2-1},\ldots,b_{k-1},\ldots,b_{k-M_c/2}=0\right)} \\[2ex] \quad + \displaystyle\sum_{\substack{j=0, \\ k_i=ik}}^{i-1} \lg\left(h\left(x_{k_i+j}\,\middle|\,b_{k+M_c/2},\ldots,b_k,\ldots,b_{k-M_c/2}=0\right)\right), \\[3ex] P_{\mathrm{lg},k,\left(b_{k+M_c/2-1},\ldots,b_{k-1},\ldots,b_{k-M_c/2}=1\right)} \\[2ex] \quad + \displaystyle\sum_{\substack{j=0, \\ k_i=ik}}^{i-1} \lg\left(h\left(x_{k_i+j}\,\middle|\,b_{kM_c/2},\ldots,b_k,\ldots,b_{k-M_c/2}=1\right)\right) \end{array} \right). \quad (4.12)$$

Figs. 4.7(a) and 4.7(b) illustrate the branch metric histograms for the same parameters assumed in Figs. 4.5, 4.6(a) and 4.6(b). The temporal sampling phase within the sample interval ΔT_2 was set to $\tau_2 = 0$ resulting in a sampled electrical RX signal $x(t)$ in the transitional region and in the middle of the eye diagram if we refer to Fig. 3.19(d) on page 50. The conditional histograms in Figs. 4.7(a) and 4.7(b) have different shapes therefore. In principle, we can observe only three distinct histograms for the even samples in Fig. 4.7(a) because the eye transitions in Fig. 3.19(d) are concentrated around three distinct regions. The odd samples taken in the middle of the eye coincide with those of the already presented T_b-spaced example in Ch. 4.1.2.
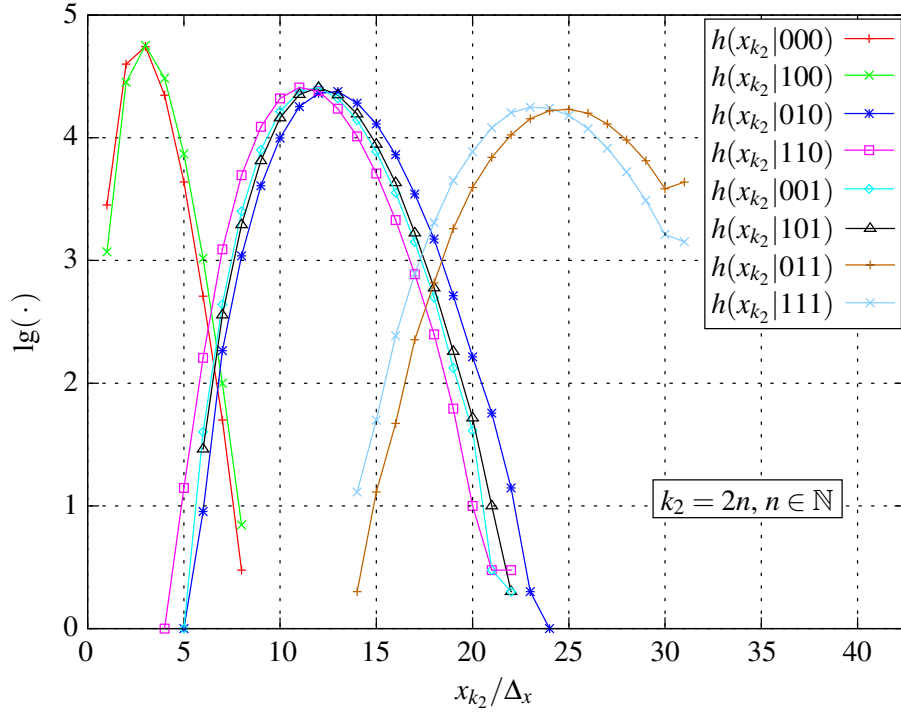
(a) Branch metrics for the even electrical RX signal samples
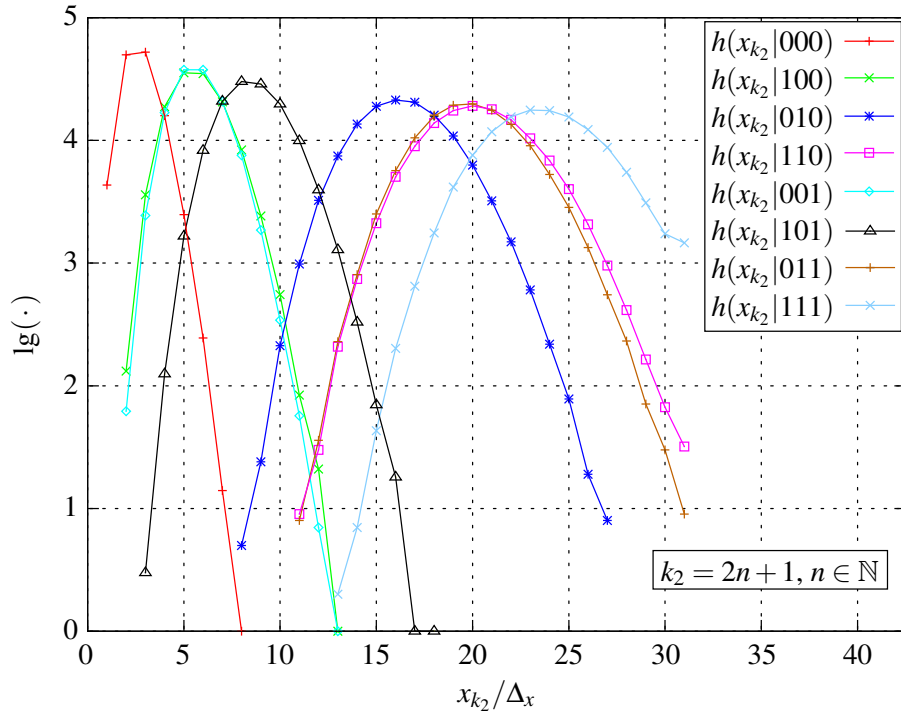
(b) Branch metrics for the odd electrical RX signal samples

Figure 4.7: Fractionally spaced branch metrics for $\Delta T_2 = T_b/2$ and $M_c = 2$ with $B_x = 5$ bit
(combined CD ($L_f = 5$ km) and first-order PMD ($\Delta\tau_{g,max} = 12.36$ ps), $\gamma_{OSNR} = 21$ dB)

In contrast to the illustrated branch metric histograms in Figs. 4.7(a) and 4.7(b), the presented simulation results in Ch. 4.3 use $\tau_i = \Delta T_i/2$. Since the eye diagram of Fig. 3.19(d) is almost symmetric with respect to its center, this setup for τ_i produces almost identical histograms for even and odd samples. This is a further possibility to reduce implementation cost.

4.2 Feedforward and Decision Feedback Equalizers

EDC using linear FFEs in combination with DFEs belongs to the class of sbs ML detection methods. Therefore, it cannot outperform MLSE-VE by nature. It tries to compensate the deterministic ISI of the transmission channel by reopening the eye diagram for the sampling instant at the RX to increase the robustness against noise. From a frequency domain perspective, FFE-DFEs can be viewed as an inverse channel modeling approach to target an ideally flat effective transfer function within the passband range of the communication channel. Parallelism can also be drawn from the fields of signal classification, feature extraction or source separation on noisy input data. Usually, textbooks [42, 81, 82] present the theory of FFE-DFEs with respect to linear ISI channels, for which we can fairly agree that removing a linear impairment by means of linear equalizer filters seems well justified. However, OA-IM/DD links also generate nonlinear ISI as we have discussed before. FFE-DFEs are suboptimal therefore. With respect to the interpretation as an inverse channel filter, they can only compensate for the linear components of ISI, which we can describe by the Fourier transform for continuous-time or the Z-transform for discrete-time representations of the communication channel. As a consequence, some investigations towards nonlinear FFE-DFEs using Volterra series [83, 84, 85, 86, 87, 88] have been executed with the aim to include the nonlinear ISI components, too. Within these advanced structures, the input signals may also appear self- and cross-mixed. Thus, Volterra based FFE-DFEs require more multiplications. This contrasts to high-speed digital implementation, for which the least possible multiplication overhead is favorable. Since our final target of investigation is digital FFE-DFE implementation, we remain with the conventional and well-known linear equalizer structure in this thesis.

4.2.1 FFE-DFE Structure

Fig. 4.8 shows the conventional structure of a FFE-DFE with a linear feed-forward and decision feedback filter. The FFE is a linear transversal filter with $M \in \mathbb{N}_1$ coefficients c_m, $m = (0, \ldots, M-1)$. The $M-1$ delay elements, which also represent the order of the polynomial FFE transfer function in the Z-transform domain, hold the electrical RX signal samples $x_{k_i+\tau_d-m}$, which have been generated by a T_b-spaced sample interval here.
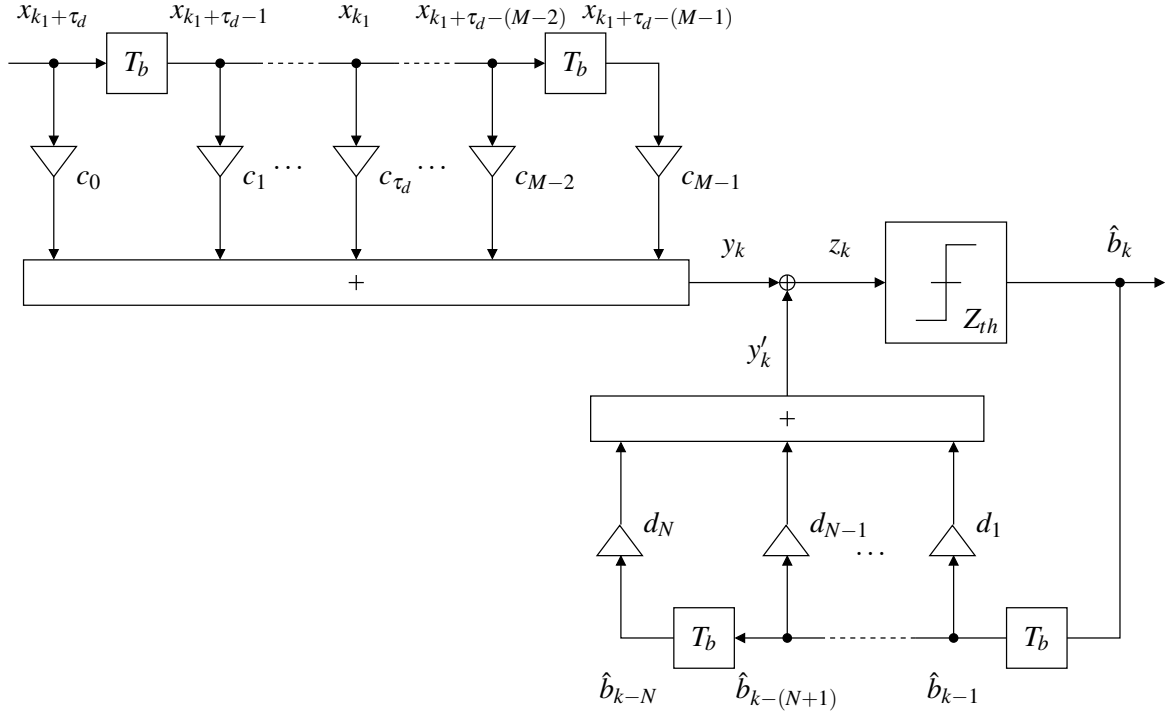
Figure 4.8: FFE-DFE structure

It is convenient to use

$$\mathbf{c} := \begin{pmatrix} c_0 \\ \vdots \\ c_{M-1} \end{pmatrix}, \quad \mathbf{c} \in \mathbb{R}^M, \tag{4.13}$$

as notation for the FFE coefficient vector, and the same can be done with the input samples $x_{k_1+\tau_d-m}$ to form the input sample vector

$$\mathbf{x}_{k_1} := \begin{pmatrix} x_{k_1+\tau_d} \\ \vdots \\ x_{k_1} \\ \vdots \\ x_{k_1+\tau_d-(M-1)} \end{pmatrix}, \quad \tau_d = 0, \ldots, M-1, \ \mathbf{x}_{k_1} \in \mathbb{R}^M. \tag{4.14}$$

The artificially introduced advancement τ_d of the elements in $\mathbf{x}_{k_1}$ will be explained further below. Thus, we can compactly formulate the FFE filter operation with an inner product

$$y_k = \sum_{m=0}^{M-1} c_m x_{k_1+\tau_d-m}$$
$$= \mathbf{c}^{\mathrm{T}} \mathbf{x}_{k_1}. \tag{4.15}$$

Although the mix of the time indices k and k_1 for y_k and $\mathbf{x}_{k_1}$ seems a bit confusing in

Eq. (4.15), we will require it when we explain fractionally spaced feed-forward equalizer (FSFFE) operation later on. For the moment, we refer to Eq. (3.122) on page 47, where we have already indicated the identity $k \equiv k_1$.

The output y'_{k_1} of the DFE filter with $N \in \mathbb{N}_1$ coefficients d_n, $n = (1, \ldots, N)$, is comprised of a linear filter operation on the previous bit estimates $\hat{b}_{k-n}$. Although the filter operation itself is linear, the whole structure must be considered as nonlinear due to the highly discontinuous slicer characteristic providing the input to the DFE.

In order to stay compliant with the FFE description, we also introduce a vector notation with

$$\mathbf{d} := \begin{pmatrix} d_1 \\ \vdots \\ d_N \end{pmatrix}, \quad \mathbf{d} \in \mathbb{R}^N, \tag{4.16}$$

for the DFE coefficients and

$$\hat{\mathbf{b}}_{k-1} := \begin{pmatrix} \hat{b}_{k-1} \\ \vdots \\ \hat{b}_{k-N} \end{pmatrix}, \quad \hat{\mathbf{b}}_{k-1} \in \{0,1\}^N, \tag{4.17}$$

for the input vector of bit estimate to the DFE. Thus, the compact notation for the output of the DFE filter is

$$\begin{aligned} y'_k &= \sum_{n=1}^{N} d_n \hat{b}_{k-n} \\ &= \mathbf{d}^{\mathrm{T}} \hat{\mathbf{b}}_{k-1}. \end{aligned} \tag{4.18}$$

The FFE-DFE output z_k, which is also referred to as *decision statistic*, is calculated by

$$\begin{aligned} z_k &= y_k + y'_k \\ &= \mathbf{c}^{\mathrm{T}} \mathbf{x}_{k_1} + \mathbf{d}^{\mathrm{T}} \hat{\mathbf{b}}_{k-1}. \end{aligned} \tag{4.19}$$

Especially for the following derivations, it is sometimes useful to further compact Eq. (4.19) with

$$z_k = \check{\mathbf{c}}^{\mathrm{T}} \check{\mathbf{x}}_{k_1}, \tag{4.20}$$

for which we introduce the overall coefficient vector

$$\check{\mathbf{c}} := \begin{pmatrix} \mathbf{c} \\ \mathbf{d} \end{pmatrix} \tag{4.21}$$

and the overall FFE-DFE input vector

$$\check{\mathbf{x}}_{k_1} := \begin{pmatrix} \mathbf{x}_{k_1} \\ \hat{\mathbf{b}}_{k-1} \end{pmatrix}. \tag{4.22}$$

The FFE-DFE output z_k is subject to sbs ML as illustrated in Fig. 4.8 by the slicer with the decision threshold Z_{th}. We always optimize $Z_{th} \in \mathbb{R}$ for each OA-IM/DD link parameter set as already indicated in Ch. 3.3.2. The final bit estimate $\hat{b}_k$ corresponds to the TX bit b_k and is forwarded for further processing and put into the delay chain of the DFE part for the next FFE-DFE operation cycle.

Concerning coefficient adjustment for optimal EDC performance, FFE-DFE offers $M + N$ degrees of freedom. Another degree related to the FFE part is the parameter *decision delay* τ_d. Having a closer look at the cross-correlation of the transmitted bits b_k and the electrical RX signal sample x_{k_1+j} for different time lags $j \in \mathbb{Z}$ as depicted in Fig. 4.9 reveals that CD and PMD induced ISI in OA-IM/DD links spreads symmetrically. Owing to the fact that we
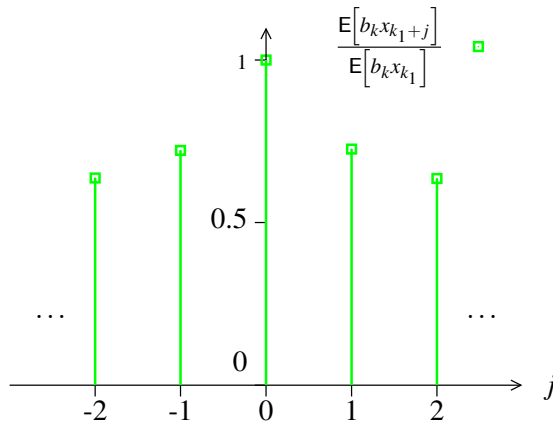

Figure 4.9: Cross-correlation between the TX bits and the electrical RX samples for different time lags
(combined CD ($L_f = 5$ km) and first-order PMD ($\Delta\tau_g = 12.5$ ps), $\gamma_{OSNR} = 21$ dB)

have intentionally reverted the common group delay within the simulation environment as mentioned in Ch. 3.2.4, the cross-correlation between the TX bit b_k and the electrical RX signal samples x_{k_1+j} is largest for $j = 0$ and declines almost in the same way for positive and negative time lags[1]. This gives reason for the assessment

$$\left| \mathsf{E}\left[b_k x_{k_1}\right] \right| \geq \left| \mathsf{E}\left[b_k x_{k_1-1}\right] \right| \approx \left| \mathsf{E}\left[b_k x_{k_1+1}\right] \right| \geq \left| \mathsf{E}\left[b_k x_{k_1-2}\right] \right| \approx \left| \mathsf{E}\left[b_k x_{k_1+2}\right] \right| \geq \dots \, .$$

If we want to recover a distorted signal affected by ISI, it is intuitive to include those samples for the recovery process which have the highest affinity to it in a statistical sense. This is

---

[1] In the discussion of MLSE in Ch. 4.1, we have accounted for this by introducing the channel memory parameter M_c, which extends the channel memory symmetrically in both temporal directions.

given in a linear manner by the most correlated samples x_{k_1+j} to b_k with j around zero. While M determines how many samples the FFE takes into account, we use the decision delay $\tau_d = 0, \ldots, M-1$ to identify the coefficient c_{τ_d} within the FFE, by which the input sample x_{k_1}, which is most correlated to b_k, is multiplied when the decision statistic y_k to get the estimate $\hat{b}_k$ is generated. Thus, we may use

$$\mathbf{x}_{k_1} = \begin{pmatrix} x_{k_1} \\ \vdots \\ x_{k_1-(M-1)} \end{pmatrix}, \quad \ldots, \quad \mathbf{x}_{k_1} = \begin{pmatrix} x_{k_1+(M-1)} \\ \vdots \\ x_{k_1} \end{pmatrix}$$

as input to the FFE when we determine $\hat{b}_k$. There exist some studies [89, 90, 91] on the optimal choice of τ_d but all with the prerequisite of a linear finite impulse response (FIR) channel affected by AWGN. Since we have to deal with an end-to-end nonlinear channel given by the OA-IM/DD link and signal-dependent noise, we rather optimize τ_d to exploit any degree of freedom. The degrees of freedom for FFE-DFE adjustment increases to $M+N+1$ therefore. The optimization of the decision delay reflects itself in the repeated calculation of FFE-DFE coefficients for each value of τ_d with respect to the parameter set describing the OA-IM/DD link and the applied coefficient adjustment criteria, which we will present in the following.

4.2.2 FFE-DFE Coefficient Adjustment Criteria

4.2.2.1 Minimal BER Criterion

Assessment of digital communication systems and the involved TX formats and RX processing methods often requires the measurement or even analytical calculation of the BER as a fundamental quantity comprising all detrimental effects of the system. Deducing the link quality only from noiseless eye diagrams or waveform observations is sometimes not satisfactory since rough assumptions are involved which allow a relative judgment but do not reflect the absolute performance. This is even true for simulation models in which the modeling itself includes some abstractions and deviations from the real system behavior. Thus, adjustment of the FFE-DFE coefficients with respect to MIN-BER represents the optimum in order to study its absolute EDC performance.

If we collect all parameters and possible effects of the considered OA-IM/DD link, we may formulate the task of FFE-DFE coefficient adjustment for MIN-BER as follows

$$\check{\mathbf{c}}_{BER} = \arg \min_{\check{\mathbf{c}}} BER\left(L_f, \Delta\tau_g, \gamma_{OSNR}, M, N, \check{\mathbf{c}}, \tau_d, Z_{th}\right). \tag{4.23}$$

The determination of the BER for sbs ML detection generally requires to evaluate the conditional histograms of the decision variable as shown in Ch. 3.3.2. We have already indicated there that it is quite difficult to capture the conditional histograms for an OA-IM/DD

link without FFE or DFE. Unfortunately, it is also not possible to express the relation in Eq. (4.23) in any analytical term. Thus, we cannot rely on extreme value calculation known from calculus or apply numerically stable and well understood gradient descent optimization strategies as for example in [55] for multidimensional mappings under AWGN conditions. Some authors have already turned to the question of MIN-BER FFE-DFE coefficient adjustment and have proposed some approximate analytical solutions for linear channels with AWGN [92, 93, 94, 95] and even OA-IM/DD links [96]. While an analytical solution seems plausible for the first few references due to linearity and additive noise, the latter one makes use of a much simplified OA-IM/DD system model with linear modulation of the optical CW carrier signal and without optical and electrical filtering. In order to cover MIN-BER coefficient adjustment anyway, a numerical method called *downhill simplex method* was found in literature [97]. This method relies on repeatedly executed simulations and evaluations of

$$BER\left(L_f, \Delta\tau_g, \gamma_{OSNR}, M, N, \check{\mathbf{c}}, \tau_d, Z_{th}\right)$$

for $M+N+1$ initial setups of $\check{\mathbf{c}}$. These coefficient setups form a so-called *simplex*, which is a geometric body in the $(M+N)$-dimensional solution space with the $M+N+1$ realizations of $\check{\mathbf{c}}$ acting as its vertices. Assuming that the optimal coefficient vector is somewhere contained within the volume of the simplex, we always change the worst vertex given by the coefficient vector $\check{\mathbf{c}}$ with the largest BER to finally contract the vertex towards the MIN-BER solution $\check{\mathbf{c}}_{BER}$. In [98] this trial-and-error approach has been initially applied to an OA-IM/DD link. The details about the way we have to change the set of coefficient vectors towards the optimal solution and the further steps of this algorithm are described in App. C.

4.2.2.2 Zero-Forcing Criterion

The ZF criterion to adjust the FFE-DFE coefficients bases on the channel inversion problem. In general, ZF equalization is more or less a theoretical construct, which requires a priori knowledge of the impulse response of the ISI causing communication channel. Nevertheless, we use it as a first step to bridge the gap from the purely theoretical MIN-BER adjustment towards a more practically relevant criterion which targets to improve the eye pattern at the RX. Similar to the state based system view for the derivation of the VA in Ch. 4.1, we use a discrete-time equivalent channel model with memory M_c to describe the input-output relation of the considered OA-IM/DD system. The concatenation with the properly designed ZF FFE-DFE should eliminate the ISI of the channel and lead to an ideal overall impulse response of $\delta(t)$ in the continuous-time or to the unit impulse δ_k in the discrete-time domain given by

$$\delta_k := \begin{cases} 1 & : & k = 0 \\ 0 & : & k \neq 0 \end{cases}. \tag{4.24}$$

4.2.2.2.1 LLS FIR Channel Approximation

Since we focus on linear channel inversion filters in this section, we consequently require a linear FIR approximation of the OA-IM/DD link as depicted in Fig. 4.10. However, we have
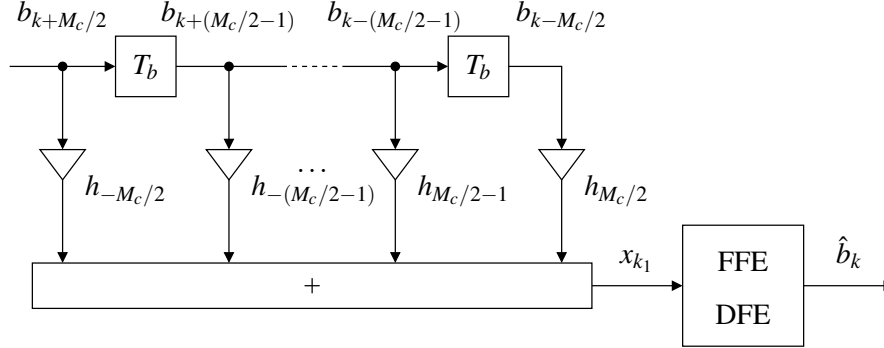

Figure 4.10: LLS FIR channel approximation of the OA-IM/DD link

already discussed in detail in Chs. 2 and 3 that OA-IM/DD links are end-to-end nonlinear with respect to the electrical domains from the TX to RX. Therefore, a linear FIR approximation is not able to reproduce the exact system behavior, and nonlinear components of ISI are ignored by this procedure. However, since FFE-DFE is only able to mitigate linear ISI, the linear channel approximation becomes justified again.

Assuming a channel memory $M_c = 2n$, $n \in \mathbb{N}$, as defined for the VA, we measure an equivalent discrete-time linear least squares (LLS) FIR approximation of the OA-IM/DD link to obtain the channel coefficient vector

$$\mathbf{h} := \begin{pmatrix} h_{-M_c/2} \\ \vdots \\ h_0 \\ \vdots \\ h_{M_c/2} \end{pmatrix} \quad M_c = 2n, n \in \mathbb{N}. \tag{4.25}$$

The coefficient h_0 shall be the main coefficient, which has generally the largest magnitude, and which shall be multiplied with the input bit b_k of the bit vector

$$\mathbf{b}_k := \begin{pmatrix} b_{k-M_c/2} \\ \vdots \\ b_k \\ \vdots \\ b_{k+M_c/2} \end{pmatrix} \tag{4.26}$$

if the electrical RX signal sample x_{k_1} is approximated by a discrete-time convolution

$$x_{k_1} \approx \sum_{j=-M_c/2}^{M_c/2} h_j \, b_{k-j}$$

$$= \mathbf{h}^{\mathrm{T}} \mathbf{b}_k. \tag{4.27}$$

Consequently, the inherent delay of the linear channel approximation filter is fixed to $M_c/2$ as Fig. 4.10 illustrates. The channel coefficients h_j, $j = -M_c/2,\ldots,M_c/2$, are determined by a LLS fitting procedure explained in App. D. Note that the non-causal modeling and indexing of the linear FIR channel approximation filter is only possible within a computer simulation environment but consistent with the conventions in previous chapters. The LLS fitting procedure is based on noisy input data which are output from the simulation model of the OA-IM/DD link. The linear approximation may differ for different values of the OSNR therefore.

4.2.2.2.2 Concatenated LLS FIR Channel Approximation and FFE Response

After having the channel coefficients available, we may write for the output of the concatenation of the LLS FIR channel approximation and the FFE with Eqs. (4.15) and (4.27)

$$y_k = \sum_{m=0}^{M-1} c_m \underbrace{x_{k_1+\tau_d-m}}_{\approx h_j * b_{k+\tau_d}} \approx \sum_{m=0}^{M-1} c_m \left(\sum_{j=-M_c/2}^{M_c/2} h_j \, b_{k+\tau_d \underbrace{-m-j}_{i:=m+j}} \right)$$

$$= \sum_{j=-M_c/2}^{M_c/2} \sum_{i=j}^{j+M-1} h_j \, c_{i-j} \, b_{k+\tau_d-i}$$

$$= \sum_{i=-M_c/2}^{M_c/2+M-1} \underbrace{\sum_{j=\max(-M_c/2,\,i-(M-1))}^{\min(-M_c/2,\,i)} h_j \, c_{i-j}}_{=:h_i'(\mathbf{c})} \, b_{k+\tau_d-i}$$

$$= \sum_{i=-M_c/2}^{M_c/2+M-1} h_i'(\mathbf{c}) \, b_{k+\tau_d-i} \tag{4.28}$$

We intentionally neglect the DFE for the moment and turn our attention to it later again.

The non-causal concatenated system response has $M_c + M$ coefficients, which we summarize by

$$\mathbf{h}'(\mathbf{c}) = \begin{pmatrix} h'_{-M_c/2}(\mathbf{c}) \\ \vdots \\ h'_{M_c/2+M-1}(\mathbf{c}) \end{pmatrix}. \tag{4.29}$$

The notation as a function of the FFE coefficient vector $\mathbf{c}$ for $\mathbf{h}'(\mathbf{c})$ and its elements $h_i'(\mathbf{c})$ shall emphasize this dependence.

We can rewrite Eq. (4.28) and separate the terms to get

$$y_k = h_{\tau_d}'(\mathbf{c})\, b_k + \underbrace{\sum_{\substack{i=-M_c/2 \\ i \neq \tau_d}}^{M_c/2+M-1} h_i'(\mathbf{c})\, b_{k+\tau_d-i}}_{ISI}. \tag{4.30}$$

The main coefficient of the concatenated system response has the index $i = \tau_d$, which is a further convenience of our non-causal view on the system. The first term in Eq. (4.30) contains the information we try to recover while the second one becomes ISI if it is not zero.

Since we evaluate y_k with respect to a decision threshold for sbs ML detection, we are interested in improving the eye opening to increase the tolerance against noise. Equivalently, we can minimize the peak eye distortion defined by

$$\rho_e(\mathbf{c}) := \sum_{\substack{i=-M_c/2 \\ i \neq \tau_d}}^{M_c/2+M} \left| h_i'(\mathbf{c}) \right|. \tag{4.31}$$

The task of FFE design is to minimize $\rho_e(\mathbf{c})$ by the proper choice of the FFE coefficients c_m, $m = 0, \ldots, M-1$. In [99] it has been shown that the peak eye distortion is a convex function with respect to $\mathbf{c}$. This property leads to a unique optimal solution. Further insight into this optimization task reveals that minimizing the peak distortion is equivalent to force $M-1$ samples of the concatenated system response to zero [100], which has implicated the name *zero-forcing* for this type of FFE-DFE adjustment. Consequently, reduction or even removal of the ISI term in Eq. (4.30) requires a concatenated system response according to the ZF criterion expressed by

$$h_i'(\mathbf{c}) \approx h_{ZF,i}' := \delta_{i-\tau_d}, \quad i = -M_c/2, \ldots, M_c/2+M-1. \tag{4.32}$$

Its explicit form is given by

$$\mathbf{h}'(\mathbf{c}) \approx \mathbf{h}_{ZF}' = \begin{pmatrix} h_{ZF,-M_c/2}' \\ \vdots \\ h_{ZF,\tau_d-1}' \\ h_{ZF,\tau_d}' \\ h_{ZF,\tau_d+1}' \\ \vdots \\ h_{ZF,M_c/2+M-1}' \end{pmatrix} := \begin{pmatrix} 0 \\ \vdots \\ 0 \\ 1 \\ 0 \\ \vdots \\ 0 \end{pmatrix}. \tag{4.33}$$

In order to explain the application of the ZF criterion, it is appropriate to reformulate the finite length convolution leading to the concatenated system response of Eq. (4.28) by using the vector notation introduced in Eq. (4.29). We can define a so-called $(M_c + M) \times M$ *convolution matrix* for the linear FIR channel approximation. This matrix is constructed by shifting a transposed and temporally reversed version of the channel coefficient vector **h** from the left-hand side row by row in the matrix. We pad the not touched positions with zeros and cut those elements which exceed the row dimension border of the matrix. A matrix constructed by this principle is generally known as *Toeplitz matrix*, and its structure is in our case

$$
\mathbf{H} := \begin{bmatrix}
h_{-M_c/2} & 0 & \dots & \dots & \dots & 0 \\
h_{-(M_c/2-1)} & h_{-M_c/2} & 0 & \dots & \dots & 0 \\
\vdots & \dots & \vdots & \dots & \vdots & \dots \\
h_{\tau_d-1} & \dots & \dots & h_{-1} & \dots & h_{-(M-1)+\tau_d-1} \\
h_{\tau_d} & \dots & \dots & h_0 & \dots & h_{-(M-1)+\tau_d} \\
h_{\tau_d+1} & \dots & \dots & h_1 & \dots & h_{-(M-1)+\tau_d+1} \\
\vdots & \dots & \vdots & \dots & \vdots & \dots \\
0 & \dots & \dots & 0 & h_{M_c/2} & h_{M_c/2-1} \\
0 & \dots & \dots & \dots & 0 & h_{M_c/2}
\end{bmatrix}_{(M_c+M) \times M} . \tag{4.34}
$$

Using the vector notation for the concatenated system response $\mathbf{h}'$, the convolution matrix $\mathbf{H}$ and the FFE coefficient vector $\mathbf{c}$ of Eq. (4.13), we may express the result of the discrete-time convolution in Eq. (4.28) in compact vector notation with

$$
\mathbf{h}'(\mathbf{c}) = \mathbf{Hc}. \tag{4.35}
$$

After insertion of $\mathbf{h}'(\mathbf{c}) \approx \mathbf{h}'_{ZF}$ according to Eq. (4.33), we may use

$$
\mathbf{h}'_{ZF} \approx \mathbf{Hc} \iff
$$

$$
\begin{pmatrix} 0 \\ \vdots \\ 0 \\ 1 \\ 0 \\ \vdots \\ 0 \end{pmatrix} \approx \begin{bmatrix}
h_{-M_c/2} & 0 & \dots & \dots & \dots & 0 \\
h_{-(M_c/2-1)} & h_{-M_c/2} & 0 & \dots & \dots & 0 \\
\vdots & \dots & \vdots & \dots & \vdots & \dots \\
h_{\tau_d-1} & \dots & \dots & h_{-1} & \dots & h_{-(M-1)+\tau_d-1} \\
h_{\tau_d} & \dots & \dots & h_0 & \dots & h_{-(M-1)+\tau_d} \\
h_{\tau_d+1} & \dots & \dots & h_1 & \dots & h_{-(M-1)+\tau_d+1} \\
\vdots & \dots & \vdots & \dots & \vdots & \dots \\
0 & \dots & \dots & 0 & h_{M_c/2} & h_{M_c/2-1} \\
0 & \dots & \dots & \dots & 0 & h_{M_c/2}
\end{bmatrix}_{(M_c+M) \times M} \begin{pmatrix} c_0 \\ \vdots \\ c_{\tau_d} \\ \vdots \\ c_{M-1} \end{pmatrix}
$$

$$
\tag{4.36}
$$

to determine the corresponding ZF FFE coefficient vector $\mathbf{c}$. A closer look at the row and

column dimensions of the convolution matrix $\mathbf{H}$ with $M_c + M > M$ reveals that the number of equations is larger than the number of variables. Such a system of equations is said to be overdetermined, and we can only approximate the desired concatenated ZF system response. This fact is also supported by the Z-transform domain consideration of Eq. (4.28) and the ZF criterion of Eq. (4.32) with

$$z^{-\tau_d} \approx H(z)C(z) \quad \Longleftrightarrow \quad C(z) = c_0 + c_1 z^{-1} + \ldots + c_{M-1} z^{-(M-1)} \approx \frac{z^{-\tau_d}}{H(z)}. \quad (4.37)$$

This relation states that, given the LLS FIR channel approximation with the Z-transform $H(z)$, the ideal equalizer filter $C(z)$ should be a recursive one approximating the inverse channel transfer function. We could think of straightforward channel inversion using a recursive filter as an alternative to the FFE. However, this might cause stability problems if the LLS FIR channel approximation filter is not minimum phase. Application of series expansion theory as in [54] also shows that using a linear FFE with $M \ll \infty$ cannot exactly yield the inverse approximate channel transfer function for T_b-spaced sampling. Consequently, we have to tolerate a residual amount of ISI, which manifests itself in a nonzero peak eye distortion.

Coming back to the time domain problem formulation of Eq. (4.36), we have to choose M out of the $M_c + M$ equations to determine the ZF solution for the FFE coefficients. Therefore, let

$$\mathbb{I} := \left\{ -M_c/2, \ldots, M_c/2 + M - 1 \right\} \quad (4.38)$$

be the index set comprising all row indices of system of equations in Eq. (4.36), then we may separate those equations with respect to the row indices in two mutually exclusive sets

$$\mathbb{I}_{FFE} = \mathbb{I} \setminus \mathbb{I}_{ISI}, \quad |\mathbb{I}_{FFE}| = M, \tau_d \in \mathbb{I}_{FFE}, \quad (4.39)$$

$$\mathbb{I}_{ISI} = \mathbb{I} \setminus \mathbb{I}_{FFE}, \quad |\mathbb{I}_{ISI}| = M_c. \quad (4.40)$$

We use the equations represented by the indices in $\mathbb{I}_{FFE}$ to calculate the ZF solution for the FFE while the others contained in $\mathbb{I}_{ISI}$ contribute to the residual ISI. The index τ_d for the row in which we set the one in the ZF condition vector $\mathbf{h}'_{ZF}$ shall always be contained in $\mathbb{I}_{FFE}$.

Eq. (4.41) illustrates this kind of separation of the rows with

$$
\begin{pmatrix} 0 \\ 0 \\ \vdots \\ 0 \\ 1 \\ 0 \\ \vdots \\ 0 \\ 0 \end{pmatrix} \approx \left. \begin{bmatrix} h_{-M_c/2} & 0 & \dots & \dots & \dots & 0 \\ h_{-(M_c/2-1)} & h_{-M_c/2} & 0 & \dots & \dots & 0 \\ \vdots & \dots & \vdots & \dots & \vdots & \dots \\ h_{\tau_d-1} & \dots & \dots & h_{-1} & \dots & h_{-(M-1)+\tau_d-1} \\ h_{\tau_d} & \dots & \dots & h_0 & \dots & h_{-(M-1)+\tau_d} \\ h_{\tau_d+1} & \dots & \dots & h_1 & \dots & h_{-(M-1)+\tau_d+1} \\ \vdots & \dots & \vdots & \dots & \vdots & \dots \\ 0 & \dots & \dots & 0 & h_{M_c/2} & h_{M_c/2-1} \\ 0 & \dots & \dots & \dots & 0 & h_{M_c/2} \end{bmatrix} \right\rbrace
\begin{matrix} \\ \in \mathbb{I}_{FFE \oplus ISI} \\ \\ \in \mathbb{I}_{FFE} \\ \\ \in \mathbb{I}_{FFE \oplus ISI} \\ \\ \end{matrix}
\begin{pmatrix} c_0 \\ \vdots \\ c_{\tau_d} \\ \vdots \\ c_{M-1} \end{pmatrix},
$$
$$(M_c+M) \times M$$

$$(4.41)$$

for which the composition of $\mathbb{I}_{FFE}$ and $\mathbb{I}_{ISI}$ is arbitrary but exclusive as indicated by the notation $\mathbb{I}_{FFE} \oplus \mathbb{I}_{ISI}$.

With the rows corresponding to $\mathbb{I}_{FFE}$ in Eq. (4.36), we generate a reduced M-dimensional ZF condition vector $\mathbf{h}'_{ZF,FFE}$ and a $M \times M$ convolution matrix $\mathbf{H}_{FFE}$. We use this subsystem of equations to determine the FFE coefficients with

$$\mathbf{h}'_{ZF,FFE} = \mathbf{H}_{FFE}\,\mathbf{c} \Longleftrightarrow \mathbf{c} = \mathbf{H}_{FFE}^{-1}\,\mathbf{h}'_{ZF,FFE}. \tag{4.42}$$

Since $\mathbf{h}'_{ZF,FFE}$ has the simple form of a unit vector with a single element set to one, the ZF solution for the FFE is apparently the corresponding column of the inverse $M \times M$ convolution matrix $\mathbf{H}_{FFE}^{-1}$. This inverse exists if $\mathbf{H}_{FFE}$ has full rank, or equivalently, if all rows of the convolution matrix $\mathbf{H}$, from which $\mathbf{H}_{FFE}$ is extracted, are linearly independent. The Toeplitz structure of the convolution matrix guarantees this behavior.

Reinsertion of the determined coefficient vector $\mathbf{c}$ into Eq. (4.35) gives us the actual concatenated system response $\mathbf{h}'(\mathbf{c})$ and allows us determine the corresponding peak eye distortion $\rho_e(\mathbf{c})$ using Eq. (4.31). Owing to the formulated ZF condition, we have

$$h'_i(\mathbf{c}) = 0 \,\forall\, i \in \mathbb{I}_{FFE} \setminus \{\tau_d\}, \tag{4.43}$$

and the M_c coefficients of the complementary set

$$h'_i(\mathbf{c}) \neq 0 \,\forall\, i \in \mathbb{I}_{ISI} \tag{4.44}$$

contribute to the residual ISI, which we have to tolerate.

Since the composition of $\mathbb{I}_{FFE}$ and the choice of the decision delay τ_d are crucial for the amount of residual ISI, we vary them to identify the optimal ZF coefficient vector $\mathbf{c}_{ZF}$ with respect to globally minimal peak eye distortion. We may also not forget about the assumed channel memory M_c, which is also empirically adjusted when different parameter sets of the OA-IM/DD link have been simulated to generate the results presented later in this thesis. Hence, for each OA-IM/DD link parameter set and each decision delay τ_d ranging from $0, \ldots, M-1$, we have to check $\binom{M_c+M-1}{M-1}$ different combinations of $\mathbf{H}_{FFE}$. Since we always have $\tau_d \in \mathbb{I}_{FFE}$, we can only choose $M-1$ further rows.

4.2.2.2.3   Inclusion of the DFE

We are now ready to include the DFE in the demonstrated procedure for the FFE at hand. According to our initial illustration in Fig. 4.8 on page 68 and recalling Eqs. (4.18), (4.19) and (4.28), we just have to add the contribution of the DFE to the concatenated system response and get

$$
\begin{aligned}
z_k &= y_k + y_k' \\
&= \sum_{i=-M_c/2}^{M_c/2+M-1} h_i'(\mathbf{c})\, b_{k+\tau_d-i} + \sum_{n=1}^{N} d_n \hat{b}_{k-n}
\end{aligned}
\tag{4.45}
$$

as input to the decision slicer.

Similar to Eq. (4.30), we may split up this equation not in two but in three different terms for now with

$$
z_k = h_{\tau_d}'(\mathbf{c})\, b_k + \sum_{\substack{i=-M_c/2 \\ i \neq \tau_d}}^{M_c/2+M-1} h_i'(\mathbf{c})\, b_{k+\tau_d-i} + \sum_{n=1}^{N} d_n \hat{b}_{k-n}.
\tag{4.46}
$$

Presuming that

$$
0 \leq \tau_d \leq \min\left(M-1, \frac{M_c}{2} + M - 1 - N \right),
\tag{4.47}
$$

we may further extract and reorder

$$
z_k = h_{\tau_d}'(\mathbf{c})\, b_k + \sum_{i=-M_c/2}^{\tau_d-1} h_i'(\mathbf{c})\, b_{k+\tau_d-i} + \underbrace{\sum_{i=\tau_d+1}^{\tau_d+N} h_i'(\mathbf{c})\, b_{k+\underbrace{\tau_d-i}_{n:=i-\tau_d}}}_{=\sum_{n=1}^{N} h_{n+\tau_d}' b_{k-n}}
$$

$$
+ \underbrace{\sum_{n=1}^{N} d_n \hat{b}_{k-n}}_{\text{assume } \hat{b}_{k-n}=b_{k-n}} + \sum_{i=\tau_d+N+1}^{M_c/2+M-1} h_i'(\mathbf{c})\, b_{k+\tau_d-i}
$$

$$
\begin{aligned}
= h'_{\tau_d}(\mathbf{c})\,b_k + \underbrace{\sum_{i=-M_c/2}^{\tau_d-1} h'_i(\mathbf{c})\,b_{k+\tau_d-i} + \sum_{i=\tau_d+N+1}^{M_c/2+M-1} h'_i(\mathbf{c})\,b_{k+\tau_d-i}}_{\text{ISI to be eliminated by FFE}} \\
+ \underbrace{\sum_{n=1}^{N}\left(h'_{n+\tau_d}(\mathbf{c}) + d_n\right)b_{k-n}}_{\text{ISI eliminated by DFE}}.
\end{aligned}
\tag{4.48}
$$

The first term contains the desired bit symbol we try to recover, the second and third one contain the amount of ISI which has to be eliminated by the FFE as before, and the last one arises from the application of the DFE under the assumption of correct bit decisions with $\hat{b}_{k-n} = b_{k-n}$, $n = 1,\ldots,N$. We can easily eliminate the latter term by setting

$$
d_n := -h'_{n+\tau_d}(\mathbf{c}), \quad n = 1,\ldots,N.
\tag{4.49}
$$

This is the equation to determine the ZF DFE coefficients. Since all coefficients $h_{n+\tau_d}(\mathbf{c})$, $n = 1,\ldots,N$, depend on $\mathbf{c}$, the DFE coefficients d_n, $n = 1,\ldots,N$, do either.

Assuming that the DFE coefficients are set up according to Eq. (4.49), and that correct bit decisions are forwarded to the DFE, the effective concatenated system response becomes

$$
z_k = h'_{\tau_d}(\mathbf{c})\,b_k + \underbrace{\sum_{\substack{i=-M_c/2 \\ i\neq\left(\tau_d,\ldots,\tau_d+N\right)}}^{M_c/2+M-1} h'_i(\mathbf{c})\,b_{k+\tau_d-i}}_{\text{by DFE reduced ISI}}.
\tag{4.50}
$$

As a result of the DFE, the number of sum elements in the residual ISI term is reduced compared to Eq. (4.30). However, the residual ISI term increases if error propagation by wrong decisions fed into the DFE delay chain occurs.

Inclusion of the DFE partially changes the prerequisites to adjust the FFE. Since the concatenated channel coefficients $h'_{\tau_d+1}(\mathbf{c}),\ldots,h'_{\tau_d+N}(\mathbf{c})$ are forced to zero by the DFE, the determination procedure for the FFE coefficients does not have to take them into account and can be used to fulfill the ZF criterion for the remaining equations. Therefore, we may separate the system of equations arising from the ZF condition in Eq. (4.36),

$$
\begin{pmatrix} 0 \\ 0 \\ \vdots \\ 0 \\ 1 \\ 0 \\ \vdots \\ \vdots \\ 0 \\ 0 \end{pmatrix} \approx \left[\begin{array}{cccccc} h_{-M_c/2} & 0 & \ldots & \ldots & \ldots & 0 \\ h_{-(M_c/2-1)} & h_{-M_c/2} & 0 & \ldots & \ldots & 0 \\ \vdots & \ldots & \vdots & \ldots & \vdots & \ldots \\ h_{\tau_d-1} & \ldots & \ldots & h_{-1} & \ldots & h_{-(M-1)+\tau_d-1} \\ h_{\tau_d} & \ldots & \ldots & h_0 & \ldots & h_{-(M-1)+\tau_d} \\ h_{\tau_d+1} & \ldots & \ldots & h_1 & \ldots & h_{-(M-1)+\tau_d+1} \\ \vdots & \ldots & \vdots & \ldots & \vdots & \ldots \\ \vdots & \ldots & \vdots & \ldots & \vdots & \ldots \\ 0 & \ldots & \ldots & 0 & h_{M_c/2} & h_{M_c/2-1} \\ 0 & \ldots & \ldots & \ldots & 0 & h_{M_c/2} \end{array}\right]_{(M_c+M)\times M} \begin{pmatrix} c_0 \\ \vdots \\ c_{\tau_d} \\ \vdots \\ c_{M-1} \end{pmatrix},
$$

with the bracketed row groupings labelled $\in\mathbb{I}_{FFE}\oplus\mathbb{I}_{ISI}$, $\in\mathbb{I}_{FFE}$, $\in\mathbb{I}_{DFE}$, $\in\mathbb{I}_{FFE}\oplus\mathbb{I}_{ISI}$

$$(4.51)$$

into three disjoint sets

$$\mathbb{I}_{FFE} = \mathbb{I}\setminus(\mathbb{I}_{DFE}\cup\mathbb{I}_{ISI}),\qquad |\mathbb{I}_{FFE}| = M,\tau_d\in\mathbb{I}_{FFE}, \tag{4.52}$$

$$\mathbb{I}_{DFE} = \{\tau_d+1,\ldots,\tau_d+N\},\quad |\mathbb{I}_{DFE}| = N, \tag{4.53}$$

$$\mathbb{I}_{ISI} = \mathbb{I}\setminus(\mathbb{I}_{FFE}\cup\mathbb{I}_{DFE}),\quad |\mathbb{I}_{ISI}| = M_c-M-N. \tag{4.54}$$

$\mathbb{I}_{DFE}$ represents the rows of equations which are eliminated by the DFE. We use the remaining rows $\mathbb{I}\setminus\mathbb{I}_{DFE}$ to extract $\mathbb{I}_{FFE}$ for the determination of the FFE coefficients (cf. the procedure for the FFE). When we have a solution $\mathbf{c}$ for the FFE coefficients available, we determine the coefficients $h'_{\tau_d+1}(\mathbf{c}),\ldots,h'_{\tau_d+N}(\mathbf{c})$ of the concatenated system response using those equations belonging to the rows represented by $\mathbb{I}_{DFE}$. Then, Eq. (4.49) leads to the values for the DFE coefficients. $\mathbb{I}_{ISI}$ defines coefficients of the concatenated system response again which contribute to the residual ISI. Eq. (4.54) reveals that $|\mathbb{I}_{ISI}| = 0$ if $M+N = M_c$. In this case, the ISI term in Eq. (4.48) vanishes completely, i.e. $\rho_e(\mathbf{c}) = 0$ is the resulting peak eye distortion. We can summarize the ZF coefficient adjustment criterion by

$$\check{\mathbf{c}}_{ZF} = \arg\min_{\check{\mathbf{c}}} \rho_e(\mathbf{c},\tau_d,\mathbb{I}_{FFE},\mathbb{I}_{DFE}). \tag{4.55}$$

4.2.2.2.4 Numerical Examples

At the end of this section, the procedure of ZF coefficient adjustment shall be shortly illustrated for FFE and FFE-DFE applied to an OA-IM/DD link. The optical signal is affected by CD ($L_f = 5$ km), first-order PMD ($\Delta\tau_g = 12.5$ ps) and an ASE noise level of $\gamma_{OSNR} = 21$ dB.

The channel estimation initially assumes a channel memory of $M_c = 10$. The coefficients of the measured LLS FIR channel approximation are depicted in Fig. 4.11, and the convolution matrix is given below. Obviously, the initial assumption of $M_c = 10$ is by far sufficient to reflect the spread of ISI for the given characteristic of the OA-IM/DD link.
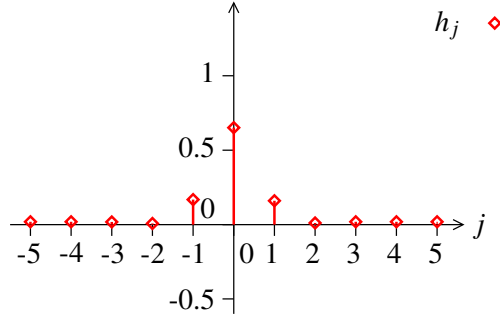

Figure 4.11: LS FIR channel approximation for $M_c = 10$ (combined CD ($L_f = 5$ km) and first-order PMD ($\Delta\tau_g = 12.5$ ps), $\gamma_{OSNR} = 21$ dB)

$$
\mathbf{H} = \begin{bmatrix}
0.018903 & 0 & 0 \\
0.0186982 & 0.018903 & 0 \\
0.0177406 & 0.0186982 & 0.018903 \\
0.00813599 & 0.0177406 & 0.0186982 \\
0.168011 & 0.00813599 & 0.0177406 \\
0.651009 & 0.168011 & 0.00813599 \\
0.160494 & 0.651009 & 0.168011 \\
0.0114613 & 0.160494 & 0.651009 \\
0.0185639 & 0.0114613 & 0.160494 \\
0.0191788 & 0.0185639 & 0.0114613 \\
0.0190456 & 0.0191788 & 0.0185639 \\
0 & 0.0190456 & 0.0191788 \\
0 & 0 & 0.0190456
\end{bmatrix}
\begin{matrix}
(i = -5) \\
(i = -4) \\
(i = -3) \\
(i = -2) \\
(i = -1) \\
(i = 0) \\
(i = 1) \\
(i = 2) \\
(i = 3) \\
(i = 4) \\
(i = 5) \\
(i = 6) \\
(i = 7)
\end{matrix} .
$$

- **ZF-FFE ($M = 3$):**

After the sweep over the possible values of the decision delay $\tau_d \in \{0, 1, 2\}$, $\tau_d = 1$ has resulted in the minimal peak eye distortion $\rho_e(\mathbf{c}) = 0.264$, and we have reached $BER = 1.49e\text{-}3$. The coefficients depicted here have been generated with the equation subset $\mathbb{I}_{FFE} = \{0, 1, 2\}$. Thus, the concatenated system response has the one at $i = 1$, i.e. $h'_1 = 1$, and the zeros at $i = 0$ and $i = 2$, i.e. $h'_0 = h'_2 = 0$, as proven by Fig. 4.12(b).

- **ZF-FFE-DFE ($M = 3$, $N = 2$):**

In this example depicted in in Figs. 4.13(a) – 4.13(c), $N = 2$ DFE coefficients have been added to the FFE with $M = 3$ coefficients. The optimal decision delay has turned out to be
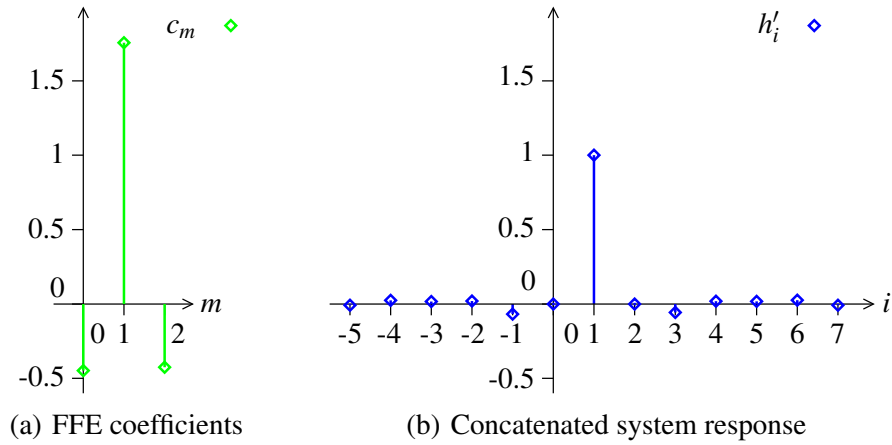
Figure 4.12: ZF-FFE example ($M = 3$)

$\tau_d = 2$ with a minimal peak eye distortion of $\rho_e(\mathbf{c}) = 0.176$ and *BER* = 4.26e-4. Compared to the FFE example, we state that the smaller peak eye distortion of the FFE-DFE also coincides with a smaller BER. The rows of the convolution matrix $\mathbf{H}$ used to calculate the FFE coefficients were $\mathbb{I}_{FFE} = \{0, 1, 2\}$ and those which are eliminated by the DFE were $\mathbb{I}_{DFE} = \{3, 4\}$. Again, we can verify that the concatenated system response has a one at $i = 2$, i.e. $h'_2 = 1$, and zeros at $i \in \mathbb{I}_{FFE} \cup \mathbb{I}_{DFE} = \{0, 1, 3, 4\}$ with $h'_0 = h'_1 = h'_3 = h'_4 = 0$.
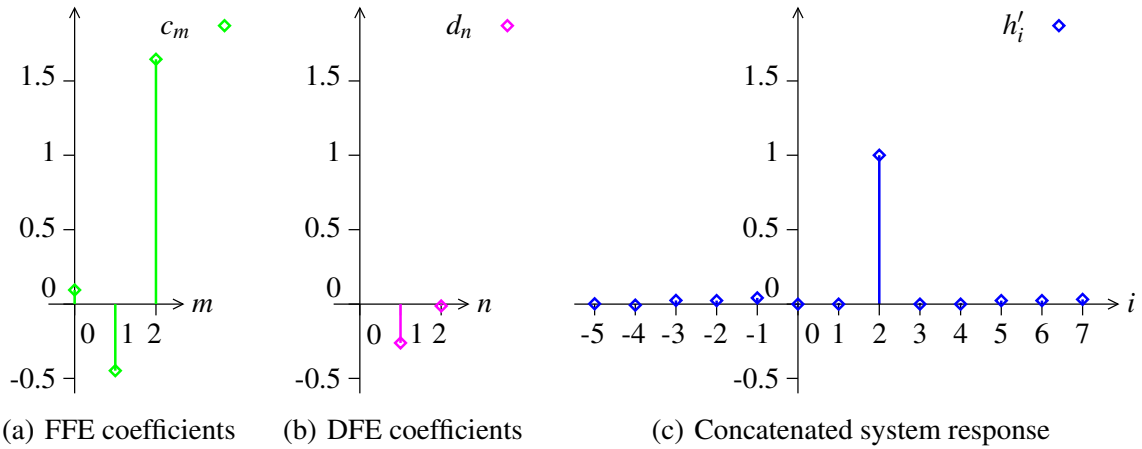

Figure 4.13: ZF-FFE-DFE example ($M = 3$, $N = 2$)

• **Misleading ZF Behavior:**

Unfortunately, the statement that a smaller peak eye distortion of the FFE-DFE also coincides with a smaller BER is not always true in general. If we have a look at the discrete-time Fourier transform [82] of the FFE defined by

$$C(j\omega) = \sum_{m=0}^{M-1} c_m e^{-j\omega m}, \quad \omega \in [-\pi, \pi), \tag{4.56}$$

and sketch its magnitude, Fig. 4.14 agrees with the results for $M = 3$ from above insofar that the magnitude at high frequencies is less for the FFE-DFE than for the pure FFE. Consequently, possible noise amplification at high frequencies, which has not been considered in the equalizer design so far, is less with the DFE and shows better BER performance therefore. However, it is also worth to take notice of the contradictory case in which a FFE-DFE shows worse BER than the FFE although it reaches less peak eye distortion as given for the second example in Fig. 4.14. It is based on a FFE with $M = 5$ and a FFE-DFE with $M = 5$ and $N = 2$. The magnitude amplification of the FFE part of the FFE-DFE at high frequencies is much higher than for the pure FFE. The worse BER performance of the FFE-DFE can be explained by the fact that amplified noise in the FFE can lead to wrong decisions, which are fed to the DFE filter and lead to further error propagation. This reveals the necessity to balance the coefficient adjustment criterion as a trade-off between deterministic signal equalization and reduction of stochastic noise influence.
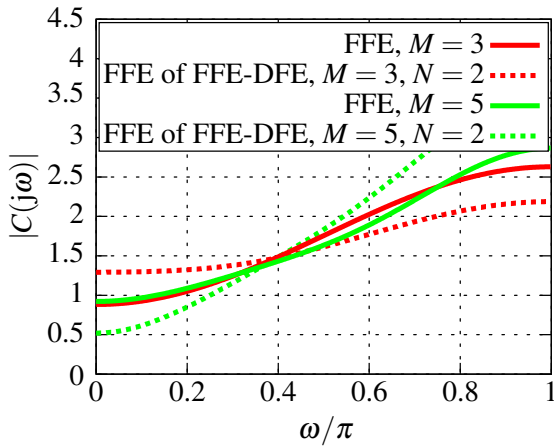

FFE-DFE	BER	$\rho_e(\mathbf{c})$	τ_d
$M = 3, N = 0$	1.49e-3	0.264	1
$M = 3, N = 2$	4.26e-4	0.176	2
$M = 5, N = 0$	1.25e-3	0.171	3
$M = 5, N = 2$	3.95e-3	0.102	3

Figure 4.14: Discrete-time Fourier transform magnitude spectra of the ZF-FFE with and without DFE (combined CD ($L_f = 5$ km) and first-order PMD ($\Delta\tau_g = 12.5$ ps), $\gamma_{OSNR} = 21$ dB)

Table 4.1: ZF-FFE-DFE performance metrics (combined CD ($L_f = 5$ km) and first-order PMD ($\Delta\tau_g = 12.5$ ps), $\gamma_{OSNR} = 21$ dB)

4.2.2.3 MMSE Criterion

The MMSE criterion for FFE-DFE adjustment is related to signal estimation from noisy input samples and can be analyzed using the *Wiener filter* theory [101]. In order to overcome the deficiencies of noise amplification within the ZF criterion, we directly employ the noisy electrical RX signal samples x_{k_1} to determine the optimal coefficients without any special channel estimation procedure.

4.2.2.3.1 Basic Theory

The starting point is the definition of a so-called error signal with

$$e_k(\check{\mathbf{c}}) = b_k - z_k = b_k - \check{\mathbf{c}}^\mathrm{T}\check{\mathbf{x}}_{k_1}. \tag{4.57}$$

This error signal measures the difference between the ideally expected signal levels and the continuously distributed output signal of the FFE-DFE as depicted in the block diagram of Fig. 4.15(a). It can be interpreted as an observer for the eye diagram quality as depicted in Fig. 4.15(b) for the noise free case. Of course, bypassing the OA-IM/DD link and having the TX bits b_k right available at the RX is a rather theoretical construct, but we will show in Ch. 5 how to circumvent this problem.
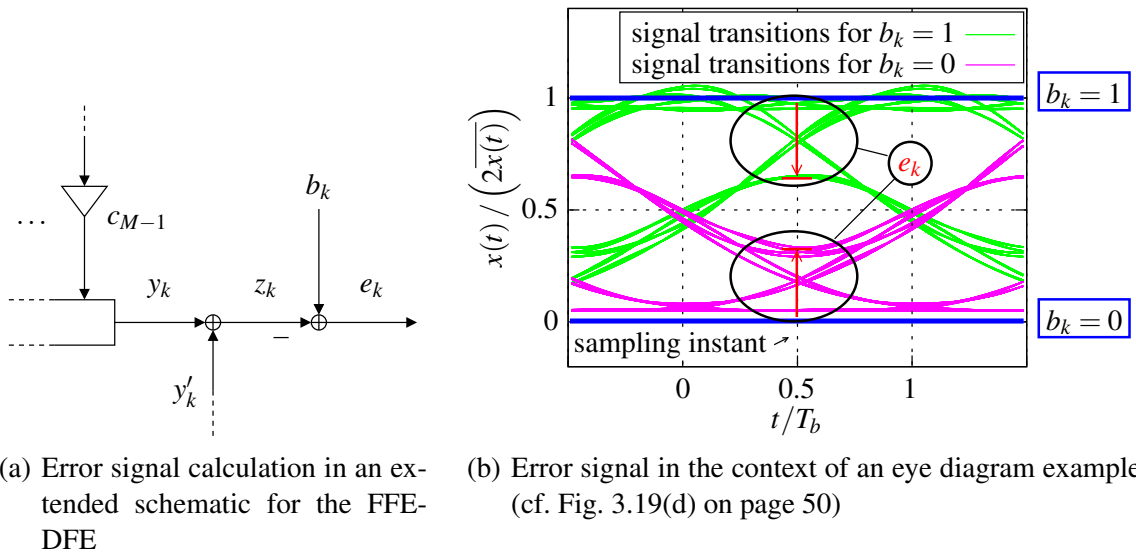

(a) Error signal calculation in an extended schematic for the FFE-DFE

(b) Error signal in the context of an eye diagram example (cf. Fig. 3.19(d) on page 50)

Figure 4.15: Illustration of the error signal definition

Using the definition of the error signal $e_k(\check{\mathbf{c}})$, we can derive a general, convex optimization function with respect to the FFE-DFE coefficient vector $\check{\mathbf{c}}$ resulting in the minimum mean $2n$-th order (MMN) error approach

$$\check{\mathbf{c}}_{MMN} = \arg\min_{\check{\mathbf{c}}} \mathsf{E}\left[\left|e_k(\check{\mathbf{c}})\right|^{2n}\right], \, n \in \mathbb{N}_1. \tag{4.58}$$

If we choose the exponential scale parameter $n = 1$, Eq. (4.58) represents the widespread mean squared error (MSE) optimization criterion used for many optimization problems in engineering. We can solve Eq. (4.58) for the optimum MMSE FFE-DFE coefficient vector $\check{\mathbf{c}}_{MMSE}$ [42, 81] in a closed form. If $n > 1$, iterative algorithms similar to the one we will present in Ch. 5 have to be applied. Applying an even multiple of the power of two to the magnitude of the error signal guarantees convexity, which leads to a unique solution. This is illustrated in Fig. 4.16 for the common MMSE approach with $n = 1$ and a FFE with $M = 2$ coefficients. More FFE coefficients straightly lead to a multidimensional convex paraboloid.
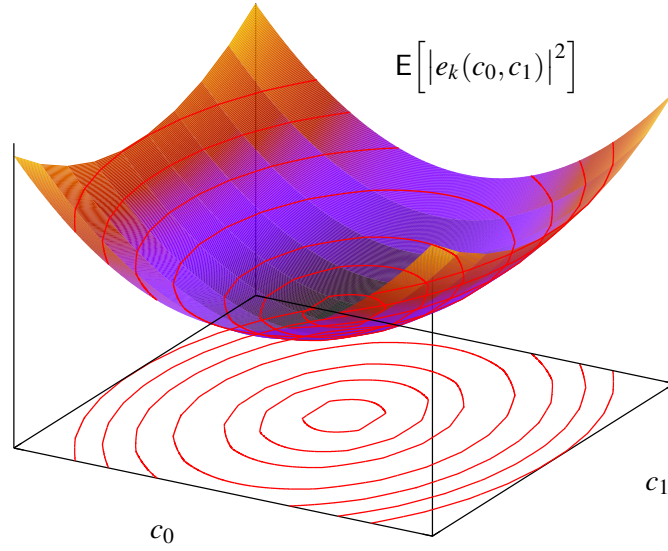
Figure 4.16: Example of the MSE surface reduced to $M = 2$ FFE coefficients

The actual procedure to determine the MMSE FFE-DFE coefficient vector $\check{\mathbf{c}}$ resembles to the LLS FIR channel estimation procedure as introduced as a prerequisite for the ZF criterion. It has already been derived in App. D. The main advancement compared to this is that we do not only perform channel estimation but channel inversion in one step. The noisy electrical RX signal samples x_{k_1} are used for the input to the yet unknown MMSE FFE-DFE filter with the signal levels of the TX bits b_k being the desired output. This relation is already incorporated in the error signal definition of Eq. (4.57). Thus, the output of the FFE-DFE approximates

$$b_k \approx \check{\mathbf{c}}^{\mathrm{T}} \check{\mathbf{x}}_{k_1} \Longleftrightarrow \arg \min_{\check{\mathbf{c}}} \mathsf{E}\left[\left| e_k(\check{\mathbf{c}}) \right|^2 \right] \tag{4.59}$$

in the MSE sense.

Concerning the implemented MSE optimization algorithm within our simulations, we assume ergodicity of the TX signal and the OA-IM/DD link. This allows us to turn the MSE coefficient optimization criterion into a LLS problem formulation with

$$\check{\mathbf{c}} = \arg \min_{\check{\mathbf{c}}} \mathsf{E}\left[\left| e_k(\check{\mathbf{c}}) \right|^2 \right] \overset{\text{ergodicity}}{=} \arg \min_{\check{\mathbf{c}}} \lim_{K_{MMSE} \to \infty} \frac{1}{K_{MMSE}} \sum_{\substack{k_1 = 0, \\ k \equiv k_1}}^{K_{MMSE}-1} \left| e_k(\check{\mathbf{c}}) \right|^2. \tag{4.60}$$

It is evident that we cannot maintain the limit operation within a computer simulation. A sufficiently high number for $K_{MMSE} \approx 1e6$ ensures a good quality estimate for $\mathsf{E}[|e_k(\check{\mathbf{c}})|^2]$. Thus, we omit taking the limit in the following derivations.

Using the error signal definition of Eq. (4.57) and the general input-output relation of the

FFE-DFE filter, we may determine the gradient vector of the MSE with respect to $\check{\mathbf{c}}$ by

$$
\frac{1}{K_{MMSE}} \nabla_{\check{\mathbf{c}}} \sum_{\substack{k_1=0, \\ k \equiv k_1}}^{K_{MMSE}-1} \left| e_k(\check{\mathbf{c}}) \right|^2 = \frac{1}{K_{MMSE}} \nabla_{\check{\mathbf{c}}} \sum_{\substack{k_1=0, \\ k \equiv k_1}}^{K_{MMSE}-1} \left| b_k - z_k \right|^2
$$

$$
= \frac{1}{K_{MMSE}} \nabla_{\check{\mathbf{c}}} \sum_{\substack{k_1=0, \\ k \equiv k_1}}^{K_{MMSE}-1} \Big| \underbrace{b_k - \check{\mathbf{c}}^{\mathsf{T}} \check{\mathbf{x}}_{k_1}}_{\in \mathbb{R}} \Big|^2
$$

$$
= \frac{1}{K_{MMSE}} \nabla_{\check{\mathbf{c}}} \sum_{\substack{k_1=0, \\ k \equiv k_1}}^{K_{MMSE}-1} \left(b_k - \check{\mathbf{c}}^{\mathsf{T}} \check{\mathbf{x}}_{k_1} \right)^2
$$

$$
= \frac{1}{K_{MMSE}} \nabla_{\check{\mathbf{c}}} \sum_{\substack{k_1=0, \\ k \equiv k_1}}^{K_{MMSE}-1} \left(b_k^2 - 2 b_k \check{\mathbf{c}}^{\mathsf{T}} \check{\mathbf{x}}_{k_1} + \underbrace{\left(\check{\mathbf{c}}^{\mathsf{T}} \check{\mathbf{x}}_{k_1} \right)^2}_{= \check{\mathbf{c}}^{\mathsf{T}} \check{\mathbf{x}}_{k_1} \check{\mathbf{x}}_{k_1}^{\mathsf{T}} \check{\mathbf{c}}} \right)
$$

$$
= \frac{1}{K_{MMSE}} \nabla_{\check{\mathbf{c}}} \sum_{\substack{k_1=0, \\ k \equiv k_1}}^{K_{MMSE}-1} b_k^2 - 2 \nabla_{\check{\mathbf{c}}} \check{\mathbf{c}}^{\mathsf{T}} \underbrace{\frac{1}{K_{MMSE}} \sum_{\substack{k_1=0, \\ k \equiv k_1}}^{K_{MMSE}-1} b_k \check{\mathbf{x}}_{k_1}}_{=: \, \mathbf{p}_{b\check{\mathbf{x}}}}
$$

$$
+ \nabla_{\check{\mathbf{c}}} \check{\mathbf{c}}^{\mathsf{T}} \underbrace{\frac{1}{K_{MMSE}} \sum_{\substack{k_1=0, \\ k \equiv k_1}}^{K_{MMSE}-1} \check{\mathbf{x}}_{k_1} \check{\mathbf{x}}_{k_1}^{\mathsf{T}} \check{\mathbf{c}}}_{=: \, \mathbf{R}_{\check{\mathbf{x}}\check{\mathbf{x}}}}
$$

$$
= 0 - 2 \mathbf{p}_{b\check{\mathbf{x}}} + 2 \mathbf{R}_{\check{\mathbf{x}}\check{\mathbf{x}}} \check{\mathbf{c}} \tag{4.61}
$$

and introduce the abbreviations $\mathbf{p}_{b\check{\mathbf{x}}}$ for the cross-correlation vector between the TX bits and the FFE-DFE input vector and $\mathbf{R}_{\check{\mathbf{x}}\check{\mathbf{x}}}$ for the autocorrelation matrix of the FFE-DFE input vector.

We obtain the *Wiener-Hopf equation* in matrix form [102] by setting this gradient to zero and get the MMSE FFE-DFE coefficients by solving

$$
\frac{1}{K_{MMSE}} \nabla_{\check{\mathbf{c}}} \sum_{\substack{k_1=0, \\ k \equiv k_1}}^{K_{MMSE}-1} \left| e_{k_1}(\check{\mathbf{c}}) \right|^2 \overset{!}{=} 0 \quad \Longleftrightarrow \quad \check{\mathbf{c}} = \mathbf{R}_{\check{\mathbf{x}}\check{\mathbf{x}}}^{-1} \mathbf{p}_{b\check{\mathbf{x}}}. \tag{4.62}
$$

Again, we evaluate Eq. (4.62) with respect to different values for the decision delay parameter τ_d to finally obtain the optimal coefficient vector $\check{\mathbf{c}}_{MMSE}$ with

$$
\check{\mathbf{c}}_{MMSE} = \arg \min_{\check{\mathbf{c}}} \mathsf{E}\left[\left| e_k(\check{\mathbf{c}}, \tau_d) \right|^2 \right]. \tag{4.63}
$$

It is worth to note that in contrast to the ZF procedure no separate treatment of the FFE and

DFE parts is required here.

4.2.2.3.2 Numerical Examples

Fig. 4.17 and Table 4.2 directly allow to compare the behavior of the MMSE coefficient adjustment with the results of the ZF criterion of Fig. 4.14 and Table 4.1. All magnitude spectra show less amplification at high frequencies, and the achieved MMSEs coincide with the BER results. This is especially true for $M = 5$, for which we have observed the deficiency of the ZF criterion, and for which the least peak eye distortion for $N = 2$ was misleading. Here, we even observe a decaying magnitude transfer characteristic for this case at high frequencies, which leads to further noise suppression. That is why the MMSE criterion generally shows better BER performance than the ZF criterion. The simulation results at the end of this chapter will point this out over a wider range of parameter sets for OA-IM/DD links.
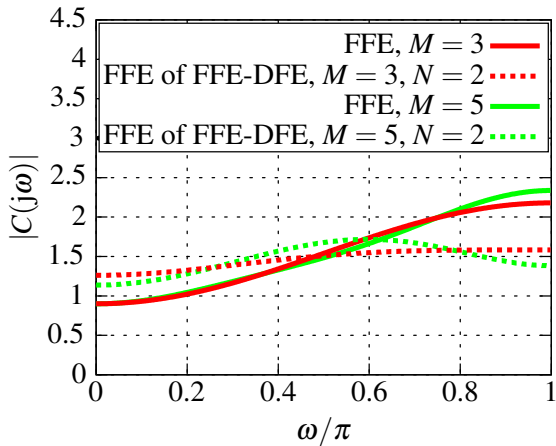

FFE-DFE	BER	$MMSE$	τ_d
$M = 3, N = 0$	1.05e-3	0.0256	1
$M = 3, N = 2$	4.24e-4	0.0225	1
$M = 5, N = 0$	9.44e-4	0.0251	3
$M = 5, N = 2$	4.03e-4	0.0219	2

Figure 4.17: Discrete-time Fourier transform magnitude spectra of the MMSE-FFE with and without DFE (combined CD ($L_f = 5$ km) and first-order PMD ($\Delta\tau_g = 12.5$ ps), $\gamma_{OSNR} = 21$ dB)

Table 4.2: MMSE-FFE-DFE performance metrics (combined CD ($L_f = 5$ km) and first-order PMD ($\Delta\tau_g = 12.5$ ps), $\gamma_{OSNR} = 21$ dB)

4.2.3 Fractionally Spaced FFE-DFE

Fractionally spaced processing applied to FFE-DFEs affects only the FFE as depicted in Fig. 4.18. We use the terminology ΔT_i-FSFFE to emphasize the difference to the ordinary T_b-spaced FFE. Assuming an equal number of coefficients for the FFE and FSFFE, the FSFFE takes less temporal spread of ISI into account than T_b-spaced processing. Obviously, this is due to the narrower temporal sample interval. We might conclude that fractionally spaced processing would require more filter coefficients to compensate for this seemingly

disadvantage. However, it will turn out that fractionally spaced processing is able to improve equalization performance for even less coefficients.
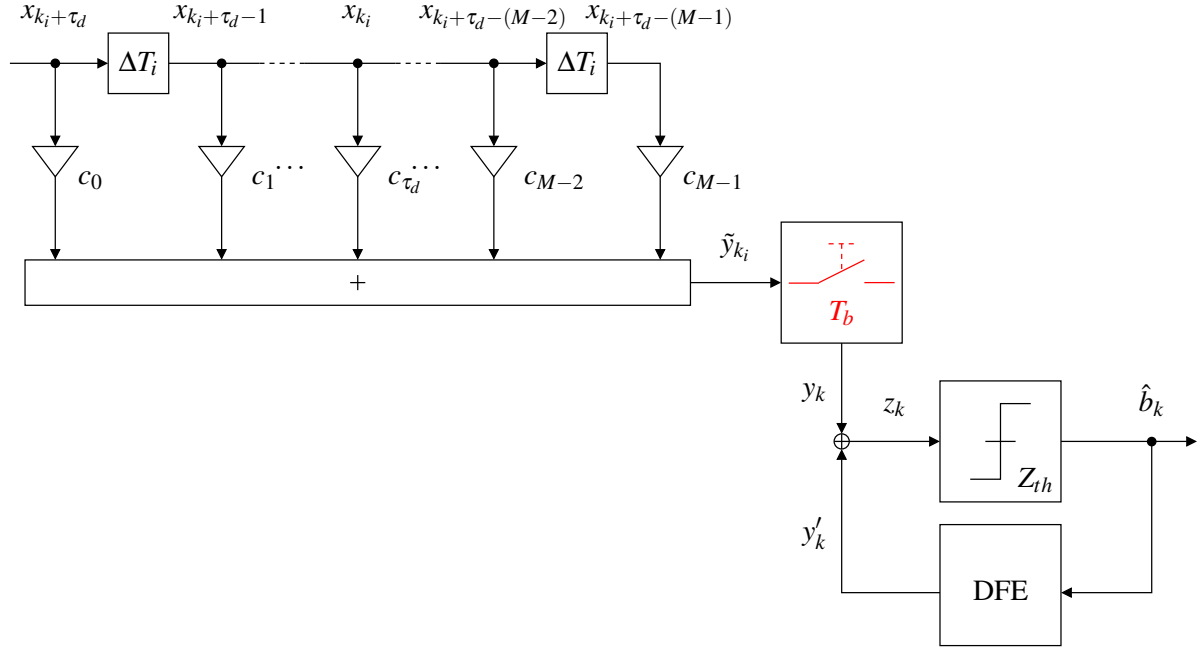

Figure 4.18: Fractionally spaced processing of the FFE-DFE (FSFFE-DFE)

Referring to Ch. 3.2.4, where we have introduced the fractionally spaced time index k_i, $i \in \mathbb{N}_1$, to indicate the fractional spacing of the EDC input samples x_{k_i} with the sample interval $\Delta T_i = \frac{T_b}{i}$, we can write for the FSFFE output

$$
\begin{aligned}
\tilde{y}_{k_i} &= \sum_{m=0}^{M-1} c_m x_{k_i + \tau_d - m} \\
&= \mathbf{c}^{\mathrm{T}} \mathbf{x}_{k_i}.
\end{aligned}
\tag{4.64}
$$

The parameter τ_d accounts for the decision delay in the fractionally spaced sample interval now and

$$
\mathbf{x}_{k_i} := \begin{pmatrix} x_{k_i + \tau_d} \\ \vdots \\ x_{k_i} \\ \vdots \\ x_{k_i + \tau_d - (M-1)} \end{pmatrix}
\tag{4.65}
$$

is the corresponding fractionally spaced input sample vector.

Since, in the end, FFE-DFE tries to recover the initial eye opening at the T_b-spaced sampling points, the FSFFE output $\tilde{y}_{k_i}$ is sampled at a rate of $1/T_b$ to get the actual FFE output y_k in

the T_b-spaced sample interval. We can express the subsampling of the FSFFE output by

$$
\begin{aligned}
y_k := \tilde{y}_{k_i} \sum_{k=-\infty}^{\infty} \delta_{k_i - ik} &= \tilde{y}_{ik} \\
&= \sum_{m=0}^{M-1} c_m x_{ik+\tau_d-m} \\
&= \mathbf{c}^{\mathrm{T}} \mathbf{x}_{ik}.
\end{aligned}
\tag{4.66}
$$

After this sampling procedure, the temporal subscript k_i turns into ik in the result of Eq. (4.66) according to the relation $k = k_i$ div i of Eq. (3.125) on page 48.

The FSFFE-DFE output is finally given by

$$
\begin{aligned}
z_k = \tilde{y}_{ik} + y_k' &= \mathbf{c}^{\mathrm{T}} \mathbf{x}_{ik} + \mathbf{d}^{\mathrm{T}} \hat{\mathbf{b}}_{k-1} \\
&= \check{\mathbf{c}}^{\mathrm{T}} \check{\mathbf{x}}_{ik}
\end{aligned}
\tag{4.67}
$$

with the definition of the overall FSFFE-DFE input sample vector

$$
\check{\mathbf{x}}_{ik} := \begin{bmatrix} \mathbf{x}_{ik} \\ \hat{\mathbf{b}}_{k-1} \end{bmatrix}.
\tag{4.68}
$$

It has quite the similar form as for the T_b-spaced case in Eq. (4.22).

In principle, we can use Eq. (4.67) to extend the already presented mathematical derivations of the MIN-BER, ZF and MMSE criteria for T_b-spaced equalization to the more general fractionally spaced method by applying subsampling to the FSFFE output. However, we will not repeat them step by step but rather indicate and discuss the benefits of fractionally spaced processing for the ZF criterion since it gives best insight into ISI removal by FFE-DFE filters.

The ZF ability of the FFE depends mainly on the relation between the channel memory M_c and the number of FFE coefficients M resulting in the system of equations

$$
\begin{pmatrix} 0 \\ \vdots \\ 0 \\ 1 \\ 0 \\ \vdots \\ 0 \end{pmatrix} = \begin{bmatrix} h_{-M_c/2} & 0 & \dots & \dots & 0 \\ h_{-(M_c/2-1)} & h_{-M_c/2} & \dots & \dots & 0 \\ \vdots & \dots & \vdots & \dots & \vdots \\ h_{\tau_d-1} & \dots & \dots & \dots & h_{-(M-1)+\tau_d-1} \\ h_{\tau_d} & \dots & \dots & \dots & h_{-(M-1)+\tau_d} \\ h_{\tau_d+1} & \dots & \dots & \dots & h_{-(M-1)+\tau_d+1} \\ \vdots & \dots & \vdots & \dots & \vdots \\ 0 & \dots & \dots & h_{M_c/2} & h_{M_c/2-1} \\ 0 & \dots & \dots & 0 & h_{M_c/2} \end{bmatrix}_{(M_c+M)\times M} \begin{pmatrix} c_0 \\ \vdots \\ c_{\tau_d} \\ \vdots \\ c_{M-1} \end{pmatrix}
$$

repeated from Eq. (4.36). As we know, there are $M_c + M$ requirements facing only M degrees of freedom, which leads to unavoidable residual peak eye distortion. We have also seen that the inclusion of a DFE improves this balance. However, we neglect the DFE for the moment because fractionally spaced processing is only relevant for the FSFFE. This is just for convenience and would not touch validity if we take the DFE into consideration again. Now, let us consider a fixed temporal spread of ISI represented by the channel memory M_c for T_b-spaced processing. Consequently, the equivalent channel memory for arbitrary fractionally spaced processing with T_b/i sample spacing becomes iM_c. If we further assume that M is equal for the FFE and the FSFFE, the corresponding systems of equations for the FSFFE is

$$
\begin{pmatrix} \vdots \\ \mathsf{X} \\ 0 \\ \mathsf{X} \\ \vdots \\ \mathsf{X} \\ 0 \\ \mathsf{X} \\ \vdots \\ \mathsf{X} \\ 1 \\ \mathsf{X} \\ \vdots \\ \mathsf{X} \\ 0 \\ \mathsf{X} \\ \vdots \\ \mathsf{X} \\ 0 \\ \mathsf{X} \\ \vdots \end{pmatrix}
=
\begin{bmatrix}
h_{-iM_c/2} & 0 & \dots & \dots & \dots & 0 \\
h_{-(iM_c/2-1)} & h_{-iM_c/2} & 0 & \dots & \dots & 0 \\
\vdots & & \dots & \vdots & \dots & \vdots & \dots \\
\vdots & & \dots & \vdots & \dots & \vdots & \dots \\
\vdots & & \dots & \vdots & \dots & \vdots & \dots \\
\vdots & & \dots & \vdots & \dots & \vdots & \dots \\
\vdots & & \dots & \vdots & \dots & \vdots & \dots \\
h_{\tau_d-1} & \dots & \dots & h_{-1} & \dots & h_{-(M-1)+\tau_d-1} \\
h_{\tau_d} & \dots & \dots & h_0 & \dots & h_{-(M-1)+\tau_d} \\
h_{\tau_d+1} & \dots & \dots & h_1 & \dots & h_{-(M-1)+\tau_d+1} \\
\vdots & & \dots & \vdots & \dots & \vdots & \dots \\
\vdots & & \dots & \vdots & \dots & \vdots & \dots \\
\vdots & & \dots & \vdots & \dots & \vdots & \dots \\
\vdots & & \dots & \vdots & \dots & \vdots & \dots \\
0 & \dots & \dots & 0 & h_{iM_c/2} & h_{iM_c/2-1} \\
0 & \dots & \dots & \dots & 0 & h_{iM_c/2}
\end{bmatrix}_{(iM_c+M)\times M}
\begin{pmatrix} c_0 \\ \vdots \\ c_{\tau_d} \\ \vdots \\ c_{M-1} \end{pmatrix}, \quad (4.69)
$$

for which we have extended the sample interval of the convolution matrix to the fractionally spaced one. The The number of equations has increased to $iM_c + M$ while the number of variables represented by the M_c FSFFE coefficients remain the same. At the first glance, this seems counterproductive. However, since the output of the FSFFE is subsampled at the T_b-spaced interval, only every i-th row of the system of equations is relevant for the minimization of the peak eye distortion while each $i - 1$ rows in between as indicated by X, which has the meaning of "don't care", may be skipped in advance. In fact, the number of

requirements has decreased by subsampling to

$$\underbrace{(M_c + M - \tau_d) \text{ div } i}_{\leq \frac{M_c + M - \tau_d}{i}} + \underbrace{\tau_d \text{ div } i}_{\leq \frac{\tau_d}{i}} + \underbrace{\tau_d \bmod i}_{< i} < \frac{M_c + M}{i} + i. \qquad (4.70)$$

The div and mod operations applied to τ_d on the left-hand side take into account that the set of remaining rows after subsampling may vary depending τ_d. If we analyze the upper bound on the number of requirement for the FSFFE, we may deduce with

$$\frac{M_c + M}{i} + i \leq M \quad \Longleftrightarrow \quad M \geq \frac{M_c + i^2}{i - 1} \qquad (4.71)$$

that the balance of requirements and degrees of freedom can be adjusted by choosing the number of FSFFE coefficients M with respect to the fractionally spaced sampling parameter i and the given channel memory M_c. If equality holds for the relation above, the system of equations has a unique solution, and the residual ISI becomes zero in this case. Otherwise, the system of equations is even over-determined. This implies that we could reduce the number of FSFFE coefficients M with no loss of ISI compensation capability until equality is given. This confirms the initial statement that a FSFFE does not necessarily have to have the fractionally spaced equivalent number of coefficients than a T_b-spaced one to achieve zero peak eye distortion. This is also one explanation for the improved ISI compensation capabilities of fractionally spaced processing, which is equivalently reviewed in frequency domain in [103].

4.3   Simulation Results and Discussion

In Chs. 2 and 3 we have identified dispersion given by CD and several types of PMD as well as ASE noise as the main contributions to signal degradation in OA-IM/DD links. Up to now we have just considered the individual parameters defining the amount of CD, PMD and ASE noise without pointing to a general framework on how to evaluate their influence on OA-IM/DD link reliability in a joint manner. Eye diagrams can give us a good impression about the effect of different kinds of ISI on the noise free analog electrical RX signal. The vertical and horizontal eye openings are first indications on the noise and sampling phase sensitivity of the system. However, they still lack of the inclusion of random noise. If the noise process was AWGN, we could apply the principle of superposition to the eye diagram and noise and determine a worst-case estimation for the BER using commonly known formulas which are based on Q-functions and effective SNRs [42, 104]. Q-factor measurements use these relations as an AWGN approximation for OA-IM/DD links [63, 64, 66]. Actually, OA-IM/DD links suffer from signal-dependent ASE noise after direct detection. Beside BER vs. OSNR plots for distinct parameter sets with constant CD and PMD, a common means for illustrating both, the effect of varying the amount of ISI with different CD and/or PMD

parameters and the randomness of signal-dependent ASE noise, is favorable. Hence, we take the BER vs. OSNR plots for each CD and/or PMD characteristic of the OA-IM/DD link and extract the *required* OSNR at a certain BER level of interest. In general, a BER of 1e-3 before FEC decoding often serves as this reference level because appropriate FEC codes are quite powerful to close the gap to a BER of 1e-12 required in reliable video transmission for example. Thus, the collected results let us illustrate the *required* OSNR @ *BER* = 1e-3 for the predominant dispersion effect. In the case of CD, the abscissa is labeled by the corresponding CD value r_D. If we consider first-order PMD as the only source of ISI, we plot the required OSNR vs. DGD value $\Delta\tau_g$. This kind of illustration also allows us to derive the necessary OSNR budget for temporarily varying PMD if we consider a certain DGD as upper tolerance limit. As a third case, we consider a combination of CD and first-order PMD. Both physical quantities, the CD value r_D and the DGD value $\Delta\tau_g$, actually originate from the characteristic CD and PMD dispersion coefficients, D_λ and τ_{PMD}, respectively, and the length L_f of the SSMF. Using this length dependence and recalling Eq. (3.74) on page 32 and Eqs. (3.92) – (3.94) on page 39, we can consequently express the mean DGD as a function of the CD value with

$$\mathsf{E}\big[\Delta\tau_g\big] = 0.921 \cdot \tau_{PMD} \sqrt{L_f}$$
$$\stackrel{(3.74)}{=} 0.921 \cdot \tau_{PMD} \sqrt{\frac{r_D}{D_\lambda}}. \tag{4.72}$$

Since PMD is a stochastic process, and the instantaneous DGD may vary with time and frequency, we impose an additional worst case assumption and require that an OA-IM/DD link has to be capable of handling at least three times its PMD value as already discussed in Ch. 3.2.2.2.3. Therefore, the actual value of the DGD within our combined CD and first-order PMD simulations has been set to

$$\Delta\tau_{g,max} := 3\,\mathsf{E}\big[\Delta\tau_g\big] = 3 \cdot 0.921 \cdot \tau_{PMD} \sqrt{\frac{r_D}{D_\lambda}}. \tag{4.73}$$

We place this worst case assumption on the DGD value right below the corresponding CD value of the abscissa labels as exemplified in Figs. 4.19(a) and 4.19(b).

The created plots for the required OSNR @ BER 1e-3 vs. CD, first-order PMD or combined CD and fist-order PMD give rise to several explanations and comparisons as indicated by the plotted curves and the attached points in Fig. 4.19(a) and 4.19(b).

If A is the reference point on the straight-lined reference curve in Fig. 4.19(a), we can evaluate and compare it to other simulation results represented by the dashed curves

- along the horizontal direction, which defines the lines of constant required OSNR and allows us to draw conclusions about dispersion tolerance improvement or degradation. For example, the green dashed curve with its intersection point B shows more dispersion tolerance and is an example of superior link dispersion margin for a given OSNR.
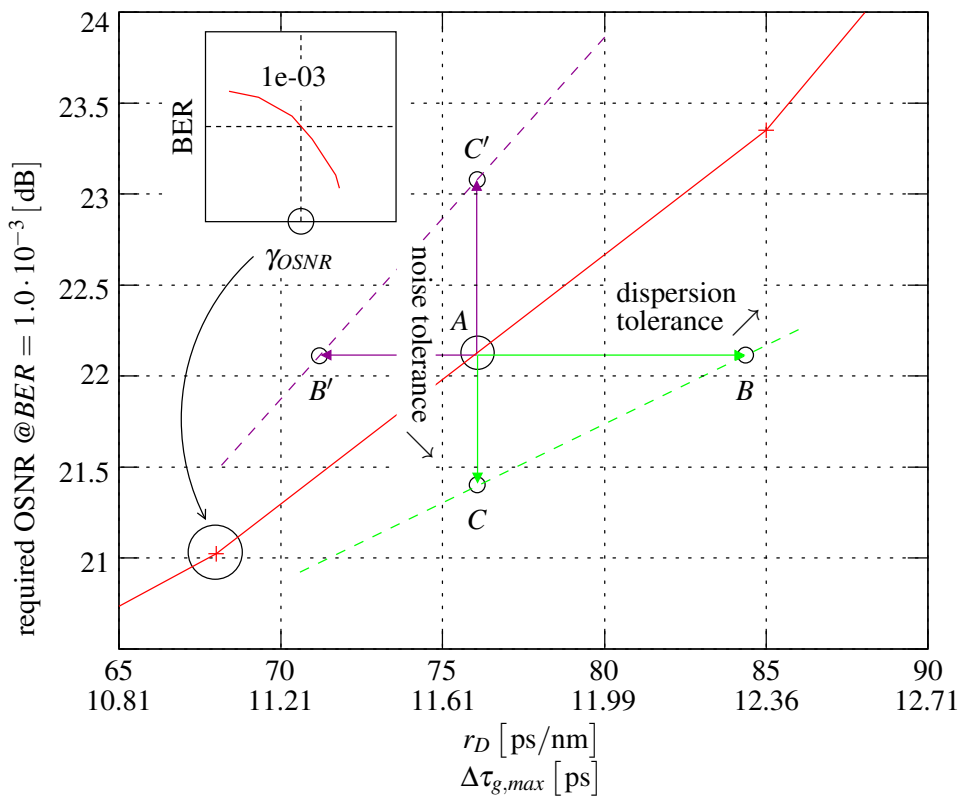
(a) Required OSNR plot vs. combined CD and first-order PMD
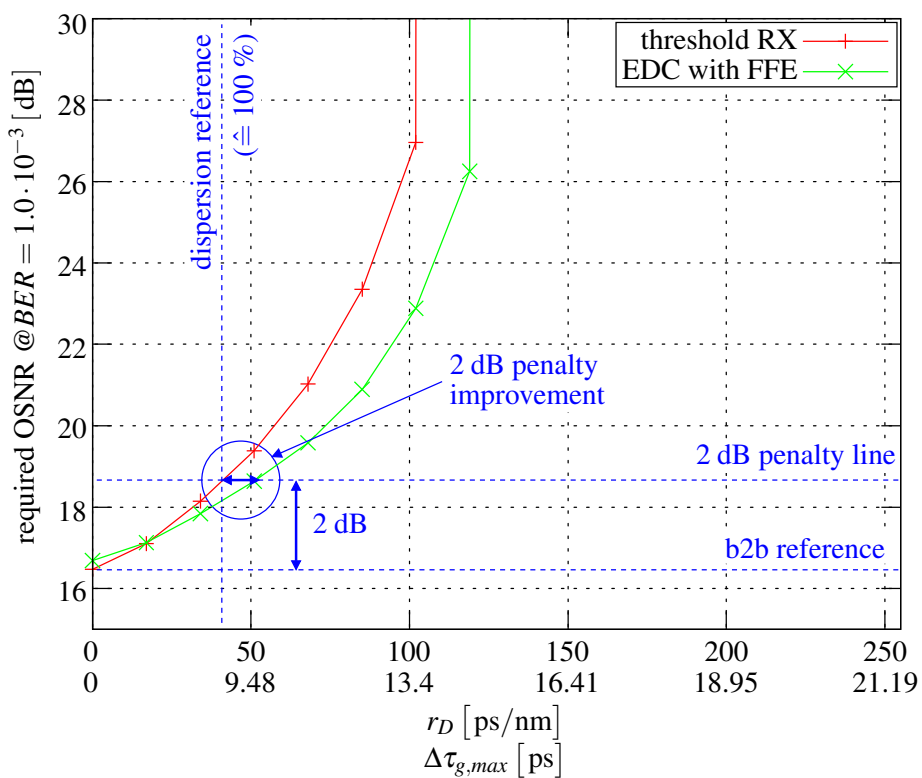
(b) Illustration of 2 dB penalty improvement benchmarking

Figure 4.19: Introduction to required OSNR vs. CD and first-order PMD plots and 2 dB penalty improvement benchmarking

The purple one with intersection point B' represents worse dispersion tolerance compared to the straight-lined reference curve and is an example of minor link dispersion margin for a given OSNR. The amount of improvement or degradation is often given in percentages with respect to the reference point A,

- along the vertical direction, which defines the lines of constant dispersion effects and allows us to draw conclusions about noise tolerance improvement or degradation. The green dashed curve with its intersection point C shows more noise tolerance and is an example of superior noise margin for given dispersion effects. The purple one with intersection point C' represents worse dispersion tolerance compared to the green reference curve and is an example of minor noise margin for given dispersion effects,

- along the diagonal direction from upper left to lower right, which gives us a rough impression on the general dispersion and noise related system behavior ranging from worse in the upper left to improved in the lower right corner.

The reference point A is normally set to the required OSNR of the b2b setup with a simple, optimized threshold RX, i.e. $L_f = 0$ km and, consequently, $r_D = 0$ ps/nm and $\Delta\tau_g = 0$ ps. A commonly applied benchmark to compare different RX architectures and/or EDC methods is the so-called *2 dB penalty improvement* given in percent. Fig. 4.19(b) illustrates this benchmarking procedure. It expresses the dispersion tolerance improvement at an excess penalty level of 2 dB with respect to the b2b setup with simple threshold RX. The intersection point of the 2 dB penalty line with the threshold RX curve marks the 100 % dispersion reference. We relate the abscissa values of the intersection points of other curves with the 2 dB penalty line showing $100 \pm x$ % to this dispersion reference. The tolerance improvement is just given by this excess percentage $\pm x$ %. It is worth to note at this point that also other than 2 dB for the penalty value are in use, and that the 2 dB penalty benchmarking technique might be misleading since it does not necessarily allow to interpret the relative behavior if we operate the OA-IM/DD link far away from it, i.e. at much shorter or longer distances.

Beside this major kind of plots, which reflect the total system behavior, we still come back to eye diagram considerations if appropriate. Since we principally examine discrete-time equalization methods, we have only the discrete-time output available. Thus, we have to replace the ordinary eye diagram by an almost sampled version known as *scatter plot*. A scatter plot comprises all possible discrete-time sample values and marks them with respect to the transmitted reference levels. This is $b_k = 0$ and $b_k = 1$ in our case. The minimal distance between the two sample groups indicate the noise tolerance like the vertical eye opening for a continuous-time eye diagram. We have provided an example of a scatter plot which contains the electrical RX signal samples x_{k_1} in Fig. 4.20 along with the eye diagram of the analog electrical RX signal $x(t)$ as a reference. A wide grey line indicates the minimal distance between the two sample groups.
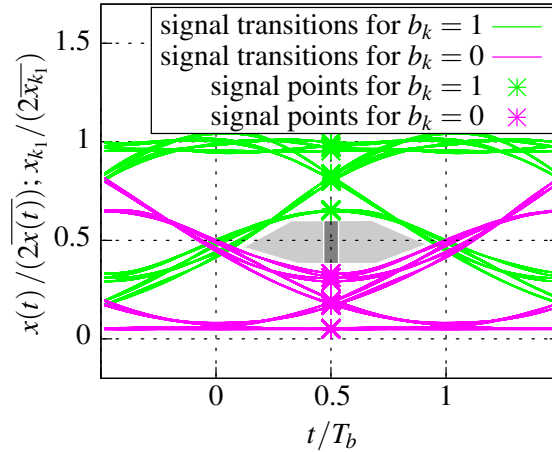
Figure 4.20: Example of a scatter plot

The following discussion of the simulation results obtained for the previously described discrete-time FFE-DFE EDC methods not only addresses the general system behavior but also implementation feasibility at very high data rates in particular. That is why we have not intentionally sought for the absolute optimum but for the least complex FFE-DFEs still providing acceptable EDC performance. Consequently, we have organized the results in a proper manner:

- With special focus on the complexity aspect, the results on the optimal low-complexity number of FFE-DFE coefficients are presented first. They have been generated for FFE-DFEs as well as ΔT_2-FSFFE-DFEs using the MMSE criterion since it has most relevance for practical implementation later on.

- A further section deals with the suitability of the MMSE criterion for OA-IM/DD links.

- Then, based on the initial results, a further subsection compares T_b- and ΔT_2-spaced sample processing. We will also have a look on optimal sampling phase adjustment there.

- Finally, we classify the EDC performance of FFE-DFE and ΔT_2-FSFFE-DFE EDC by comparing them to the simple threshold RX and the MLSE-VE. The latter shall be the predominant EDC method we benchmark against in this thesis.

4.3.1 Low-Complexity FFE-DFE Structure Optimization

4.3.1.1 FFE

Figs. 4.21 – 4.23 show simulation results for FFEs with different number of coefficients. The special case of $M = 1$ is equivalent to the simple threshold detection system and is included to give a first impression on the general improvement using a FFE. A separate consideration of CD and first-order PMD as in Figs. 4.21 and 4.22 reveals that increasing the number of coefficients above $M = 5$ does not provide any significant improvement. More coefficients only take little effect for higher CD or DGD values. This small performance gain is disproportionate to the additionally required implementation efforts. A further similarity in the CD and PMD behavior of a FFE is that both curves resemble some kind of hyperbola within the simulated parameter range. At distinct higher CD and DGD values, a pole-like behavior of the curves occurs. In case of CD, this pole is approximately at $r_D = 120$ ps/nm, which is equivalent to around $7 - 8$ km of SSMF. Any FFE with $M \leq 20$ incorporating the special case of simple threshold RX systems with $M = 1$ is not able to provide adequate performance beyond this pole with $BER \leq$ 1e-3. The required OSNR goes to infinity proving that the eye is almost closed. The pole for first-order PMD behavior lies between 20 ps and 25 ps since the gross bit rate of $R_b = 42.7$ Gbit/s is equivalent to a bit interval of $T_b = 23.42$ ps. The location of this pole is explained by the discussed nature of first-order PMD in Chs. 3.2.2.2.1 and 3.3.1. If the DGD approaches $\Delta\tau_g = T_b$, the eye is closed. Moreover, the effective first-order PMD transfer function represented by Eq. (3.87) on page 38 has a zero at $f = 1/(2T_b)$. As known from theory, a zero in a transfer function cannot be compensated by an inverse linear equalization filter since infinite gain would be required at the frequency of the zero. Beyond the pole near $\Delta\tau_g = T_b$, we observe the same behavior as for CD beyond its pole. No FFE with $M \leq 20$ is capable to provide a BER of 1e-3 with finite OSNR. Since we intend to operate any FFE on a 42.7 Gbit/s input signal, reasonable implementations should provide $M < 10$. An FFE can consequently support only short-haul OA-IM/DD links with $L_f \approx 7 - 8$ km of uncompensated SSMF.

Finally, Fig. 4.23 shows the FFE performance for the combined effect of CD and first-order PMD according the OA-IM/DD link parameters explained at the beginning of this chapter. In principle, the resulting shapes of the curves explain themselves from the separate considerations in Figs. 4.21 and 4.22. All curves rise steeper due to increased ISI, i.e. we require larger OSNR values to reach a BER of 1e-3. Interestingly, the location of the pole differs for the simple threshold RX system and the ones equipped with a FFE. For the first case, the pole is located at $r_D \approx 100$ ps/nm and $\Delta\tau_{g,max} \approx 13.4$ ps, which corresponds to $L_f \approx 6$ km, whereas for the latter ones, we observe $r_D \approx 120$ ps/nm and $\Delta\tau_{g,max} \approx 14.7$ ps with $L_f \approx 7$ km. Thus, EDC by means of a FFE effectively allows to operate an OA-IM/DD link in a region where it would fail otherwise. Another important finding is that the number of necessary coefficients can be kept at $M = 5$ for the combined dispersion effects. An increase to $M = 7$ does only provide slight improvement near the pole region.
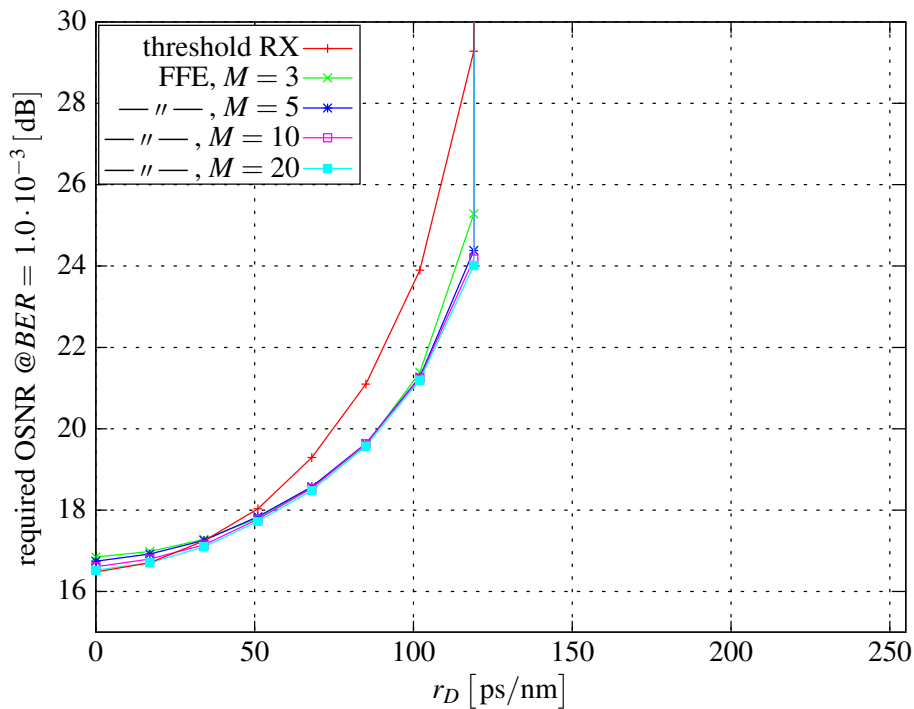
Figure 4.21: Optimal number of FFE coefficients for CD (based on MMSE adjustment)
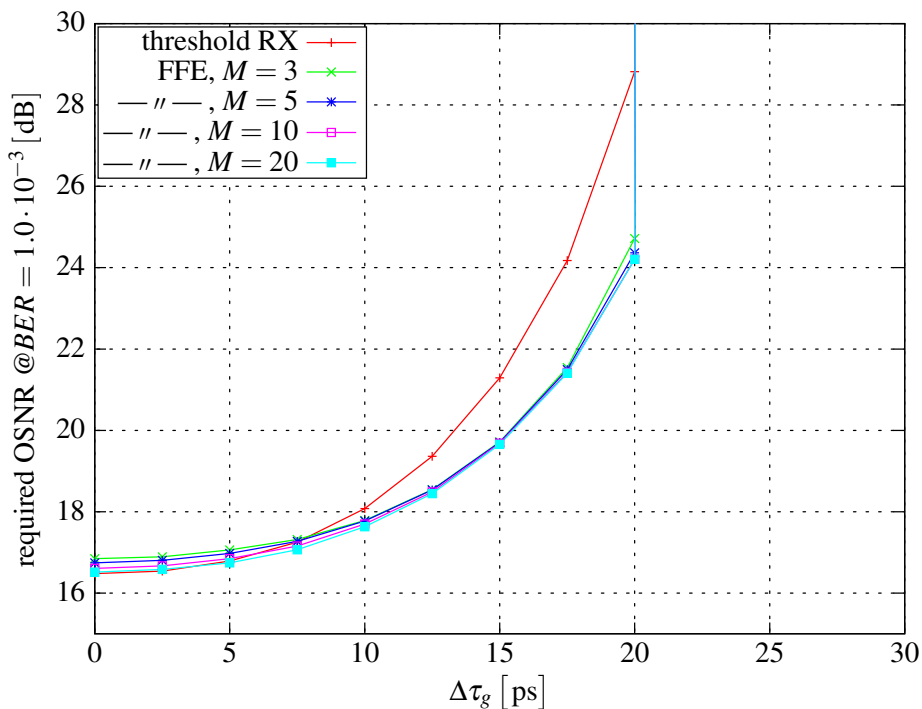

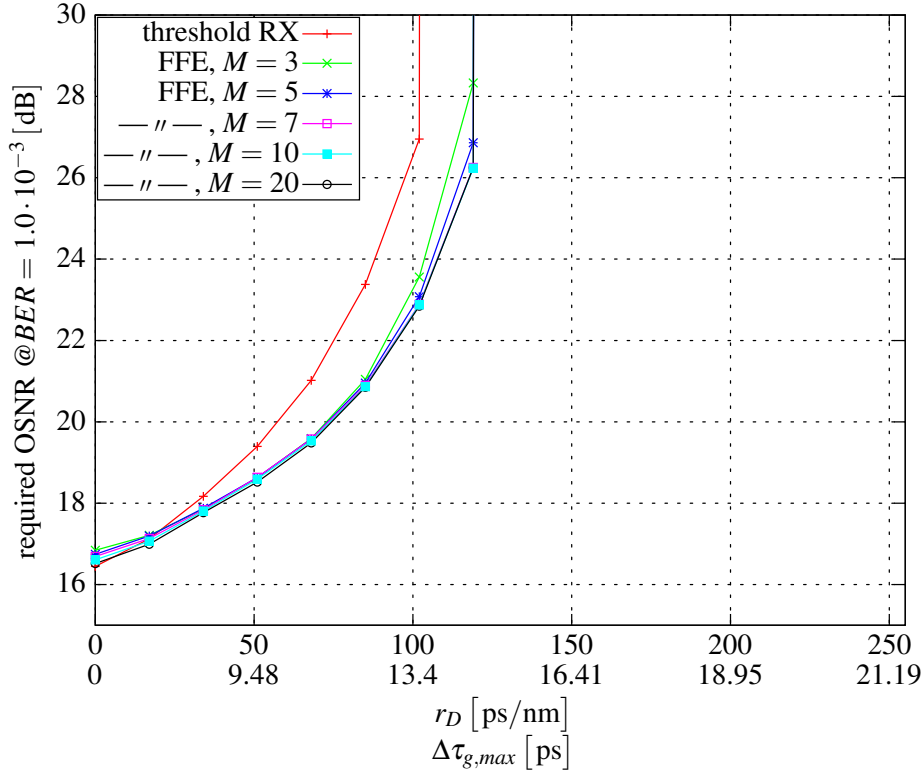**Figure 4.22:** Optimal number of FFE coefficients for first-order PMD (based on MMSE adjustment)

Figure 4.23: Optimal number of FFE coefficients for combined CD and first-order PMD (based on MMSE adjustment)

4.3.1.2 FFE-DFE

Fig. 4.24 contains the obtained results for an OA-IM/DD link which is affected by CD. Generally, we observe an almost equal performance of all simulated FFE-DFEs up to a CD value of about $r_D = 120$ ps/nm. Consequently, the implementation complexity remains quite manageable with $M = 2$ or 3 and $N = 1$ for the short range distance of $L_f \approx 7 - 8$ km. Beyond this range, the behavior is quite different. We recognize an improved performance for $M = 3, 5$ or 10 if we increase the number of DFE coefficients from $N = 1$ to 3. Compared to the FFE case, additional DFE coefficients with $N \geq 3$ are able to compensate the pole-like behavior known from Figs. 4.21 – 4.23. The further step to $N = 5$ does not provide significant changes for all plotted FFE parts. If we keep the number of DFE coefficients constant, a comparison of the curves for $M = 3, 5$ or 10 reveals that an increased number of FFE coefficients becomes more significant beyond $r_D = 120$ ps/nm. This finding is also emphasized by the large gap to the simulation results for $M = 20$ and $N = 1$ or 3. The difference between $N = 3$ and 5 is less distinctive. As a rule of thumb we can summarize that an increased number of DFE coefficients up to $N = 3$ only takes effect with a further increase in the number of FFE coefficients for larger CD values.

The simulation results obtained for first-order PMD in Fig. 4.25 are more uniform than those obtained for CD. If $\Delta\tau_g < T_b$, i.e. $\Delta\tau_g < 23.4$ ps for $R_b = 42.7$ Gbit/s, $M = 2, 3$ or 5 FFE coefficients and $N = 1$ DFE coefficient are sufficient. For $\Delta\tau_g > T_b$, a DFE with $N \geq 3$ is able
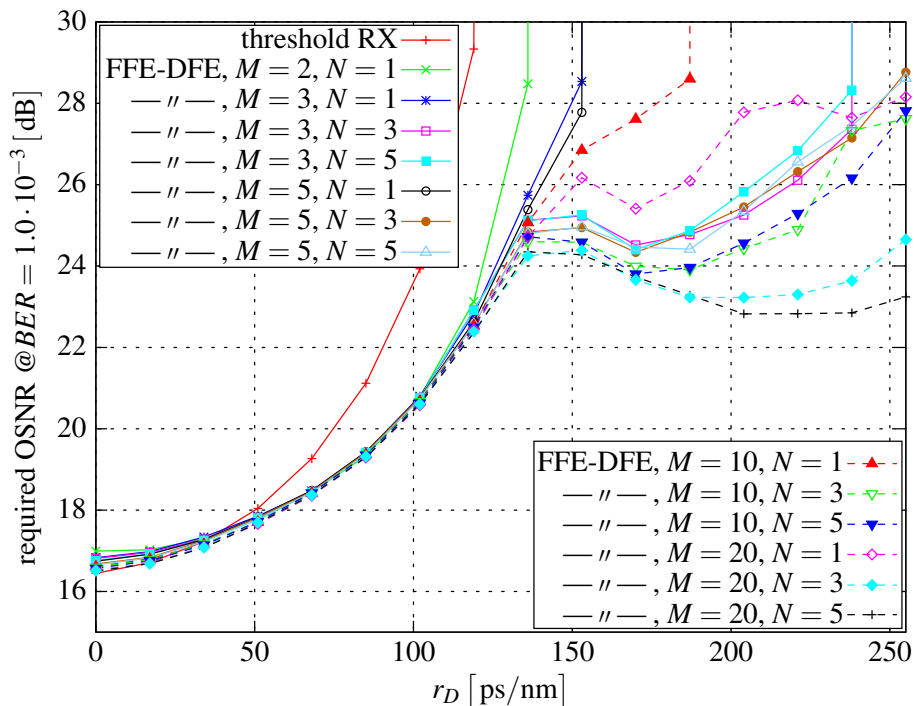
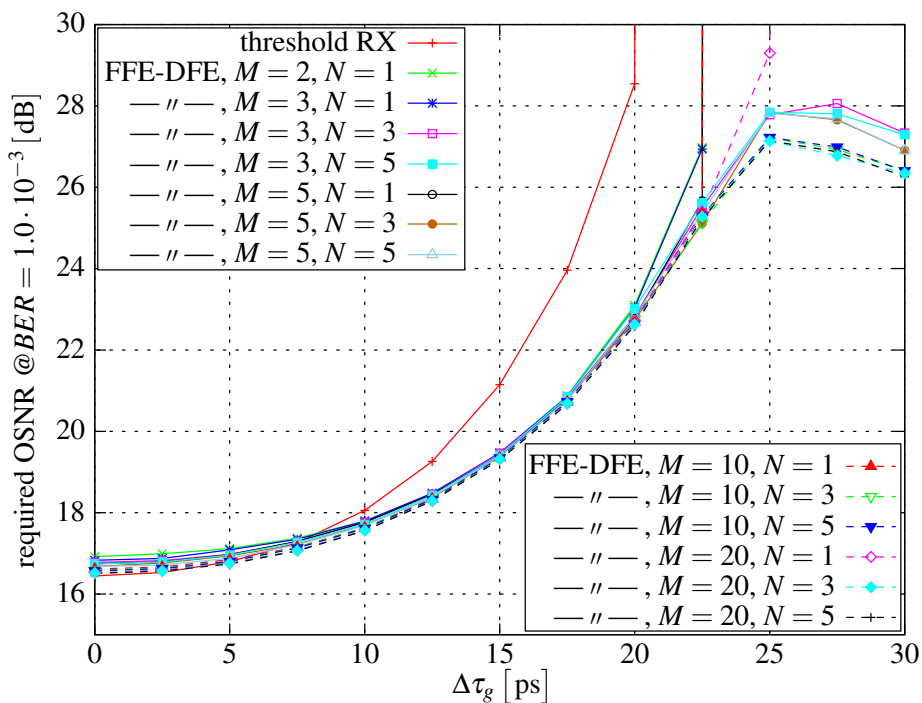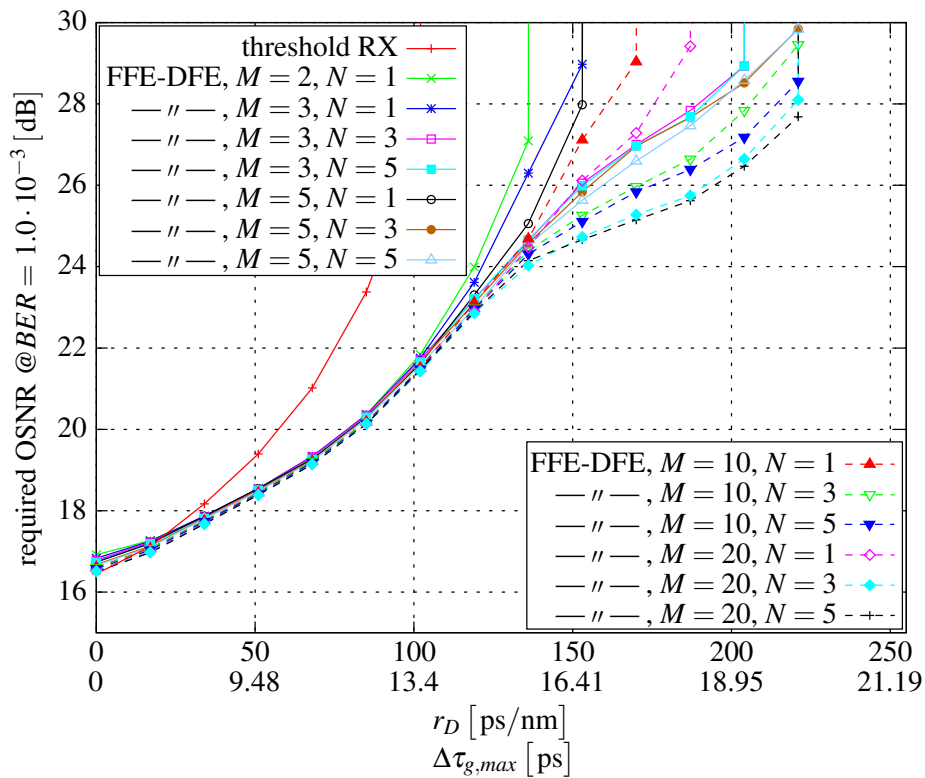**Figure 4.24:** Optimal number of FFE-DFE coefficients for CD (based on MMSE adjustment)

Figure 4.25: Optimal number of FFE-DFE coefficients for first-order PMD (based on MMSE adjustment)

to break up the pole-like behavior of the FFEs. The performance improvement from $N = 3$ to $N = 5$ is almost negligible for $M = 20$. The number of FFE coefficients has more impact for larger DGD values.

The combined dispersion effects of CD and first-order PMD are depicted in Fig. 4.26. As we expect, the general performance gets worse due to increased ISI. At least for the simulated FFE-DFEs depicted in the figure, this is the reason for the recurrence of the pole-like curve shapes. The location of the poles is different for each filter configuration. Nevertheless, the one with $M = 3$ and $N = 1$ is still competitive for short range distances. The qualitative behavior for varying the DFE from $N = 3$ to $N = 5$ resembles that of first-order PMD in Fig. 4.25, i.e. it has almost no effect.

Figure 4.26: Optimal number of FFE-DFE coefficients for combined CD and first-order PMD (based on MMSE adjustment)

4.3.1.3 ΔT_2-**FSFFE**

Fig. 4.27 shows that $M = 10$ fractionally spaced coefficients deliver sufficient EDC performance against CD for short range distances of around $L_f \approx 7 - 8$ km with $r_D \leq 120$ ps/nm. This coincides to the equivalent number of $M = 5$ T_b-spaced coefficients we have found to be appropriate for T_b-spaced processing. The hyperbolic shape of the curves with a pole is still present, but the ΔT_2-spaced processing of the ΔT_2-FSFFE seems to be able to recover from infinite required OSNR to finite results for $BER = $ 1e-3 again. After the pole the number
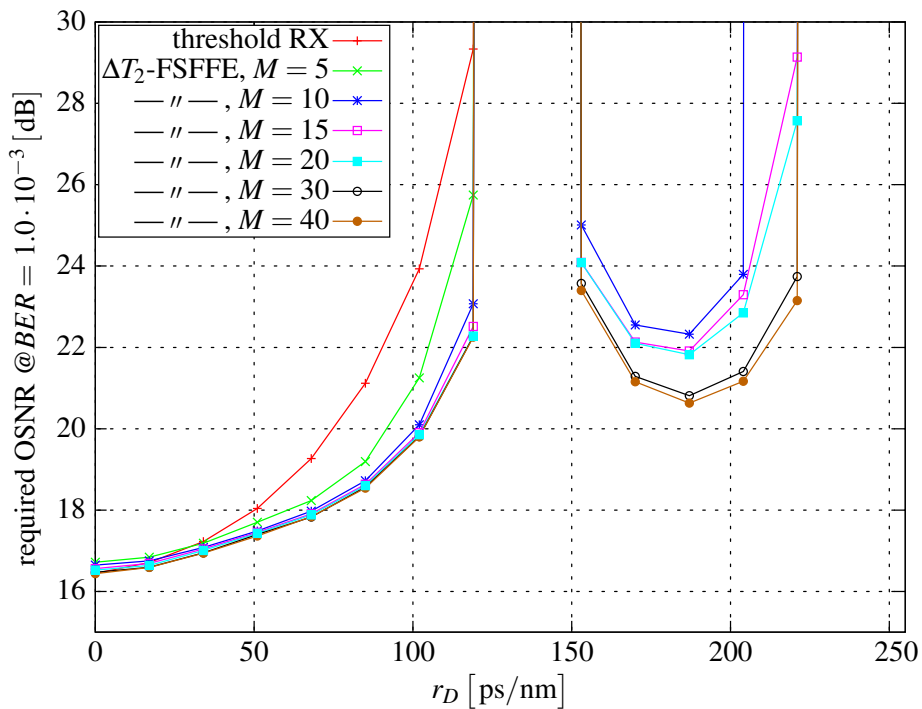
Figure 4.27: Optimal number of ΔT_2-FSFFE coefficients for CD (based on MMSE adjustment)
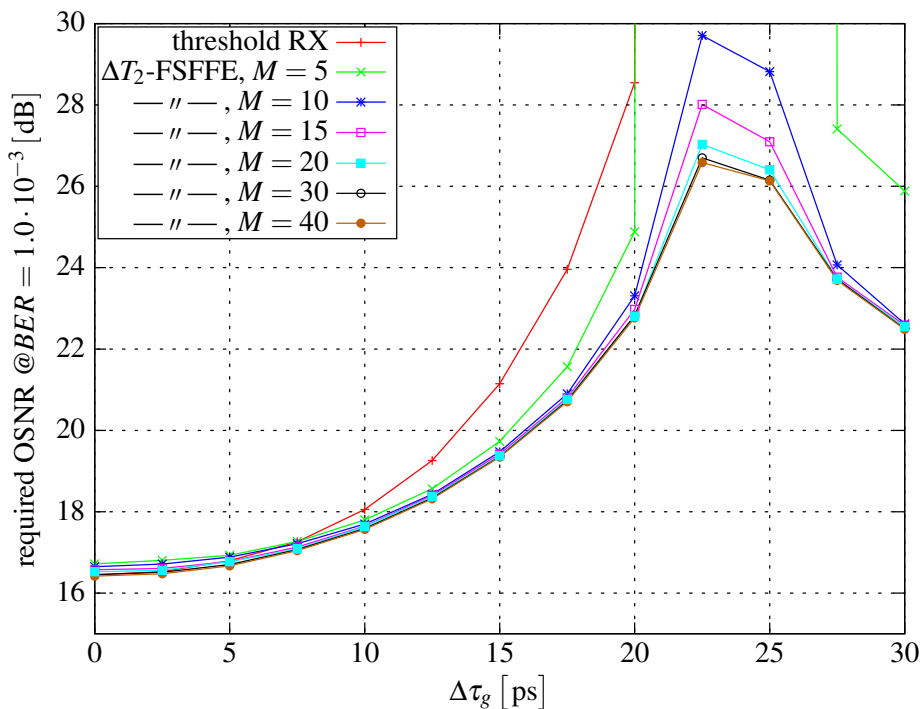

Figure 4.28: Optimal number of ΔT_2-FSFFE coefficients for first-order PMD (based on MMSE adjustment)

of coefficients seems to have more influence on the performance since the required OSNR differs about $1.5 - 2$ dB between the ΔT_2-FSFFE with $M = 10$ and $M = 30$ or 40. A second pole, whose location seems to depend on the number of coefficients, arises after this second region. This is quite different from the T_b-spaced behavior.

Concerning first-order PMD in Fig. 4.28, we can state that the performance of the different FSFFEs is almost the same for $M > 5$ and $\Delta \tau_g < T_b$, which has been the location of the pole for the T_b-spaced processing results. However, fractionally spaced processing overcomes this pole region for $M \geq 10$. The doubled temporal sampling resolution together with the signal dependence of the ASE noise beat term in the electrical RX signal improve the ability to distinguish the signal transitions and reduce the ambiguity introduced in the eye diagram for $\Delta \tau_g = T_b$ as already explained earlier in Chs. 3.2.2.2.1 and 3.3.1.

Fig. 4.29 proceeds with the combined effect of CD and first-order PMD. Besides the worse performance due to increased ISI, these curves are clearly dominated by the CD performance of Fig. 4.27. The ΔT_2-FSFFE with $M = 10$ is still the best trade-off between performance and implementation complexity.
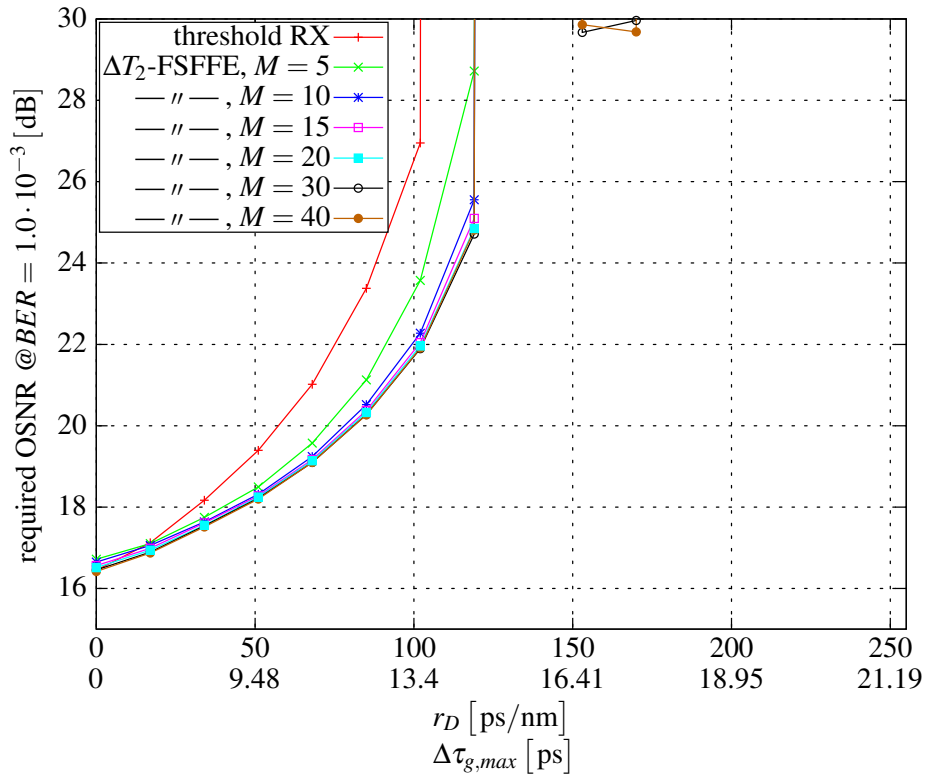

Figure 4.29: Optimal number of ΔT_2-FSFFE coefficients for combined CD and first-order PMD (based on MMSE adjustment)

4.3.1.4 ΔT_2-**FSFFE-DFE**

The CD results for the FSFFE-DFEs in Fig. 4.30 reveal that the hyperbolic shape of the curves has almost disappeared. At least, the location of the poles known from T_b-spaced processing has shifted for $N = 1$ and is not present in the given simulation range for $N \geq 3$. Within the short range SSMF dispersion region up to $L_f \approx 7 - 8$ km with $r_D \approx 120$ ps/nm, all FSFFE-DFEs perform almost equally. The additional DFE even allows to reduce the number of FSFFE coefficients from $M = 10$ for the FSFFE to $M = 5$ for the FSFFE-DFE. Thus, the DFE leads to a major reduction of computational complexity in the FSFFE filter. Increased effects of ISI after this first region leads to more diversification of the results. They clearly indicate that it is not worth to increase the number of DFE coefficients from $N = 3$ to 5. We can identify more potential in the increase of the FSFFE coefficients as plotted for $M = 5, 10, 20$ up to 40. Although complexity becomes infeasible for even more FSFFE coefficients, we can deduce that system performance would benefit from further increase.

Fig. 4.31 also emphasizes the trend of the CD results for first-order PMD. We cannot observe a pole anymore. Compared to the CD results, the difference between the various FSFFE-DFEs is not really pronounced. Even for $\Delta \tau_g > T_b$, increasing the number of coefficients in the FSFFE part from $M = 10$ to 40 does not show significant effects.

In Fig. 4.32, all FSFFE-DFEs show nearly the same performance for combined CD and first-order PMD for short-haul OA-IM/DD links. The previously described qualitative behavior of CD and first-order PMD are both present in the curves of Fig. 4.32. The poles for $N = 1$ resembles the CD curves. DFEs with $N > 1$ are not worth to spend implementation effort. The first-order PMD behavior dominates beyond $r_D \approx 150$ ps/nm and $\Delta \tau_{g,max} \approx 16.5$ ps since increasing the number of FSFFE coefficients has hardly a positive effect on the performance.

4.3.1.5 Summary and Conclusion

Table 4.3 gives a concise summary of the results for the number of FFE, FFE-DFE, ΔT_2-FSFFE and ΔT_2FSFFE-DFE coefficients with respect to the requirements of sufficient EDC performance in short-haul OA-IM/DD links ($D_\lambda = 17$ ps/(nm·km), $\tau_{PMD} = 2$ ps/$\sqrt{km}$, $L_f \approx 7 - 8$ km) and low implementation complexity.

	FFE	FFE-DFE	ΔT_2-FSFFE	ΔT_2-FSFFE-DFE
M	5	3	10	5
N	0	1	0	1

Table 4.3: Optimal numbers of coefficients for low-complexity FFE-DFEs and FSFFE-DFEs
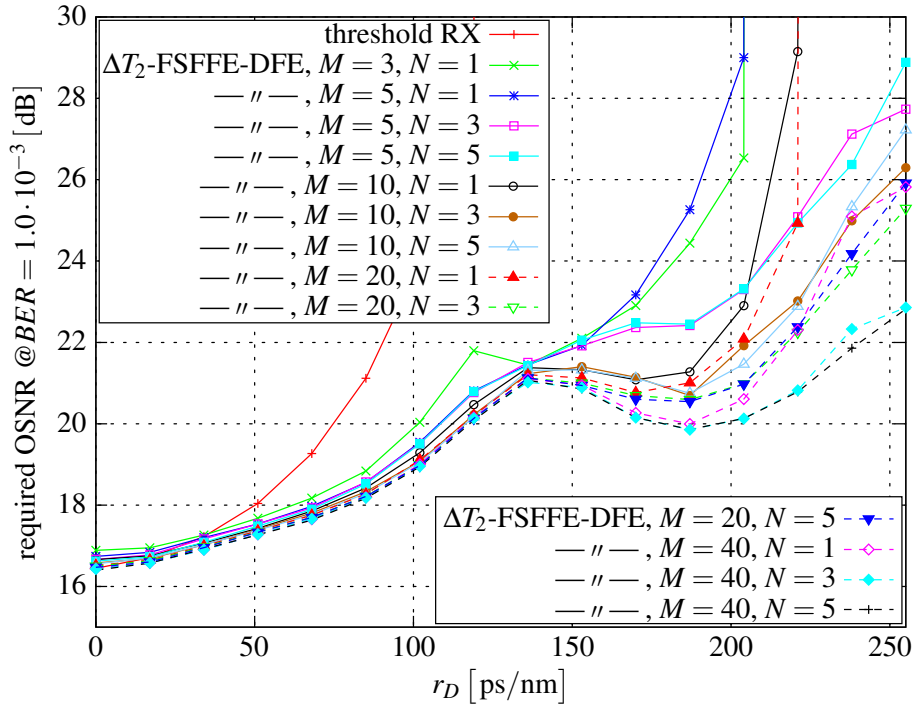
Figure 4.30: Optimal number of ΔT_2-FSFFE-DFE coefficients for CD (based on MMSE adjustment)
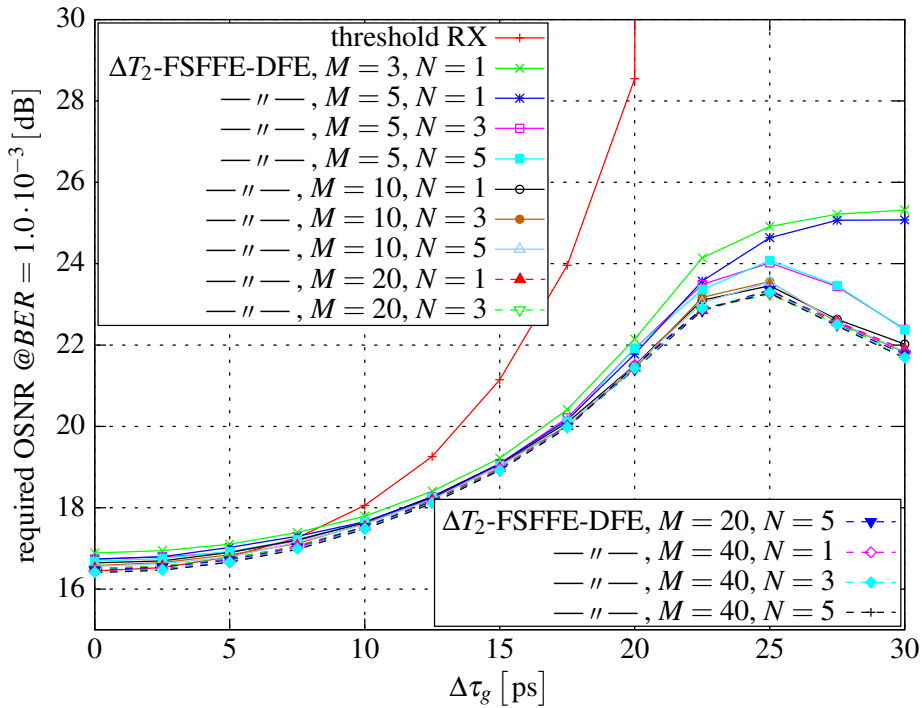

Figure 4.31: Optimal number of ΔT_2-FSFFE-DFE coefficients for first-order PMD (based on MMSE adjustment)
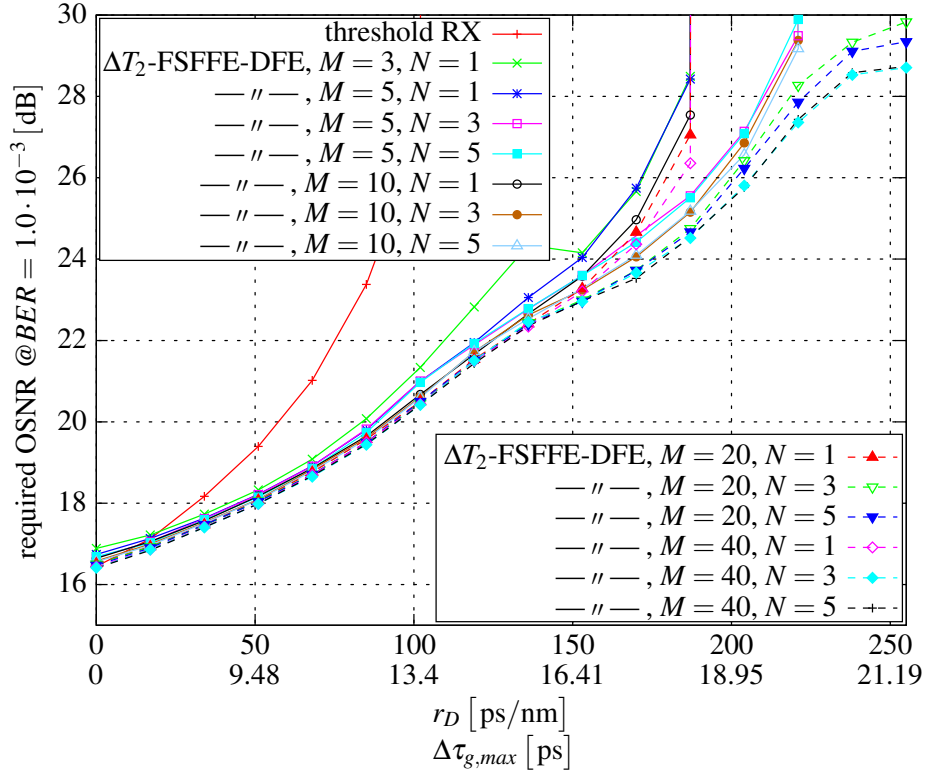
Figure 4.32: Optimal number of ΔT_2-FSFFE-DFE coefficients for combined CD and first-order PMD (based on MMSE adjustment)

Fortunately, these optimal numbers do not differ much for the different sources of ISI such as CD, first-order PMD or both combined. Thus, a single EDC unit which comprises one of the configurations of Table 4.3 is sufficient irrespective of the actually dominating impairments. The combined case of CD and first-order PMD is therefore our preferred scenario for the following studies in this thesis. We only come back to a separate consideration and discussion of CD and first-order PMD behavior if it provides further insight.

4.3.2 MMSE Suitability for OA/IM-DD Links

The left-hand plots of Figs. 4.33 – 4.36 compare the performance of various FFE-DFEs with respect to different coefficient adjustment criteria for combined CD and first-order PMD. The MIN-BER, the ZF and the MMSE criterion show almost the same performance for the FFE and ΔT_2-FSFFE in Figs. 4.33(a) and 4.35(a), respectively. Especially for the dispersion-limited region, where the required OSNR is already high, the curves proceed as expected from theory stating that the ZF approaches the MMSE results if the SNR goes to infinity [46]. The FFE-DFE and ΔT_2-FSFFE-DFE curves in Figs. 4.34(a) and 4.36(a) are more distinct with respect to the applied coefficient adjustment criteria. This clearly indicates that the DFE equipped EDC is qualitatively more susceptible to the respective coefficient adjustment criterion.
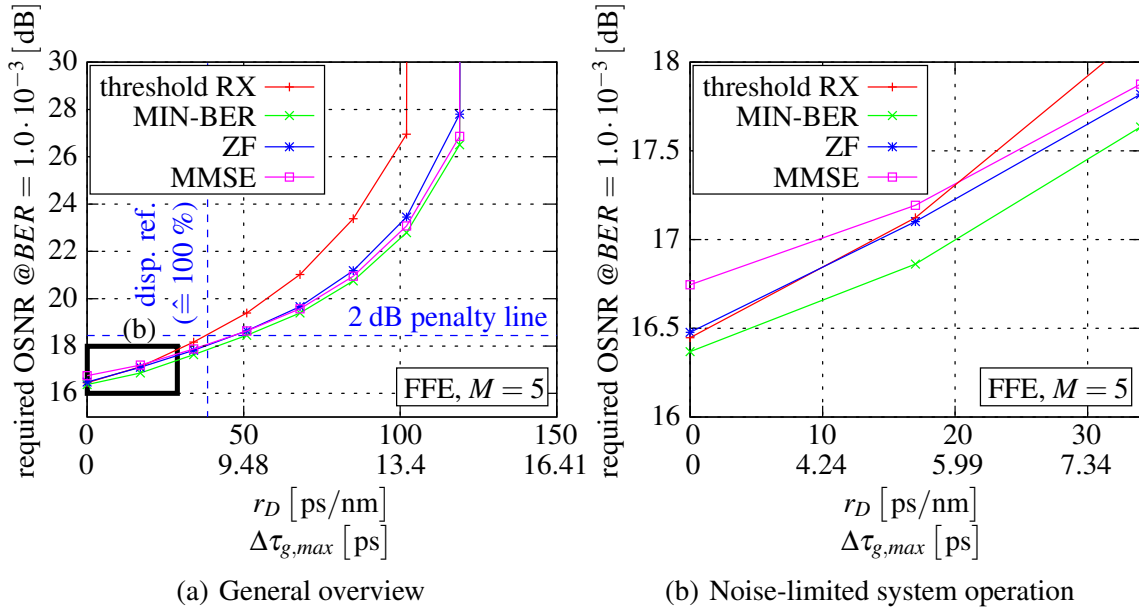
(a) General overview

(b) Noise-limited system operation

Figure 4.33: Optimality of MMSE for FFE illustrated by the example of combined CD and first-order PMD

(a) General overview

(b) Noise-limited system operation
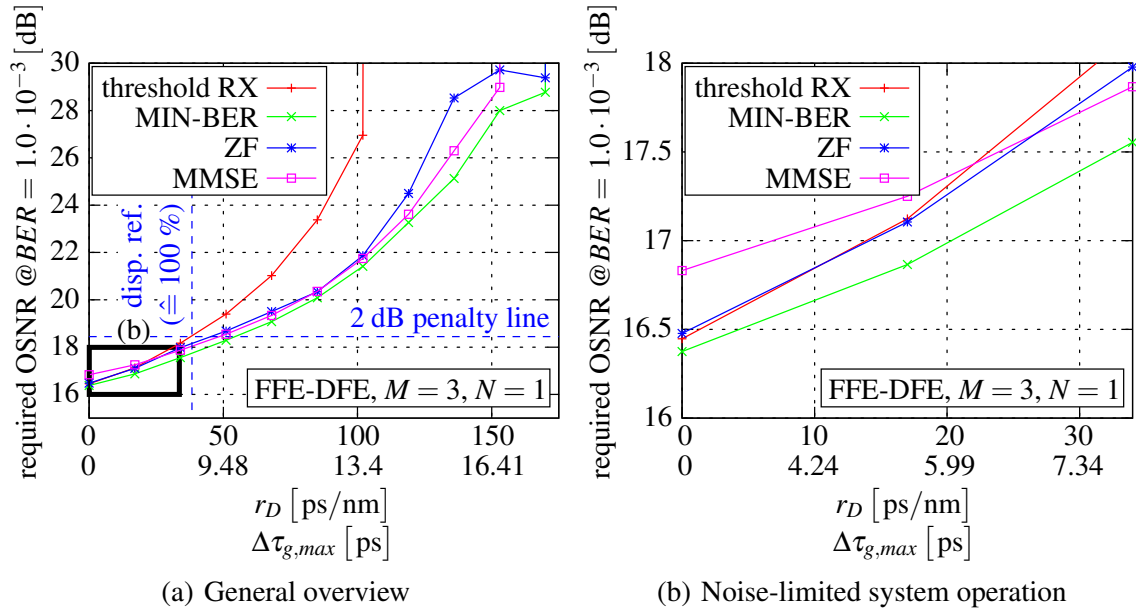
Figure 4.34: Optimality of MMSE for FFE-DFE illustrated by the example of combined CD and first-order PMD

(a) General overview   (b) Noise-limited system operation
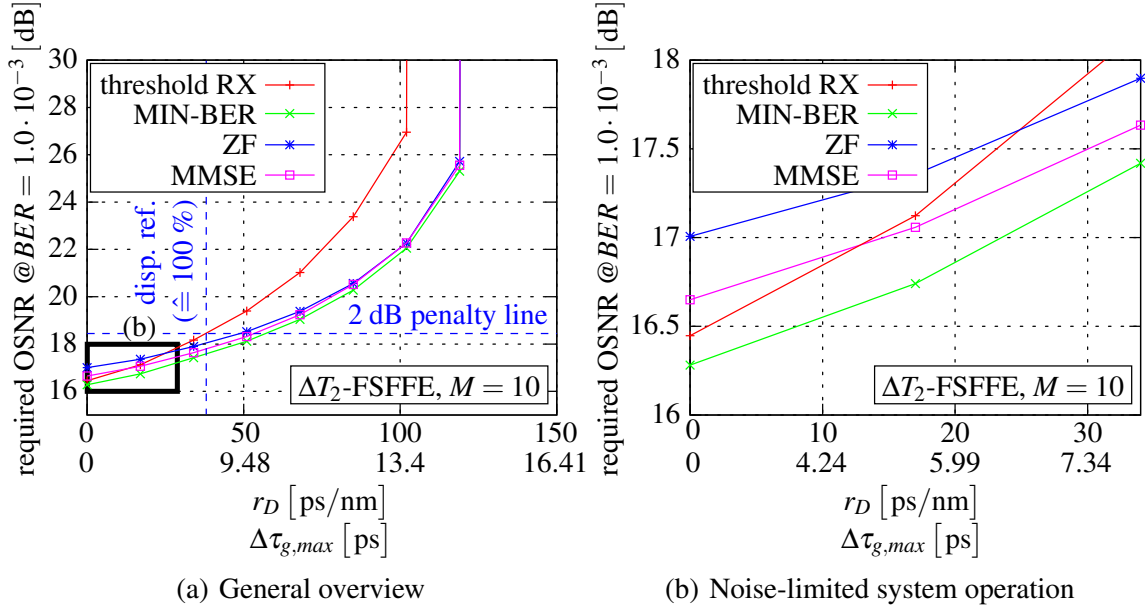
Figure 4.35: Optimality of MMSE for ΔT_2-FSFFE illustrated by the example of combined CD and first-order PMD

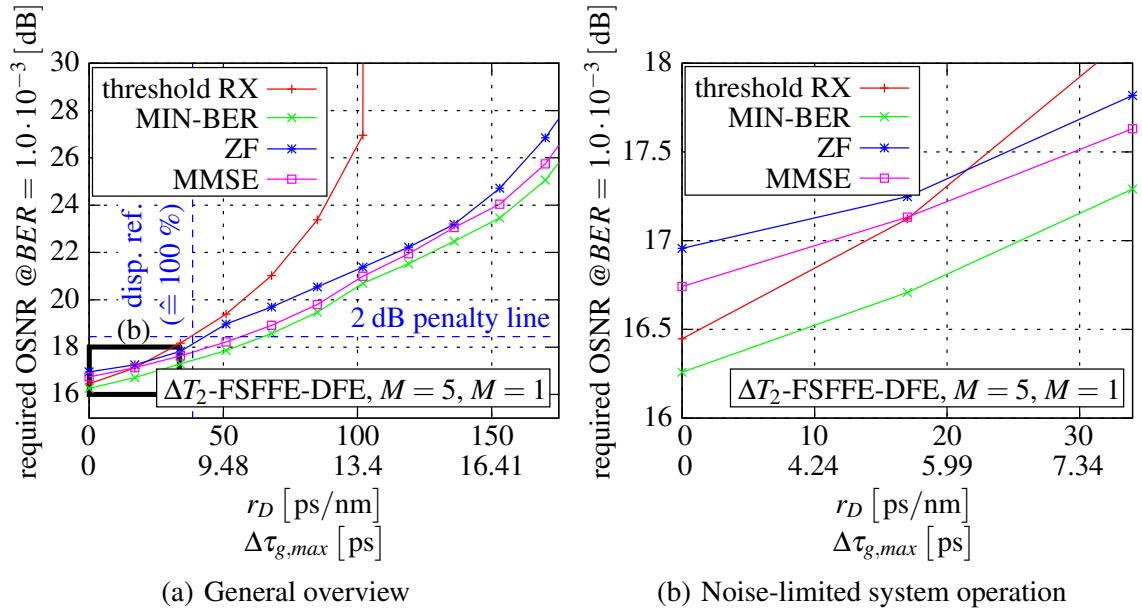(a) General overview   (b) Noise-limited system operation

Figure 4.36: Optimality of MMSE for ΔT_2-FSFFE-DFE illustrated by the example of combined CD and first-order PMD

In the noise-limited region, i.e. for very low r_D and $\Delta\tau_g$, the results are hardly to distinguish in Figs. 4.33(a) – 4.36(a). Therefore, Figs. 4.33 – 4.36 show this region in a zoomed window. The zoom area is indicated by a black lined box with subscript (b) on the corresponding left-hand side plots (a). Figs. 4.33(b) - 4.36(b) reveal a special phenomenon of MMSE applied to FFE-DFE methods in OA-IM/DD links. Irrespective of the FFE-DFE structure, EDC performance degrades even below the threshold RX system. This has also been reported by others in [105, 106, 107].

Table 4.4 quantifies the b2b penalties of the applied coefficient adjustment criteria measured with the b2b performance of the threshold RX system as reference. The additionally required OSNR is about $0.2 - 0.4$ dB for the MMSE criterion, which is even outperformed by the ZF criterion for the FFE and the FFE-DFE setup with 0.03 dB. The MIN-BER criterion has a negative penalty, i.e. it reduces the required b2b OSNR penalty. This gives clear evidence that plain application of the MMSE criterion is not well suited for noise-limited OA-IM/DD. Concerning the dispersion-limited region, we can also observe that there is still some margin wasted compared to MIN-BER.

	MIN-BER	ZF	MMSE
FFE, $M = 5$	-0.0782 dB	0.0307 dB	0.2981 dB
FFE-DFE, $M = 3, N = 1$	-0.0721 dB	0.0307 dB	0.3851 dB
ΔT_2-FSFFE, $M = 10$	-0.1658 dB	0.5595 dB	0.2026 dB
ΔT_2-FSFFE-DFE, $M = 3, N = 1$	-0.1878 dB	0.5099 dB	0.2944 dB

Table 4.4: b2b penalty listing for different FFE-DFE and ΔT_2-FSFFE-DFE setups with corresponding coefficient adjustment criteria

The illustrations of Figs. 4.37 – 4.39 give further insight into the worse performance of the MMSE criterion in OA-IM/DD links. Fig. 4.37 contains scatter plots for different FFE-DFE structures with respect to the applied coefficient adjustment criteria. The equalizer coefficients have been calculated for a combined CD and first-order PMD scenario. As with the generation of eye diagrams, we evaluate the calculated coefficients together with noise free yet dispersion affected electrical RX input samples to determine the vertical margins of different EDC methods. Although the MIN-BER coefficient adjustment criterion performs best in terms of required OSNR, it shows the least vertical margins of all methods. ZF, which does not consider noise in the coefficient calculation at all, has a better vertical margin and a required OSNR performance than MMSE for T_b-spaced processing in the noise-limited region. This is somewhat contradictory since the intended benefit of applying the MMSE criterion is to include noise characteristics in the equalizer coefficient calculation. For ΔT_2-spaced processing, MMSE outperforms ZF in terms of required OSNR although the vertical margins are almost the same. However, the MMSE criterion still has a positive OSNR penalty compared to the simple threshold RX. Thus, we may conclude that the MMSE criterion overestimates the noise within the electrical RX signal samples, which biases the coefficients to
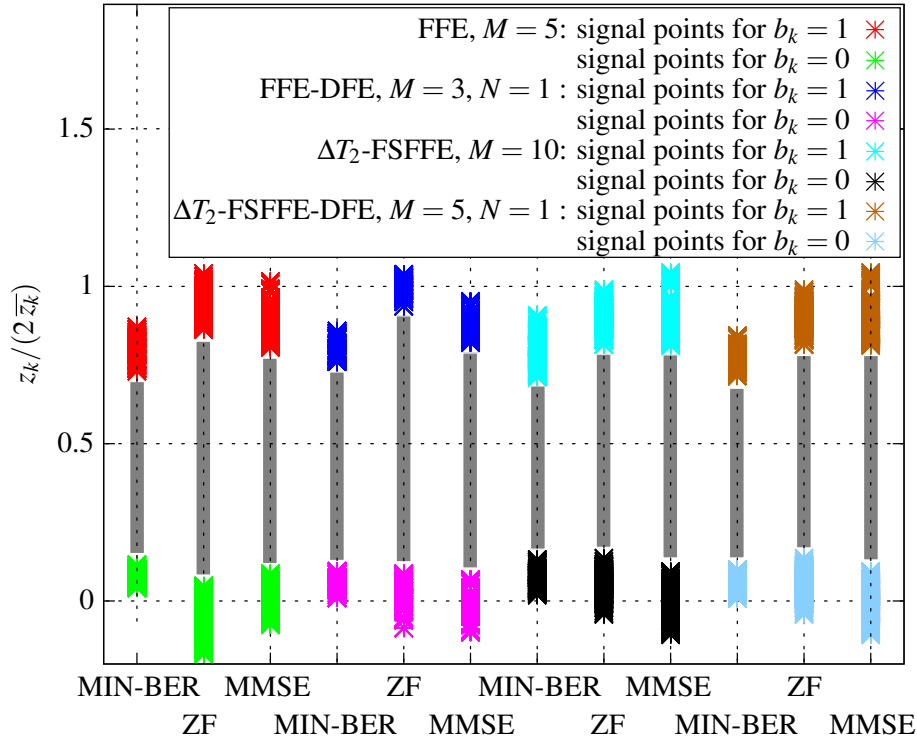
Figure 4.37: Scatter plots for different coefficient adjustment criteria (generated with coefficients resulting from combined CD ($L_f = 5$ km) and first-order PMD ($\Delta\tau_{g,max} = 12.36$ ps), $\gamma_{OSNR} = 21$ dB)

suboptimal values. This impression is confirmed by the conditional histogram measurements depicted in Figs. 4.38 and 4.39 for a FFE operated in the noise- and dispersion-limited region, respectively. Although the maximal frequencies of the MIN-BER histograms have the least distance for both, the noise- and dispersion-limited region, the variance of these curves is smaller than for the ZF and MMSE case. For the noise-limited region, the MMSE histograms show the maximal variance which is a clear indication of higher noise power being present in the decision statistics z_{k_1}.

We conclude the discussion of suitability of the MMSE criterion with the numerical results of Fig. 4.40, which shows the 2 dB penalty improvement gap between the MMSE and the MIN-BER criterion by means of a bar plot in Fig. 4.40(a). The bars indicate the percentage how much better a MIN-BER adjusted FFE-DFE or ΔT_2-FSFFE-DFE method for EDC improves the dispersion tolerance at a 2 dB offset level compared to the MMSE criterion as exemplified in Fig. 4.40(b). The 100 % dispersion reference is derived from the threshold RX performance and already marked in the previous plots of Figs. 4.33(a) – 4.36(a). Coefficient adjustment with respect to the MIN-BER criterion is able to further improve the CD tolerance from 9.75 % for the ΔT_2-FSFFE up to 22.28 % for ΔT_2-FSFFE-DFE. For first-order PMD, the numbers range from 4.04 % for ΔT_2-FSFFE to 8.08 % for ΔT_2-FSFFE-DFE. If we express the percentages of the performance gap between the MMSE and MIN-BER criteria in equivalent length margin as given by Eqs. (3.74) on page 32 and (4.73) on page 93,
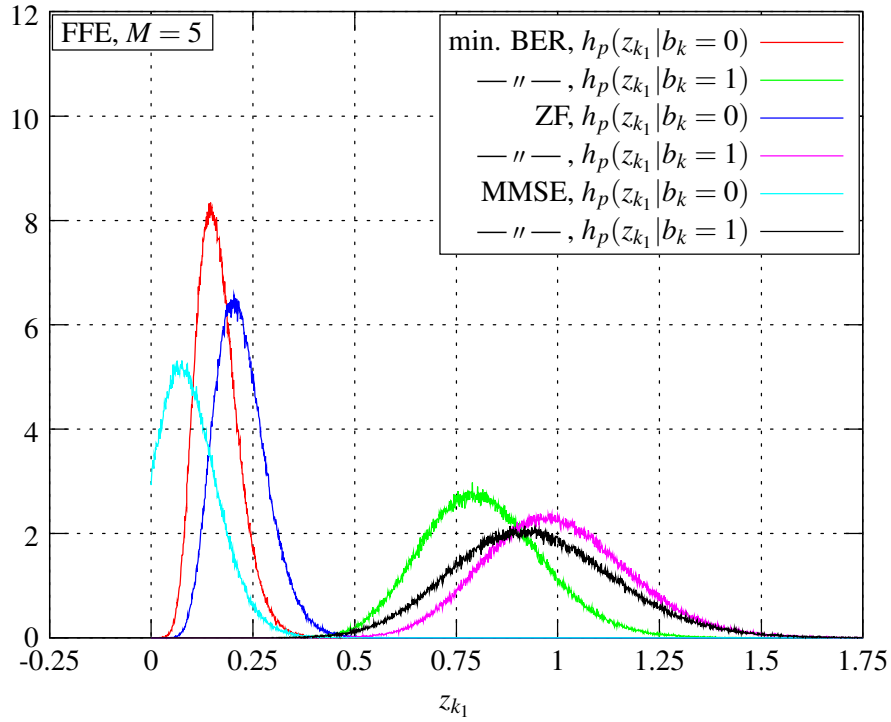
Figure 4.38: Conditional histograms after FFE with $M = 5$ for a noise-limited OA-IM/DD link ($L_f = 0$ km, $\Delta\tau_g = 0$ ps, $\gamma_{OSNR} = 17$ dB and $BER < 1.0e\text{-}3$)
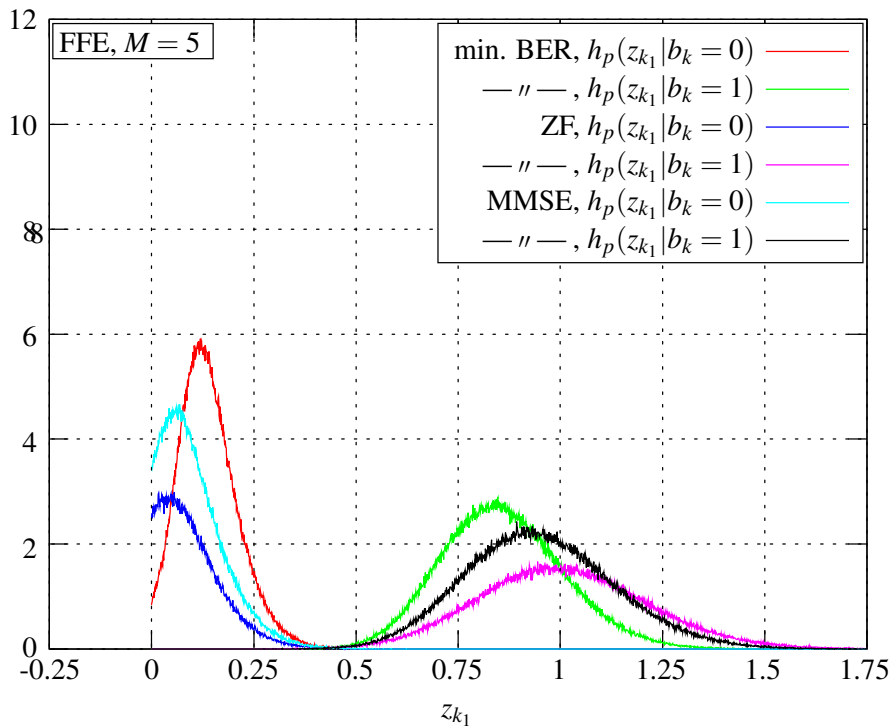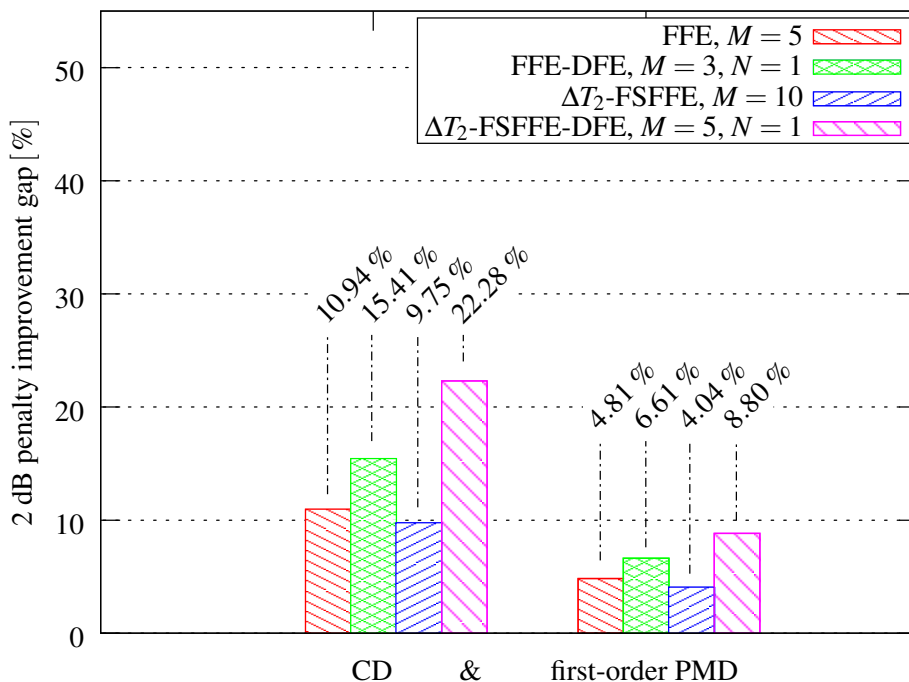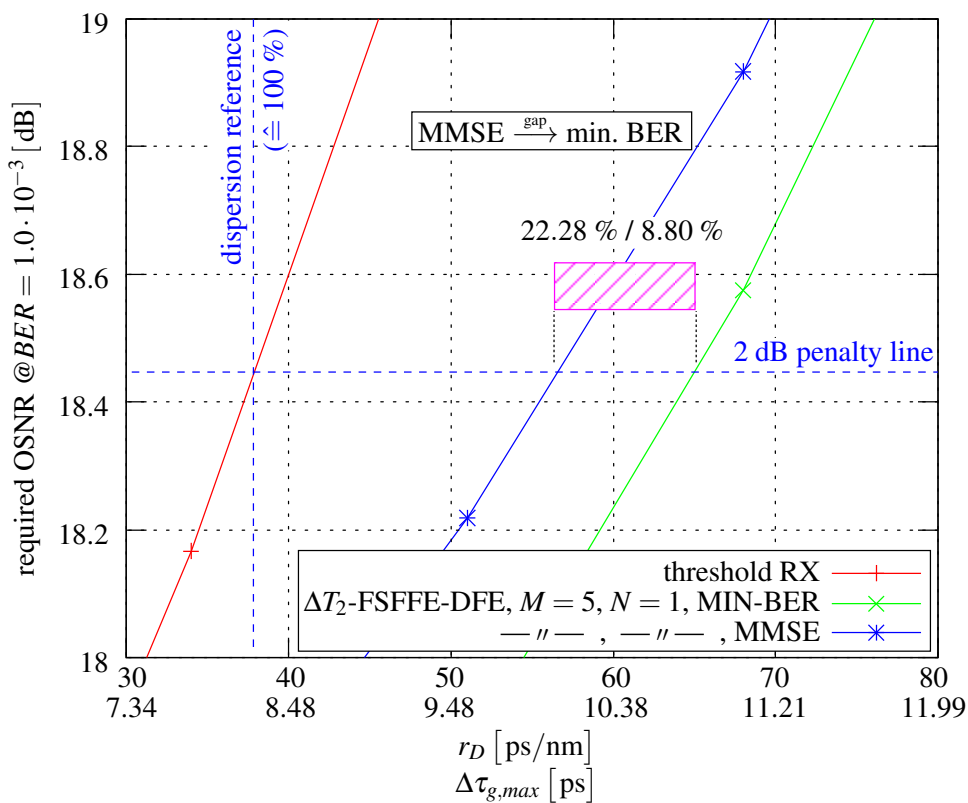

Figure 4.39: Conditional histograms after FFE with $M = 5$ for a dispersion-limited OA-IM/DD link ($L_f = 5$ km, $\Delta\tau_g = 12.36$ ps, $\gamma_{OSNR} = 21$ dB and $BER < 1.0e\text{-}3$)

(a) 2 dB penalty improvement gap between the MIN-BER and MMSE criterion for combined CD and first-order PMD

(b) Example for the determination of the 2 dB penalty improvement gap percentage (ΔT_2-FSFFE-FFE for combined CD and first-order PMD)

Figure 4.40: 2 dB tolerance improvement loss due to MMSE coefficient adjustment

we may state that we can extend the range of the OA-IM/DD link to about $0.22 - 0.5$ km at $R_b = 42.7$ Gbit/s. For long-haul wide area networks (WANs) this is not worth discussing, but it could be an advantage for short-haul distances within metropolitan area networks (MANs) or local area networks (LANs). The performance gap between MIN-BER and MMSE is larger for FFE-DFE structures than for FFE only. This points out the higher susceptibility of FFE-DFE structures with regard to the applied coefficient adjustment criterion.

At least in the noise-limited operation range, there are various possibilities how to cope with this obviously adverse situation of MMSE deficiency:

1. We could signal to the RX to switch off its EDC unit and just act as a simple threshold RX. This would require an additional signaling channel or even some overhead.

2. If possible, we could just accept the BER performance loss introduced by EDC with a FFE-DFE.

3. We could increase the optical TX power for compensation, which also requires some kind of feedback channel.

4. We could improve the noise immunity of the MMSE coefficient adjustment algorithm and benefit from a reduced optical TX power as for example with the MIN-BER criterion.

Of course, the latter option is favorable and requires us to have a better understanding of the mathematical mechanisms involved in MMSE coefficient adjustment, especially, how the ASE noise is treated there with direct detection.

Assuming that the optical RX is directly connected to the optical TX, the LLS FIR channel approximation as introduced previously is approximately given by a single tap filter with $M_c = 0$. If we use a quite simple system model as depicted in Fig. 4.41,

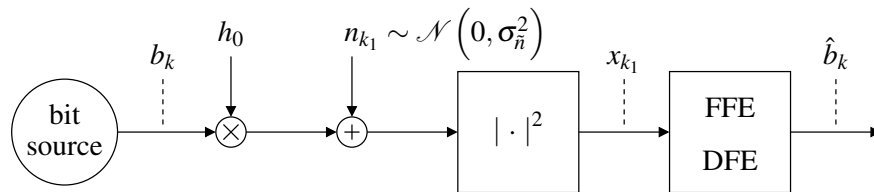**Figure 4.41:** Simplified noise-limited direct detection system

its output is given by

$$
\begin{aligned}
x_{k_1} &= \left| h_0 b_k + n_{k_1} \right|^2, \quad b_k \in \{0,1\}, h_0, n_{k_1} \in \mathbb{R}, \\
&= \left(h_0 b_k + n_{k_1} \right)^2 \\
&= h_0^2 b_k^2 + 2 h_0 b_k n_{k_1} + n_{k_1}^2.
\end{aligned}
$$

(4.74)

n_{k_1} represents an AWGN noise process modeling the ASE noise of the EDFA, and the squared magnitude operation represents direct detection by the photodiode.

Referring the MMSE coefficient calculation of Eq. (4.62) but with restriction to a FFE, we need the autocorrelation matrix $\mathbf{R_{xx}}$ and the cross-correlation vector $\mathbf{p}_{b\mathbf{x}}$ to determine

$$\mathbf{c} = \mathbf{R_{xx}^{-1}} \mathbf{p}_{b\mathbf{x}}.$$

The elements of the autocorrelation matrix are generally given by

$$
\begin{aligned}
r_{x_{k_1+\tau_d-t}x_{k_1+\tau_d-u}} &= \mathsf{E}\Big[x_{k_1+\tau_d-t}x_{k_1+\tau_d-u}\Big] \stackrel{\text{ergodicity}}{=} \mathsf{E}\Big[x_{k_1-t}x_{k_1-u}\Big] \\
&= \mathsf{E}\Big[\Big(h_0^2 b_{k-t}^2 + 2h_0 b_{k-t}n_{k_1-t} + n_{k_1-t}^2\Big)\Big(h_0^2 b_{k-u}^2 + 2h_0 b_{k-u}n_{k_1-u} + n_{k_1-u}^2\Big)\Big] \\
&= h_0^4 \mathsf{E}\Big[b_{k-t}^2 b_{k-u}^2\Big] + 2h_0^3 \mathsf{E}\Big[b_{k-t}^2 b_{k-u}\Big]\underbrace{\mathsf{E}\Big[n_{k_1-u}\Big]}_{=0} + h_0^2 \mathsf{E}\Big[b_{k-t}^2\Big]\mathsf{E}\Big[n_{k_1-u}^2\Big] \\
&\quad + 2h_0^3 \mathsf{E}\Big[b_{k-t}b_{k-u}^2\Big]\underbrace{\mathsf{E}\Big[n_{k_1-u}\Big]}_{=0} + 4h_0^2 \mathsf{E}\Big[b_{k-t}b_{k-u}\Big]\mathsf{E}\Big[n_{k_1-t}n_{k_1-u}\Big] \\
&\quad + 2h_0 \mathsf{E}\Big[b_{k-t}\Big]\underbrace{\mathsf{E}\Big[n_{k_1-t}n_{k_1-u}^2\Big]}_{=0} \\
&\quad + h_0^2 \mathsf{E}\Big[n_{k_1-t}^2\Big]\mathsf{E}\Big[b_{k-u}^2\Big] + 2h_0\underbrace{\mathsf{E}\Big[n_{k_1-t}^2 n_{k_1-u}\Big]}_{=0}\mathsf{E}\Big[b_{k-u}\Big] + \mathsf{E}\Big[n_{k_1-t}^2 n_{k_1-u}^2\Big] \\
&= h_0^4 \mathsf{E}\Big[b_{k-t}^2 b_{k-u}^2\Big] + h_0^2 \mathsf{E}\Big[b_{k-t}^2\Big]\mathsf{E}\Big[n_{k_1-u}^2\Big] \\
&\quad + 4h_0^2 \mathsf{E}\Big[b_{k-t}b_{k-u}\Big]\underbrace{\mathsf{E}\Big[n_{k_1-t}n_{k_1-u}\Big]}_{=0:\,t\neq u} \\
&\quad + h_0^2 \mathsf{E}\Big[n_{k_1-t}^2\Big]\mathsf{E}\Big[b_{k-u}^2\Big] + \mathsf{E}\Big[n_{k_1-t}^2 n_{k_1-u}^2\Big] \\
&\stackrel{\text{ergodicity}}{=} \begin{cases} h_0^4 \mathsf{E}\Big[b_k^4\Big] + 6h_0^2 \mathsf{E}\Big[b_k^2\Big]\mathsf{E}\Big[n_{k_1}^2\Big] + \mathsf{E}\Big[n_{k_1}^4\Big] & :\ t = u \\ h_0^4 \Big(\mathsf{E}\Big[b_k^2\Big]\Big)^2 + 2h_0^2 \mathsf{E}\Big[b_k^2\Big]\mathsf{E}\Big[n_{k_1}^2\Big] + \Big(\mathsf{E}\Big[n_{k_1}^2\Big]\Big)^2 & :\ t \neq u \end{cases} \\
&= \begin{cases} h_0^4 \mathsf{E}\Big[b_k^4\Big] + 6h_0^2 \mathsf{E}\Big[b_k^2\Big]\mathsf{E}\Big[n_{k_1}^2\Big] + \mathsf{E}\Big[n_{k_1}^4\Big] & :\ t = u \\ \Big(h_0^2 \mathsf{E}\Big[b_k^2\Big] + \mathsf{E}\Big[n_{k_1}^2\Big]\Big)^2 & :\ t \neq u \end{cases},
\end{aligned}
$$

$$t, u = 0, \ldots, M-1;\ k \equiv k_1. \tag{4.75}$$

Note that we have partially applied the statistical independence of signal and noise and that the noise process itself has zero mean AWGN characteristic.

If we replace the model in Fig. 4.41 by a linear AWGN channel, the autocorrelation matrix

$\mathbf{R_{xx}}$ has diagonal form when no ISI is present, i.e.

$$x_{k_1} = h_0 b_k + n_{k_1} \iff r_{x_{k_1+\tau_d-t} x_{k_1+\tau_d-u}} = \ldots = \begin{cases} h_0^2 \mathsf{E}\left[b_k^2\right] + \mathsf{E}\left[n_{k_1}^2\right] & : \quad t = u \\ 0 & : \quad t \neq u \end{cases} \tag{4.76}$$

If we compare this to Eq. (4.75), we recognize that $r_{x_{k_1+\tau_d-t} x_{k_1+\tau_d-u}} \neq 0$ for $t \neq u$ which will bias the final MMSE solution in an OA-IM/DD link.

The same can be done for the elements of the crosscorrelation vector $\mathbf{p}_{b\mathbf{x}}$ with

$$\begin{aligned} p_{b\mathbf{x},t} &= \mathsf{E}\left[b_k x_{k_1+\tau_d-t}\right] = \mathsf{E}\left[b_k \left(h_0 b_{k+\tau_d-t} + n_{k_1+\tau_d-t}\right)^2\right] \\ &= \mathsf{E}\left[b_k \left(h_0^2 b_{k+\tau_d-t}^2 + 2h_0 b_{k+\tau_d-t} n_{k_1+\tau_d-t} + n_{k_1+\tau_d-t}^2\right)\right] \\ &= h_0^2 \mathsf{E}\left[b_k b_{k+\tau_d-t}^2\right] + 2h_0 \mathsf{E}\left[b_k b_{k+\tau_d-t}\right] \underbrace{\mathsf{E}\left[n_{k_1+\tau_d-t}\right]}_{=0} + \mathsf{E}[b_k]\,\mathsf{E}\left[n_{k_1+\tau_d-t}^2\right] \\ &= h_0^2 \mathsf{E}\left[b_k b_{k+\tau_d-t}^2\right] + \mathsf{E}[b_k]\,\mathsf{E}\left[n_{k_1+\tau_d-t}^2\right] \\ &\overset{\text{ergodicity}}{=} \begin{cases} h_0^2 \mathsf{E}\left[b_k^3\right] + \mathsf{E}[b_k]\,\mathsf{E}\left[n_{k_1}^2\right] & : \quad t = \tau_d \\ h_0^2 \mathsf{E}[b_k]\,\mathsf{E}\left[b_k^2\right] + \mathsf{E}[b_k]\,\mathsf{E}\left[n_{k_1}^2\right] & : \quad t \neq \tau_d \end{cases} \\ &= \begin{cases} h_0^2 \mathsf{E}\left[b_k^3\right] + \mathsf{E}[b_k]\,\mathsf{E}\left[n_{k_1}^2\right] & : \quad t = \tau_d \\ \mathsf{E}[b_k] \left(h_0^2 \mathsf{E}\left[b_k^2\right] + \mathsf{E}\left[n_{k_1}^2\right]\right) & : \quad t \neq \tau_d \end{cases} \\ &\quad t = 0, \ldots, M-1; \ k \equiv k_1. \end{aligned} \tag{4.77}$$

Again, we put the reference of a linear AWGN channel against this result by

$$x_{k_1} = h_0 b_k + n_{k_1} \iff p_{b\mathbf{x},t} = \ldots = \begin{cases} h_0 \mathsf{E}\left[b_k^2\right] & : \quad t = \tau_d \\ 0 & : \quad t \neq \tau_d. \end{cases} \tag{4.78}$$

The cross-correlation for the linear AWGN channel has only a single nonzero element at position τ_d. Therefore, since the autocorrelation matrix $\mathbf{R_{xx}}$ has diagonal form as already explained, the MMSE coefficient vector has also only one single nonzero element at position τ_d given by

$$c_{\tau_d} = \frac{h_0 \mathsf{E}\left[b_k^2\right]}{h_0^2 \mathsf{E}\left[b_k^2\right] + \mathsf{E}\left[n_{k_1^2}\right]}. \tag{4.79}$$

If we compare this to Eq. (4.77), we recognize again that $p_{b\mathbf{x},t} \neq 0$ for $t \neq \tau_d$. Together with the non-diagonal autocorrelation matrix $\mathbf{R_{xx}}$ of Eq. (4.75) the final MMSE solution has also nonzero coefficients at other than the central position, i.e. $c_m \neq 0$, $m = 0, \ldots, M-1$. This

explains why plain MMSE performs worse in noise-limited OA-IM/DD links and shows a performance gap to the MIN-BER criterion for the dispersion-limited region.

If we inspect Eqs.(4.75) and (4.77) for the cases $t \neq u$ and $t \neq \tau_d$, respectively, we may recognize that their final results have the term $h_0^2 \mathsf{E}[b_k^2] + \mathsf{E}[n_{k_1}^2]$ in common, which is actually the statistical mean value of the EDC input samples given by

$$
\begin{aligned}
\mathsf{E}\left[x_{k_1}\right] &= \mathsf{E}\left[\left(h_0 b_k + n_{k_1}\right)^2\right] \\
&= h_0^2 \mathsf{E}\left[b_k^2\right] + 2h_0 \mathsf{E}[b_k] \underbrace{\mathsf{E}\left[n_{k_1}\right]}_{=0} + \mathsf{E}\left[n_{k_1}^2\right] \\
&= h_0^2 \mathsf{E}\left[b_k^2\right] + \mathsf{E}\left[n_{k_1}^2\right].
\end{aligned}
\tag{4.80}
$$

Consequently, the MMSE solution seems to be biased by the statistical mean value of the EDC input signal. If we think this idea the other way round, we can make $\mathbf{R_{xx}}$ diagonal with $r_{x_{k_1 + \tau_d - t} \cdot x_{k_1 + \tau_d - u}} = 0$ for $t \neq 0$ and ensure that $p_{b\mathbf{x},t} = 0$ for $t \neq \tau_d$ again if we provide a zero-mean input signal to the FFE-DFE. Then, this should almost deliver the same performance as for the linear AWGN channel. Antipodal and zero-mean impulse shaping is not possible to implement in the TX of OA-IM/DD links. However, if we assume ergodicity and perform averaging on the EDC input samples x_{k_1}, we can set

$$
x_{ZM,k_1} := x_{k_1} - \overline{x_{k_1}} \overset{\text{ergodicity}}{\Longleftrightarrow} \mathsf{E}\left[x_{k_1} - \overline{x_{k_1}}\right] = 0
\tag{4.81}
$$

and feed these zero-mean samples to the usual MMSE criterion.

Fig. 4.42 shows the simulation results with the zero-mean adjustment of the EDC input samples. The negative OSNR penalty for the noise-limited region has been eliminated completely. Towards the dispersion-limited region, the curves of the zero-mean adjusted MMSE coincides with the MIN-BER results. This is originally known form linear AWGN channels. Just for the very high dispersion region, the zero-mean MMSE results deviate at least for FFE-DFE.
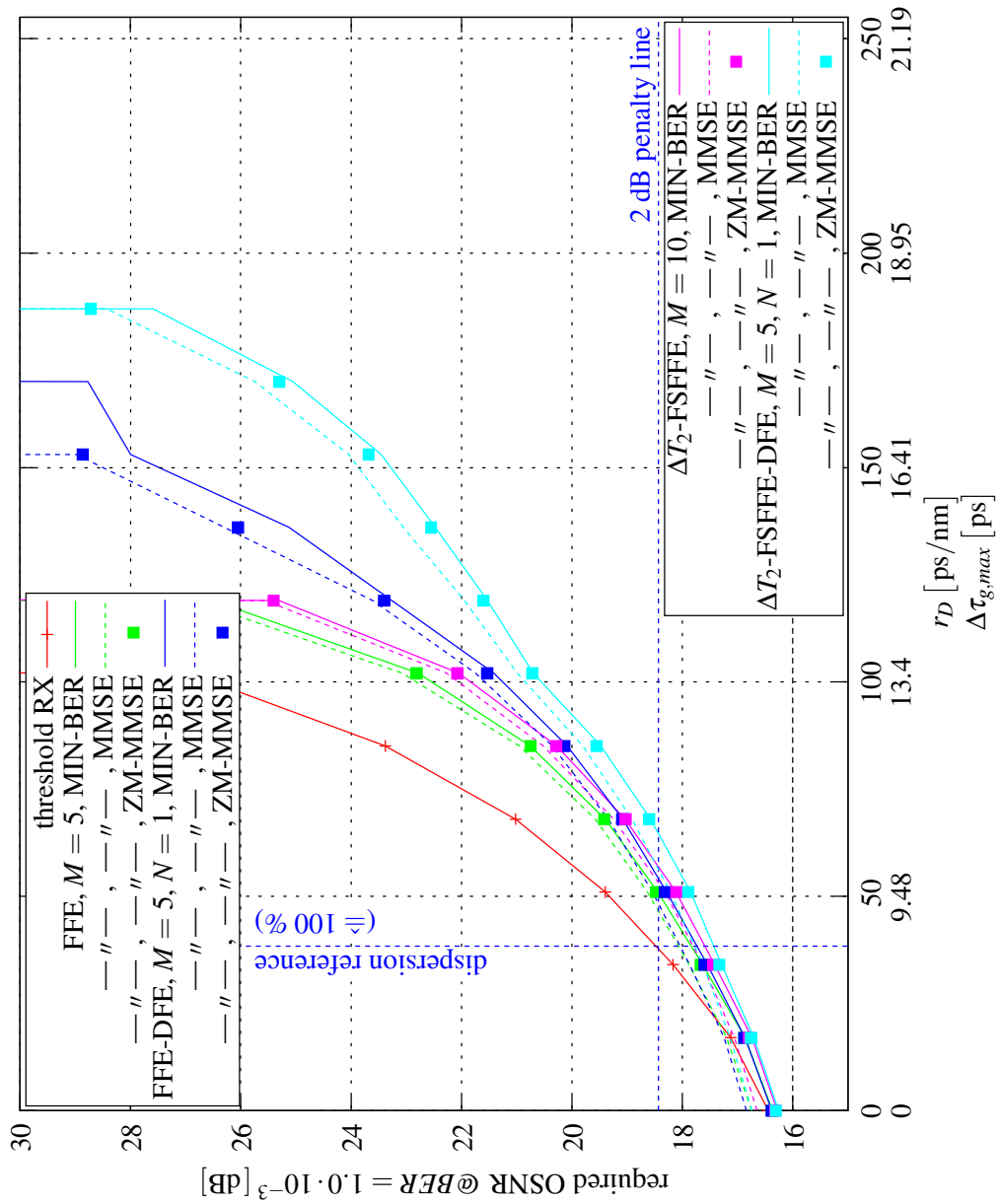
Figure 4.42: MMSE deficiency compensation by zero-mean input adjustment for combined CD and first-order PMD

4.3.3 Benefits and Implications of Fractionally Spaced Processing

4.3.3.1 EDC Performance Enhancement

Figs. 4.43 – 4.45 compare the performance of T_b-spaced to ΔT_2-spaced FFE-DFEs. The equalizer coefficients have been generated each time with the MMSE criterion. Fig. 4.46 contains the extracted 2 dB penalty improvements out of Figs. 4.43 – 4.45.

Concerning CD, the 2 dB penalty improvement of 14.94 % for the FFE is more than doubled by the ΔT_2-FSFFE with 39.10 %. The same doubling holds for the corresponding DFE variants with 19.06 % for T_b-spaced processing and even 44.52 % for ΔT_2-spaced processing. Since the residual dispersion value r_D scales linearly with length, these quantities directly increase the possible OA-IM/DD link length by the same percentage. The ΔT_2-FFE-DFE demonstrate its dispersion compensation capabilities even for larger CD values beyond the pole-like region for the T_b-spaced processing methods.

It is also the additional DFE in conjunction with ΔT_2-spaced processing which delivers the best 2 dB penalty performance gain with 21.21 % for first-order PMD in Fig. 4.44. In contrast, the percentages of the other methods represent only moderate improvements which increase almost linearly from 12.87 % for the FFE to 16.05 % for the ΔT_2-FSFFE according to Fig. 4.46. The required OSNR @ $BER = 1.0e\text{-}3$ for the FFE-DFE and the ΔT_2-FSFFE are almost the same for larger $\Delta \tau_g$. However, the ΔT_2-spaced processing is capable of overcoming the pole-like region which is also present for first-order PMD.

Fig. 4.45 shows the results for the combined effects of CD and first-order PMD. Compared to the single effect considerations, the 2 dB penalty improvement percentages are higher with respect to CD while the PMD penalty gain remains almost the same.

4.3.3.2 Sampling Phase Susceptibility

Another interesting aspect for comparing T_b- and ΔT_2-spaced processing is the impact of sampling phase adjustment. Therefore, we have simulated the FFE-DFE and ΔT_2-FSFFE-DFE with different sampling phases. Recalling the definitions in Eqs. (3.120), (3.123) and (3.127) on pages 46 – 48, by which we have introduced our notation for electrical RX signal sampling, we have set the sampling phases τ_1 for T_b-spaced processing to $\tau_1 = 0, 0.25T_b, 0.5T_b$ and $0.75T_b$. The same setup has been applied to τ_2 for ΔT_2-spaced sampling with $\tau_2 = 0, 0.25\Delta T_2, 0.5\Delta T_2$ and $0.75\Delta T_2$.

The achieved results for T_b-spaced processing are illustrated in Fig. 4.47. The FFE and FFE-DFE performance heavily depends on the adjusted sampling phase. The FFE shows best performance if we sample the electrical RX signal right in the middle where we expect the maximal residual eye opening, i.e. at $\tau_1 = 0.5T_b$. Since our computer simulation model is not
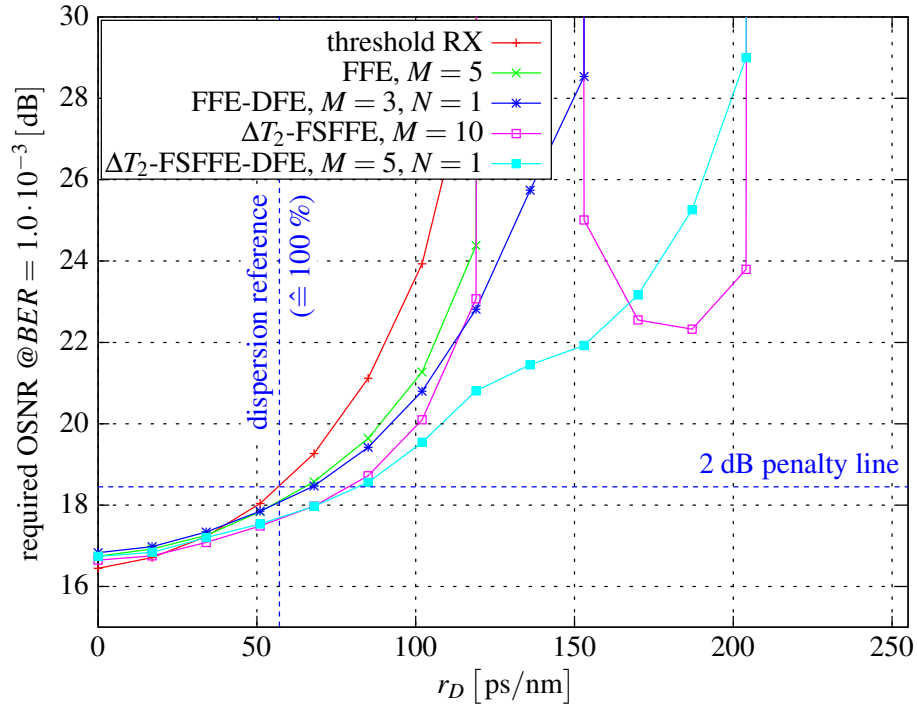
Figure 4.43: FFE-DFE vs. ΔT_2-spaced FSFFE-DFE EDC for CD (based on MMSE adjustment)
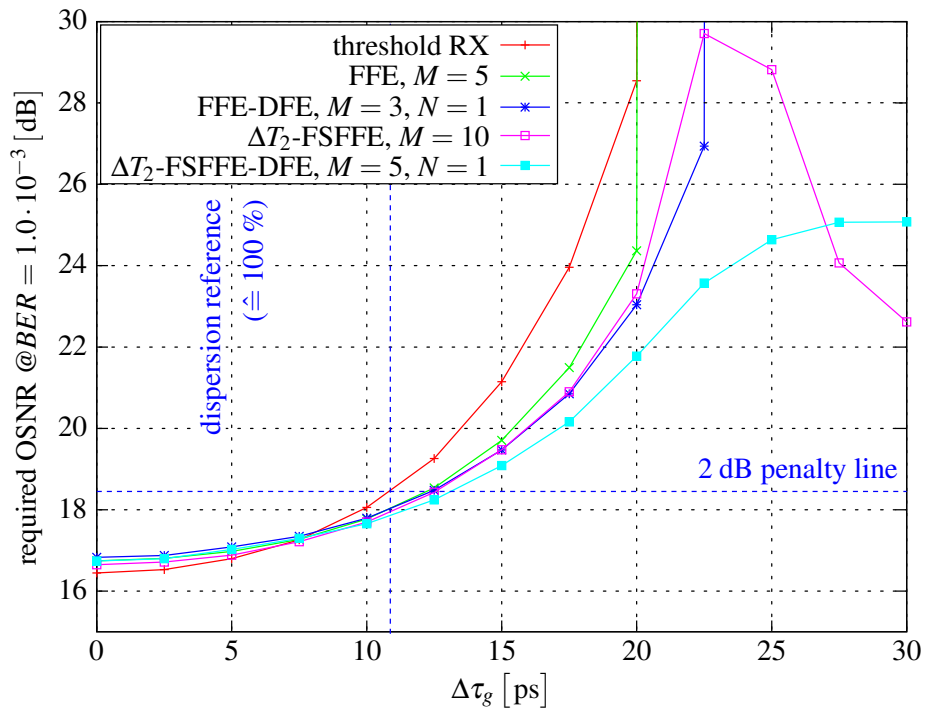

Figure 4.44: FFE-DFE vs. ΔT_2-spaced FSFFE-DFE EDC for first-order PMD (based on MMSE adjustment)
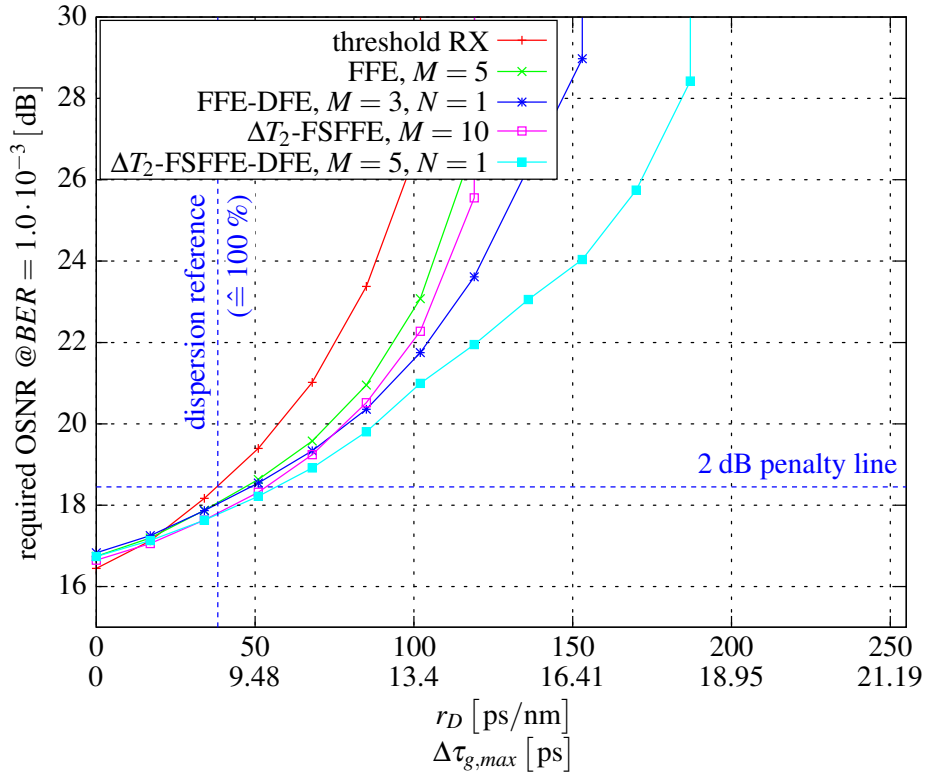
Figure 4.45: FFE-DFE vs. ΔT_2-spaced FSFFE-DFE EDC for combined CD and first-order PMD (based on MMSE adjustment)
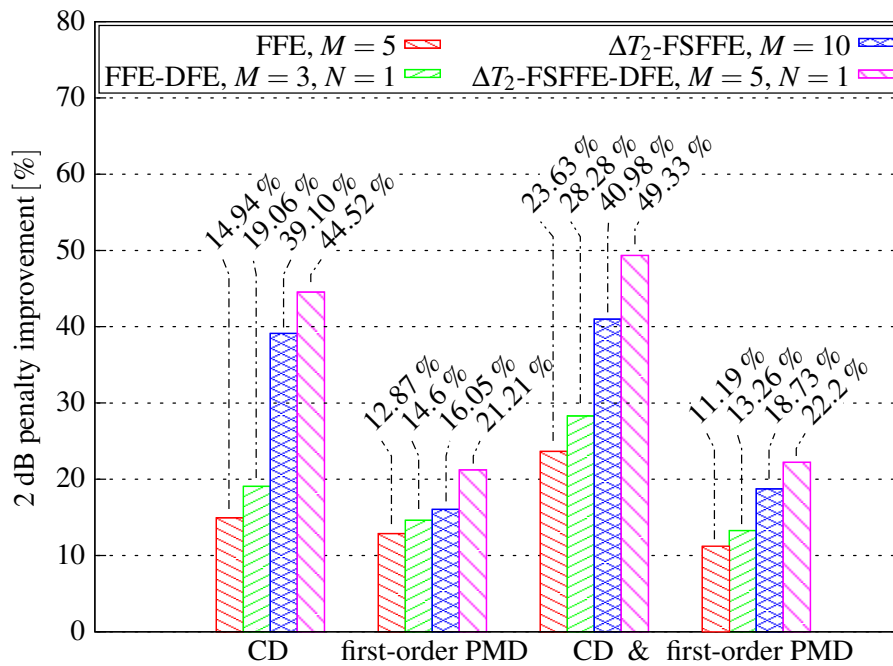

Figure 4.46: 2 dB penalty improvement of FFE-DFE vs. ΔT_2-FSFFE-DFE EDC (based on MMSE adjustment)

Figure 4.47: Effect of different sampling phase adjustments for FFE and FFE-DFE illustrated by the example of combined CD and first-order PMD (based on MMSE adjustment)

causal, the ISI generated by CD and first-order PMD spreads symmetrically to the neighboring TX symbols. This explains the almost identical curves for $\tau_1 = 0.25T_b$ and $\tau_1 = 0.75T_b$. Sampling at the signal transition instants with $\tau_1 = 0$ leads to almost undefined signal states and its curve is out of diagram scope. The behavior of the FFE-DFE is quite different. Intuitively, the result for $\tau_1 = 0.5T_b$ is expected to perform best as for the FFE. However, the curves for $\tau_1 = 0, 0.25T_b$ and $0.75T_b$ outperform it in the dispersion-limited region by a considerable amount. Especially for $\tau_1 = 0$, much more dispersion tolerance improvement is possible for $r_D > 120$. Thus, we can conclude that proper T_b-spaced processing requires appropriate sampling phase adjustment depending on the OA-IM/DD link characteristics. This is the task of a so-called clock and data recovery (CDR) unit with tunable phase adjustment circuitry, whose realization is quite challenging for very high bit rates.

Fig. 4.48 reveals that sampling phase adjustment is not necessary for ΔT_2-spaced processing. The performance is almost independent of the applied sampling phase. Besides better EDC performance, fractionally spaced processing also offers the benefit of getting rid of CDR phase tuning. However, the already high bit rates also impose challenges on fractionally spaced processing.
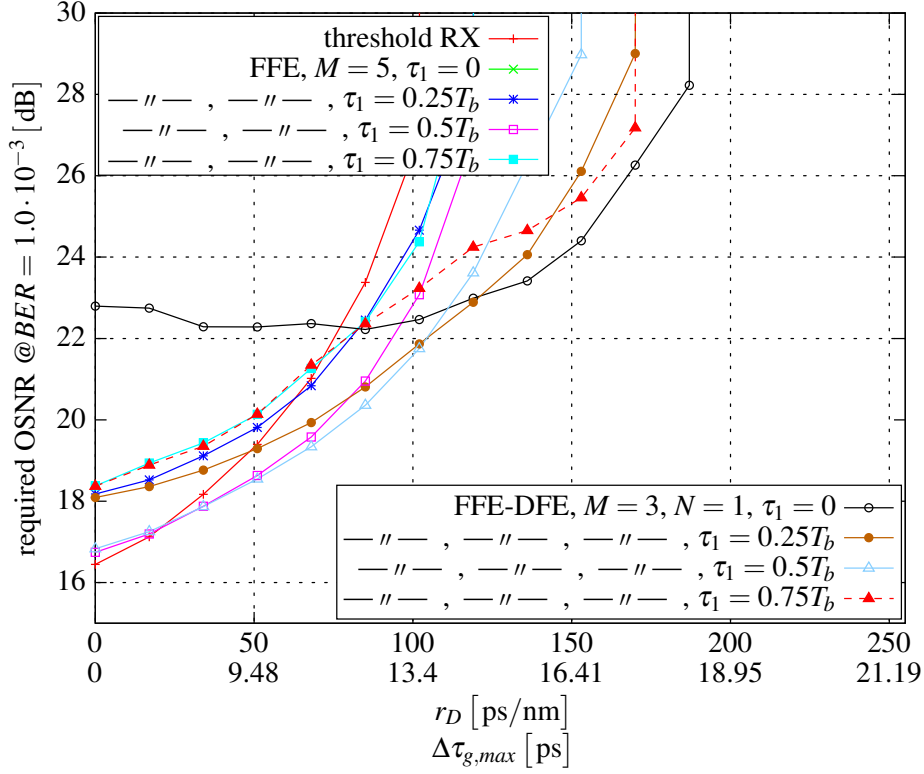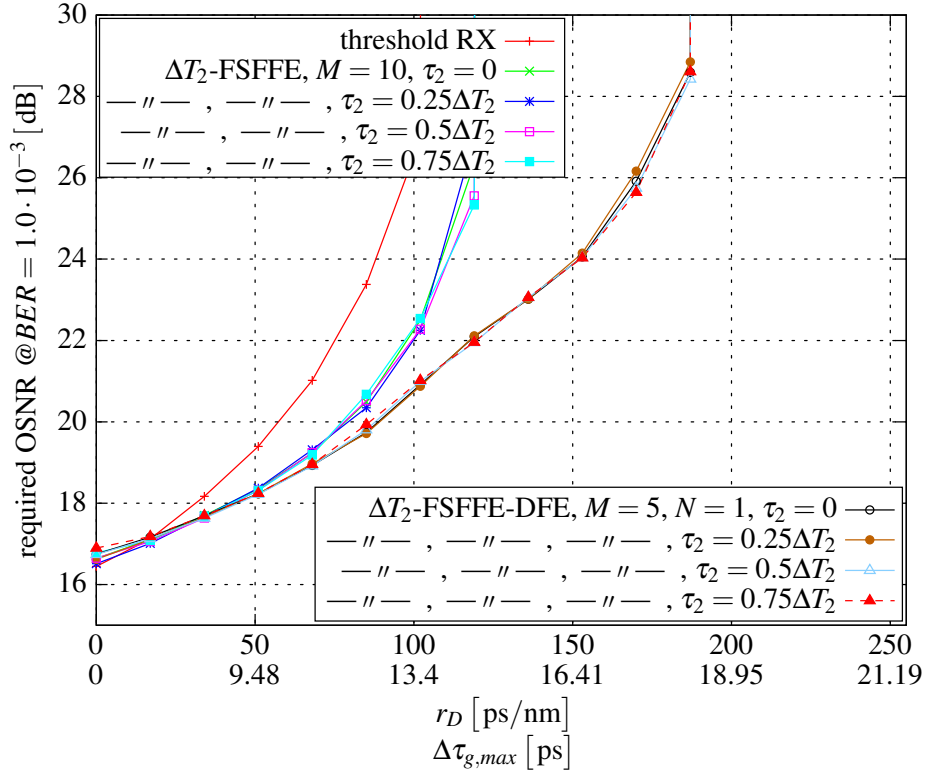
Figure 4.48: Effect of different sampling phase adjustments for FSFFE
and FSFFE-DFE illustrated by the example of combined
CD and first-order PMD (based on MMSE adjustment)

4.3.3.3 Fractional Sample Spacings Below ΔT_2

We close the discussion of fractionally spaced processing benefits by answering the remaining question that, if we further decrease the sample spacing, we can even more improve EDC performance. Fig. 4.49 contains FSFFE and FSFFE-DFE results for ΔT_2-, ΔT_4- and ΔT_8-spaced processing. The temporal spread of the FSFFE has been kept constant within the groups of FSFFEs and FSFFE-DFEs simulations. That is why the number of coefficients are doubled from one sample spacing to the next lower. Previously presented results, which have considered the step from T_b- to ΔT_2-spaced processing, have shown that ΔT_2-spaced processing either allows to decrease the number of FSFFE coefficients while maintaining the same EDC performance, or it improves performance if the number of FSFFE coefficients increases. According to Fig. 4.49, the step from ΔT_2 to ΔT_4 shows only some small performance gain for the FSFFE. For all other cases, the overall performance hardly increases, i.e. fractionally spaced processing below ΔT_2 does not justify to pursue.
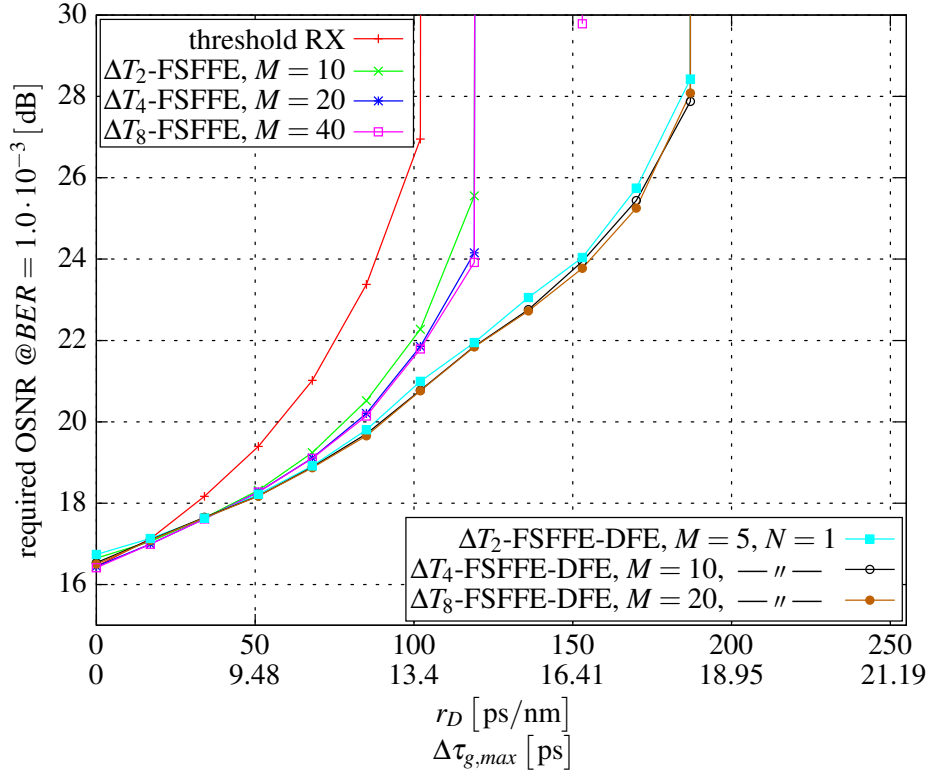
Figure 4.49: Further decreasing sample spacing illustrated by the example of combined CD and first-order PMD (based on MMSE adjustment)

4.3.4 Comprehensive FFE-DFE Performance Analysis vs. MLSE Viterbi Equalizer

After the detailed consideration of FFE-DFE-based EDC and its behavior in OA-IM/DD links, we turn to the more general assessment by comparing the performance of FFE-DFEs to the theoretically more advanced MLSE-VE with all the implications already addressed in Ch. 4.1. MLSE-VE shall serve as the benchmarking EDC technique for this thesis since some practical realizations have already been reported [20, 28, 80]. Thus, the parameters channel memory and ADC resolution for the MLSE-VE have been chosen accordingly with $M_c = 2$ and $B_x = 5$ as the benchmarking reference. It is worth to note that MAP turbo equalization [33, 34, 35, 72, 108, 109, 110] would show even better performance than MLSE-VE. However, computational complexity would even more increase compared to MLSE-VE due to its iterative nature.

Fig. 4.50 compares the results for CD. Within both sample spacing groups, MLSE-VE performs best as expected. The performance gain of MLSE-VE is extraordinary higher for ΔT_2-spaced processing compared to any other depicted EDC method. The MLSE-VE results show an almost linear increase of the required OSNR. This is different to the less effective FFE-DFEs and ΔT_2-FSFFE-DFEs curves and manifests the generally superior EDC

performance. Another interesting fact is that all fractionally spaced FFE-DFEs outperform T_b-spaced MLSE-VE for short-haul OA-IM/DD links. The ΔT_2-FSFFE-DFE offers almost a 25 % improved dispersion tolerance for CD compared to MLSE-VE, and the T_b-space FFE-DFE lacks only around 6 % at much lower implementation cost.

The comparison for first-order PMD reveals a different situation in Fig. 4.51. The dispersion tolerance improvement is quite moderate for any EDC method. MLSE-VE performs best here irrespective of the applied processing rate. The ΔT_2-FSFFE-DFE is the only which can keep up with the MLSE-VE performance.

Joint CD and first-order PMD results are depicted in Fig. 4.52. In principle, they nearly provide a superposition of the previous separate CD and first-order PMD results. The ΔT_2-MLSE-VE with around 45 % 2 dB penalty improvement outperforms the other methods by far having an almost 1.5-fold improvement compared to the next best MLSE-VE and ΔT_2-FSFFE-DFE with around 30 % each. It is just the latter one out of all FFE-DFE and FSFFE-DFE and the MIN-BER coefficient adjustment, which is able to reach nearly MLSE-VE performance for short-haul distances. On the other hand, being able to do so by a much more simpler equalization method with the only burden of having twice the sampling rate makes this solution especially in the short-haul domain, where unit cost is critical, very attractive.

Fig. 4.53 lists the corresponding 2 dB penalty improvements as a numerical reference to the individual penalty improvements extracted from Figs 4.50 – 4.52.

4.4 Summary and Conclusion

In this chapter, we have discussed the general suitability of low-complexity FFE-DFE structures and their feasibility for application in short-haul OA-IM/DD. It can be stated that it is a real and low complex alternative to more advanced yet more processing intensive detection schemes. The deficiencies of the MMSE criterion as doubted by [105, 106, 107] can be alleviated by proper signal conditioning.

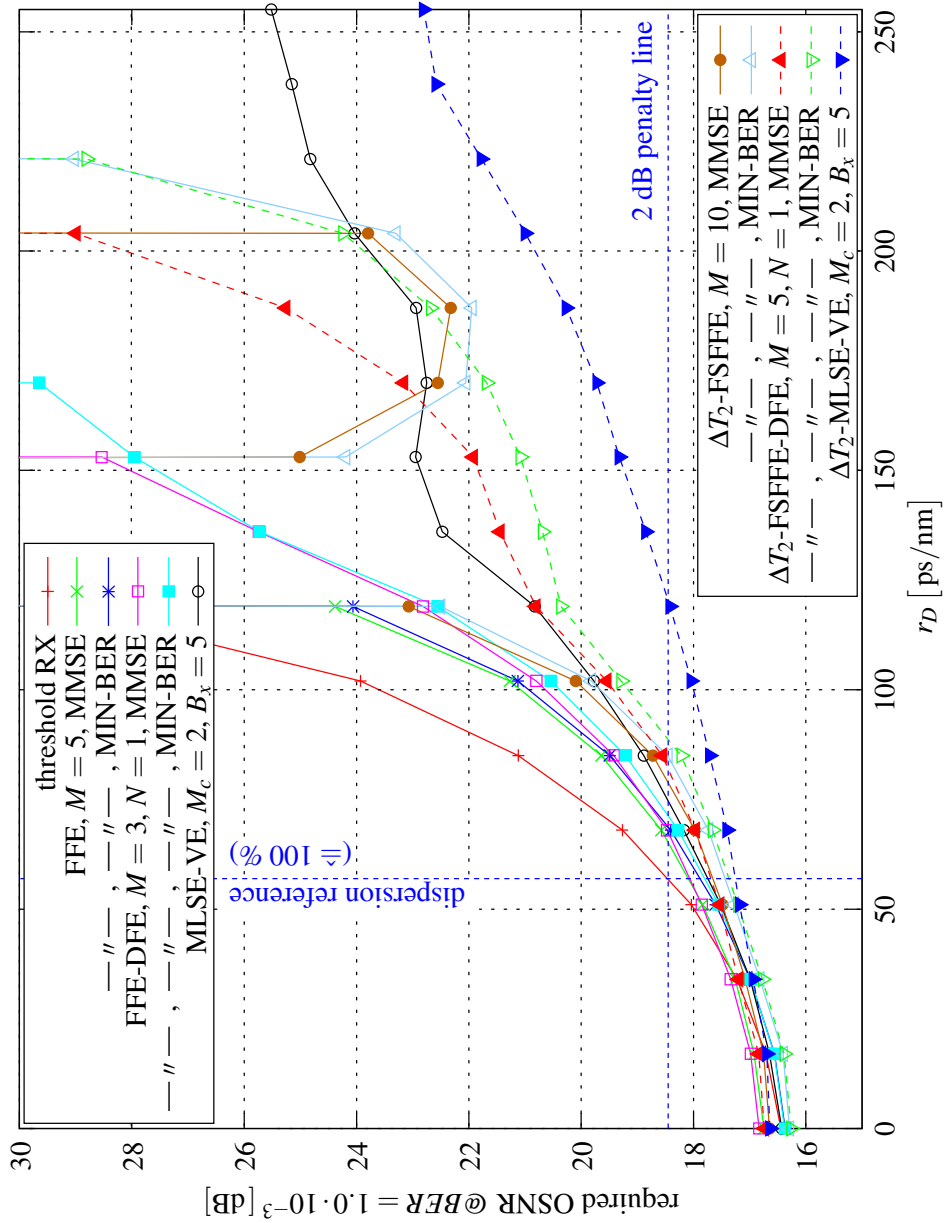**Figure 4.50:** General performance of FFE-DFE EDC vs. threshold detection and MLSE-VE for CD
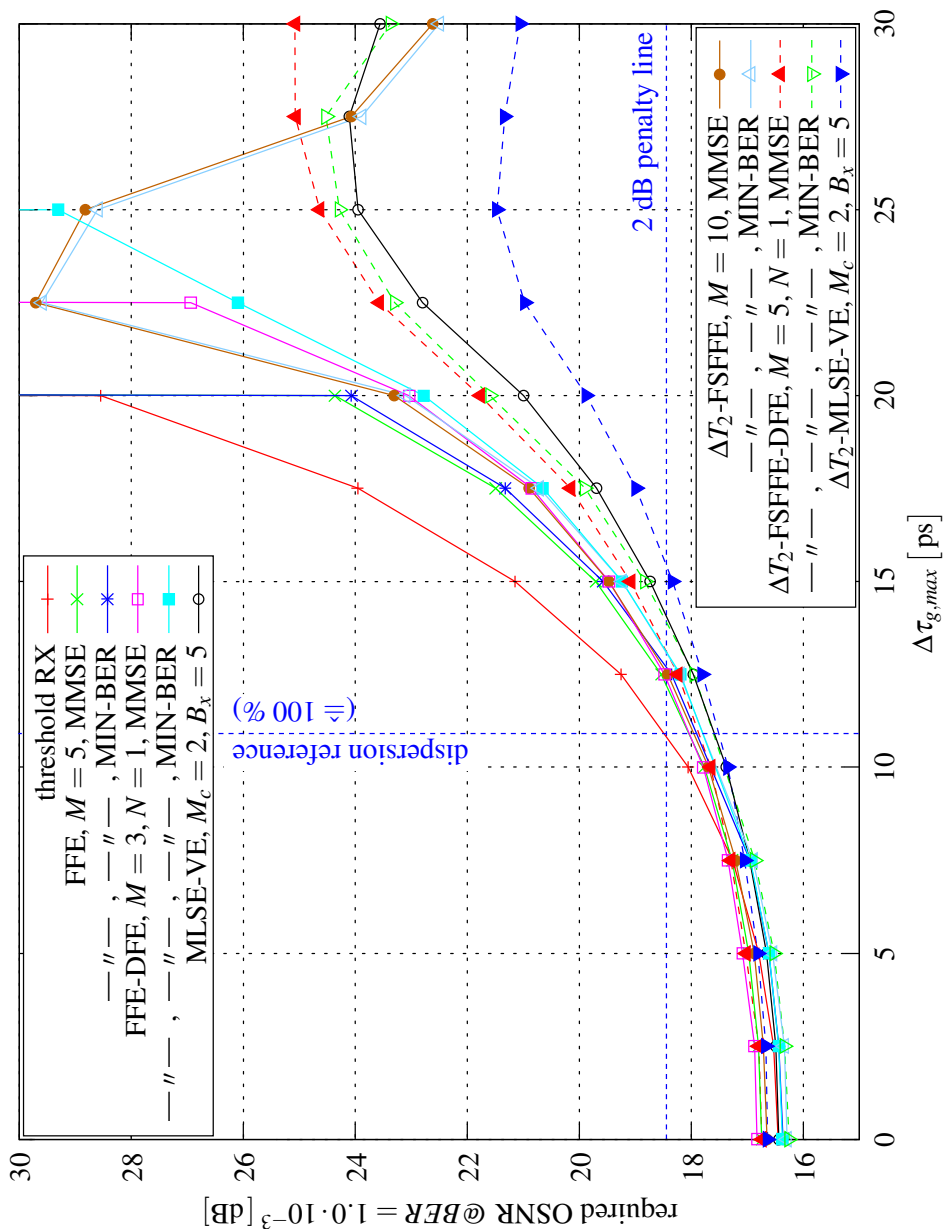
Figure 4.51: General performance of FFE-DFE EDC vs. threshold detection and MLSE-VE for first-order PMD
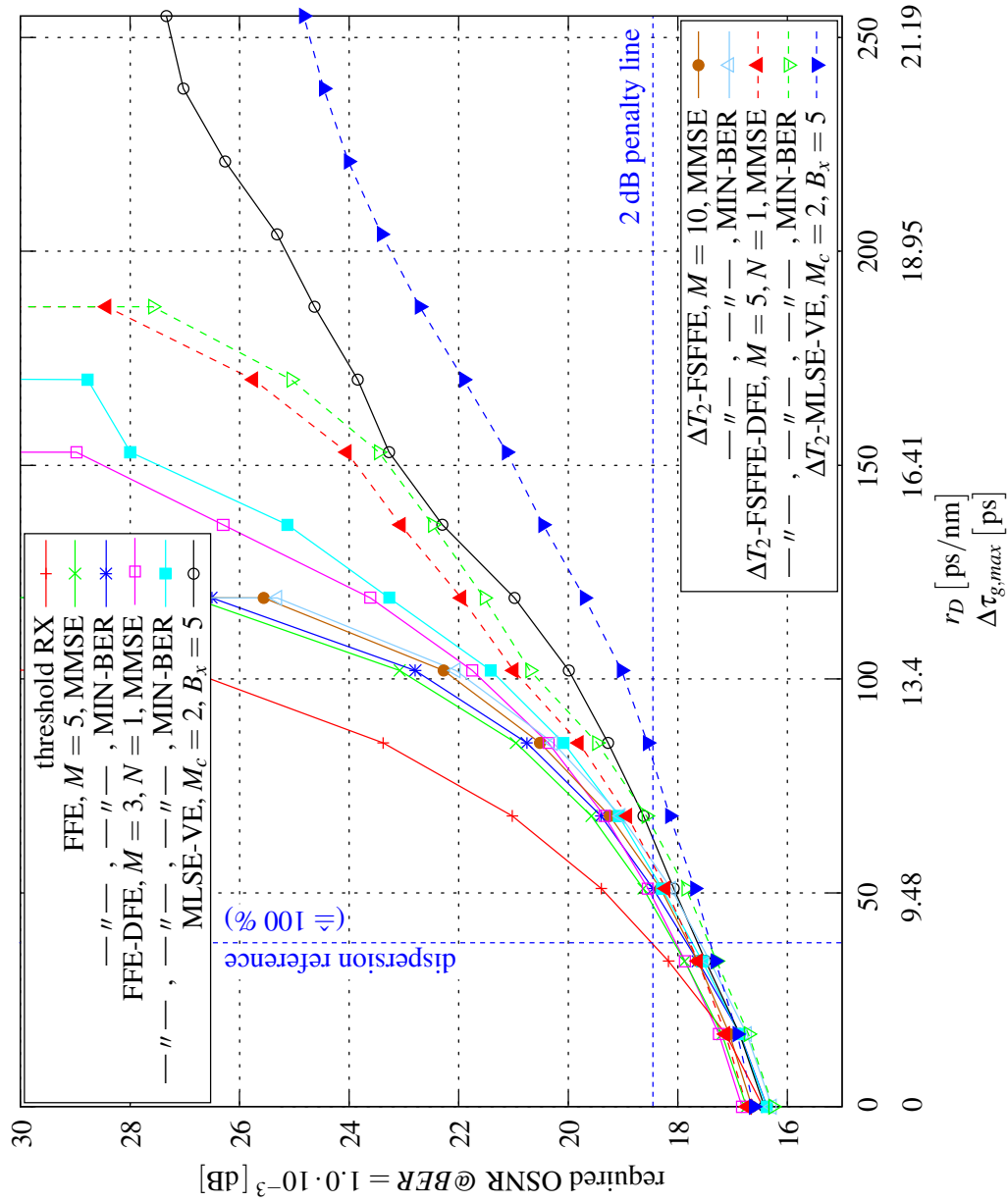
Figure 4.52: General performance of FFE-DFE EDC vs. threshold detection and MLSE-VE for combined CD and first-order PMD
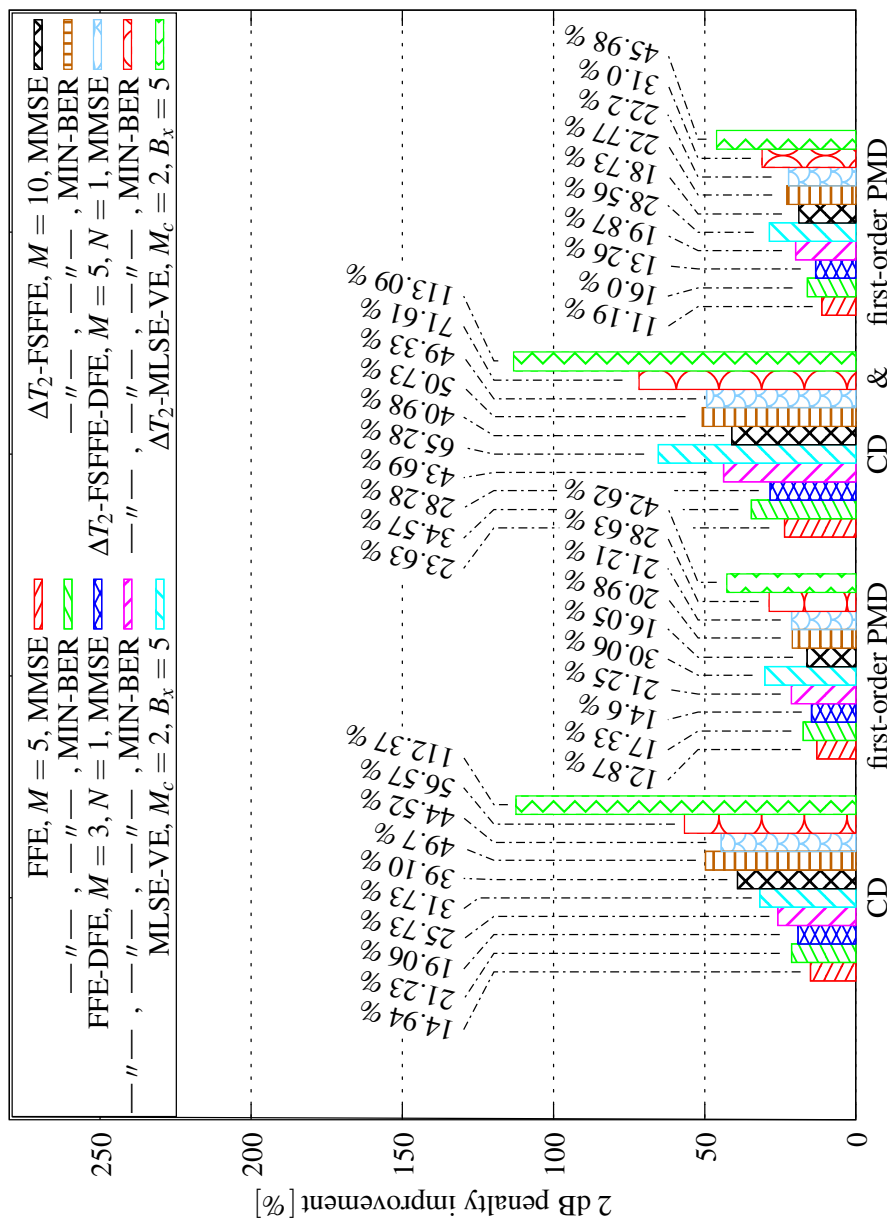
Figure 4.53: 2 dB penalty improvements of FFE-DFE and ΔT_2-FSFFFE-DFE vs. MLSE-VE EDC

Chapter 5

Adaptive Equalizers

Until now we have considered optical channel impairments of CD and PMD as constant during the principal comparison of different EDC methods. However, especially PMD varies over time. The statistical description of the DGD over time and wavelength follows a Maxwell-Boltzmann distribution as introduced in Ch. 3.2.2.2.3. Measurements have shown that the optical link characteristics do not alter in the sub-second domain as in highly dynamic mobile channels but on the basis of hours or days. However, the time scale at which a change of link characteristics happens can be below 10 ms as reported in [111]. Therefore, we have to adapt the coefficients of the FFE-DFE EDC unit to account for the dynamic changes of the OA-IM/DD link characteristic. It would be favorable that the coefficient adaptation process can keep up with the dynamics of the channel fluctuations and with dynamically switched optical network topologies in order to prevent an unintentional breakdown of the OA-IM/DD link. According to the high-speed implementation requirements, the computational overhead of the adaptation algorithm should be kept at a minimum. This is the reason for the deeper investigations which will lead us to algorithmic simplifications.

5.1 LMS Algorithm

5.1.1 Basic Theory

In Ch. 4.2.2.3 we have used the commonly known MSE minimization approach to adjust the equalizer filter coefficients if the OA-IM/DD link characteristics are known in advance. The MSE is a strictly convex function in the coefficients $\check{\mathbf{c}}$ leading to a unique minimum. The geometrical interpretation is that of a multidimensional hyperbola in coefficient space as depicted in Fig. 5.1. If we know the channel characteristics in advance, we have either a direct analytical description or, as in this case, an indirect ergodic measurement of the parabolic MSE surface $E[|e_k(\check{\mathbf{c}})|^2]$ available and can start the optimization procedure to obtain the equalizer coefficients as in Ch. 4.2.2.3. The time needed to measure $E[|e_k(\check{\mathbf{c}})|^2]$ accurately is too long for a fast coefficient adaptation method. Furthermore, the involved

Figure 5.1: Illustration of the LMS adaptation process for $M = 2$ FFE coefficients with additional projection of the contour lines and stochastic gradient vectors onto the coordinate plain

matrix inversion in Eq. (4.62) on page 87 is computationally complex and hard to realize at high processing speeds. That is why we exploit the strict convexity of the MSE surface in another way. At each point $\check{\mathbf{c}} = (c_0, \ldots, c_{M-1}, d_1, \ldots, d_N)^{\mathsf{T}}$ of the MSE hyperbola, the direction to the minimum of $\mathsf{E}[|e_k(\check{\mathbf{c}})|^2]$ is given by the negative gradient vector.

If we start at time instant $k = 0$ with an arbitrary but nonzero initial coefficient vector $\check{\mathbf{c}}_0$, we use the iterative mathematical rule

$$\check{\mathbf{c}}_{k+1} := \check{\mathbf{c}}_k - \frac{1}{2}\mu \underbrace{\nabla_{\check{\mathbf{c}}}\mathsf{E}\left[\left|e_k(\check{\mathbf{c}}_k)\right|^2\right]}_{\substack{\nabla_{\check{\mathbf{c}}} \cdot \text{ and } \mathsf{E}[\cdot] \text{ linear operations} \\ \Rightarrow \text{associative}}}$$

$$= \check{\mathbf{c}}_k - \frac{1}{2}\mu\mathsf{E}\left[\nabla_{\check{\mathbf{c}}}|\underbrace{e_k(\check{\mathbf{c}}_k)}_{=b_k-\check{\mathbf{c}}_k^{\mathsf{T}}\check{\mathbf{x}}_{k_1}\in\mathbb{R}}|^2\right]$$

$$= \check{\mathbf{c}}_k - \frac{1}{2}\mu\mathsf{E}\left[\nabla_{\check{\mathbf{c}}}\left(b_k - \check{\mathbf{c}}_k^{\mathsf{T}}\check{\mathbf{x}}_{k_1}\right)^2\right]$$

$$= \check{\mathbf{c}}_k - \frac{1}{2}\mu \underbrace{\mathsf{E}\left[\nabla_{\check{\mathbf{c}}}\left(b_k - \check{\mathbf{c}}_k^{\mathsf{T}}\check{\mathbf{x}}_{k_1}\right)^2\right]}_{=\mathsf{E}[-2\underbrace{(b_k-\check{\mathbf{c}}_k^{\mathsf{T}}\check{\mathbf{x}}_{k_1})}_{=e_k(\check{\mathbf{c}}_k)}\check{\mathbf{x}}_{k_1}]}$$

$$= \check{\mathbf{c}}_k + \mu\mathsf{E}\left[e_k(\check{\mathbf{c}}_k)\check{\mathbf{x}}_{k_1}\right], \quad \mu \in \mathbb{R}_+, \tag{5.1}$$

to determine the next coefficient values for time instant $k + 1$. In order to account for the temporal dependence of the coefficients, we have introduced an additional temporal subscript

into the notation here. The parameter $\mu \in \mathbb{R}_+$ is the step size which scales the gradient vector and is a means to control the speed of convergence. Eq. (5.1) is known as *gradient* or *steepest descent algorithm* [102]. It is nothing but an iterative solution of the MMSE coefficient adjustment algorithm of Eq. (4.62) on page 87. In this form, it is not yet suitable for application in real-time systems since evaluation of the expectation operator $\mathsf{E}[\cdot]$ requires to have knowledge about the underlying statistics of the argument term $e_k(\check{\mathbf{c}})\check{\mathbf{x}}_{k_1}$. Thus, the problem seems just shifted from measuring $\mathsf{E}[|e_k(\check{\mathbf{c}})|^2]$ in the initial MMSE approach to an ergodic measurement of $\mathsf{E}[e_k(\check{\mathbf{c}})\,\check{\mathbf{x}}_{k_1}]$ instead.

We circumvent this final problem by using a *stochastic gradient* approach [112, 113], in which we just omit the expectation operator in Eq. (5.1). This leads to the LMS adaptation rule

$$\check{\mathbf{c}}_{k+1} := \check{\mathbf{c}}_k + \mu e_k \check{\mathbf{x}}_{k_1}. \tag{5.2}$$

For ease of notation, we omit the explicit dependence of $e_k(\check{\mathbf{c}})$ on $\check{\mathbf{c}}$ and write e_k instead in the LMS algorithm.

Many textbooks [114, 102] analyze the convergence of the LMS algorithm of Eq. (5.2) under the assumption of an i.i.d. input signal to the adaptive filter. Then, the LMS algorithm converges in the mean square sense if the step size μ is chosen to be smaller than the reciprocal of the largest eigenvalue of the input autocorrelation matrix $\mathbf{R}_{\check{\mathbf{x}}_{k_1}\check{\mathbf{x}}_{k_1}}$ [102]. However, we do not have knowledge about the statistics of the input and must rely on empirical simulations to adjust μ. Fig. 5.1 illustrates an example of an adaptation trace on the MSE surface towards the optimal MMSE coefficient vector for $M = 2$. The term *stochastic gradient* becomes obvious in the fact that the stochastic gradient vectors do not point perpendicular to the contour lines towards the steepest. This is the result of having omitted the expectation operator in Eq. (5.2), which, together with the nonzero step size μ, has the consequence that the optimum MMSE coefficient vector cannot be reached exactly. Even near the optimum, we always face some random but small walk, which leads to an excess MSE.

The initial definition of the error signal e_k in Eq. (4.57) on page 85 comprises the transmitted bit b_k as a reference. This implies that the information about the transmitted bit sequence is already available at the RX. This seems to be somewhat curious and contradictory anyway. However, it can still be trimmed for real-world application if we periodically insert a known training sequence at the TX and install some synchronization mechanism at the RX for proper alignment and recognition. For example, the training sequence may be part of a packet header or other control data which is embedded in the payload. In any case, it adds to the overhead already given by FEC. Another possibility to avoid the transmission of a training sequence is to operate the LMS in the so-called *decision-directed mode* [115] with

$$\check{\mathbf{c}}_{k+1} := \check{\mathbf{c}}_k + \mu \underbrace{\left(\hat{b}_k - z_k\right)}_{=:\,e_k} \check{\mathbf{x}}_{k_1}. \tag{5.3}$$

The adaptive LMS FFE-DFE structure featuring the decision-directed mode is illustrated in

Fig. 5.2. Here, we use the already decided bit estimate $\hat{b}_k$ to determine the error signal. Of course, the LMS algorithm converges in the decision-directed mode only if correct decisions are prevalent for the majority of $\hat{b}_k$ [116]. Considered with respect to the electrical RX signal, the vertical eye has still to be open at time instant $k = 0$ with the initial coefficient vector $\check{\mathbf{c}}_0$ as a prerequisite. Some incorrectly received bits do not disturb the adaptation process severely. They may influence adaptation speed or amplify random walk. However, if the eye is closed, too many incorrect bit estimates arrive at the adaptation unit and either equalizer training or completely *blind adaptive* algorithms like the constant modulus (CM) algorithm [117, 118, 119] have to be applied. Since the decision variable z_k in Eq. (4.67) on page 90 for
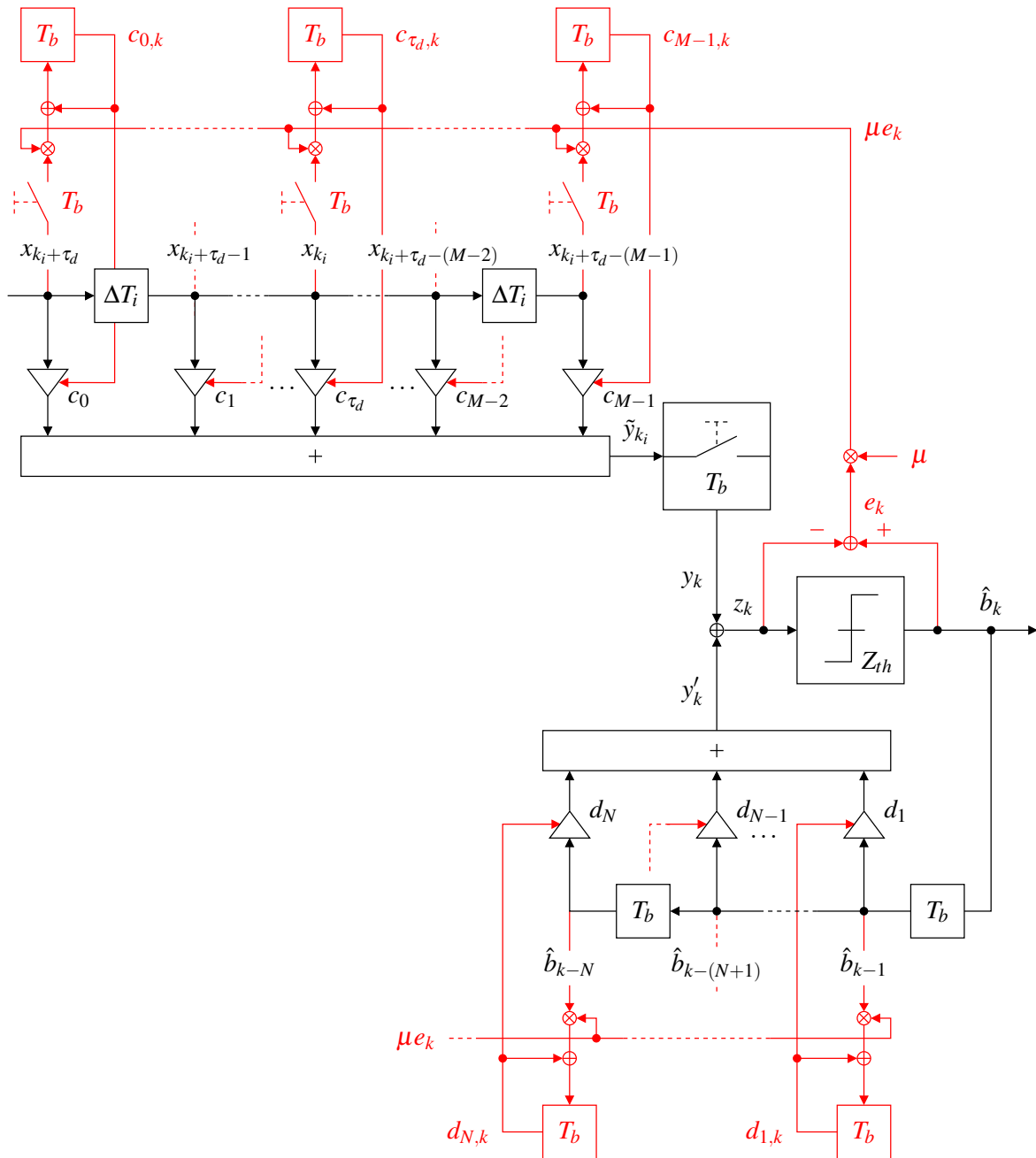

Figure 5.2: Adaptive LMS FSFFE-DFE structure

general ΔT_i-FSFFE-DFEs originates from T_b-spaced subsampling of the ΔT_i-FSFFE output, the LMS adaptation rule of Eq. (5.3) can only generate a new set of coefficients at the rate of $1/T_b$ irrespective of the applied fractionally spaced sample processing. In the block diagram of Fig. 5.2, this has been accounted for by inserting sampling devices for the input samples x_{k_i} forwarded into the adaptation loop. The DFE adaptation loop does not need additional sampling because it already operates at the $1/T_b$ rate.

Beside the ordinary LMS algorithm of Eq. (5.2), further modifications like the normalized least mean square (NLMS) algorithm exist. It is based on the general approach of Eq. (4.58) on page 85 using $\mathrm{E}[|e_k(\check{\mathbf{c}})|^{2n}]$, $n \in \mathbb{N}_1$, as convex optimization cost function. If we turn this general cost function into an iterative, stochastic gradient adaption rule, we arrive at the least mean $2n$-th order (LMN) algorithm [105, 120, 121] given by

$$\check{\mathbf{c}}_{k+1} := \check{\mathbf{c}}_k + n\mu e_k^{2n-1}\check{\mathbf{x}}_{k_1}. \tag{5.4}$$

The corresponding hardware implementation has to generate the required error signal e_k^{2n-1}. Compared to the single subtraction of Fig. 5.2 to get the error signal e_k, the additional multiplications to calculate its power with respect to the exponent $2n-1$ increase the computational overhead and may limit high speed operation.

For the sake of completeness, recursive least squares (RLS) and Kalman filters (KFs) as other popular algorithms for adaptive parameter adjustment shall be mentioned here. Since these require complex matrix operations, they are not feasible at high processing speeds. Other known and already evaluated techniques are based on dithered random search [27, 122], on feedback signals generated by eye monitoring [123, 124] or on FEC evaluation with appropriate feedback to the EDC unit [125]. Some of them have already been applied to high-speed analog FFEs [24, 107, 126, 127, 128] for 40 Gbit/s systems. However, the convergence rate of random search techniques is quite slow [129] compared to the directed, gradient based methods like the LMS algorithm.

5.1.2 Convergence Behavior

After having discussed the theoretical basics for the LMS algorithm, we turn to its evaluation in OA-IM/DD links equipped with an adaptive FFE-DFE EDC unit. Thereby, we are at least interested in the adaptation speed or convergence rate λ_{LMS} and the coefficient accuracy or adaptation offset $\Delta_{rel,LMS}$. The adaptation rate is primarily influenced by the step size μ and describes the reaction of the adaptation algorithm to abrupt changes in the OA-IM/DD link characteristics given by CD, mainly time-variant PMD and OSNR. It also depends on the number of FFE-DFE coefficients since the higher this number the longer the adaptation time will be. The reason is that the variance of the error signal e_k increases with higher dimensionality of the involved stochastic gradient vectors in the LMS adaptation rule. That is why we focus without loss of generality and according to our results in Ch. 4.3 on a FFE with

$M = 5$ coefficients and the decision delay set to $\tau_d = 2$ for these investigations. The performance measure of accuracy is taken in steady state and expresses itself by the possible offset to the directly calculated MMSE coefficient vector $\check{\mathbf{c}}_{MMSE}$ according to the procedure presented in Ch. 4.2.2.3. Both performance measures, λ_{LMS} and $\Delta_{rel,LMS}$, will be defined during the course of discussing the results for the LMS algorithm. The underlying OA-IM/DD link for the evaluation shall simultaneously be affected by CD and first-order PMD at a length of $L_f = 5$ km and ASE noise set to $\gamma_{OSNR} = 21$ dB. This parameter set corresponds to the region between noise and dispersion-limited region. Due to the randomness of noise, it is obvious that operation towards the noise-limited region would be less advantageous for the adaptation process than towards the dispersion-limited one. Thus, our operation point states a compromise. Furthermore, the initial coefficient vector is the unit vector in the τ_d-th dimension given by

$$\check{\mathbf{c}}_0 := \mathbf{1}_{\tau_d}, \tag{5.5}$$

i.e. we study the transient behavior right at link setup as worst case scenario for the adaptation process.

Fig. 5.3(a) shows the average behavior of the squared error magnitude $|e_k|^2$ over time for an adaptation step size of $\mu = 0.01$. Note that the value range for μ corresponds to our normalized representation of the physical system model used for simulations while real-world implementation might need some scaling. Beside the discrete time index k, we see the abscissa also labeled with absolute time in μs to give an impression of the absolute adaptation speed. Despite the averaging over 1000 adaptation runs, $|e_k|^2$ shows still heavy oscillations. Considering its envelope, we can identify two regions. The first one starts at $k = 0$ and shows a high squared error magnitude with steep decay of the envelope. The second one starting at around $k \approx 10000 - 20000 \, (\hat{=} \, t \approx 0.23 - 0.47 \, \mu\text{s} \, @ \, R_b = 42.7 \, \text{Gbit/s})$ shows a constant envelope and can be considered as steady state. However, oscillation of the mean squared error magnitude representing the random walk around the optimum MMSE coefficient setup $\check{\mathbf{c}}_{MMSE}$ is still present there.

In order to have an objective measure for the adaptation process, which allows us to extract a tendency from the noisy data by an analytical mathematical description, we apply some smoothing with a post-processing moving average (MAV) filter [102]. This MAV filter performs a simple averaging over 1000 samples of $|e_k|^2$ with

$$MAV\left(|e_k|^2\right) := \frac{1}{1000} \sum_{k}^{k+999} |e_k|^2, \quad k = K - 1000, \ldots, 0; \, K \in \mathbb{N}_{1000}. \tag{5.6}$$

The parameter $K \in \mathbb{N}_{1000}$ represents the sequence length for which $|e_k|^2$ has been simulated up to steady state. In general, we have to set $K \gg 1000$ (e.g. $K = 151000 \hat{=} t \approx 3.54 \, \mu\text{s} \, @ \, R_b = 42.7 \, \text{Gbit/s}$ in Fig. 5.3(a)) to reach steady state behavior reliably. Letting k run from $K - 1000$ down to 0 in Eq. (5.6) can be interpreted as processing the squared error magnitudes $|e_k|^2$ in reverse order as illustrated in Fig. 5.5(a). The reason for this implicit reversal is to
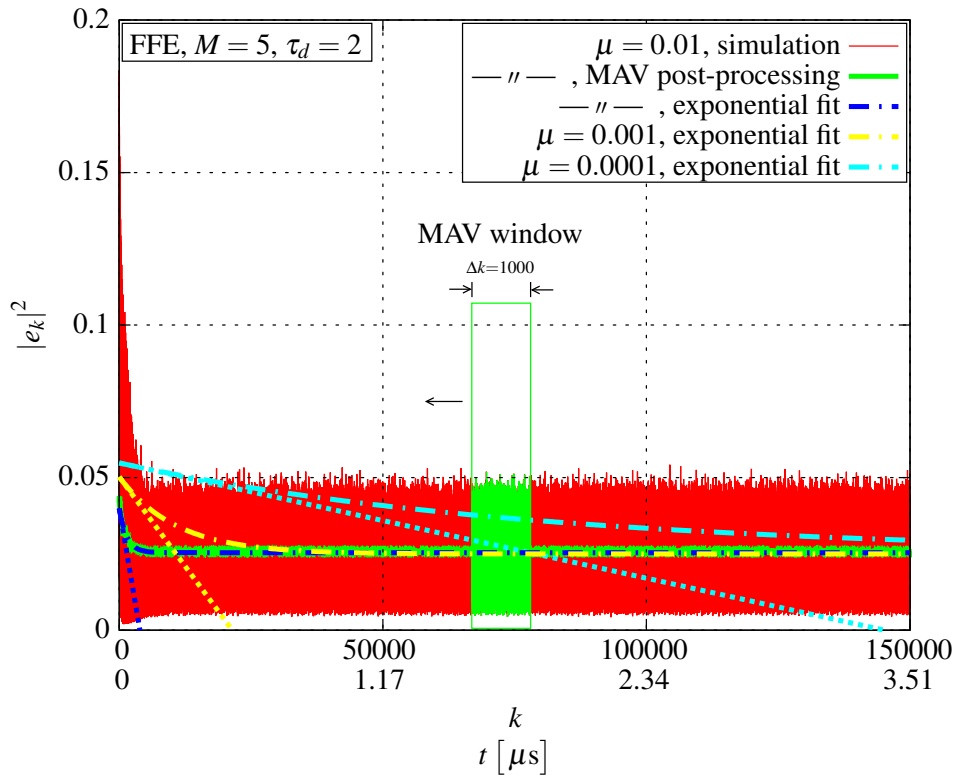
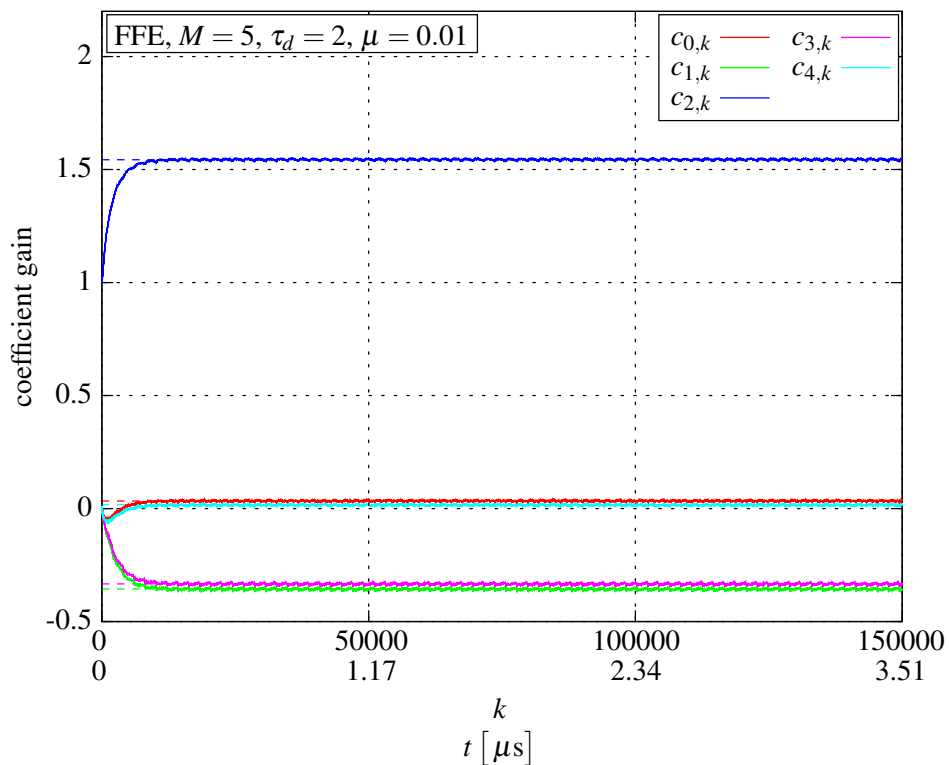(a) Squared error magnitude with influence of the adaptation step size

(b) LMS coefficients for $\mu = 0.01$ (constant MMSE coefficients dashed)

Figure 5.3: Average LMS-FFE adaptation behavior ($L_f = 5$ km, combined CD and first-order PMD ($r_D = 85$ ps/nm, $\Delta\tau_{g,max} = 12.36$ ps), $\gamma_{OSNR} = 21$ dB, 1000 adaptation runs averaged)

have a fair and proper internal state of the MAV filter when it comes to process the usually higher magnitudes of $|e_k|^2$ for the region $k \approx 0$. Otherwise, if the MAV filter would use the common input order starting at $k = 0$ with zero initial state, the already high values of $|e_k|^2$ in this region would experience an additional emphasis leading to a falsified impression. Thus, the reversal guarantees that we evaluate the adaptation behavior from steady but not from uninitialized state. The result of MAV post-processing can be seen in the correspondingly labeled curve in Fig. 5.3(a) for $\mu = 0.01$.

In a next step, a least squares exponential curve fitting routine which complies with the mathematical model

$$\arg \min_{A,B,C \in \mathbb{R}_+} \left| MAV \left(|e_k|^2 \right) - \left(A\mathrm{e}^{-Bk} + C \right) \right|^2 \tag{5.7}$$

is applied to the result of MAV filtering. The exponential part $A\mathrm{e}^{-Bk}$ of the curve fitting in Eq. (5.7) shall account for the first region of the smoothed squared error magnitude data whereas the constant C shall represent steady state. The results of this exponential fit with offset have been plotted for different step sizes in Fig. 5.3(a) (dash-dotted curves). The fitted curve for $\mu = 0.01$ shows good agreement with the MAV filter output and proves graphically the validity of the underlying mathematical model of Eq. (5.7).

The use of such a model allows us to derive the (initial) adaptation rate as its slope at $k = 0$ with

$$\lambda_{LMS} := \left| \frac{\partial}{\partial k} \left(A\mathrm{e}^{-Bk} + C \right) \right|_{k=0} = AB. \tag{5.8}$$

This is an intuitive definition since a steeper slope at the beginning of the adaptation process coincides with a higher adaptation rate. We can interpret it as the (linear) per time step reduction of the squared error magnitude $|e_k|^2$. The adaptation rates are indicated visually by the tangents in Fig. 5.3(a). Table 5.1 contains the corresponding numerical values of λ_{LMS} for different step sizes.

If we extend Eq. (5.7) by T_b with

$$A\mathrm{e}^{-\frac{B}{T_b}k \cdot T_b} + C \quad \Longrightarrow \quad \left| \frac{\partial}{\partial kT_b} \left(A\mathrm{e}^{-\frac{B}{T_b}kT_b} + C \right) \right|_{kT_b=0} \quad \Longrightarrow \quad \lambda'_{LMS} := \frac{AB}{T_b} = \frac{\lambda_{LMS}}{T_b}, \tag{5.9}$$

the resulting adaptation rate λ'_{LMS} can be interpreted as a squared error reduction frequency. Therefore, we apply the dimension of a frequency in Table 5.1 to this extended parameter.

The other performance measure $\Delta_{rel,LMS}$ addresses the adaptation accuracy and is extracted by considering the coefficient offsets with respect to the constant MMSE coefficients in steady state. It shall be defined by the square root of the weighted sum of squared differences between the LMS coefficients and the MMSE coefficients. The definition of this mean steady

	$\mu = 0.01$	$\mu = 0.001$	$\mu = 0.0001$
λ_{LMS}	1.02e-5	2.34e-6	3.78e-7
λ'_{LMS} [kHz]	434.62	99.93	16.13
$\Delta_{rel,LMS}$	2.23e-3	5.42e-4	2.20e-1

Table 5.1: Adaptation rates and mean steady state coefficient offsets of the LMS algorithm for different step sizes

state coefficient offset is given by

$$\Delta_{rel,LMS} := \sqrt{\sum_{m=0}^{M-1} \frac{\left|c_{MMSE,m}\right|}{\left|\mathbf{c}_{MMSE}\right|} \left|c_{LMS,m} - c_{MMSE,m}\right|^2} \tag{5.10}$$

and has the form of a standard deviation. If required, it can easily be extended to investigations including a DFE. Since coefficients with a larger magnitude are more likely to influence equalization performance, the weighting factor of $\left|c_{MMSE,m}\right| / \left|\mathbf{c}_{MMSE}\right|$ in Eq. (5.10) takes this into account. For the results based on Eq. (5.10), we derive a mean steady state value for $\mathbf{c}_{LMS}$ taken from the last 1000 coefficient values, whose corresponding squared error values $\left|e_k\right|^2$ have been used to initialize the MAV filter of Eq. (5.6), i.e.

$$\mathbf{c}_{LMS} := \frac{1}{1000} \sum_{k=K-1000}^{K-1} \mathbf{c}_k. \tag{5.11}$$

Fig. 5.3(b) contains the temporal behavior of the coefficients, and the dashed lines represent the MMSE coefficients aside. We can observe that the LMS coefficients visually approximate the MMSE coefficients well in steady state for $\mu = 0.01$. The very low value of $\Delta_{rel,LMS} = 2.23$e-3 for $\mu = 0.01$ coincides with this impression. Since the FFE has not yet reached steady state for $\mu = 0.0001$ within the considered window of Fig. 5.3(b), we observe a large deviation of $\Delta_{rel,LMS} = 0.22$. If we would enlarge the simulation window, this value should decrease even below the others because the random walk effects are less for lower adaptation step sizes.

Recalling again that PMD might change its characteristics within a time span of around 10 ms [111], which corresponds to a rate of 100 Hz for changes of OA-IM/DD link characteristics, we can finally state that LMS adaptation is able to react fast and accurate. If we stress the adaptation process with a transient change of the channel characteristics, it converges within less than a microsecond as represented by Fig. 5.3(a) and the corresponding performance measures. This is almost three orders of magnitude below the reported PMD transition time. We can expect therefore that an adaptive LMS FFE-DFE can keep pace with variations of optical channel impairments and even track its behavior. This is very important since it can prevent a link from total breakdown or aid in the installation of optically switched networks.

5.2 Reduced Complexity LMS Algorithms

Although we have seen that the standard LMS algorithm converges sufficiently fast and accurate in OA-IM/DD links, its implementation in parallel to an already running FFE-DFE imposes further challenges at the very high bit rates considered here. In the best case, the adaptation loop should not exceed a single processing cycle of the FFE-DFE. Despite its simple structure, Eqs. (5.2) or (5.3) show that at least three consecutive steps have to be performed within a processing interval T_b:

1. the multiplication of the error signal e_k with the adaptation step size μ to get the term μe_k,

2. $M+N$ parallel multiplications of the term μe_k with the elements of the FFE-DFE input sample vector $\check{\mathbf{x}}_{k_1}$ to reach at the stochastic gradient term $\mu e_k \check{\mathbf{x}}_{k_1}$, and

3. further $M+N$ parallel additions to calculate the final coefficient updates $\check{\mathbf{c}}_{k+1} = \check{\mathbf{c}}_k + \mu e_k \mathbf{x}_{k_1}$.

If we take into account the fact that the straightforward FFE-DFE operation already needs $M+N$ parallel multiplications followed by $\lceil \mathrm{ld}(M+N) \rceil$ consecutive addition stages and the final slicer operation, any relaxation of the timing budget is favorable. This justifies any reasonable temporal relaxations of the calculations in the adaptation loop to achieve an adaptive digital FFE-DFE EDC unit. The idea is to use coarsely quantized values of μ, e_k and the FFE related components $\mathbf{x}_{k_1}$ of the EDC input sample vector $\check{\mathbf{x}}_{k_1}$ in order to replace the multiplications by simple sign operations as already suggested in literature for the LMS algorithm [102]. Coarse quantization and the corresponding multiplications can easily be implemented by comparators in the analog or digital domain. However, the quantized versions of the LMS algorithm may have some impact on convergence speed and accuracy. Therefore, we study the quantized versions of the LMS algorithm for the special signal characteristics of an OA-IM/DD link in this chapter. The results of these algorithmic simplifications are still presented with floating-point precision for the input signal vector $\check{\mathbf{x}}_{k_1}$, the FFE-DFE coefficients $\check{\mathbf{c}}_k$ and the FFE-DFE output z_k in the analog, discrete-time domain. A digital implementation should be straightforward. As we will see, a tradeoff solution which still meets nearly the same performance as the standard LMS algorithm is favorable. A concise summary about the main ideas and initial results have already been presented in [98] whereas we develop a more systematic analysis here.

5.2.1 Error Sign Quantization

The error signal e_k occurs as positive and negative values at the output of a FFE-DFE EDC unit in an OA-IM/DD link and has approximately zero mean. The indication of the error

signal with respect to the different TX signal levels in Fig. 4.15(b) on page 85 shows a rough graphical proof of this statement. A coarse quantization of e_k must always retain the sign of e_k because the sign controls the direction of the gradient term in the LMS adaptation rule. Therefore, if we want to quantize the error signal with the most coarsest resolution, the coefficient update equation becomes

$$\check{\mathbf{c}}_{k+1} := \check{\mathbf{c}}_k + \mu \operatorname{sgn}(e_k) \check{\mathbf{x}}_{k_1} \tag{5.12}$$

with the definition of

$$\operatorname{sgn}(x) := \left\{ \begin{array}{lll} x \geq 0 & : & 1 \\ x < 0 & : & -1 \end{array} \right. , x \in \mathbb{R}, \tag{5.13}$$

for the sign function. We call this version error-sign LMS (ES-LMS) algorithm. Fig. 5.4 documents the necessary changes to the block diagram of Fig. 5.2. We only need an additional comparator after the determination of the error signal. In a digital two's complement representation of e_k, the comparator for sign detection reduces to simply picking up the most significant bit (MSB) of e_k.
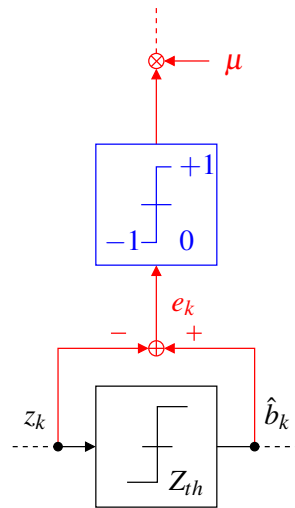

Figure 5.4: Modification of Fig. 5.2 to obtain the ES-LMS algorithm

Using the adaptation rule of Eq. (5.12), the same simulations as for the LMS algorithm have been executed. The results are depicted in Fig. 5.5 and listed in Table 5.2. Concerning the course of $|e_k|^2$ in Fig. 5.5(a) and the adaptation rates in Table 5.2, a comparison to the LMS algorithm shows that the ES-LMS algorithm adapts almost three times faster for all adaptation step sizes. The LMS algorithm scales the gradient term $\mu e_k \check{\mathbf{x}}_{k_i}$ by the actual error magnitude $|e_k| \in \mathbb{R}_+$ while the ES-LMS has a constant scaling set to $|e_k| := 1$. Therefore, the ES-LMS algorithm accelerates the adaptation process in the first phase of adaptation but amplifies random walk. The mean steady state coefficient offset for $\mu = 0.01$ calculates to $\Delta_{rel,ES-LMS} = 2.43\text{e-}2$ and is one order of magnitude larger than the value of $\Delta_{rel,LMS} = 2.23\text{e-}3$ for the LMS algorithm. The mean steady state coefficient offset compared to the MMSE coefficients becomes also visible in the coefficient plot of Fig. 5.5(b).
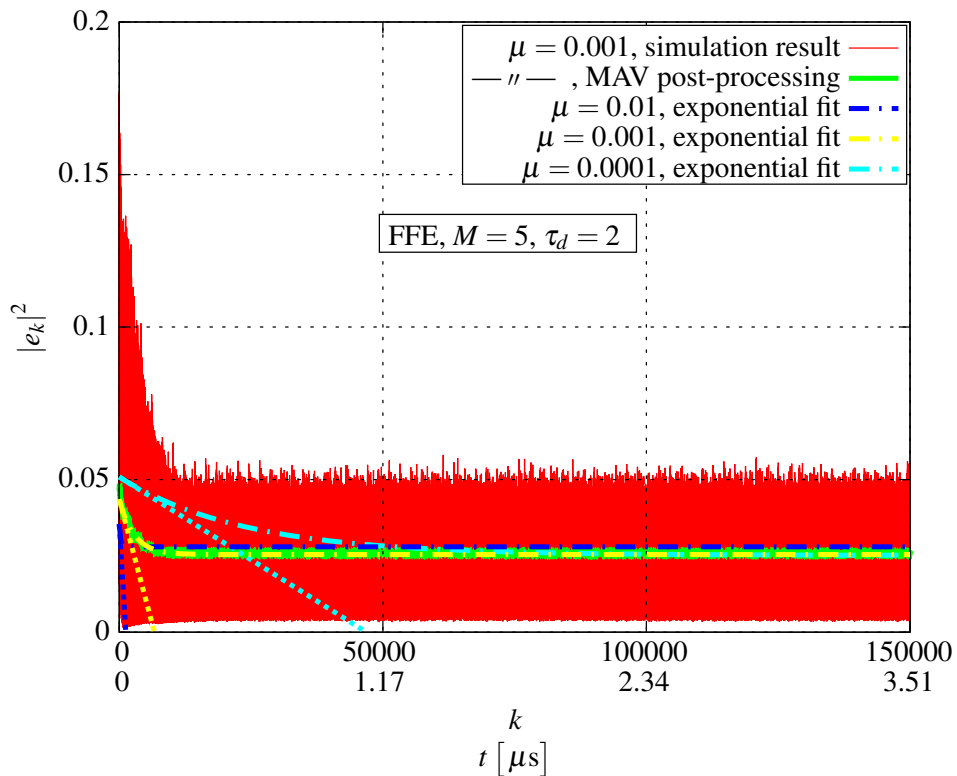
(a) Squared error magnitude with influence of the adaptation step size
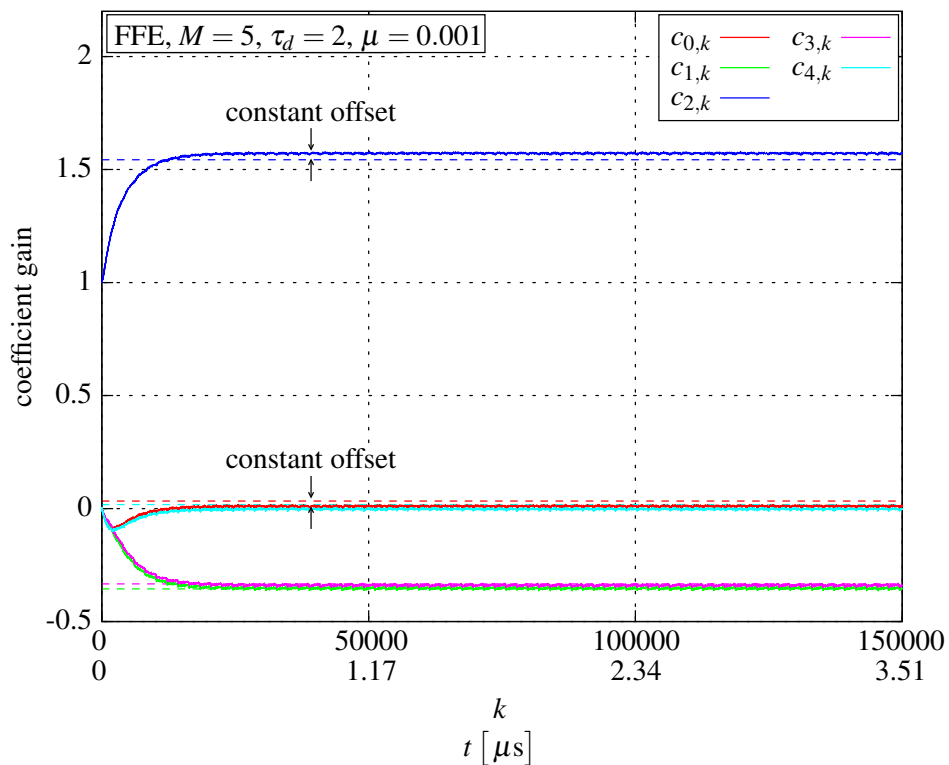
(b) ES-LMS coefficients for $\mu = 0.001$ (constant MMSE coefficients dashed)

Figure 5.5: Average ES-LMS-FFE adaptation behavior ($L_f = 5$ km, combined CD and first-order PMD ($r_D = 85$ ps/nm, $\Delta\tau_{g,max} = 12.36$ ps), $\gamma_{OSNR} = 21$ dB, 1000 adaptation runs averaged)

As a conclusion, we may state that the ES-LMS algorithm is more susceptible to the choice of the adaptation step size. If we can tolerate a much slower adaptation rate adjusted by a small μ, the mean steady state coefficient offset to the MMSE coefficients can be reduced and made comparable to the LMS behavior.

	$\mu = 0.01$	$\mu = 0.001$	$\mu = 0.0001$
λ_{ES-LMS}	2.84e-5	6.55e-6	1.08e-6
$\lambda'_{ES-LMS}\,[\text{kHz}]$	1211.10	279.50	46.33
$\Delta_{rel,ES-LMS}$	2.43e-2	2.44e-2	1.33e-2

Table 5.2: Adaptation rate and mean steady state coefficient offsets of the ES-LMS algorithm for different adaptation step sizes

5.2.2 FFE Input Sample Quantization

The next step of simplification refers only to the FFE input vector $\mathbf{x}_{k_1}$ since the DFE input is already quantized by the slicer, which has already produced the bit estimates $\hat{b}_{k-1}, \ldots, \hat{b}_N$ in previous processing cycles. The proposed sign operation to the elements of $\mathbf{x}_{k_1}$ in [102] would be of no advantage in OA-IM/DD links since direct detection results in $x_{k_1} \geq 0$ and signal-dependent noise even makes optimization of the simple threshold RX necessary. Therefore, we have to change the sign approach by introducing a quantizer for the EDC input samples with

$$Q_{Q_x}(x_{k_1}) := \frac{1}{Q_x - 1} \cdot \begin{cases} \left\lfloor x_{k_1}(Q_x - 1) + \frac{1}{2} \right\rfloor & : \ x_{k_1} < 1 - \frac{1}{2(Q_x-1)} \\ Q_x - 1 & : \ x_{k_1} \geq 1 - \frac{1}{2(Q_x-1)} \end{cases} \ , \quad Q_x \in \mathbb{N}_2. \quad (5.14)$$

The number of quantization steps $Q_x \in \mathbb{N}_2$ is an adjustable parameter leading to the quantizer levels

$$0, \frac{1}{Q_x - 1}, \frac{2}{Q_x - 1}, \ldots, \frac{Q_x - 2}{Q_x - 1}, 1, \quad (5.15)$$

for x_{k_1} and forces $0 \leq Q_{Q_x}(x_{k_1}) \leq 1$ for our normalized signal representation. The subscript $\cdot_x$ in Q_x actually refers to x_{k_1}. However, we omit the additional subscript k_1 for ease of notation and readability.

We reach the lowest resolution and computational complexity for $Q_x = 2$. In this case, the adaptation rule for the quantized input LMS (QI-LMS) algorithm applied to the FFE is

$$\mathbf{c}_{k+1} := \mathbf{c}_k + \mu e_k Q_2(\mathbf{x}_{k_1}). \quad (5.16)$$

The quantization function is applied to each element of the FFE input sample vector $\mathbf{x}_{k_1}$. Fig. 5.6 shows the corresponding block diagram supplements for one branch of the adaptation loop. The quantizer element has to be supplied for each branch and implementation

cost is therefore much higher than for the ES-LMS algorithm with only one additional comparator for the error signal. Another possibility for implementation of the QI-LMS algorithm would be to have just one quantizer at the input to the FFE followed by a clocked delay chain in parallel to the FFE carrying the elements of $Q_2(\mathbf{x}_{k_1})$.
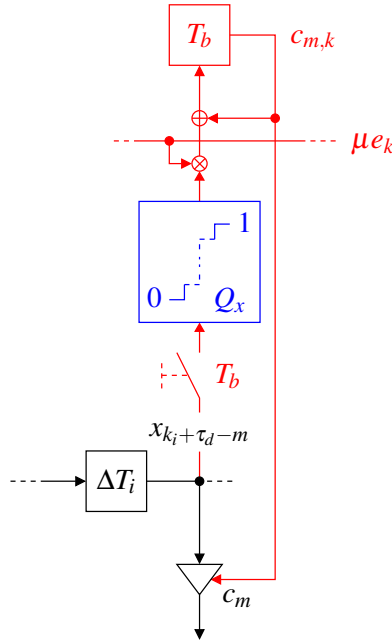

Figure 5.6: Modification of Fig. 5.2 to obtain the QI-LMS algorithm

Fig. 5.7 shows the simulation results for the QI-LMS algorithm for $Q_x = 2$. The principal squared error behavior in Fig. 5.7(a) does not deviate much from the standard LMS or ES-LMS algorithms. The adaptation rate of $\lambda'_{QI-LMS} = 426.11$ kHz for $\mu = 0.001$ according to Table 5.3 is slightly lower than that of the standard LMS with $\lambda'_{LMS} = 434.62$ kHz for $\mu = 0.01$. Having a look at the coefficient values for this step size in Fig. 5.7(b) reveals, that the steady state offset has increased compared to the ES-LMS algorithm. For $\mu = 0.01$ and 0.001 it is even one order of magnitude larger compared to the ES-LMS and even two orders for the standard LMS algorithm. Although the adaptation rates are comparable for the QI-LMS and the ES-LMS algorithm, the accuracy of the QI-LMS version seems to be quite susceptible. The geometrical interpretation of the term $\mu e_k Q_2(\check{\mathbf{x}}_{k_1})$ in Eq. (5.16) as a gradient vector means that we only allow certain directions to follow during the coefficient update process. We can only reach the optimum MMSE coefficient vector $\check{\mathbf{c}}_{MMSE}$ if we can write it as a linear combination of the starting coefficient vector $\check{\mathbf{c}}_0$ and some of the possible quantized gradients. The best approaching one of those linear combinations determines the offset we have to tolerate in Fig. 5.7(b). In order to reach the same level of accuracy, we have two possibilities: we either reduce the adaptation step size to compensate for the coarse quantization of the EDC input samples with $Q_x = 2$ at the expense of reducing the adaptation rate, too, or we increase the resolution of the input quantization.
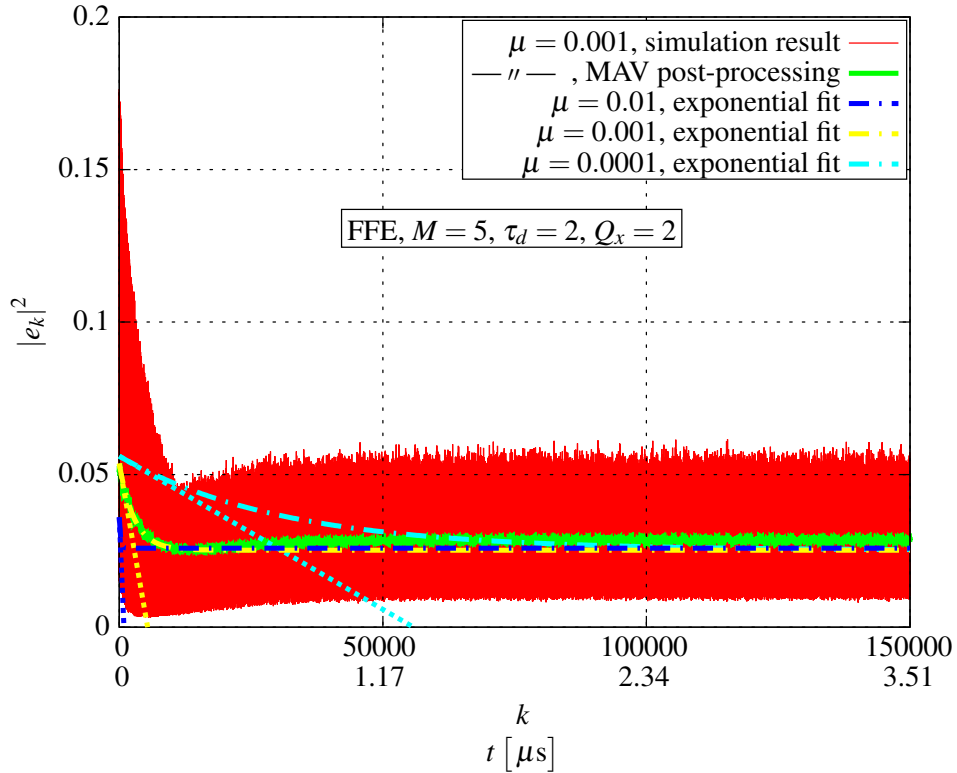
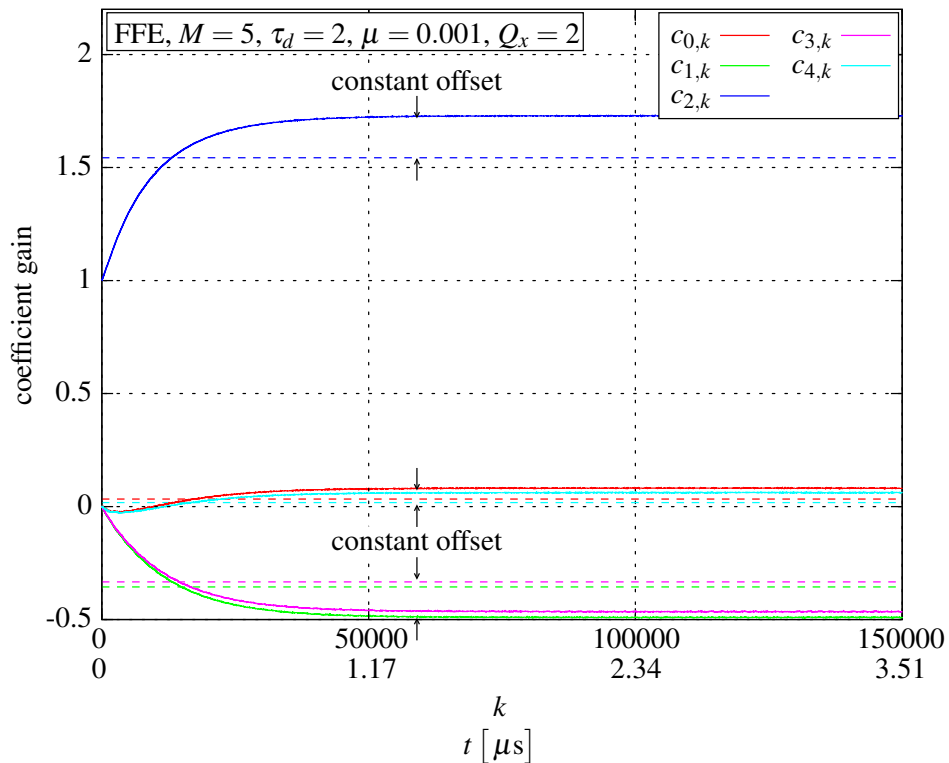(a) Squared error magnitude with influence of the adaptation step size

(b) QI-LMS coefficients $\mu = 0.001$ (constant MMSE coefficients dashed)

Figure 5.7: Average QI-LMS-FFE adaptation behavior for $Q_x = 2$ ($L_f = 5$ km, combined CD and first-order PMD ($r_D = 85$ ps/nm, $\Delta\tau_{g,max} = 12.36$ ps), $\gamma_{OSNR} = 21$ dB, 1000 adaptation runs averaged)

	$\mu = 0.01$	$\mu = 0.001$	$\mu = 0.0001$
λ_{QI-LMS}	4.06e-5	9.98e-6	1.00e-6
λ'_{QI-LMS} [kHz]	1735.48	426.11	42.90
$\Delta_{rel,QI-LMS}$	1.70e-1	1.70e-1	2.66e-2

Table 5.3: Adaptation rate and mean steady state coefficient offsets of the QI-LMS algorithm for $Q_x = 2$ and different adaptation step sizes

Fig. 5.8 and Table 5.4 show that an increase of the signal resolution to $Q_x = 3$ with adaptation rule

$$\check{\mathbf{c}}_{k+1} := \check{\mathbf{c}}_k + \mu e_k \mathbf{Q}_3 \left(\check{\mathbf{x}}_{k_1} \right) \tag{5.17}$$

improves the adaptation performance in terms of accuracy for $\mu = 0.01$ and 0.001 again. The visible coefficient offset in Fig. 5.8(b) is comparable to the ES-LMS algorithm with almost the same numerical values for the mean steady state coefficient offset. However, the adaptation rates have even decreased below the values of the standard LMS algorithm in Table 5.1.

	$\mu = 0.01$	$\mu = 0.001$	$\mu = 0.0001$
λ_{QI-LMS}	7.62e-6	2.19e-6	3.29e-7
λ'_{QI-LMS} [kHz]	325.42e3	93.70e3	14.05e3
$\Delta_{rel,QI-LMS}$	3.17e-2	3.43e-2	2.50e-1

Table 5.4: Adaptation rate and mean steady state coefficient offsets of the QI-LMS algorithm for $Q_x = 3$ and different adaptation step sizes

5.2.3 Thresholded Error Sign Quantization

In principle, the next step of simplification would be to combine the ES-LMS and QI-LMS algorithm. However, the results in [98] have shown that, at least for the coarsest quantization with error sign and $Q_x = 2$ for the input sample vector $\mathbf{x}_{k_1}$ to the adaptation loop, the coefficient offset increases further. This is not surprising as the individual investigations for the ES-LMS and QI-LMS algorithms have already shown a deviation. Especially, the latter one shows worse performance at higher implementation cost in terms of quantizer units while the ES-LMS is quite simple in its structure but shows a faster adaptation rate at comparatively small impact on accuracy compared to the standard LMS algorithm. Consequently, we have to seek for methods to reduce the offset from the precalculated MMSE coefficients for further improvement. Recalling that the reason for the mean steady state coefficient offset
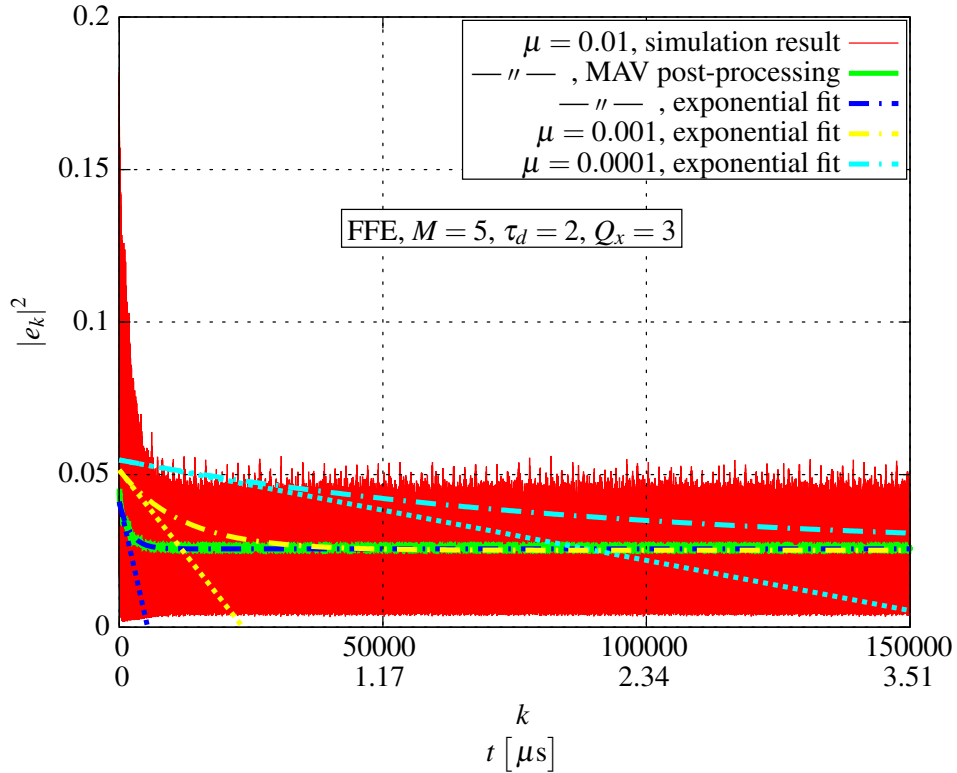
(a) Squared error magnitude with influence of the adaptation step size
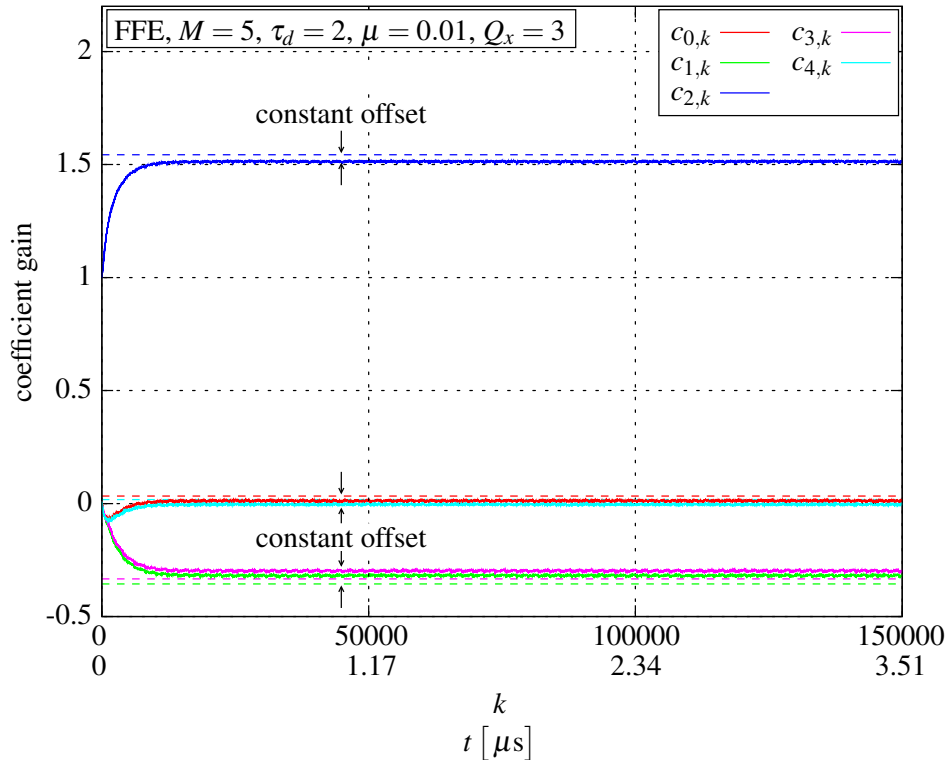

(b) QI-LMS coefficients for $\mu = 0.01$ (constant MMSE coefficients dashed)

Figure 5.8: Average QI-LMS-FFE adaptation behavior for $Q_x = 3$ ($L_f = 5$ km, combined CD and first-order PMD ($r_D = 85$ ps/nm, $\Delta\tau_{g,max} = 12.36$ ps), $\gamma_{OSNR} = 21$ dB, 1000 adaptation runs averaged)

is random walk around the optimum MMSE coefficient vector $\check{\mathbf{c}}_{MMSE}$, we introduce a measure within the adaptation rule, which indicates that the adaptation process has reached the optimum MMSE coefficient vector $\check{\mathbf{c}}_{MMSE}$ sufficiently enough. If we reach a certain value of this measure, we switch off the adaptation loop and keep the current coefficients. The error magnitude is a natural indicator for this optimality. The adaptation rule of the improved ES-LMS algorithm can be written as

$$\check{\mathbf{c}}_{k+1} := \check{\mathbf{c}}_k + \begin{cases} \mu \operatorname{sgn}(e_k)\,\check{\mathbf{x}}_{k_1} & : \quad |e_k| \geq |E|_{th} \\ 0 & : \quad |e_k| < |E|_{th} \end{cases} . \tag{5.18}$$

The symbolic notation of $|E|_{th}$ denotes the threshold for the error signal magnitude, below which we keep the current coefficients. We call this adaptation method thresholded error-sign LMS (TES-LMS) algorithm. A possible hardware block diagram is given in Fig. 5.9. It shows that, besides the already known sign determination branch of the ES-LMS algorithm, we just need a device determining the error signal magnitude followed by another comparator in parallel. This second branch may act as a switch for the whole adaptation unit.
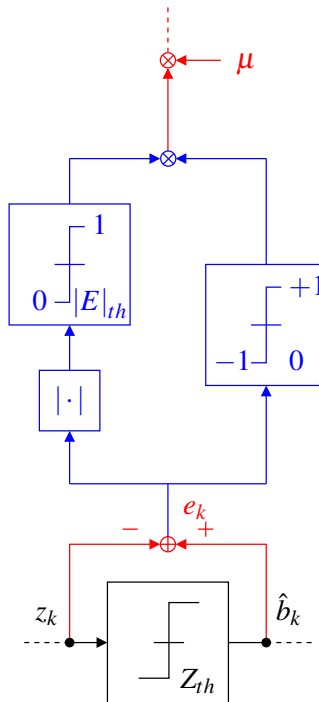

Figure 5.9: Modification of Fig. 5.2 to obtain the TES-LMS algorithm

The evaluation of the TES-LMS algorithm leads to the results in Fig. 5.10 and Table 5.5. Besides the optimal adaptation step size, we have also to find the best value for the error magnitude threshold. The optimal error threshold was found to be $|E|_{th} = 0.15$ after having searched with a resolution of 0.05. Comparing adaptation rates with respect to different adaptation step sizes, the TES-LMS algorithm is always between the fast adapting ES-LMS and the slower standard LMS algorithm. However, by introducing an error threshold, we
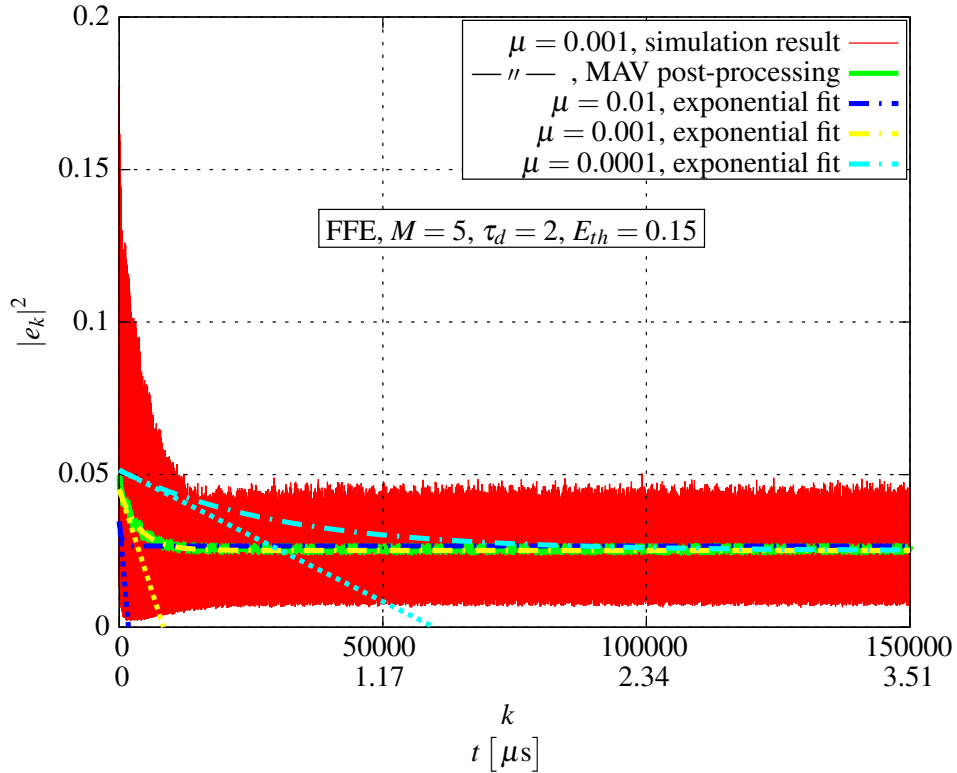
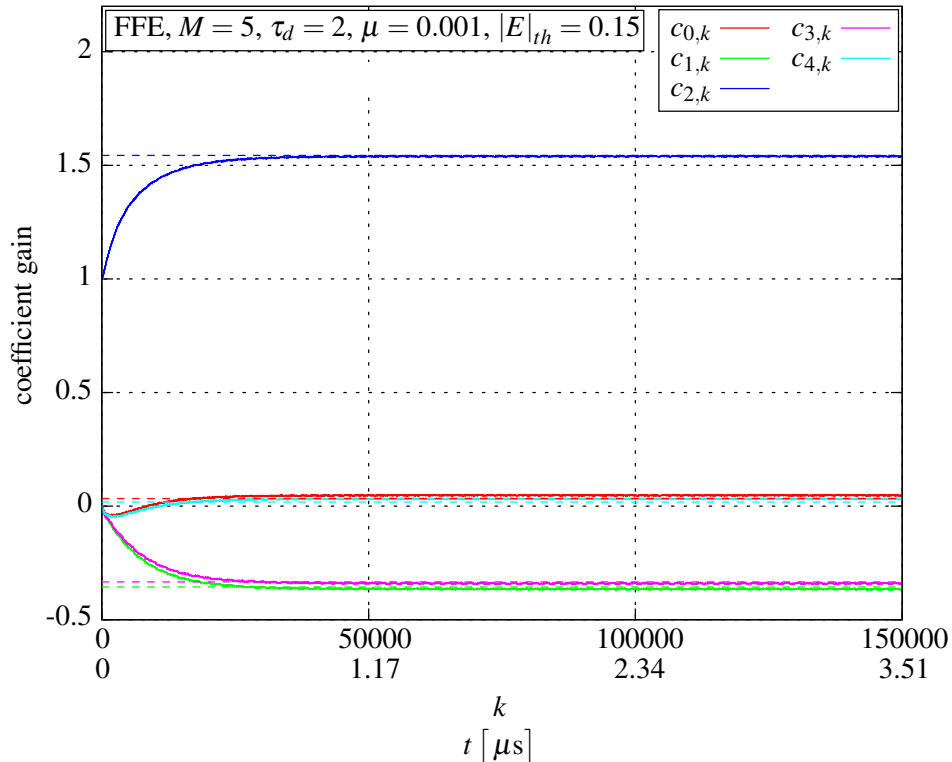(a) Squared error magnitude with influence of the adaptation step size

(b) TES-LMS coefficients for $\mu = 0.001$ (constant MMSE coefficients dashed)

Figure 5.10: Average TES-LMS-FFE adaptation behavior ($L_f = 5$ km, combined CD and first-order PMD ($r_D = 85$ ps/nm, $\Delta\tau_{g,max} = 12.36$ ps), $\gamma_{OSNR} = 21$ dB, 1000 adaptation runs averaged)

could improve accuracy in terms of mean steady state coefficient offset by almost a factor of 10 compared to the ES-LMS algorithm.

	$\mu = 0.01$	$\mu = 0.001$	$\mu = 0.0001$
$\lambda_{TES-LMS}$	1.97e-5	5.38e-6	8.61e-7
$\lambda'_{TES-LMS}\,[\mathrm{kHz}]$	842.41	229.76	36.78
$\Delta_{rel,TES-LMS}$	4.65e-3	5.51e-3	5.35e-2

Table 5.5: Adaptation rate and mean steady state coefficient offsets of the TES-LMS algorithm for different adaptation step sizes

5.3   Summary and Conclusion

Finally, Table 5.6 summarizes the performance measures found for different adaptation algorithms.

	$\mu = 0.01$	$\mu = 0.001$	$\mu = 0.0001$
λ_{LMS}	1.02e-5	2.34e-6	3.78e-7
λ_{ES-LMS}	2.84e-5	6.55e-6	1.08e-6
$\lambda_{QI-LMS\ (Q_x=2)}$	4.06e-5	9.98e-6	1.00e-6
$\lambda_{QI-LMS\ (Q_x=3)}$	7.62e-6	2.19e-6	3.29e-7
$\lambda_{TES-LMS}$	1.97e-5	5.38e-6	8.61e-7
$\lambda'_{LMS}\,[\mathrm{kHz}]$	434.62	99.93	16.13
$\lambda'_{ES-LMS}\,[\mathrm{kHz}]$	1211.10	279.50	46.33
$\lambda'_{QI-LMS}\,[\mathrm{kHz}]\ (Q_x=2)$	1735.48	426.11	42.90
$\lambda'_{QI-LMS}\,[\mathrm{kHz}]\ (Q_x=3)$	325.42e3	93.70e3	14.05e3
$\lambda'_{TES-LMS}\,[\mathrm{kHz}]$	842.41	229.76	36.78
$\Delta_{rel,LMS}$	2.23e-3	5.42e-4	2.20e-1
$\Delta_{rel,ES-LMS}$	2.43e-2	2.44e-2	1.33e-2
$\Delta_{rel,QI-LMS\ (Q_x=2)}$	1.70e-1	1.70e-1	2.66e-2
$\Delta_{rel,QI-LMS\ (Q_x=3)}$	3.17e-2	3.43e-2	2.50e-1
$\Delta_{rel,TES-LMS}$	4.65e-3	5.51e-3	5.35e-2

Table 5.6: Summary of adaptation rates and mean steady state coefficient offsets for different adaptation step sizes

Fig. 5.11 represents results for the required OSNR vs. CD and first-order PMD, which have not yet been involved in the discussion so far. It compares the LMS and the TES-LMS behavior with precalculated MMSE. These curves are insofar interesting that they have been recorded with initial setup of $\mathbf{c}_0 = \mathbf{1}_{\tau_d}$ while constantly measuring the BER. We can state

that the initial adaptation process has no severe influence on BER performance compared to the precalculated MMSE coefficients. Furthermore, all simulations have been executed with the same adaptation step size μ and error magnitude threshold $|E|_{th}$. This means that these parameters are fortunately valid for all OA-IM/DD parameter sets. A closer look at the noise-limited region reveals that the TES-LMS algorithm outperforms the standard LMS due to random walk suppression by the threshold operation. For the dispersion-limited region both algorithm perform equally which justifies to replace the LMS algorithm in favor of the TES-LMS algorithm.
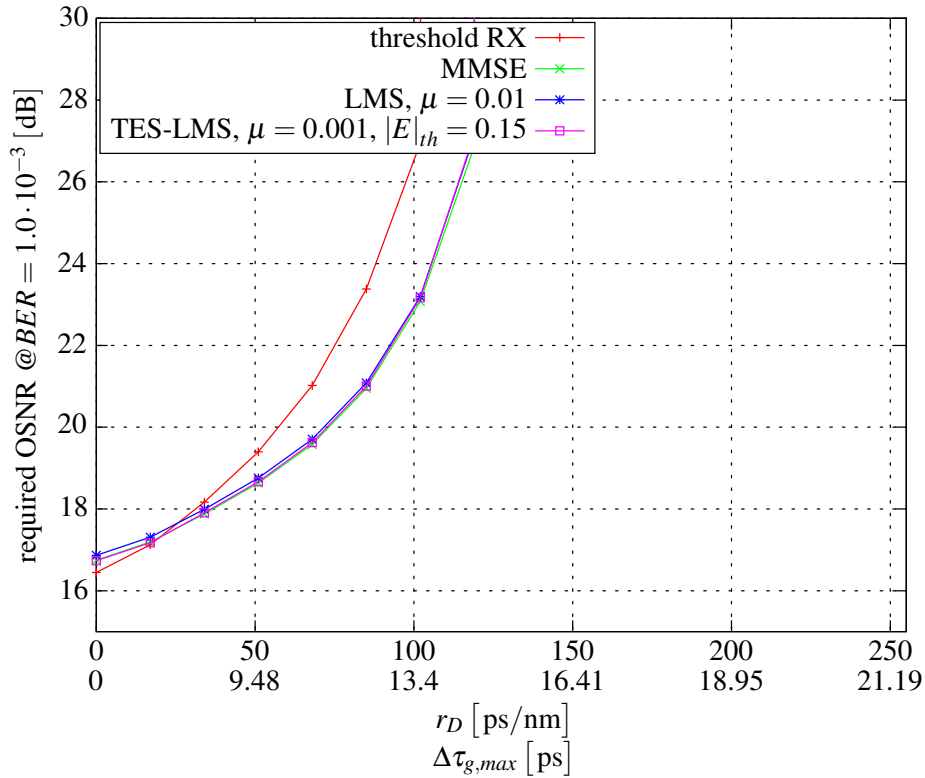

Figure 5.11: Effect of adaptive FFE on required OSNR performance for combined CD and first-order PMD

Chapter 6

Conclusion

This thesis has investigated low-complexity feed-forward and decision feedback equalizers for electronic dispersion compensation (FFE-DFE EDC) applied to optically amplified, intensity modulated links with direct detection (OA-IM/DD). It has proven that these methods are implementation- and cost-effective electronic dispersion compensation (EDC) methods for short-haul metropolitan area (MAN), aggregation or local area networks (LAN) to mitigate the intersymbol interference (ISI) impairments caused by chromatic (CD) and time-variant polarization mode dispersion (PMD).

Starting with the detailed description of modeling the special signal and noise characteristics of optically amplified, intensity modulated links with direct detection (OA-IM/DD) in Chs. 2 and 3, principle methods for electronic dispersion compensation (EDC) have been introduced with special focus on feed-forward and decision feedback equalizers (FFE-DFE) including their fractionally spaced counterparts. Different coefficient adjustment criteria ranging from minimal bit error ratio (MIN-BER) to minimum mean squared error (MMSE) have been introduced and studied intensively. First simulation results have revealed that low-complexity feed-forward (FFE) with $M = 5$ and feed-forward and decision feedback equalizers (FFE-DFE) with $M = 3$ and $N = 1$ coefficients are sufficient to cope with more advanced maximum likelihood sequence estimation based Viterbi equalizers (MLSE-VE) for the very short-haul range. Additionally, performance can be improved by application of fractionally spaced processing at twice the symbol rate. A fractionally spaced feed-forward equalizer (ΔT_2-FSFFE) with $M = 10$ and a fractionally spaced feed-forward and decision feedback equalizer (ΔT_2-FSFFE-DFE) with $M = 5$ and $N = 1$ have been found to be optimal with respect to electronic dispersion compensation (EDC) performance and implementation complexity. Compared to symbol rate processing, fractionally spaced processing improves electronic dispersion compensation (EDC) performance and simplifies clock and data recovery (CDR) circuitry at the expense of doubled clock rate for the equalizer operation. Furthermore, the supposed deficiency of minimum mean squared error (MMSE) coefficient adjustment in optically amplified, intensity modulated links with direct detection (OA-IM/DD) has been resolved after a detailed analysis of the calculations involved in the minimum mean squared error (MMSE) criterion. Instead of using the biased signal of the direct detection receiver directly for the minimum mean squared error (MMSE) coefficient adjustment, a zero-mean adjusted input

can provide almost the same electronic dispersion compensation (EDC) performance as the minimum bit error rate (MIN-BER) criterion. Finally, different adaptation algorithms based on the least mean square (LMS) algorithm have been introduced and studied extensively. The thresholded error-sign least mean square (TES-LMS) algorithm has been identified as a compromise between adaptation speed and accuracy while also reducing implementation cost.

Future investigations could extend the concept of thresholded error operation to the threshold operation of the decision feedback equalizer (DFE). Since the thresholded error-sign least mean square (TES-LMS) algorithm introduces a lower bound on the error magnitude, we could also think of having a threshold with respect to an upper bound for the maximally allowed error magnitude. This could lead to even more precision in the decision feedback equalizer (DFE) and adaptation loop and could be a means for reducing error propagation.
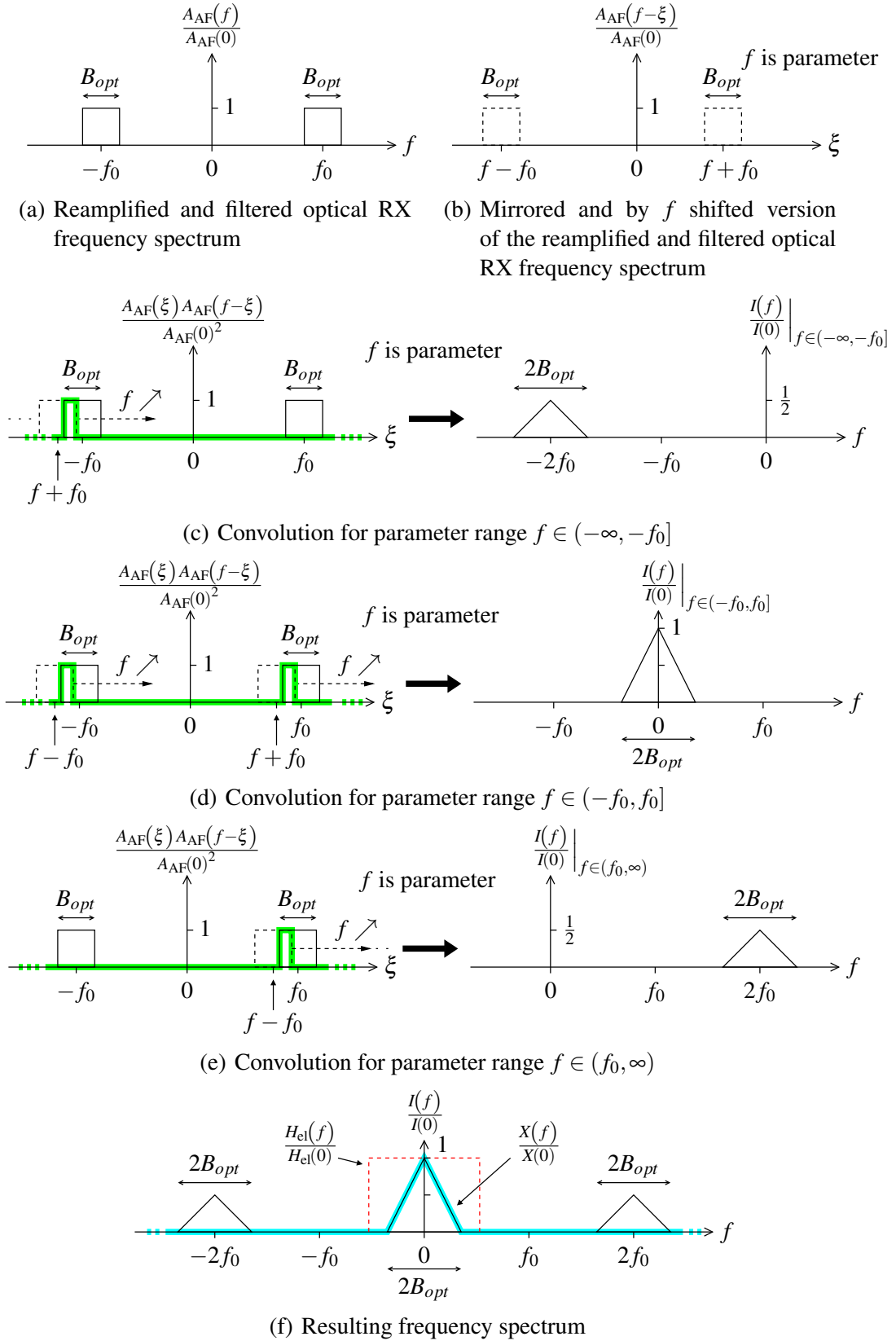
Appendix A

Principle of Envelope Detection in OA-IM/DD Links

Recalling Eqs. (2.13) and (2.14), which contain the frequency domain solution of the analog input frequency spectrum to the EDC device, with

$$
\begin{aligned}
X(f) &= I(f)\, H_{\mathrm{el}}(f) \\
&= I_{E0}\left(A_{\mathrm{AF}}(f) * A_{\mathrm{AF}}(f)\right) H_{\mathrm{el}}(f) \\
&= I_{E0}\left(\int_{-\infty}^{\infty} A_{\mathrm{AF}}(\xi)\, A_{\mathrm{AF}}(f-\xi)\, d\xi\right) H_{\mathrm{el}}(f),
\end{aligned}
\tag{A.1}
$$

the required calculation steps are illustrated in Fig. A.1. Thereby, we assume that the useful part of the reamplified and filtered optical RX frequency spectrum $A_{\mathrm{AF}}(f)$ is real-valued, has rectangular shape and is strictly bandlimited with $B_{opt} \ll f_0$.

Figs. A.1(a) and A.1(b) show the reamplified and filtered optical RX frequency spectrum $A_{\mathrm{AF}}(f)$ and the mirrored and by f shifted counterpart $A_{\mathrm{AF}}(f-\xi)$ (dashed) according to the above restrictions. Figs. A.1(c)–A.1(e) develop the different partial results from the convolution to obtain $I(f) \bullet\!\!-\!\!\circ i(t)$. Note that f acts as a parameter in the left-hand side subfigures and determines when $A_{\mathrm{AF}}(\xi)$ (continuous-lined) and $A_{\mathrm{AF}}(f-\xi)$ (dashed) overlap (highlighted bold) so that the convolution has a nonzero result. For the given frequency spectrum $A_{\mathrm{AF}}(f)$ in Fig. A.1(a) we may therefore identify three different parameter ranges $f \in (-\infty, -f_0]$, $f \in (-f_0, f_0]$ and $f \in (f_0, \infty)$ contributing to $I(f)$. The rectangularly shaped $A_{\mathrm{AF}}(f)$ in Fig. A.1(a) causes the partial results in Figs. A.1(c)–A.1(e) to have triangular shape while doubling the covered bandwidth to $2\,B_{opt}$. All partial results of $I(f)$ having equal resulting shapes and the doubling of the covered bandwidth to $2\,B_{opt}$ is a general property of envelope detection for any arbitrary shape of $A_{\mathrm{AF}}(f)$. The final result for $I(f)$ is depicted in Fig. A.1(f). Only the part of $I(f)$ near $f = 0$ Hz remains for $X(f)$ after lowpass filtering as indicated by Fig. A.1(f).

(a) Reamplified and filtered optical RX frequency spectrum

(b) Mirrored and by f shifted version of the reamplified and filtered optical RX frequency spectrum

(c) Convolution for parameter range $f \in (-\infty, -f_0]$

(d) Convolution for parameter range $f \in (-f_0, f_0]$

(e) Convolution for parameter range $f \in (f_0, \infty)$

(f) Resulting frequency spectrum

Figure A.1: Principle of envelope detection

Appendix B

Equivalent Baseband Transformation of the OA-IM/DD Link

Here, we give the detailed derivation approving the transformation of Eq. (2.12) in Ch. 2 to its equivalent baseband counterpart of Eq. (3.31) in Ch. 3.1.4.

First, we repeat the necessary partial results and transform them to frequency domain if not yet present:

- Eq. (2.4), page 7:

$$a_{\text{TX}}(t) = \ldots \approx a_e(t) \cos\left(2\pi f_0 t + \varphi_0\right) \tag{B.1}$$

$$A_{\text{TX}}(f) = \frac{1}{2}\left(e^{\text{j}\varphi_0} A_e(f - f_0) + e^{-\text{j}\varphi_0} A_e(f + f_0)\right) \tag{B.2}$$

- Eq. (2.7), page 8:

$$a_{\text{RX}}(t) \circ\!\!-\!\!\bullet A_{\text{RX}}(f) = \ldots = A_{\text{TX}}(f) H_{\text{f}}(f) \tag{B.3}$$

- Eq. (2.8), page 9:

$$a_{\text{AF}}(t) = \ldots \approx G a_{\text{RX}}(t) \tag{B.4}$$

$$\begin{aligned} A_{\text{AF}}(f) &= G A_{\text{RX}}(f) \\ &\stackrel{\text{(B.3)}}{=} G A_{\text{TX}}(f) H_{\text{f}}(f) \\ &\stackrel{\text{(B.2)}}{=} \frac{G}{2}\left(e^{\text{j}\varphi_0} A_e(f - f_0) + e^{-\text{j}\varphi_0} A_e(f + f_0)\right) H_{\text{f}}(f) \end{aligned} \tag{B.5}$$

- Eq. (2.14), page 10:

$$X(f) = I_{E0}\left(A_{\text{AF}}(f) * A_{\text{AF}}(f)\right) H_{\text{el}}(f)$$

$$= I_{E0} \left(\int_{-\infty}^{\infty} A_{\mathrm{AF}}(\xi)\, A_{\mathrm{AF}}(f-\xi)\, \mathrm{d}\xi \right) H_{\mathrm{el}}(f) \tag{B.6}$$

Then, we insert Eq. (B.5) into (B.6) and get

$$X(f) = I_{E0} \int_{-\infty}^{\infty} \left(\frac{G}{2} \left(\mathrm{e}^{\mathrm{j}\varphi_0} A_e(\xi-f_0) + \mathrm{e}^{-\mathrm{j}\varphi_0} A_e(\xi+f_0) \right) H_{\mathrm{f}}(\xi) \right.$$

$$\left. \frac{G}{2} \left(\mathrm{e}^{\mathrm{j}\varphi_0} A_e(f-\xi-f_0) + \mathrm{e}^{-\mathrm{j}\varphi_0} A_e(f-\xi+f_0) \right) H_{\mathrm{f}}(f-\xi) \right) \mathrm{d}\xi\, H_{\mathrm{el}}(f)$$

$$= \frac{I_{E0} G^2}{4} \left(\int_{-\infty}^{\infty} \mathrm{e}^{\mathrm{j}2\varphi_0} A_e(\xi-f_0)\, A_e(f-\xi-f_0)\, H_{\mathrm{f}}(\xi)\, H_{\mathrm{f}}(f-\xi)\, \mathrm{d}\xi \right.$$

$$+ \int_{-\infty}^{\infty} A_e(\xi-f_0)\, A_e(f-\xi+f_0)\, H_{\mathrm{f}}(\xi)\, H_{\mathrm{f}}(f-\xi)\, \mathrm{d}\xi$$

$$+ \int_{-\infty}^{\infty} A_e(\xi+f_0)\, A_e(f-\xi-f_0)\, H_{\mathrm{f}}(\xi)\, H_{\mathrm{f}}(f-\xi)\, \mathrm{d}\xi$$

$$\left. + \int_{-\infty}^{\infty} \mathrm{e}^{-\mathrm{j}2f_0} A_e(\xi+f_0)\, A_e(f-\xi+f_0)\, H_{\mathrm{f}}(\xi)\, H_{\mathrm{f}}(f-\xi)\, \mathrm{d}\xi \right)$$

$$H_{\mathrm{el}}(f). \tag{B.7}$$

For further calculations, we make the following substitutions:

- for the integrals in the first two lines of Eq. (B.7):

$$\xi' := \xi - f_0 \Rightarrow \begin{cases} \xi = \xi' + f_0 \\ \frac{\mathrm{d}\xi}{\mathrm{d}\xi'} = 1 \end{cases} \tag{B.8}$$

- for the integrals in the last two lines of Eq. (B.7):

$$\xi'' := f - \xi - f_0 \Rightarrow \begin{cases} \xi = f - \xi'' + f_0 \\ \frac{\mathrm{d}\xi}{\mathrm{d}\xi''} = -1 \end{cases} \tag{B.9}$$

Using the substitutions in (B.8) and (B.9) for the corresponding partial integrals, we get

$$
X(f) = \frac{I_{E0}G^2}{4} \left(\int_{-\infty}^{\infty} e^{j2\varphi_0} A_e\left(\xi'\right) A_e\left(f - \xi' - 2f_0\right) H_f\left(\xi' + f_0\right) H_f\left(f - \xi' - f_0\right) d\xi' \right.
$$

$$
+ \int_{-\infty}^{\infty} A_e\left(\xi'\right) A_e\left(f - \xi'\right) H_f\left(\xi' + f_0\right) H_f\left(f - \xi' - f_0\right) d\xi'
$$

$$
\stackrel{+}{-} \int_{\infty}^{-\infty} A_e\left(f - \xi''\right) A_e\left(\xi''\right) H_f\left(f - \xi'' - f_0\right) H_f\left(\xi'' + f_0\right) d\xi''
$$

$$
\left. \stackrel{+}{-} \int_{\infty}^{-\infty} e^{-j2f_0} A_e\left(f - \xi''\right) A_e\left(\xi'' + 2f_0\right) H_f\left(f - \xi'' - f_0\right) H_f\left(\xi'' + f_0\right) d\xi'' \right)
$$

$$
H_{\text{el}}(f). \tag{B.10}
$$

In the integrals of the last two lines in Eq. (B.10) we have already interchanged the signs and the limits.

For ease of notation, we may switch back to common integration variables with $\xi' \to \xi$ and $\xi'' \to \xi$ and get

$$
X(f) = \frac{I_{E0}G^2}{4} \left(\underbrace{\int_{-\infty}^{\infty} e^{j2\varphi_0} A_e\left(\xi\right) A_e\left(f - \xi - 2f_0\right) H_f(\xi + f_0) H_f(f - \xi - f_0) d\xi}_{①} \right.
$$

$$
+ \underbrace{\int_{-\infty}^{\infty} A_e\left(\xi\right) A_e\left(f - \xi\right) H_f(\xi + f_0) H_f(f - \xi - f_0) d\xi}_{②}
$$

$$
+ \underbrace{\int_{-\infty}^{\infty} A_e\left(f - \xi\right) A_e\left(\xi\right) H_f(f - \xi - f_0) H_f(\xi + f_0) d\xi}_{③}
$$

$$
\left. + \underbrace{\int_{-\infty}^{\infty} e^{-j2f_0} A_e\left(f - \xi\right) A_e\left(\xi + 2f_0\right) H_f(f - \xi - f_0) H_f(\xi + f_0) d\xi}_{④} \right)
$$

$$
H_{\text{el}}(f). \tag{B.11}
$$

We are now able to identify the different contributing partial integrals ①–④ to the solution of $X(f)$ in Eq. (B.11) with respect to the different ranges of the frequency parameter f given the electrical LPF $H_{\mathrm{el}}(f)$. Similar assumptions as in Ch. 2 or in App. A hold for the reamplified and filtered optical RX frequency spectrum

$$\left|\frac{A_{\mathrm{AF}}(f)}{A_{\mathrm{AF}}(0)}\right| \approx \begin{cases} > 0 & : \quad f \in \left[-f_0 - \frac{B_{opt}}{2}, -f_0 + \frac{B_{opt}}{2}\right] \vee \left[f_0 - \frac{B_{opt}}{2}, f_0 + \frac{B_{opt}}{2}\right] \\ 0 & : \quad elsewhere \end{cases}$$

where all other than the the useful components of $A_{\mathrm{AF}}(f)$ are approximately zero and are neglected. The corresponding useful signal bandwidth is $B_{opt} \ll f_0$. Interrelated by Eq. (B.5), the properties of $A_{\mathrm{AF}}(f)$ are also applicable to $A_e(f)$ by

$$\left|\frac{A_e(f)}{A_e(0)}\right| \approx \begin{cases} > 0 & : \quad f \in \left[-\frac{B_{opt}}{2}, \frac{B_{opt}}{2}\right] \\ 0 & : \quad elsewhere \end{cases} .$$

The partial integrals ①–④ of Eq. (B.11) are nonzero if the multiplication of their functional arguments are nonzero, which in turn means that they overlap as already illustrated in App. A. Since the frequency range of the SSMF transfer function $H_{\mathrm{f}}(f)$ exceeds the optical signal bandwidth, the overlapping region mainly depends on $A_e(f)$. The particular arguments during integration have to be in the range $\left[-B_{opt}/2, B_{opt}/2\right]$. The overlapping regions to contribute to $X(f)$ and the corresponding parameter range for the frequency f are then:

①: boundary points of overlapping region of $A_e(\xi)$ and $A_e(f - \xi - 2f_0)$ for

$$\xi = \pm\frac{B_{opt}}{2} \quad \vee \quad f - \xi - 2f_0 = \pm\frac{B_{opt}}{2}$$

$$\Rightarrow \begin{cases} \xi = \frac{B_{opt}}{2} & : \quad f - \frac{B_{opt}}{2} - 2f_0 = \frac{B_{opt}}{2} \Rightarrow f = 2f_0 + B_{opt} \\ \xi = -\frac{B_{opt}}{2} & : \quad f + \frac{B_{opt}}{2} - 2f_0 = -\frac{B_{opt}}{2} \Rightarrow f = 2f_0 - B_{opt} \end{cases}$$

$$\Rightarrow f \in \left[2f_0 - B_{opt}, 2f_0 + B_{opt}\right] \tag{B.12}$$

②: boundary points of overlapping region of $A_e(\xi)$ and $A_e(f - \xi)$ for

$$\xi = \pm\frac{B_{opt}}{2} \quad \vee \quad f - \xi = \pm\frac{B_{opt}}{2}$$

$$\Rightarrow \begin{cases} \xi = \frac{B_{opt}}{2} & : \quad f - \frac{B_{opt}}{2} = \frac{B_{opt}}{2} \Rightarrow f = B_{opt} \\ \xi = -\frac{B_{opt}}{2} & : \quad f + \frac{B_{opt}}{2} = -\frac{B_{opt}}{2} \Rightarrow f = -B_{opt} \end{cases}$$

$$\Rightarrow f \in \left[-B_{opt}, B_{opt}\right] \tag{B.13}$$

③: boundary points of overlapping region of $A_e(f-\xi)$ and $A_e(\xi)$ for

$$f-\xi = \pm\frac{B_{opt}}{2} \quad \vee \quad \xi = \pm\frac{B_{opt}}{2}$$

$$\Rightarrow \begin{cases} \xi = f-\frac{B_{opt}}{2} \ : \ f-\frac{B_{opt}}{2} = \frac{B_{opt}}{2} \ \Rightarrow \ f = B_{opt} \\ \xi = f+\frac{B_{opt}}{2} \ : \ f+\frac{B_{opt}}{2} = -\frac{B_{opt}}{2} \ \Rightarrow \ f = -B_{opt} \end{cases}$$

$$\Rightarrow f \in \left[-B_{opt}, B_{opt}\right] \tag{B.14}$$

④: boundary points of overlapping region of $A_e(f-\xi)$ and $A_e(\xi+2f_0)$ for

$$f-\xi = \pm\frac{B_{opt}}{2} \quad \vee \quad \xi+2f_0 = \pm\frac{B_{opt}}{2}$$

$$\Rightarrow \begin{cases} \xi = f-\frac{B_{opt}}{2} \ : \ f-\frac{B_{opt}}{2}+2f_0 = \frac{B_{opt}}{2} \ \Rightarrow \ f = -2f_0+B_{opt} \\ \xi = f+\frac{B_{opt}}{2} \ : \ f+\frac{B_{opt}}{2}+2f_0 = -\frac{B_{opt}}{2} \ \Rightarrow \ f = -2f_0-B_{opt} \end{cases}$$

$$\Rightarrow f \in \left[-2f_0-B_{opt}, -2f_0+B_{opt}\right] \tag{B.15}$$

In the light of the frequency ranges, which have been found in Eqs. (B.12)–(B.15), and the fact that the cutoff frequency of the electrical LPF $H_{el}(f)$ is $f_{3\,dB,el} \ll f_0$, the partial integrals ① and ④ vanish. The analog input signal to the EDC device simplifies then to

$$X(f) \overset{f_{3\,dB,el}\ll f_0}{\approx} \frac{I_{E0}G^2}{4} \left(\int_{-\infty}^{\infty} A_e(\xi)\, H_f(\xi+f_0)\, A_e(f-\xi)\, H_f(f-\xi-f_0)\, \mathrm{d}\xi \right.$$

$$\left. + \int_{-\infty}^{\infty} A_e(\xi)\, H_f(\xi+f_0)\, A_e(f-\xi)\, H_f(f-\xi-f_0)\, \mathrm{d}\xi \right) H_{el}(f)$$

$$= \frac{I_{E0}G^2}{2} \left(\int_{-\infty}^{\infty} \underbrace{A_e(\xi)\, H_f(\xi+f_0)}_{=\mathscr{F}\left\{a_e(t)*\left(h_f(t)\,\mathrm{e}^{-\mathrm{j}2\pi f_0 t}\right)\right\}} \underbrace{A_e(f-\xi)\, H_f(f-\xi-f_0)}_{=\mathscr{F}\left\{a_e(t)*\left(h_f(t)\,\mathrm{e}^{\mathrm{j}2\pi f_0 t}\right)\right\}} \mathrm{d}\xi \right) H_{el}(f)$$

$$\tag{B.16}$$

with some resorting of the function arguments $A_e(\cdot)$ and $H_f(\cdot)$ as well as summing up. In the result of Eq. (B.16) we obtain towards $f = 0$ frequency shifted versions of the SSMF transfer function. The corresponding time domain expressions of the function argument of the convolution integral are highlighted underbraced by the Fourier transform operator $\mathscr{F}\{\cdot\}$. Finally, we use them to switch back to the time domain solution

$$x(t) = \frac{I_{E0}G^2}{2} \left(\left(a_e(t)*\left(h_f(t)\,\mathrm{e}^{-\mathrm{j}2\pi f_0 t}\right)\right) \left(a_e(t)*\left(h_f(t)\,\mathrm{e}^{\mathrm{j}2\pi f_0 t}\right)\right) \right) * h_{el}(t)$$

$$= \frac{I_{E0}G^2}{2} \left| a_e(t) * \left(h_{\mathrm{f}}(t)\, \mathrm{e}^{\mathrm{j}2\pi f_0 t} \right) \right|^2 * h_{\mathrm{el}}(t) \tag{B.17}$$

where we have exploited that the two time domain convolution expressions are related by complex conjugation.

Appendix C

Downhill Simplex Optimization Method

We shortly highlight the algorithmic steps of the downhill simplex method tailored to adjust a FFE-DFE with respect to minimal BER [130]. Its performance depends heavily on the initial coefficient setup. The method itself does not promise to converge to the globally optimal solution if the function to be optimized is not strictly monotone, i.e. it has several local optimums. Fortunately, strict monotony is given for our problem, and we have not observed any convergence problems with our optimization target function, which we recall from Eq. (4.23) on page 71 with

$$\check{\mathbf{c}}_{BER} = \arg \min_{\check{\mathbf{c}}} BER\left(L_f, \Delta\tau_g, OSNR, M, N, \mathbf{c}_{tot}, \tau_d, Z_{th} \right). \tag{C.1}$$

We assume that the OA-IM/DD link and RX processing parameters L_f, $\Delta\tau_g$, $OSNR$, M, N and Z_{th} are arbitrary but fixed during the execution of the algorithm. Therefore, we omit the cumbersome BER notation with those parameter from above but keep the dependence on them in mind.

In the very first step, we have to define $M+N+1$ initial coefficient setups $\check{\mathbf{c}}_j$, $j=0,\dots,M+N$, which are the vertices of a simplex in the $(M+N)$-dimensional solution space as illustrated in Figure C.1 for $M+N=3$.
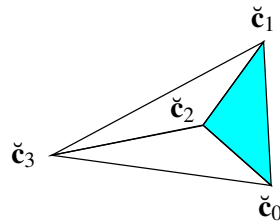

Figure C.1: Initial simplex for $M+N=3$

Within our simulations, we always set

$$
\check{\mathbf{c}}_j := \begin{cases} \mathbf{0} & : & j = 0 \\ \mathbf{1}_j & : & j > 0 \end{cases}
$$

with $\mathbf{1}_j$ being the unit vector of the j-th dimension. This initial simplex represents the diagonally halved $(M+N)$-dimensional unit cube, which leads to the pyramidal shape in Figure C.1 for three dimensions.

Then, we repeat the following steps for each value of the decision delay τ_d separately:

1. Simulate the BERs for all $\check{\mathbf{c}}_j$, $j = 0, \ldots, M+N$.

2. Extract the best performing coefficient setup with

$$
\check{\mathbf{c}}_{j_{min}} := \arg \min_{\check{\mathbf{c}}_j} BER(\check{\mathbf{c}}_j),
$$

   the worst performing coefficient setup with

$$
\check{\mathbf{c}}_{j_{max,1}} := \arg \max_{\check{\mathbf{c}}_j} BER(\check{\mathbf{c}}_j)
$$

   and the second worst performing coefficient setup with

$$
\check{\mathbf{c}}_{j_{max,2}} := \arg \max_{\substack{\check{\mathbf{c}}_j \\ \check{\mathbf{c}}_j \neq \check{\mathbf{c}}_{j_{max,1}}}} BER(\check{\mathbf{c}}_j).
$$

3. Determine the relative BER difference between the best and worst performing coefficient setup with

$$
BER_{rel} = \frac{BER\left(\check{\mathbf{c}}_{j_{max,1}}\right) - BER\left(\check{\mathbf{c}}_{j_{min}}\right)}{\frac{BER\left(\check{\mathbf{c}}_{j_{max,1}}\right) + BER\left(\check{\mathbf{c}}_{j_{min}}\right)}{2}}
$$

   and use it as a termination criterion, i.e. check BER_{rel} against a positive constant $\delta \in \mathbb{R}_+$.

4. If $BER_{rel} < \delta$, we have found the δ-optimal minimal BER adjustment for a FFE-DFE and given decision delay τ_d, and we can terminate the algorithm.

   Otherwise, we proceed with the actual algorithm steps:

5. First, we reflect the worst performing coefficient setup at the mean value of all other setups to get

$$
\check{\mathbf{c}}'_{j_{max,1}} := \frac{2}{M+N} \sum_{\substack{j=0 \\ j \neq j_{max,1}}}^{M+N} \check{\mathbf{c}}_j - \check{\mathbf{c}}_{j_{max,1}}
$$

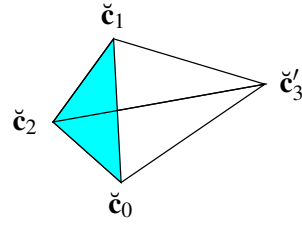as depicted in Figure C.2 and determine $BER\left(\breve{\mathbf{c}}'_{j_{max,1}}\right)$.

Figure C.2: Reflection of the worst performing vertex with $j_{min} = 0$ and $j_{max,1} = 3$ for $M + N = 3$

6. If the tested coefficient setup $\breve{\mathbf{c}}'_{j_{max,1}}$ …

   • …performs best with

   $$BER\left(\breve{\mathbf{c}}'_{j_{max,1}}\right) < BER\left(\breve{\mathbf{c}}_{j_{min}}\right),$$

   then expand further in that direction as shown in Figure C.3 and replace $\breve{\mathbf{c}}_{j_{max,1}}$ using the recursive relation

   $$\breve{\mathbf{c}}_{j_{max,1}} := \frac{3}{M+N} \sum_{\substack{j=0 \\ j \neq j_{max,1}}}^{M+N} \breve{\mathbf{c}}_j - \breve{\mathbf{c}}_{j_{max,1}}.$$

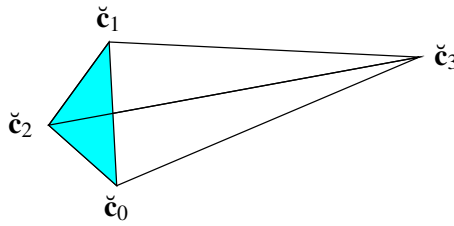   Use the new set of coefficient setups and restart the algorithm.

Figure C.3: Reflection and expansion of the worst performing vertex with $j_{min} = 0$ and $j_{max,1} = 3$ for $M + N = 3$

   • …constitutes an improvement by outperforming the second worst setup with

   $$BER\left(\breve{\mathbf{c}}_{j_{max,2}}\right) > BER\left(\breve{\mathbf{c}}'_{j_{max,1}}\right) > BER\left(\breve{\mathbf{c}}_{j_{min}}\right),$$

   then keep the reflected vertex and replace

   $$\breve{\mathbf{c}}_{j_{max,1}} := \breve{\mathbf{c}}'_{j_{max,1}}.$$

   Use the new set of vertices and restart the algorithm.

- ...still performs worse than all others with

$$BER\left(\check{\mathbf{c}}'_{j_{max,1}}\right) \geq BER(\check{\mathbf{c}}_j), \quad j = 0,\ldots,M+N,$$

then try a single vertex contraction defined by

$$\check{\mathbf{c}}''_{j_{max,1}} := \frac{1}{2}\left(\frac{1}{M+N}\sum_{\substack{j=0\\j\neq j_{max,1}}}^{M+N}\check{\mathbf{c}}_j + \check{\mathbf{c}}_{j_{max,1}}\right),$$

which is covered by the illustration in Figure C.4, and determine $BER\left(\check{\mathbf{c}}''_{j_{max,1}}\right)$ again.
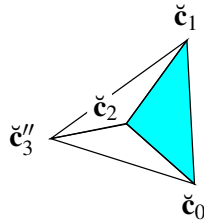

Figure C.4: Single contraction of the worst performing vertex with $j_{min} = 0$ and $j_{max,1} = 3$ for $M+N = 3$

7. If the contracted coefficient setup $\check{\mathbf{c}}''_{j_{max}}$ leads to ...

- ...a further improvement with

$$BER\left(\check{\mathbf{c}}''_{j_{max,1}}\right) < BER\left(\check{\mathbf{c}}_{j_{max,1}}\right),$$

keep the contracted vertex and replace

$$\check{\mathbf{c}}_{j_{max,1}} := \check{\mathbf{c}}''_{j_{max,1}}.$$

Use the new set of vertices and restart the algorithm.

- ...no improvement, which expresses itself in

$$BER\left(\check{\mathbf{c}}''_{j_{max,1}}\right) \geq BER\left(\check{\mathbf{c}}_{j_{max,1}}\right),$$

then contract all vertices of the simplex near the best performing one illustrated in Figure C.5 and expressed in mathematical terms by

$$\check{\mathbf{c}}_j := \frac{1}{2}\left(\check{\mathbf{c}}_{j_{min}} + \check{\mathbf{c}}_j\right), \quad j = 0,\ldots,M+N.$$

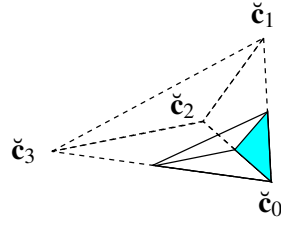Use the new set of vertices and restart the algorithm.

Figure C.5: Multiple contraction of all vertices near the best performing one with $j_{min} = 0$ and $j_{max,1} = 3$ for $M + N = 3$

Finally, we compare the coefficient setup results of all runs with different decision delays and fix this parameter to its optimum, too.

Concerning numerical stability, we have found out that we were able to set $BER_{rel} = 0$ as termination criterion without any stability problems. This implies that

$$BER(\check{\mathbf{c}}_0) = BER(\check{\mathbf{c}}_1) = \ldots BER\big(\check{\mathbf{c}}_{M+N}\big) \iff \check{\mathbf{c}}_0 = \check{\mathbf{c}}_1 = \ldots = \check{\mathbf{c}}_{M+N}$$

after the termination of the algorithm, and that we have arrived at a unique solution.

Appendix D

LLS FIR Channel Approximation of the OA-IM/DD Link

Since the application of the ZF criterion to FFE-DFE EDC configurations requires knowledge of the FIR filter model of the underlying communications channel, we have to apply appropriate means to determine the coefficients of this FIR filter for the OA-IM/DD link. We rely on the well-known LLS approach as implementation of a *Wiener filter* assuming ergodicity. Note that this procedure is only able to account for the linear behavior of the OA-IM/DD link. The inherent nonlinearity adds to the deviation of the model from the actual behavior.

The principal setup of the procedure for general ΔT_i-spaced sampling is depicted in Fig. D.1. The OA-IM/DD link of Fig. 2.1 on page 6 together with appropriate sampling of the electrical RX signal and the LLS FIR approximation are placed in parallel. Both have the input bit stream b_k in common.

The task is to find an optimal coefficient setup for the LLS FIR filter, which approximates the output of the OA-IM/DD system by

$$x_{k_i} \approx x'_{k_1} = \sum_{j=-M_c/2}^{M_c/2} h_j b_{k_i-j} = \mathbf{h}^\mathrm{T}\mathbf{b}_{k_i}. \tag{D.1}$$

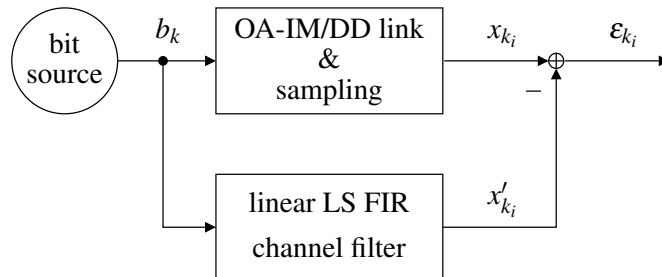The indexing of the bit sequence with the general EDC input sample index k_i shall implicitly

Figure D.1: Setup to determine the LLS FIR channel approximation

represent the upsampling operation

$$b_{k_i} := \begin{cases} b_k & : & k_i \bmod i = 0 \\ 0 & : & elsewhere \end{cases}, \quad i \in \mathbb{N}_1, \tag{D.2}$$

which we apply to the original TX bit sequence b_k. In addition, we have introduced a scalar product notation for the convolution in Eq. (D.1) with the vectors

$$\mathbf{h} := \begin{pmatrix} h_{-M_c/2} \\ \vdots \\ h_{h_{M_c/2}} \end{pmatrix} \quad \text{and} \quad \mathbf{b}_{k_i} := \begin{pmatrix} b_{k_i+M_c/2} \\ \vdots \\ b_{k_i-M_c/2} \end{pmatrix}. \tag{D.3}$$

According to this notation, the actual delay of the LLS filter is set to $M_c/2$ within our non-causal modeling approach (cf. the introduction of the decision delay parameter for the FFE in Ch. 4.2). This turns out to be beneficial for the further derivations in the main part of this thesis. Since an OA-IM/DD link is affected by ASE noise together with direct detection, linear fitting is suboptimal, and we have to tolerate a deviation measured by

$$e_{k_i} = x_{k_i} - x'_{k_i}. \tag{D.4}$$

The general approach of Wiener filtering, which minimizes this deviation in the mean square sense, is to say

$$\mathbf{h} = \arg \min_{\mathbf{h}} \mathsf{E}\left[\left|e_{k_i}(\mathbf{h})\right|^2\right] \stackrel{ergodicity}{=} \arg \min_{\mathbf{h}} \lim_{K_{LS} \to \infty} \frac{1}{iK_{LS}} \sum_{k_i=0}^{iK_{LS}-1} \left|e_{k_i}(\mathbf{h})\right|^2. \tag{D.5}$$

This results in the common LLS problem formulation if we assume ergodic signal characteristics. The parameter K_{LS} denotes the number of TX bits b_k, which contribute to this channel estimation procedure. It is obvious that we cannot determine the limit for $K_{LS} \to \infty$ within our computer simulations. However, a number of $K_{LS} \approx 1\mathrm{e}6$ has proven to produce an unbiased estimate for the limit with sufficiently low statistical significance. Therefore, we neglect the limiting operation in the following. Using the squared magnitude of e_{k_i} results in a convex optimization problem, for which a unique minimum exists.

The calculations to determine the coefficients of the LLS FIR filter follow the common procedure of minimizing continuous and differentiable functions. Using Eqs. (D.1)–(D.4), we can calculate the gradient with respect to the channel coefficient vector $\mathbf{h}$ and get

$$\frac{1}{iK_{LS}} \nabla_{\mathbf{h}} \sum_{k_i=0}^{iK_{LS}-1} \left|e_{k_i}(\mathbf{h})\right|^2 = \frac{1}{iK_{LS}} \nabla_{\mathbf{h}} \sum_{k_i=0}^{iK_{LS}-1} \left|x_{k_i} - x'_{k_i}(\mathbf{h})\right|^2$$

$$= \frac{1}{iK_{LS}} \nabla_{\mathbf{h}} \sum_{k_i=0}^{iK_{LS}-1} \left|x_{k_i} - \mathbf{h}^{\mathsf{T}} \mathbf{b}_{k_i}\right|^2$$

$$= \frac{1}{iK_{LS}} \nabla_{\mathbf{h}} \sum_{k_i=0}^{iK_{LS}-1} \left(x_{k_i} - \mathbf{h}^{\mathrm{T}} \mathbf{b}_{k_i} \right)^2$$

$$= \frac{1}{iK_{LS}} \nabla_{\mathbf{h}} \sum_{k_i=0}^{iK_{LS}-1} \left(x_{k_i}^2 - 2 x_{k_i} \mathbf{h}^{\mathrm{T}} \mathbf{b}_{k_i} + \underbrace{\left(\mathbf{h}^{\mathrm{T}} \mathbf{b}_{k_i} \right)^2}_{= \mathbf{h}^{\mathrm{T}} \mathbf{b}_{k_i} \mathbf{b}_{k_i}^{\mathrm{T}} \mathbf{h}} \right)$$

$$= \frac{1}{iK_{LS}} \nabla_{\mathbf{h}} \sum_{k_i=0}^{iK_{LS}-1} x_{k_i}^2 - 2 \nabla_{\mathbf{h}} \mathbf{h}^{\mathrm{T}} \underbrace{\frac{1}{iK_{LS}} \sum_{k_i=0}^{iK_{LS}-1} x_{k_i} \mathbf{b}_{k_i}}_{=: \mathbf{p}_{x\mathbf{b}}}$$

$$+ \nabla_{\mathbf{h}} \mathbf{h}^{\mathrm{T}} \underbrace{\frac{1}{iK_{LS}} \sum_{k_i=0}^{iK_{LS}-1} \mathbf{b}_{k_i} \mathbf{b}_{k_i}^{\mathrm{T}} \mathbf{h}}_{=: \mathbf{R}_{\mathbf{bb}}}$$

$$= 0 - 2 \mathbf{p}_{x\mathbf{b}} + 2 \mathbf{R}_{\mathbf{bb}} \mathbf{h}, \quad b_{k_i} \in \mathbb{N}, \ h_j, x_{k_i}, x'_{k_i} \in \mathbb{R}. \tag{D.6}$$

The vector $\mathbf{p}_{x\mathbf{b}}$ is the cross-correlation vector between the electrical RX signal samples x_{k_i} and the upsampled bit vector $\mathbf{b}_{k_i}$. The matrix $\mathbf{R}_{\mathbf{bb}}$ is the autocorrelation matrix of the upsampled bit sequence. $\mathbf{R}_{\mathbf{bb}} \neq \mathbf{I}$, since $\mathbf{b}_{k_i}$ originates from a PRBS, whose underlying structure is a LFSR.

Setting the gradient of Eq. (D.6) to zero results in the required LLS approximation coefficients with

$$\frac{1}{iK_{LS}} \nabla_{\mathbf{h}} \sum_{k_i=0}^{iK_{LS}-1} \left| e_{k_i}(\mathbf{h}) \right|^2 \overset{!}{=} 0 \quad \Longleftrightarrow \quad \mathbf{h} = \mathbf{R}_{\mathbf{bb}}^{-1} \mathbf{p}_{x\mathbf{b}}. \tag{D.7}$$

We can deduce from Eq. (D.7) that we have to measure $\mathbf{R}_{\mathbf{bb}}$ and $\mathbf{p}_{x\mathbf{b}}$ with a sufficient number of electrical RX samples and TX bits to get accurate estimates. A numerical matrix inversion of $\mathbf{R}_{\mathbf{bb}}$ followed by the right-hand side multiplication with $\mathbf{p}_{x\mathbf{b}}$ is the concluding step to determine the coefficients of the LLS FIR channel approximation.

References

[1] K. Kao and G. Hockham, "Dielectric-fibre surface waveguides for optical frequencies," *Proceedings of the Institution of Electrical Engineers*, vol. 113, no. 7, pp. 1151–1158, July 1966.

[2] *IEEE 802.3: LAN/MAN CSMA/CDE (ETHERNET) ACCESS METHOD*, IEEE Std.

[3] P. J. Winzer and R.-J. Essiambre, "Receivers for advanced optical modulation formats," in *Proc. 16th Annual Meeting of the IEEE Lasers and Electro-Optics Society LEOS*, vol. 2, 2003, pp. 759–760.

[4] P. Winzer, R. J. Essiambre, and S. Chandrasekhar, "Dispersion-tolerant optical communication systems," in *Proc. European Conference on Optical Communications (ECOC)*, 2004.

[5] M. Ohm, "Multilevel optical modulation formats with direct detection," Ph.D. dissertation, Institut für Nachrichtenübertragung, Universität Stuttgart, 2006.

[6] M. Serbay, C. Wree, and W. Rosenkranz, "Experimental investigation of RZ-8DPSK at 3-times 10.7 Gb/s," in *Proc. 18th Annual Meeting of the IEEE Lasers and Electro-Optics Society LEOS 2005*, 2005, pp. 483–484.

[7] G. P. Agrawal, *Nonlinear fiber optics*, 4th ed. Elsevier/Academic Press, 2007.

[8] M. Bohn, G. Mohs, C. Scheerer, C. Glingener, C. Wree, and W. Rosenkranz, "An adaptive optical equalizer concept for single channel distortion compensation," in *27th European Conference on Optical Communication (ECOC)*, vol. 1, 30 Sept.-4 Oct. 2001.

[9] M. Secondini, E. Forestieri, and G. Prati, "Performance of MSE configured PLC optical equalizers for chromatic dispersion compensation," *IEEE Photon. Technol. Lett.*, vol. 15, no. 2, pp. 248–250, 2003.

[10] ——, "PLC optical equalizer for chromatic and polarization-mode dispersion compensation based on MSE control," *IEEE Photon. Technol. Lett.*, vol. 16, no. 4, pp. 1173–1175, 2004.

References

[11] C. Doerr, S. Chandrasekhar, P. Winzer, A. Chraplyvy, A. Gnauck, L. Stulz, R. Pafchek, and E. Burrows, "Simple Multichannel Optical Equalizer Mitigating Intersymbol Interference for 40-Gb/s," *Journal of Lightwave Technology*, vol. 22, no. 1, pp. 249–256, January 2004.

[12] M. Bohn, P. Krumrich, and W. Rosenkranz, "Automatic control of optical equalizers," in *Optical Fiber Communication Conference OFC/NFOEC*, vol. 3, 6-11 March 2005.

[13] R. I. Killey, P. M. Watts, V. Mikhailov, M. Glick, and P. Bayvel, "Electronic dispersion compensation by signal predistortion using digital processing and a dual-drive Mach-Zehnder Modulator," *IEEE Photon. Technol. Lett.*, vol. 17, no. 3, pp. 714–716, 2005.

[14] J. H. Winters and R. D. Gitlin, "Electrical signal processing techniques in long-haul fiber-optic systems," *IEEE Trans. Commun.*, vol. 38, no. 9, pp. 1439–1453, 1990.

[15] M. Hueda, D. Crivelli, and H. Carrer, "Performance of MLSE-based receivers in lightwave systems with nonlinear dispersion and amplified spontaneous emission noise," in *IEEE Global Telecommunications Conference (GLOBECOM)*, vol. 1, 29 Nov.-3 Dec. 2004.

[16] O. Agazzi, M. Hueda, H. Carrer, and D. Crivelli, "Maximum-likelihood sequence estimation in dispersive optical channels," *Journal of Lightwave Technology*, vol. 23, no. 2, pp. 749–763, Feb. 2005.

[17] G. Bosco and P. Poggiolini, "Long-distance effectiveness of MLSE IMDD receivers," *IEEE Photonics Technology Letters*, vol. 18, no. 9, pp. 1037–1039, May 2006.

[18] T. Freckmann and J. Speidel, "Viterbi equalizer with analytically calculated branch metrics for optical ASK and DBPSK," *IEEE Photon. Technol. Lett.*, vol. 18, no. 1, pp. 277–279, 2006.

[19] R. Waegemans, S. Herbst, L. Holbein, P. Watts, P. Bayvel, C. Fürst, and R. I. Killey, "10.7 Gb/s electronic predistortion transmitter using commercial FPGAs and D/A converters implementing real-time DSP for chromatic dispersion and SPM compensation," *Opt. Express*, vol. 17, no. 10, pp. 8630–8640, 2009.

[20] A. Färbert, S. S. Langenbach, N. Stojanovic, C. Dorschky, T. Kupfer, C. Schulien, J. Elbers, H. Wernz, H. Griesser, and C. Glingener, "Performance of a 10.7 Gbit/s Receiver with Digital Equaliser using Maximum Likelihood Sequence Estimation," in *Optical Communication, 2005. ECOC 2004. 30st European Conference on*, 2004.

[21] D. Fritzsche, D. Breuer, L. Schürer, A. Ehrhardt, H. Oeruen, and C. G. Schäffer, "Experimental investigation of real time 10 Gbit/s MLSE equalizer using 4-states and 16-states Viterbi detector," in *Proceedings of the 28th IEEE conference on Global telecommunications (GLOBECOM)*, 2009, pp. 3728–3732.

[22] P. P. Monteiro, M. J. Lima, J. Ferreira da Rocha, A. L. Teixeira, B. Franz, and B. Wedding, "An electrically adjustable equalizer for very high bit rate transmission systems based on dispersion supported transmission," in *Proc. IEEE Int. Electronics, Circuits and Systems Conference*, vol. 3, 1998, pp. 193–196.

[23] H. Wu, J. A. Tierno, P. Pepeljugoski, J. Schaub, S. Gowda, J. A. Kash, and A. Hajimiri, "Integrated transversal equalizers in high-speed fiber-optic systems," *IEEE J. Solid-State Circuits*, vol. 38, no. 12, pp. 2131–2137, 2003.

[24] B. Franz, D. Rosener, R. Dischier, F. Buchali, B. Junginger, T. Meister, and K. Aufinger, "43 Gbit/s SiGe based electronic equalizer for PMD and chromatic dispersion mitigation," in *31st European Conferenceon Optical Communication (ECOC)*, vol. 3, 25-29 Sept. 2005.

[25] H. Jiang, R. Saunders, and S. Colaco, "SiGe equalizer IC for PMD mitigation and signal optimization of 40 Gbits/s transmission," in *Proc. Optical Fiber Communication Conference (OFC/NFOEC)*, vol. 3, 2005.

[26] J. Sewter and A. Chan Carusone, "A 3-Tap FIR Filter With Cascaded Distributed Tap Amplifiers for Equalization Up to 40 Gb/s in 0.18-mu CMOS," *IEEE Journal of Solid-State Circuits*, vol. 41, no. 8, pp. 1919–1929, Aug. 2006.

[27] A. Carusone and D. Johns, "Digital LMS adaptation of analog filters without gradient information," *IEEE Transactions on Circuits and Systems II: Analog and Digital Signal Processing*, vol. 50, no. 9, pp. 539–552, Sept. 2003.

[28] T. Veigel, M. Grözing, M. Berroth, and F. Buchali, "Design of a Viterbi Equalizer Circuit for Data Rates up to 43 Gb/s," in *European Solid-State Circuits Conference (ESSCIRC)*, 2009.

[29] S. Strebel, "Parallele Entzerrung und LDPC-Decodierung mit einem FPGA-Baustein," Diplomarbeit, Institut für Nachrichtenübertragung, Universität Stuttgart, 2008.

[30] M. Werner, *Information und Kodierung*, 2nd ed.   Vieweg+Teubner Verlag, 2009.

[31] H. Klimant, D. Piotraschke, and D. Schönfeld, *Informations- und Kodierungstheorie*, 3rd ed.   B.G. Teubner Verlag, 2006.

[32] S. ten Brink, "Design of concatenated coding schemes based on iterative decoding convergence," Ph.D. dissertation, Institut für Nachrichtenübertragung, Universität Stuttgart, 2002.

[33] B. Vasic and I. B. Djordjevic, "Low-density parity check codes for long-haul optical communication systems," *IEEE Photon. Technol. Lett.*, vol. 14, no. 8, pp. 1208–1210, 2002.

[34] M. Jäger, T. Rankl, J. Speidel, H. Bülow, and F. Buchali, "Performance of turbo equalizers for optical PMD channels," *Journal of Lightwave Technology*, vol. 24, no. 3, pp. 1226–1236, March 2006.

[35] T. Rankl, "Performance and Bounds of Optical Receivers with Electronic Detection and Decoding," Ph.D. dissertation, Institut für Nachrichtenübertragung, Universität Stuttgart, 2009.

[36] E. Voges and K. Petermann, *Optische Kommunikationstechnik - Handbuch für Wissenschaft und Industrie*, 1st ed. Springer-Verlag, 2002.

[37] *ITU-T Recommendation G.692: Optical interfaces for multichannel systems with optical amplifiers*, International Telecommunications Union (ITU) Std.

[38] *ITU-T Recommendation G.694.1: Spectral grids for WDM applications: DWDM frequency grid*, International Telecommunications Union (ITU) Std.

[39] *ITU-T Recommendation G.694.2: Spectral grids for WDM applications: CWDM wavelength grid*, International Telecommunication Union (ITU) Std.

[40] *ITU-T Recommendation G.698.1: Multichannel DWDM applications with single-channel optical interfaces*, International Telecommunication Union (ITU) Std.

[41] *ITU-T Recommendation G.698.2: Amplified multichannel dense wavelength division multiplexing applications with single channel optical interfaces*, International Telecommunication Union (ITU) Std.

[42] J. Proakis, *Digital Communications*, 4th ed. McGraw-Hill, 2001.

[43] M. Seimetz, *High-Order Modulation for Optical Fiber Transmission*, 1st ed. Springer-Verlag, 2009.

[44] U. Tietze, C. Schenk, and C. Schenk, *Halbleiter-Schaltungstechnik*. Springer, 2002.

[45] E. Forestieri, "Evaluating the error probability in lightwave systems with chromatic dispersion, arbitrary pulse shape and pre- and postdetection filtering," *J. Lightw. Technol.*, vol. 18, no. 11, pp. 1493–1503, 2000.

[46] J. R. Barry, E. A. Lee, and D. G. Messerschmitt, *Digital Communication*, 3rd ed. Kluwer Academic Publishers, 2003.

[47] M. C. Jeruchim, P. Balaban, and K. S. Shanmugan, *Simulation of communication systems*. Plenum Press, 1994.

[48] *ITU-T Recommendation G.975: Forward error correction for submarine systems*, International Telecommunications Union (ITU) Std.

[49] G. Bosco, A. Carena, V. Curri, R. Gaudino, and P. Poggiolini, "On the use of NRZ, RZ, and CSRZ modulation at 40 Gb/s with narrow DWDM channel spacing," *Journal of Lightwave Technology*, vol. 20, no. 9, pp. 1694–1704, Sept. 2002.

[50] G. J. Foschini and C. D. Poole, "Statistical theory of polarization dispersion in single mode fibers," *J. Lightw. Technol.*, vol. 9, no. 11, pp. 1439–1456, 1991.

[51] C. D. Poole and R. E. Wagner, "Phenomenological approach to polarisation dispersion in long single-mode fibres," *Electronics Letters*, vol. 22, no. 19, pp. 1029–1030, 1986.

[52] C. D. Poole, "Statistical treatment of polarization dispersion in single-mode fiber," *Opt. Lett.*, vol. 13, no. 8, pp. 687–689, 1988.

[53] S. Otte, "Nachrichtentechnische Modellierung und elektronische Entzerrung hochbitratiger optischer übertragungssysteme," Ph.D. dissertation, Christian-Albrechts-Universität Kiel, 2003.

[54] J. Speidel, "Communications III," Lecture, Institut für Nachrichtenübertragung, Universität Stuttgart.

[55] N. S. Muhammad, "Coding and Modulation for Spectral Efficient Transmission," Ph.D. dissertation, Institut für Nachrichtenübertragung, Universität Stuttgart, 2010.

[56] N. J. Shen, P. and. Gomes, P. A. Davies, W. P. Shillue, and P. G. Huggard, "PMD Effects on the Analogue Signal Transmission," National Radio Astronomy Observatory, Tech. Rep., 2004.

[57] J. Yang, W. L. Kath, and C. R. Menyuk, "Polarization mode dispersion probability distribution for arbitrary distances," *Opt. Lett.*, vol. 26, no. 19, pp. 1472–1474, 2001.

[58] D. Marcuse, C. R. Manyuk, and P. K. A. Wai, "Application of the Manakov-PMD equation to studies of signal propagation in optical fibers with randomly varying birefringence," *J. Lightw. Technol.*, vol. 15, no. 9, pp. 1735–1746, 1997.

[59] J. P. Gordon and H. Kogelnik, "PMD fundamentals: polarization mode dispersion in optical fibers." *Proc. of National Academy of Science USA*, vol. 97, no. 9, pp. 4541–4550, April 2000.

[60] J. Lima, I. R., R. Khosravani, P. Ebrahimi, E. Ibragimov, A. E. Willner, and C. R. Menyuk, "Polarization mode dispersion emulator," in *Proc. Optical Fiber Communication Conference (OFC)*, vol. 3, 2000, pp. 31–33.

[61] V. Systems, "VPI TransmissionMaker: Photonic modules reference manual," 2002.

[62] N. S. Bergano, F. W. Kerfoot, and C. R. Davidsion, "Margin measurements in optical amplifier system," *IEEE Photon. Technol. Lett.*, vol. 5, no. 3, pp. 304–306, 1993.

[63] S. Song, V. Bhatnagar, and J. Livas, "On the Gaussianly-distributed Q-factor in optical communication systems," in *Proc. 13th Annual Meeting IEEE Lasers and Electro-Optics Society 2000 (LEOS)*, vol. 2, 2000, pp. 409–410.

[64] J. Lima, I. T., A. O. Lima, J. Zweck, and C. R. Menyuk, "Computation of the Q-factor in optical fiber systems using an accurate receiver model," in *Proc. Optical Fiber Communications Conference (OFC)*, 2003, pp. 100–101.

[65] A. Kalra, J. Zweck, and C. R. Menyuk, "Comparison of bit-error ratios for receiver models with integrate-and-dump and realistic electrical filters using the Gaussian approximation," in *Proc. Conference on Lasers and Electro-Optics (CLEO)*, vol. 1, 2004.

[66] G. Bosco and P. Poggiolini, "On the Q-factor inaccuracy in the performance analysis of optical direct-detection DPSK systems," *IEEE Photonics Technology Letters*, vol. 16, no. 2, pp. 665–667, Feb. 2004.

[67] T. Foggi, E. Forestieri, G. Colavolpe, and G. Prati, "Maximum-likelihood sequence detection with closed-form metrics in OOK optical systems impaired by GVD and PMD," *J. Lightw. Technol.*, vol. 24, no. 8, pp. 3073–3087, 2006.

[68] H. F. Haunstein, R. Schlenk, H. M. Kallert, and V. A. Pauli, "BER measurements of a 40Gb/s receiver with adaptive threshold using polarization scrambling," in *Proc. Digest of the LEOS Summer Topical Meetings Holey Fibers and Photonic Crystals/Polarization Mode Dispersion/Photonics Time/Frequency Measurement and Control*, 2003.

[69] H. Sunnerud, P. A. Andrekson, and M. Karlsson, "Optimum receiver decision point in presence of PMD in fiber-optic communication systems," *IEEE Photon. Technol. Lett.*, vol. 15, no. 11, pp. 1651–1653, 2003.

[70] O. Coskun and K. Chugg, "Baud rate timing recovery and slicer threshold estimation for the adaptive dispersion compensation of fiber optical channels," in *Conference Record of the Thirty-Seventh Asilomar Conference on Signals, Systems and Computers*, vol. 1, 9-12 Nov. 2003.

[71] M. Siegrist, A. Dittrich, W. Sauer-Greff, and R. Urbansky, "Iterative Equalization for Nonlinear Channels with Intersymbol Interference," in *Proc. IEEE Workshop Signal Processing*, 2001, pp. 95–98.

[72] B. Vasic, I. B. Djordjevic, and R. K. Kostuk, "Low-density parity check codes and iterative decoding for long-haul optical communication systems," *J. Lightw. Technol.*, vol. 21, no. 2, pp. 438–446, 2003.

[73] A. Viterbi, "Error bounds for convolutional codes and an asymptotically optimum decoding algorithm," *IEEE Transactions on Information Theory*, vol. 13, no. 2, pp. 260–269, Apr. 1967.

[74] J. Forney, G., "Maximum-likelihood sequence estimation of digital sequences in the presence of intersymbol interference," *IEEE Trans. Inform. Theory*, vol. 18, no. 3, pp. 363–378, 1972.

[75] ——, "The Viterbi Algorithm," in *Proceedings of the IEEE*, 1973.

[76] G. Fettweis and H. Meyr, "Parallel Viterbi algorithm implementation: breaking the ACS-bottleneck," *IEEE Trans. Commun.*, vol. 37, no. 8, pp. 785–790, 1989.

[77] ——, "High-rate Viterbi processor: a systolic array solution," *IEEE Journal on Selected Areas in Communications*, vol. 8, no. 8, pp. 1520–1534, 1990.

[78] ——, "High-speed parallel Viterbi decoding: algorithm and VLSI-architecture," *IEEE Commun. Mag.*, vol. 29, no. 5, pp. 46–55, 1991.

[79] H. Dawid, G. Fettweis, and H. Meyr, "A CMOS IC for Gb/s Viterbi Decoding: System Design and VLSI Implementation," *IEEE Transactions on Very Large Scale Integration (VLSI) Systems*, vol. 4, no. 1, pp. 17–31, March 1996.

[80] J. Elbers, H. Wernz, H. Griesser, C. Glingener, A. Färbert, S. Langenbach, N. Stojanovic, C. Dorschky, T. Kupfer, and C. Schulien, "Measurement of the dispersion tolerance of optical duobinary with an MLSE-receiver at 10.7 Gb/s," in *Optical Fiber Communication Conference (OFC/NFOEC)*, vol. 4, 6-11 March 2005.

[81] S. Benedetto, E. Biglieri, and V. Castellani, *Digital Transmission Theory*. Prentice-Hall, 1987.

[82] A. Oppenheim, R. Schafer, and J. Buck, *Zeitdiskrete Signalverarbeitung*. Pearson Studium, 2004.

[83] M. Schetzen, *The Volterra and Wiener theories of nonlinear systems*. Wiley, 1980.

[84] G. Feldhaus, "Volterrafilter zur Modellierung und Entzerrung optischer übertragungssysteme mit Direktempfänger," Ph.D. dissertation, Universität Darmstadt, 2003.

[85] M. Bohn and C. Xia, "Electrical and optical equalization strategies in direct detected high-speed transmission systems," *AEU - International Journal of Electronics and Communications*, vol. 63, no. 7, pp. 526–532, 2009.

[86] C. Xia, M. Ajgaonkar, and W. Rosenkranz, "Nonlinear Electrical Equalization in MMF Links for 10-Gigabit Ethernet," in *Proc. 30th European Conference on Optical Communication (ECOC)*, vol. 4, 2004.

[87] ——, "On the performance of the electrical equalization technique in MMF links for 10-Gigabit Ethernet," *J. Lightw. Technol.*, vol. 23, no. 6, pp. 2001–2011, 2005.

[88] T. Freckmann and J. Speidel, "Linear and Nonlinear Electronic Feed-Forward Equalizers for DQPSK," in *Annual Meeting of the IEEE Lasers & Electro-Optics Society (LEOS)*, October 2007.

[89] N. Al-Dhahir and J. Cioffi, "Efficient computation of the delay-optimized finite length MMSE-DFE," *IEEE Transactions on Signal Processing*, vol. 44, no. 5, pp. 1288–1292, May 1996.

[90] Y. Gong and C. Cowan, "Optimum decision delay of the finite-length DFE," *IEEE Signal Processing Letters*, vol. 11, no. 11, pp. 858–861, nov. 2004.

[91] E. Chng and S. Chen, "Determining the optimal decision delay parameter for a linear equalizer," *International Journal of Automation and Computing*, vol. 2, pp. 20–24, 2005.

[92] C.-C. Yeh and J. Barry, "Approximate minimum bit-error rate equalization for binary signaling," vol. 2, Jun. 1997, pp. 1095–1099.

[93] ——, "Adaptive Minimum Bit-Error Rate Equalization for Binary Signaling," *IEEE Transactions on Communications*, vol. 48, no. 7, pp. 1226–1235, July 2000.

[94] V. Bhatia, B. Mulgrew, and A. T. Georgiadis, "Minimum BER DFE Equalizer in Alpha Stable Noise," in *The 2004 European Signal Processing Conference (EUSIPCO)*, 2004.

[95] J. Levendovszky, L. Kovacs, and E. van der Meulen, "Minimum Probability of Error-Based Equalization Algorithms for Fading Channels," *EURASIP Journal on Wireless Communications and Networking*, 2007.

[96] G. Katz and D. Sadot, "Minimum BER Criterion for Electrical Equalizer in Optical Communication Systems," *Journal of Lightwave Technology*, vol. 24, pp. 2844–2850, 2006.

[97] J. Nelder and R. Mead, "A simplex method for function minimization," *Computer Journal*, vol. 7, pp. 308–313, 1965.

[98] D. Efinger and J. Speidel, "Investigation of Fast and Efficient Adaptation Algorithms for Linear Transversal and Decision-Feedback Equalizers in High-Bitrate Optical Communication Systems," in *9. ITG Fachtagung Photonische Netze, Leipzig*, 2008.

[99] R. Lucky, J. Salz, and E. J. Weldon, *Principles of Data Communication*. McGraw-Hill, 1968.

[100] R. Lucky, "Automatic Equalization for Digital Communication," *Bell Systems Technical Journal*, vol. 44, pp. 547–588, 1965.

[101] N. Wiener, *Extrapolation, Interpolation, and Smoothing of Stationary Time Series*, 1st M.I.T. Paperback ed.   The MIT Press, 1964.

[102] S. Haykin, *Adaptive filter theory*, 4th ed.   Prentice Hall, 2001.

[103] J. R. Treichler, I. Fijalkow, and J. Johnson, C. R., "Fractionally spaced equalizers," *IEEE Signal Processing Mag.*, vol. 13, no. 3, pp. 65–81, 1996.

[104] J. Speidel, "Uebertragungstechnik II," Lecture, Institut für Nachrichtenübertragung, Universität Stuttgart.

[105] U.-V. Koc, K.-Y. Tu, and N. Kaneda, "Adaptive Electronic Equalization Using Higher-Order Statistics For PMD Compensation in Long-Haul Fiber-Optic Systems," in *Proc. 28th European Conf. Optical Communication ECOC 2002*, vol. 3, 2002, pp. 1–2.

[106] C. Xie, S. Chandrasekhar, D. Werner, and H. Haunstein, "Performance Evaluation of Electronic Equalizers for Dynamic PMD Compensation in Systems with FEC," in *Proc. Optical Fiber Communications Conf. OFC 2007*, March 2007.

[107] F. Buchali, "Advanced electronic equalization and signal processing for optical communication," 17th International Travelling Summer School on Microwaves and Lightwaves, July 2007.

[108] I. Djordjevic and B. Vasic, "Approaching Shannon's Capacity Limits of Fiber Optics Communications Channels Using Short LDPC Codes," in *Lasers and Electro-Optics, 2004. (CLEO). Conference on*, 2004.

[109] ——, "Iteratively Decodable Codes from Orthogonal Arrays for Optical Communication Systems," *IEEE Communications Letters*, vol. 9, no. 10, pp. 924–926, October 2005.

[110] I. Djordjevic, O. Milenkovic, and B. Vasic, "Generalized Low-Density Parity-Check Codes for Optical Communication Systems," *Journal of Lightwave Technology*, vol. 23, no. 5, pp. 1939–1946, May 2005.

[111] H. Bülow, W. Baumert, H. Schmuck, F. Mohr, T. Schulz, F. Kuppers, and W. Weiershausen, "Measurement of the maximum speed of PMD fluctuation in installed field fiber," in *Optical Fiber Communication Conference, 1999, and the International Conference on Integrated Optics and Optical Fiber Communication. OFC/IOOC '99. Technical Digest*, vol. 2, 21-26 Feb. 1999, pp. 83–85vol.2.

[112] B. Widrow and M. E. Hoff, "Adaptive Switching Circuits," in *1960 IRE WESCON Convention Record, Part 4*.   New York: IRE, 1960, pp. 96–104.

[113] B. Widrow and J. McCool, "A comparison of adaptive algorithms based on the methods of steepest descent and random search," *IEEE Trans. Antennas Propagat.*, vol. 24, no. 5, pp. 615–637, 1976.

[114] B. Widrow and S. Stearns, *Adaptive Signal Processing*. Pearson Education, 1985.

[115] R. Lucky, "Techniques for adaptive equalization of digital communication systems," *Bell System Technical Journal*, vol. 45, pp. 255–286, February 1966.

[116] J. Mazo, "Analysis of Decision-Directed Equalizer Convergence," *Bell System Technical Journal*, vol. 59, no. 10, pp. 1857 –1876, December 1980.

[117] Y. Sato, "A Method of Self-Recovering Equalization for Multilevel Amplitude-Modulation Systems," *IEEE Trans. Commun.*, vol. 23, no. 6, pp. 679–682, 1975.

[118] D. Godard, "Self-recovering equalization and carrier tracking in two-dimensional data communication systems," *IEEE Trans. Commun.*, vol. 28, no. 11, pp. 1867–1875, 1980.

[119] J. Johnson, R., P. Schniter, T. J. Endres, J. D. Behm, D. R. Brown, and R. A. Casas, "Blind equalization using the constant modulus criterion: a review," *Proc. IEEE*, vol. 86, no. 10, pp. 1927–1950, 1998.

[120] E. Walach and B. Widrow, "The least mean fourth (LMF) adaptive algorithm and its family," *IEEE Trans. Inform. Theory*, vol. 30, no. 2, pp. 275–283, 1984.

[121] M. U. Otaru, Z. A., L. Cheded, and A. Sheikh, "Adaptive Equalizer Based on a Power-of-Two-Quantized-LMF Algorithm," in *Eusipco 2006*, 2006.

[122] A. Carusone and D. Johns, "Analog filter adaptation using a dithered linear search algorithm," in *Circuits and Systems, 2002. ISCAS 2002. IEEE International Symposium on*, vol. 4, 26-29 May 2002, pp. IV–269–IV–272vol.4.

[123] F. Buchali, S. Lanne, J. Thiery, W. Baumert, and H. Bülow, "Fast eye monitor for 10 Gbit/s and its application for optical PMD compensation," in *Optical Fiber Communication Conference and Exhibit, 2001, OFC 2001*, vol. 2, 2001, pp. TuP5–1 – TuP5–3.

[124] F. Buchali and H. Bülow, "Adaptive PMD compensation by electrical and optical techniques," *Lightwave Technology, Journal of*, vol. 22, no. 4, pp. 1116–1126, April 2004.

[125] H. Haunstein, R. Schlenk, K. Sticht, A. Dittrich, W. Sauer-Greff, and R. Urbansky, "Control of combined electrical feed-forward and decision feedback equalization by conditional error counts from FEC in the presence of PMD," in *Proc. Optical Fiber Communications Conf. OFC 2003*, 2003, pp. 474–476.

[126] B. Wedding, A. Chiarotto, W. Kuebart, and H. Bülow, "Fast adaptive control for electronic equalization of PMD," in *Proc. Optical Fiber Communication Conf. and Exhibit OFC 2001*, vol. 2, 2001.

[127] F. Buchali, W. Baumert, H. Bülow, and J. Poirrier, "A 40 Gb/s eye monitor and its application to adaptive PMD compensation," in *Optical Fiber Communication Conference and Exhibit, 2002. OFC 2002*, 17-22 Mar 2002, pp. 202–203.

[128] X. Yi, F. Buchali, W. Chen, and W. Shieh, "Adaptation Algorithms for Receiver Based Electronic Dispersion Equalization," in *Optical Fibre Technology / Australian Optical Society (ACOFT/AOS), Australian Conference on*.   Australian Optical Society, July 2006, pp. 4–6.

[129] B. Franz, F. Buchali, D. Roesener, and H. Bülow, "Adaptation Techniques for Electronic Equalizers for the Mitigation of Time-Variant Distortions in 43 Gbit/s Optical Transmission Systems," in *European Conference on Optical Communications (ECOC)*, September 2007.

[130] W. Press, S. Teukolsky, W. Vetterling, and B. Flannery, *Numerical Recipes in C - The Art of Scientific Computing*, 2nd ed.   Cambridge University Press, 1992.